Electrochemical and optical modulation of selenide and telluride ternary alloy quantum dots genosensors

By

Peter Munyao Ndangili

A thesis submitted in fulfilment of the requirements for the degree of *Philosophiae Doctor* in the Department of Chemistry, University of the Western Cape

Supervisors: Prof. Emmanuel I. Iwuoha
Prof. Priscilla G. L. Baker

November 2011

Keywords

Amphiphilic bifunctional molecules

DNA sensors

Electrochemical impedance spectroscopy

Excitation/Emission matrix (EEM) fluorescence

5-enolpyruvylshikimate-3-phosphate synthase

Genetically modified organisms

Quantum dots

Electrochemical impedance spectroscopy

Ternary alloys

Gallium vacancies

Electrochemical and optical modulation of selenide and telluride ternary alloy quantum dots genosensors

P. M. Ndangili

PhD Thesis, Department of Chemistry, University of the Western Cape, November 2011.

Abstract

Electroanalytical and optical properties of nanoscale materials are very important for biosensing applications as well as for understanding the unique one-dimensional carrier transport mechanism. One-dimensional semiconductor nanomaterials such as semiconductor quantum dots are extremely attractive for designing high-density protein arrays. Because of their high surface-to-volume ratio, electro-catalytic activity as well as good biocompatibility and novel electron transport properties make them highly attractive materials for ultra-sensitive detection of biological macromolecules via bio-electronic or bio-optic devices. A genosensor or gene based biosensor is an analytical device that employs immobilized deoxyribonucleic acid (DNA) probes as the recognition element and measures specific binding processes such as the formation of deoxyribonucleic acid-deoxyribonucleic acid (DNA-DNA), deoxyribonucleic acid- ribonucleic acid (DNA-RNA) hybrids, or the interactions between proteins or ligand molecules with DNA at the sensor surface.

In this thesis, I present four binary and two ternary-electrochemically and optically modulated selenide and telluride quantum dots, all synthesised at room temperature in aqueous media. Cationic gallium (Ga^{3+}) synthesized in form of hydrated g**a**llium perchlorate salt [$Ga(ClO_4)_3.6H_2O$] from the reaction of hot perchloric acid and gallium metal was used to tailor the optical and electrochemical properties of the selenide and telluride quantum dots. The synthesized cationic gallium also allowed successful synthesis of novel water soluble and biocompatible capped gallium selenide nanocrystals and gallium telluride quantum dots. Cyclic voltammetric studies inferred that presence of gallium in a ZnSe-3MPA quantum dot lattice improved its conductivity and significantly increased the electron transfer rate in ZnTe-3MPA. Utraviolet-visible (UV-vis) studies showed that incorporation of gallium into a ZnSe-3MPA lattice resulted in a blue shift in the absorption edge of ZnSe-3MPA from 350 nm to 325 nm, accompanied by decrease in particle size. An amphiphilic bifunctional molecule, 3-Mercaptopropionic acid (3-MPA) was used as a capping agent for all quantum dots. It was found that 3-MPA fully solubilised the quantum dots, made them stable, biocompatible, non agglomerated and improved their electron transfer kinetics when immobilized on gold electrodes. Retention of the capping agent on the quantum dot surface was confirmed by Fourier transform infrared spectroscopy (FTIR) which gave scissor type bending vibrations of C-H groups in the region 1365 cm^{-1} to 1475 cm^{-1}, stretching vibrations of C=O at 1640 cm^{-1}, symmetric and asymmetric vibrations of the C-H in the region 2850 cm^{-1} to 3000 cm^{-1} as well as stretching vibrations of –O-H group at 3435 cm^{-1}. The particle size and level of non-agglomeration of the quantum dots was studied by high resolution transmission electron microscopy (HRTEM). The optical properties of the quantum dots were studied using UV-vis and fluorescence spectroscopic techniques.

Quantum dot/nanocrystal modified gold electrodes were prepared by immersing thoroughly cleaned electrodes in the quantum dot/nanocrystal solution, in dark conditions for specific periods of time. The electrochemical properties of the modified electrodes were characterized by cyclic voltammetry (CV), square wave voltammetry (SWV), electrochemical impedance and spectroscopy (EIS). Six sensing platforms were then prepared using quantum dot/nanocrystal, one of which was used for detection of dopamine while the rest were used for detection of a DNA sequence related to 5-enolpyruvylshikimate-3-phosphate synthase, a common vector gene in glyphosate resistant transgenic plants.

The first sensing platform, consisting of ZnSe-3MPA modified gold electrode (Au|ZnSe-3MPA) gave rise to a novel method of detecting dopamine in presence of excess uric acid and ascorbic acid. Using a potential window of 0 to 400 mV, the ZnSe-3MPA masked the potential for oxidation of uric and ascorbic acids, allowing detection of dopamine with a detection limit of 2.43×10^{-10} M (for SWV) and 5.65×10^{-10} M (for steady state amperometry), all in presence of excess uric acid (>6500 higher) and ascorbic acid (>16,000 times higher). The detection limit obtained in this sensor was much lower than the concentration of dopamine in human blood (1.31×10^{-9} M), a property that makes this sensor a potential device for detection of levels of dopamine in human blood.

The other sensing platforms were prepared by bioconjugation of amine-terminated 20 base oligonucleotide probe DNA (NH_2-5′-CCC ACC GGT CCT TCA TGT TC-3′) onto quantum dot modified electrodes with the aid of 1-ethyl-3-(3-dimethylaminopropyl) carbodiimide hydrochloride (EDC) and N-hydroxysuccinimide (NHS). The prepared DNA electrodes were electrostatically hybridized with different sequences which included 5′-GAA CAT GAA GGA

CCG GTG GG-3′ (complementary target), 5′-CATAGTTGCAGCTGCCACTG-3′ (non complementary target) and 5′-GATCATGAAGCACCGGAGGG-3′ (3-base mismatched target). The hybridization events were monitored using differential pulse voltammetry (DPV) and SWV by monitoring the guanine oxidation signal or using EIS by monitoring changes in the charge transfer resistance. The quantum dot genosensors were characterized by low detection limits (in the nanomolar range), long linear range (40 - 150 nM) and were able to discriminate among complementary, non-complementary and 3-base mismatched target sequences.

Dedication

I dedicate this thesis to

My mother

Mrs. Rosalia M. Ndangili

Declaration

I declare that *Electrochemical and optical modulation of selenide and telluride ternary alloy quantum dots genosensors* is my own work, that it has not been submitted for any degree or examination in any other university, and that all sources I have used or quoted have been indicated and acknowledged by complete references.

Peter Munyao Ndangili November 2011

Signed.....

Acknowledgements

First and foremost, I dearly thank the Almighty God for His grace throughout the period over which I carried out this study.

I would like to express my heartfelt thanks and profound gratitude to you, Professor Emmanuel Iwuoha and Professor Priscilla Baker (my supervisors), for not only giving me the opportunity to work with you on various projects, but also for introducing me to various exciting fields. I am indebted to you for giving me so much of your time and educating me in various aspects of laboratory and its operation whether it is regarding knowledge of equipment, their safety or operating them. Your willingness to help with anything at any time is greatly appreciated. Under your kind guidance, invaluable support, patience, keen interest, contributions and stimulating insight throughout the course of this study, I was able to complete this work and learned to become a better experimentalist and researcher.

I am grateful to Dr. Jahed Nazeem for his kindness, patience, inspired suggestions and encouragement over the years of my postgraduate studies.

I am heartily thankful to Dr. Kibe Macharia of Kenyatta University (Kenya) and Prof. Jane Catherine. Ngila of University of Johannesburg (South Africa) whose encouragement, guidance and support opened a great opportunity to my postgraduate education.

To SensorLab colleagues: Stephen Mailu, Gcineka Mbambisa, Kerileng Molapo, Godfrey Fuku, Abogile Jijana, Euodia Hess, Masikini Milua, Fanelwa Ngece, Abdu Baleg, Njagi Njomo, Rasaq Wale Olowu, Natasha West, Olubunmi Omoyeni, Tovide, Oluwakemi, Khotso

Tlhomelang, Busiswa Matyholo, Lundi Ngqongwa, Abebaw Tsegaye, Sibusiso Qwesha, Noluthando Myedi, Nolubabalo Matinise, Chinwe Ikpo, Chandre Willemse, Heidi Richards, Ismarelda Fillis, Robert Siebritz, Mawethu Bilibana, Christopher Sunday, Carlo Baugaard, Lindsay Wilson, Candice Rassie, your support and motivation is highly appreciated.

To my SensorLab postdocs: Dr. Tesfaye Waryo, Dr. Faiza Jan Iftikhar, Dr. Jasmina Martinovic, and Dr. Nicolette Hendricks, I dearly thank you for your invaluable support.

To the staff of the departments of Chemistry and Physics, UWC, thank you so much for the kind support that you accorded me during this period.

I am deeply indebted to my mother Mrs. Rosalia M. Ndangili; brothers Vincent Kioko *(RIP)*, Josphat Makau, Michael Mutuku, James Kilonzo, Joseph Muli *(RIP)* and Francis Wambua; and sisters Josephine Nthenya, Rosemary Mumbua and Elizabeth Kanini *(RIP)*. My gratitude also goes to my sisters in law, nephews and nieces for their support, wishes and constant encouragement from far away.

To Miss Juliann Makau, I deeply thank you for your unwavering moral support.

Special thanks are extended to my friends, Mr. & Mrs. Ben S. Manoo, Mr. Francis K. Nzoka, Mr. Nicholas L. Mailu, Mr.& Mrs. Gabriel M. Mbindyo, Mr.& Mrs. Musau Matheka, John Mutonya, Thaddeus M. Mwololo, Mr.& Mrs. Felix K. Musau, Mr. Mutulili and all others. I do also thank the staff of Kalulini Boys' High School for their interest in my PhD studies.

To the National Research Foundation (NRF), your financial assistance towards this research is hereby acknowledged.

Table of contents

List of figures

List of tables

List of publications

1. **Peter M. Ndangili**, Omotayo A. Arotiba, Priscilla G.L. Baker, Emmanuel I. Iwuoha (2010) A Potential masking approach in the detection of dopamine on 3-mercaptopropionic acid capped ZnSe quantum dots modified gold electrode in the presence of interferences, Journal of Electroanalytical Chemistry, 643 (1-2), 77-81.
2. **Peter M. Ndangili**, Abongile M. Jijana, Priscilla G.L. Baker, Emmanuel I. Iwuoha (2011) 3-Mercaptopropionic acid capped ZnSe quantum dot-cytochrome P450 3A4 enzyme biotransducer for 17 beta-estradiol, Journal of Electroanalytical Chemistry, *653 (1-2), 67-74*.
3. **Peter M. Ndangili**, Abongile N. Jijana, Rasaq A. Olowu, Stephen N. Mailu, Fanelwa R. Ngece, Avril Williams, Tesfaye T. Waryo, Priscilla G.L. Baker, Emmanuel I. Iwuoha (2011) Impedimetric Response of a Label-Free Genosensor Prepared on a 3-Mercaptopropionic Acid Capped Gallium Selenide Nanocrystal Modified Gold Electrode, International Journal of electrochemical Science, 6, 1438-1453.
4. **Peter M. Ndangili,** Rasaq A. Olowu, Njagi Njomo, Faiza Jan Iftikhar, Priscilla G.L. Baker, Emmanuel I. Iwuoha. Voltammetric response of a label free genosensor prepared on a 3-mercaptopropionic acid capped zinc selenide quantum dot modified gold electrode, Journal of Electroanalytical Chemistry (submitted).
5. **Peter M. Ndangili,** Rasaq A. Olowu, Njagi Njomo, Faiza Jan Iftikhar, Priscilla G.L. Baker, Emmanuel I. Iwuoha. Gallium-induced optoelectronic properties of surface capped chalcogenic (selenide) quantum dots, Langmuir (submitted).

List of abbreviations

ODN – Oligodeoxyribonucleotide

DNA – Deoxyribonucleic acid

GEOs – Genetically engineered organisms

GMOs – Genetically modified organisms

USA – United States of America

EU – European Union

PCR – Polymerase chain reaction

ELISA – Enzyme linked immunoabsorbant essay

CP4 epsps – 5-enolpyruvylshikimate-3-phosphate synthase

3-MPA – 3-mercaptopropionic acid

HRTEM – High resolution transmission electron microscopy

XRD – X -ray diffraction

FTIR – Fourier transform infra-red

CV – Cyclic voltammetry

SWV – Square wave voltammetry

DPV – Differential pulse voltammetry

DPASV – Differential Pulse anodic stripping voltammetry

EIS – Electrochemical impedance spectroscopy

AFM – Atomic force microscopy

EEM – Excitation/emission matrix

UV-vis – Ultraviolet visible

FRET – Fluorescence resonance energy transfer

Cy7 – Cyanine 7

Cy5 – Cyanine 5

PEG – Polyethylene glycol

VPE – Vapour phase epitaxy

CVD – Chemical vapour deposition

LPE – Liquid phase epitaxy

TOPO – Trioctylphosphine oxide

TOP – Trioctylphosphine

HDA – Hexadecyl amine

TDPA – Tetradecylphosphoric acid

GSH – Glutathione

PAMPAM – Poly(amidoamine)

G4 – Generation 4

G6 – Generation 6

G8 – Generation 8

HRP – Horseradish peroxidise

EDC – 1-ethyl-3-(3-dimethylaminopropyl) carbodiimide

Hb – Haemoglobin

ssDNA – Single strand deoxyribonucleic acid

dsDNA – Double strand deoxyribonucleic acid

DA – Dopamine

AA – Ascorbic acid

UA – Uric acid

RNA – Ribonucleic acid

EE – Electrochemical-electrochemical reaction

HRP – Horseradish peroxidise

DSG – Disuccinimidyl glutarate

PDC – Phenylene diisothiocyanate

NOS – Nopaline synthase

MWCTNs – Multi walled carbon nanotubes

HPV – Human Papilloma Virus

TE buffer – Tris-ethylenediamine tetraacetic acid buffer

EDTA – Ethylenediamine tetraacetic acid

PBS – Phosphate buffer saline

SCE – Saturated calomel electrode

CPE – Constant phase element

R_{ct} – Charge transfer resistance

Rs – Solution resistance

NLO – Non linear optical

IUPAC- International Union of Pure and Applied Chemistry

HOMO – Highest occupied molecular orbital

LUMO – Lowest unoccupied molecular orbital

NCS – Nanocrystals

SD – Standard deviation

LOD – Limit of detection

CHAPTER 1

General Introduction

1.1Background information

Organic and inorganic synthesis of materials for nature mimicry has attracted a lot of attention in the recent past, giving rise to, among others, synthesis of colloidal nanocrystals with tailored physical and chemical properties [1]. In particular, synthesis of nanostructured inorganic compounds has led to the development of a variety of approaches that mimic the recognition and nucleation capabilities found in biomolecules for a wide range of applications [2]. These nanocrystals present a hierarchical self-assembly of topologically complex and multifunctional architectures with properties tuneable at each level of the hierarchy [3]; an attribute that widens the scope of their applications. Among these nanostructured materials, semiconductor nanocrystals, also known as quantum dots, are an emerging class of materials that possess size-tunable optical and electronic properties. They have been one of the fastest moving and exciting interfaces of nanotechnology in the past decades [4]. This is due to their potential applications in several areas, including catalysis, coatings, textiles, data storage, biotechnology, health care, biomedical, pharmaceutical industries and most recently, in bioanalytical chemistry [5]. In bioanalytical chemistry, particular applications of quantum dots include their use as fluorescent labels, fluorescent probes, immunosensors and oligodeoxyribonucleotide (ODN) labels for deoxyribonucleic acid (DNA) sensors (genosensors) [6]. Tuning the size of quantum dots leads to quantum confinement effects, which permeates modulation of optical and electrochemical

properties of the nanocrystals [7]. The optical properties of quantum dots can as well be influenced by changing their chemical composition through alloying [8], which can be controlled at the synthesis stage. Another strategy to modulate the optical properties of quantum dots may involve substitution of host cations with metals like manganese, copper, or rare-earth elements [9]. By the incorporation of impurity atoms into the lattice of the host semiconductor, the dominant recombination route can be transferred to the impurity related trap states [7], providing an alternative pathway to the band-edge emission, which involves the highest occupied and the lowest unoccupied quantum-confined orbitals. Further modulation of their electronic properties involve suitable functionalization with amphiphilic bifunctional molecules such as marcapto carboxylic acids [HS-(CH_2)*n*-COOH, *n*=1-15] [10]. These molecules permeate rapid transfer of electrons between the small sizes of quantum dots and the surface of the target particles, resulting to a higher charge detaching efficiency [11]. Short chained capping agents such as mercaptopropionoc acid (MPA) have been used for self assembly on gold electrodes [12] and are associated with enhanced electrochemical signals of the quantum dots towards target analytes [13]. The power and scope of electrochemically and optically modulated quantum dots can be greatly enhanced by coupling them with biological recognition reactions and electrical processes, to form nanobioelectronics [14]. This coupling also requires proper surface tailoring and functionalization of the quantum dots, to make them biocompatible [15]. Besides improving the nanocrystal electrochemistry, the marcapto carboxylic acids leave free carboxylic acid groups on the surface of the quantum dots, which can covalently link favourably with amine groups of biomolecules, thus conferring biocompatibility properties on the quantum dots. Quantum dot-biopolymer conjugates have a great potential for DNA diagnostics and can have profound impact in analysis of DNA in genetically modified foods.

In recent years, agricultural enterprises in many parts of the world have developed new varieties of organisms by adopting modern technology which includes genetic transformation [16]. This has been necessitated by increasing global population and as a consequence, increasing nutritional demands [17]. With the need to overcome agricultural production constrains (drought, salinity and pests among others), agricultural biotechnology has come up with a set of biology techniques (genetic engineering) that have been used to manipulate genetic makeup of an organism by introducing, modifying or eliminating specific genes [18]. It seeks to reduce or even eliminate the need for pesticides and other agrochemicals, increase crop yield, improve micronutrient, bioavailability and other nutritional properties of most important staple food crops as well as making the crops tolerant to drought [19]. Genetic engineering also aims at remediation of contaminated areas, thereby increasing sites available for food production [20]. In genetic engineering, genes transfer between unrelated species is allowed; resulting to genetically engineered organisms (GEOs), also known as genetically modified organisms (GMOs) that contain additional or modified characteristics encoded by the introduced genes. The technology of genetically modified organisms dates back to 1984 when the first successful genetically modified tobacco, resistant to antibiotics was reported [18]. Thereafter, a genetically modified tomato (Flavr Savr tomato) produced by the Californian company Calgene, which was resistant to rotting became the first genetically engineered food to be approved for human consumption [21]. Over 40% of the corn, 50% of cotton and 45% of soybean acres planted in 1999 in United States of America (USA) were genetically modified and up to 2002, over 60% of food products in US supermarkets contained genetically modified foods [16]. Moreover, a total of 23 countries, 11 of which are developed countries and 12 developing countries had already cultivated genetically modified crops by the year 2007, with 282.4 million acres producing GMOs [18]. It

is also projected that, the acreage production of GMOs will double by the year 2015 [22]. The emergence of this new generation of genetically engineered materials, compounded with the commercial food trades that involve imports and export of these products, as well as the projected mass production of GMOs has raised concerns that confuse not only the general public but also the scientific community. The scientific concerns involve several questions. The first one is whether the introduced DNA and/or its intended expression product or intended compositional changes may negatively affect the nutritional content or cause toxicity and or allergenecity [19]. Secondly, a question of whether the introduced DNA may cause any unintended changes in nutritional content, toxicity of allergenecity by disrupting or altering the functions of non-targeted genes [19]. Thirdly, there are also concerns about possible transgene horizontal transfer. Transgene horizontal transfer involves the transfer of genetic material by an organism to another one, other than its offspring and whose process is followed by integration and expression of the genetic material [18]. The health concerns of horizontal transfer of transgenes include the potential non-expected alterations in nutritional composition, allergenecity or toxicity of the new genetically modified product [23]. There are also reports of persistence of recombinant DNA from genetically modified organisms in the environment. Losey et al 1999 [22] and Saxena et al 1999 [24], have for instance reported the persistence of recombinant DNA in air while other studies showed that recombinant DNA from decomposition of genetically modified crops could be detected several years or months later [25]. Moreover, persistence of recombinant DNA from genetically modified organisms has been detected in food chain [26] and in genetically modified crops fed to poultry and livestock [27]. In many parts of the world, legislations have been put in place to regulate the presence of genetically modified organisms in crops, foods and ingredients [16]. In South Africa for example, the Genetically Modified

Organisms Act, 1997 (Act No. 15 of 1997) was passed to regulate the importation, exportation, development, production, use, release or distribution of genetically modified organisms [28]. Such legislations have necessitated development of sensitive and reliable methods for detection, identification and quantification of genetically modified organisms (GMOs) in products. Detection or screening of GMOs is a purely qualitative aspect of analysis whose aim is to determine if a product contains a GMO or not. It gives a 'yes' or a 'no' answer. Identification serves to reveal the number of GMOs in a product and answers the question of whether the GMOs found in a product are authorized or not. If a product is found to contain one or more authorized GMOs, it becomes necessary to quantify the exact amount of GMOs in the product. This helps in determining whether the GMO product exceeds the set thresholds for GMO legislation, for instance 1% in European Union (EU) [29]. Most of the methods so far developed are protein/DNA based and include western blots [30], mass spectroscopy, near infrared spectroscopy, southern blots, lateral flow strips, polymerase chain reactions (PCR), enzyme linked immunoabsorbant essay (ELISA) or PCR-ELISA and recently electrochemical methods [31]. However, these methods vary in the degree of reliability, reproducibility, robustness, cost, complexity and speed among other key performance aspects. A summary of performance characteristics of these methods is tabulated below.

Table 1: Performance characteristics of protein and DNA based methods for detection of DNA in genetically modified foods.

Parameter	Protein based				DNA-based		
	Western blot	**ELISA**	**Lateral flow strip**	**Southern blot**	**Qualitative PCR**	**Quantitative-competitive PCR**	**Real-time PCR**
Ease of use	Difficult	Moderate	Simple	Difficult	Difficult	Difficult	Difficult
Need for special equipment	Yes	Yes	No	Yes	Yes	Yes	Yes
Sensitivity	High	High	High	Moderate	Very high	High	High
Duration	2days	30-90 min	10 min	6 hrs	1.5 days	2 days	1 day
Cost/sample (USD $)	150	5	2	150	250	350	450

Gives quantitative results	No	Yes	No	No	No	Yes	Yes
Suitable for field test	No	Yes	Yes	No	No	No	Yes
Employed mainly in	Academic labs	Test facility	Field testing	Academic labs	Test facility	Test facility	Test facility

Furthermore, most of these methods may not be effective in all the three analytical circumstances (if a product contains GMOs, the type of transgenes and the amount of transgenes). For example, ELISA methods rely on specific binding between an antibody and a protein and any conformational changes in the tertiary structure of the protein may render the method ineffective. Such conformational changes are likely to occur during food processing.

In search for alternatives to these methods, an impressive number of inventive designs for DNA based electrochemical sensing have appeared [32-33]. A common feature of all these sensors is that they combine nucleic acid layers with electrochemical transducers to produce a sensor devise which is simple, accurate, inexpensive and specific to the analyte of interest. Of great importance in this study are excellent structure-related electrochemical properties possessed by DNA, both single strand and hybridized double strands. DNA is made up of

subunits called oligonucleotides, each made up of a sugar, a phosphate and a base. There are four different bases in each DNA molecule. These are adenine (A) and guanine (G) (purine bases) as well as cytosine (C) and thymine (T) (pyrimidine bases). The chemical structure of each of these bases is given below

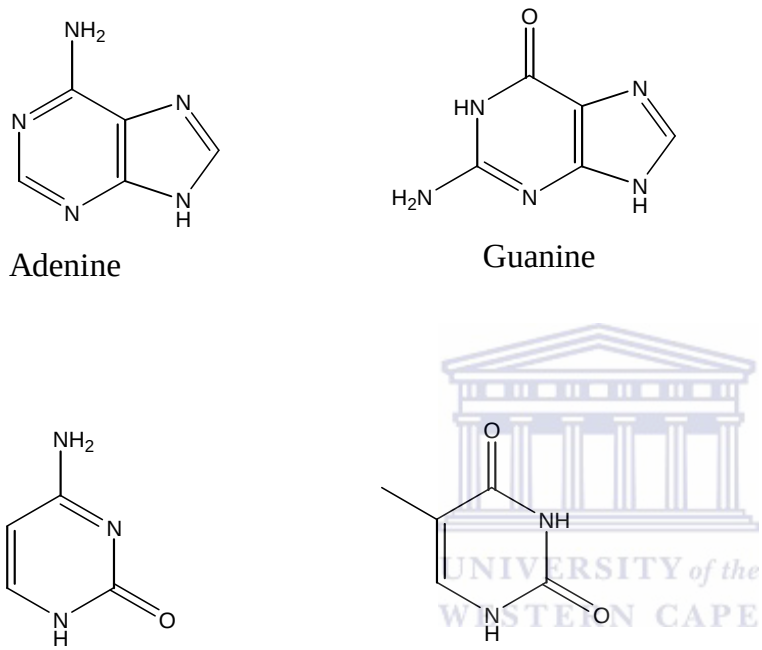

Figure 1: Chemical structure of the DNA bases

In a normal DNA structure, a Watson-Crick base pairing occurs whereby guanine forms hydrogen bonds with cytosine and while adenine forms hydrogen bonding with thymine. This process is commonly called hybridization and gives rise to double stranded oligonucleotides whose structure of given in the figure below.

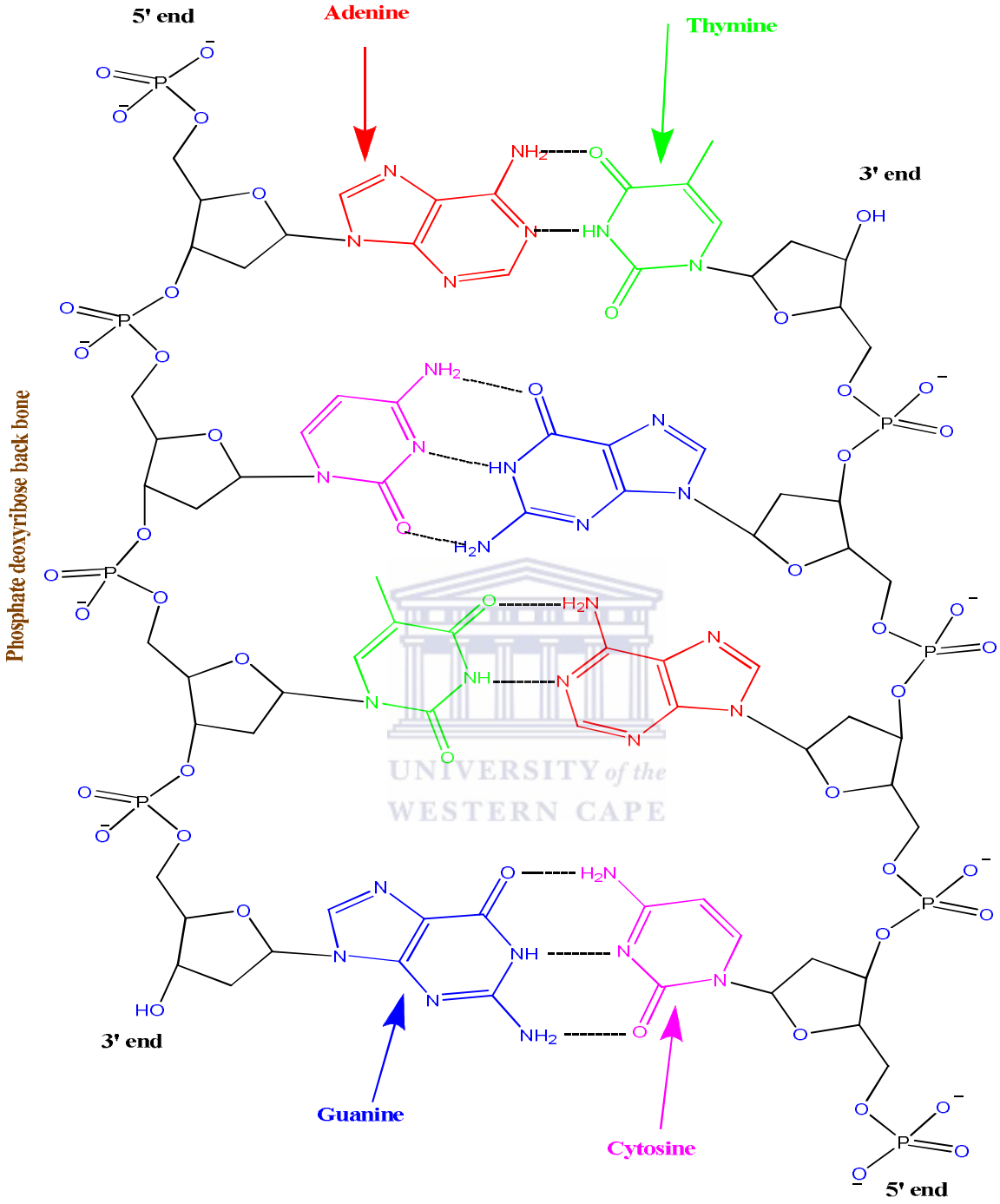

Figure 2: Canonical Watson-Crick DNA base paring through G-C and T-A intermolecular hydrogen bonds.

Of these four bases, guanine and adenine have attracted great research interest due to crucial roles that they play in metabolic and analytical processes. They participate in fundamental functions such as energy transduction, metabolic co-factors and cell signalling. They are essential building blocks of nucleic acids and determination of their individual concentrations in an organism is an important practice in biomedical analysis, molecular pathology, environmental and forensic science. This is because; deficiency of these purine bases is a key indicator of possible mutation of the immune system and aging [34].

The development of electrochemical transducer based devices for determining nucleotide sequences and measuring DNA hybridization began with the discovery of the electroactivity of nucleic acids about 50 years ago [35]. When nucleic acids interact with solid electrodes, they are strongly adsorbed and undergo charge transfer reactions, producing signals that can provide information about their type, concentration, their structural changes as well as their interaction with various compounds. Moreover, strongly adsorbed nucleic acids on solid electrodes can be the basis for fast response DNA detectors. At physiological and alkaline pH, the potential window of most solid electrodes is about 1000 mV more positive than that of the mercury electrode, which usually operates within the range 0 to -2000 mV versus saturated calomel electrode. Solid electrodes are therefore best suited for studying nucleic acids oxidation while mercury electrodes would suit studies involving reduction of nucleic acids. Amongst the components of nucleic acids, only the bases undergo reduction at mercury electrodes and oxidation at other solid electrodes such as carbon. There are however some reports of oxidation of the nucleic acids sugar residues at copper electrodes using sinusoidal voltammetry. Of the oxidizable nucleic acid bases, the purine bases (guanine and adenine) are of particular interest to

electrochemists since they undergo oxidation with relative ease and can allow for quantification of a DNA sample [36].

The negatively charged phosphate backbone of the DNA also possesses electrochemical properties that can be used for detection of DNA upon hybridization. The detection methods for electrochemical DNA hybridization are classified into two major protocols; direct and indirect detections [37]. In direct electrochemical detection of DNA hybridization, the signal monitored arises from oxidation of the purine nucleobases, adenine and guanine [38]. The oxidation of adenine and guanine at mercury electrodes has been reported [39]. However oxidation signals of these nucleobases at other solid electrodes such as gold, copper, carbon have limited use in analytical purposes since they are poorly developed with very high over potential and often merge into background discharge current. To overcome this, modified electrodes have been explored to enhance the oxidation signals of these bases. The oxidation of guanine is a complex mechanism and is thought to be a $4e^-$, $4H^+$ system. The first step is a $2e^-$, $2H^+$ electrochemical-electrochemical reaction (EE) whereby, the guanine forms 8-oxoguanine. The loss of the first electron gives an intermediate radical species. This species may dimerize to form an electroactive product which can undergo oxidation at potentials higher than those of the radical formation. The 8-oxoguanine formed in step one can further undergo a reversible $2e^-$, $2H^+$ to give highly hydrolysable products. This simplified mechanism of guanine oxidation is illustrated in the scheme below.

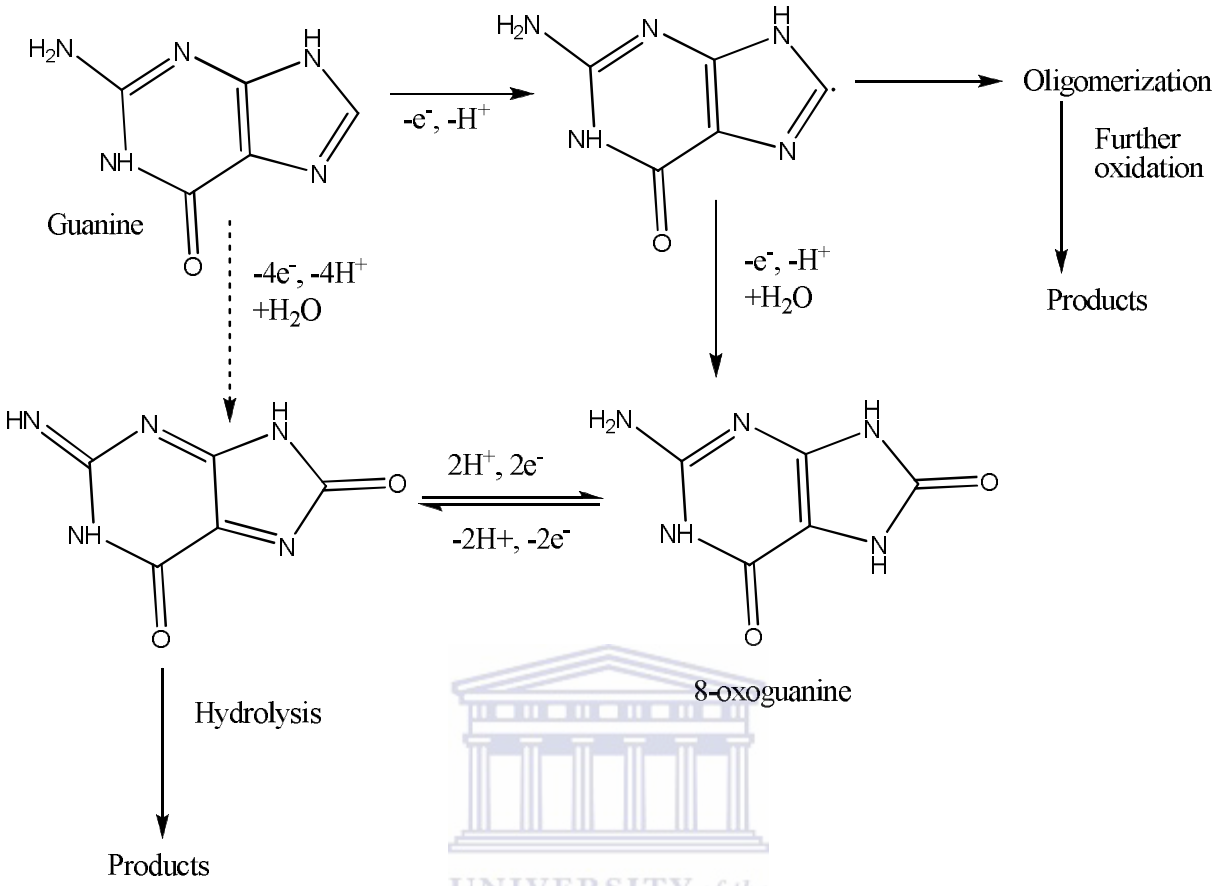

Figure 3: Simplified mechanistic pathway for the oxidation of guanine

Up on hybridization of single strand probe DNA with its complementary single strand target DNA, two major events, which affect the extent of oxidation of guanine base, take place. First, the electrochemical signal emanating from oxidation of the probe's free guanine bases decrease upon hybridization with cytosine bases on the target DNA. This is because; guanine becomes less accessible for oxidation after formation of the duplex hybrid chain. The other possibility is that, the guanine oxidation signal may increase due to increase in the total number of guanine bases in the double strand DNA compared to the single strand DNA. Measuring the decreased guanine oxidation signal in the immobilized probe is very limited as it cannot be used to quantify

target DNA containing guanine bases [40]. To overcome this, inosine modified probe DNA (free from guanine base) can be used. Inosine is an electro-inactive form of guanine, capable of forming a base pair with the cytosine residue of the target [41] and its oxidation signal is well separated from the guanine signal. Following hybridization, the duplex formation is detected by monitoring the appearance of the targets guanine signal. The guanine oxidation signal in this case increases upon hybridization. However, due to lack of probe's oxidation signal, it is difficult to follow up its signal as well as optimizing its immobilization conditions. Moreover, the introduction of an extra nucleotide (inosine) increases the biosensor preparation protocols and hence its cost. This can be improved by use of a probe which contains preferably only one or few guanine bases with several cytosines. The presence of guanine base in the probe DNA provides weak guanine oxidation signal, which allows one to monitor probe immobilization and consequently optimize its immobilization on the electrode [37, 42]. The cytosine bases in the probe are available for hybridization with target DNA that contains several guanine bases, hence enhancing the electrochemical signal. On the basis of this approach guanine oxidation signal remarkably increases after hybridization of probe with DNA target and therefore, can be easily recorded.

Indirect electrochemical DNA biosensors are based on electrical transduction of DNA hybridization by an accompanied accumulation of redox compounds at the DNA-modified electrode surface [43]. These redox compounds include organic dyes such as methylene blue [44-45] and metal complexes involving cobalt, ruthenium and osmium [46]. The hybridization reaction can as well be monitored by intrinsic signals of nucleic acids, electroactive labels such as enzymes and metal nanoparticles covalently bound to the target DNA [47-48] or changes in interfacial properties [32]. Electrochemical DNA biosensors offer high sensitivity, small

dimensions, low cost, high selectivity, and compatibility with micro fabrication technology and miniaturization of instruments [49]. The objective of this study is to develop electrochemically and optically modulated biocompatible nanocrystal architectured genosensors for quantitative detection of 5-enolpyruvylshikimate-3-phosphate synthase (CP4 *epsps)* DNA.

1.2 Problem statement

In spite of the progress made in synthesis of nanocrystals, water soluble and biocompatible gallium based quantum dots have not been explored due to rare cationic chemistry of Ga^{3+}. Whereas compounds of gallium in its univalent oxidation state have been reported, details of cationic existence of Ga^{3+} are scanty. Modulation of optical and electrochemical properties of quantum dots has in the past relied on particle size. The classical reliance of particle size to modulate quantum dot optical properties will in this work be replaced by gallium alloying. This work will therefore present a significant contribution in the scope of colloidal synthesis of nanocrystals. Proper modulation of their electrochemical and optical properties though controlled alloying will widen the scope of nanocrystal applications in electrochemical sensors and opto sensors. Successful functionalization with 3-mercaptopropionic acid, to make the nanocrystals biocompatible is envisaged to increase the scope of platforms onto which biomolecules can be attached for diagnostic purposes.

In view of the global increase in GMO production and trade, health and environmental related theories regarding consumption of GMOs, the legislations governing production and consumption of GMO products as well as challenges facing the existing analytical techniques for

analysis of transgenic products described above, it leaves no doubt that the search for low cost, user friendly, and fast response analytical devices still remains one of the main goals of scientific research. Although the electrochemical detection of DNA hybridization has witnessed progressive development as an alternative to the classical methods of DNA detection, it is limited to the use of gold nanoparticles and nanostrucured polymeric materials and composites as platforms for attachment of the probe DNA. Quantum dots are much smaller than these nanostructured materials but only a few reports have used them as labels for electrochemical detection of DNA hybridization. In this study, quantum dots will be used as biocompatible platforms for immobilization of the probe DNA. It is hoped that the large surface area of the quantum dots will offer more binding points for attachment of the probe DNA. Since high DNA loading is usually associated with enhanced efficiency, this is expected to improve sensitivity, lower detection limits and realize large detection ranges for voltammetric and impedimetric genosensors. With confinement of electrons within a very small 3 dimensional sphere in the quantum dots (due to quantum confinement effects), the electron transfer energetic are tuned such that fast electron transfer rates between oxidized guanine signals and the electrode would be high, resulting to amplified electrochemical signals.

1.3 Objectives of the research work

1.3.1 General objectives

This study was aimed at exploring cationic gallium as an impurity for modulation of optical and electrochemical properties of telluride and selenide quantum dots. It was also aimed at replacing the gold nanoparticles, nanostrucured polymeric materials and composites as platforms for attachment of the probe DNA with quantum dots; and to specifically detect an oligonucleotide sequence related to 5-enolpyruvylshikimate-3-phosphate synthase, a common vector gene in glyphosate resistant transgenic plants.

1.3.2. Specific objectives

i. Synthesis of 3-mercaptopropionic acid (3-MPA)-capped chalcogenic- selenide and telluride quantum dots.

ii. Optical interrogation of MPA-capped quantum dots by ultraviolet visible (UV-vis) and 2D as well as 3D excitation/emission matrix fluorescence.

iii. Spectroscopic and microscopic analysis of the quantum dots using high resolution transmission electron microscopy (HRTEM), X-ray diffraction (XRD) and Fourier transform infra-red spectroscopy (FTIR).

iv. Electroanalysis of the MPA-capped selenide and telluride quantum dot-modified gold electrodes using cyclic voltammetry (CV), square wave voltammetry (SWV) and electrochemical impedance spectroscopy (EIS).

v. Development of quantum dot genosensors with an amine terminated 20 bases DNA whose sequence is NH_2-5′-CCC ACC GGT CCT TCA TGT TC-3′.

vi. Modelling the impedimedric and amperometric responses of the genosensors to complimentary (5 enolpyruvylshikimate-3-phosphate synthase: 5′-GAA CAT GAA GGA CCG GTG GG-3′), non-complementary **(**5′-CAT AGT TGC AGC TGC CAC TG-3′**)** and 3-base mismatch **(**5′-GAT CAT GAA GCA CCG GAG GG-3′**)** DNA sequences.

1.4 Hypothesis of the study

i. The incorporation of gallium into ZnSe or ZnTe lattice will influence the optical and electrical properties of ZnSe and ZnTe quantum dots by providing an alternative pathway to the band-edge emission and/or electronic transitions involving the highest occupied and the lowest unoccupied quantum-confined orbitals.

ii. The capping of the quantum dots with 3-mercaptopropionic acid will permeate covalent linkage between free carboxylic acid groups on the surface of the quantum dots and amine groups of the probe DNA; giving rise to quantum dot-biopolymer conjugates which will be used for detection of the target DNA.

1.5 Thesis layout

This thesis is presented in ten chapters

Chapter one gives the background information with a brief discussion on semiconducting nanocrystals, emergence of genetically modified organisms, potential health and environmental effects as well as methods of detecting transgenic organisms. The properties possessed by DNA and its importance in analysis of genetically modified products are also highlighted.

Chapter 2 covers introduction to quantum dots, detailing their current composition, advantages over classical dyes and semiconductors as well as their properties, reportedly superior to those of classical dyes and semiconductors. A review of the progress made in the synthesis (methods) and functionalization (strategies) of quantum dots is also described in this chapter. This chapter also features a review of the applications of quantum dots, with specific attention given to optical and electrochemical biosensor applications. A further description of the applications of quantum dots in electrochemical detection of DNA hybridization is given, since it is one of the interests in this study. Various methods of electrode modification/immobilization of the probe DNA as well as different electrochemical techniques used for detection of DNA hybridization are also described in this chapter.

Chapter 3 begins by listing all reagents used in this study and their respective sources. The techniques used in this study and the principles underlying each technique are also described. A description of all procedures for synthesis and characterization of the telluride and selenide quantum dots also features in this chapter. The last part of this chapter describes the procedures for the fabrication, characterization and application of voltammetric and

impedimetric sensors and genosenors for detection of selected analytes; mainly dopamine and an oligonucleotide sequence related to 5-enolpyruvylshikimate-3-phosphate synthase, a common vector gene in glyphosate resistant transgenic plants.

Chapter 4 discusses the electrochemical, microscopic and optical properties of selenide binary and ternary quantum dots.

Chapter 5 discusses the electrochemical, microscopic and optical properties of telluride binary and ternary quantum dots.

Chapter 6 introduces us to the journey towards applications of the quantum dots by evaluating their catalytic properties. In this case, ZnSe-3MPA is chosen as a representative model and an easily oxidizable analyte (dopamine) is chosen as the analyte, in recognition of its role in functioning of cardiovascular, renal, hormonal and central nervous system. The catalytic oxidation of dopamine is studied in presence of excess co-existing uric and ascorbic acids and whose electrochemistry at unmodified electrodes in known to overlap, making it impossible to detect any of the three independently. In the process, this chapter introduces a novel method, by use of ZnSe-3MPA, to mask the potential of both uric and ascorbic acids, thus allowing detection of dopamine in their excess presence.

Chapter 7 discusses the experimental results of an “Impedimetric response of a label-free genosensor prepared on a 3-mercaptopropionic acid capped gallium selenide nanocrystal modified gold electrode”.

Chapter 8 discusses the experimental results of a “Voltammetric response of a label-free genosensor prepared on a 3-mercaptopropionic acid capped zinc selenide quantum dot modified

gold electrode. In this chapter, the few versus the many guanine bases in the probe and target DNA respectively are exploited to come up with a genosensor that relies on guanine oxidation peak as the analytical signal.

In chapter 9, the results of impedimetric response of label free genosensors prepared on three different telluride quantum dots (ZnTe-3MPA, Ga_2Te_3-3MPA and $Zn_2Ga_2Te_5$-3MPA) are discussed.

Chapter 10 presents the conclusions and recommendations.

CHAPTER 2

Literature Review

2.1 Introduction to quantum dots

Quantum dots are semiconductor fluorescing nanoparticles whose dimensions are confined to a 1-10 nm scale [50-51] or 2-20 nm [52]. The size of the particle determines the colour emitted with smaller particles emitting shorter wavelengths and larger particles emitting longer wavelengths [51, 53]. The small size and the composition of the quantum dots allow the tuning of its optical properties which allows for the large array of colours [53]. The small size of quantum dots causes the energy levels of the different bands to be quantized and therefore are directly related to the size of the dots [54]. As the particles decrease in size, the band gap increases which results in more energy needed to be absorbed to reach the higher energy levels or the band gap becomes blue shifted [55]. Therefore larger particles emit toward the infrared region while smaller particles emit toward the ultraviolet region [51]. This phenomenon is called "quantum confinement" and applies to particles that are smaller than the Bohr exciton radius (~ few nanometres) [54]. Bulk semiconductors, however, do not possess this property since the energy level spacing is small and resemble more of a continuum [56]. Therefore, above a certain size, optical properties of semiconductor particles resembles those of bulk solids and no longer does the size determine the optical property [56].

2.1.1 Composition of inorganic quantum dots

Quantum dots are based on metals such as nickel, cobalt, platinum, silver and gold among others, or mostly inorganic semiconductor compounds. Quantum dots made of metalloid materials such as silicon have also been studied [57]. In this work, we shall focus on quantum dots composed of inorganic semiconductor compounds. Inorganic semiconductor quantum dots are fabricated from elements in periodic groups II-VI (CdSe, CdS, CdTe), IV – VI (PbS, PbSe, PbTe and SnTe) and III-V (InP, InAs, GaAs) [58-59]. The compounds mentioned in these groups only present the core-materials of the quantum dots but in most cases, additional shells are usually put on the surface of these nanocrystals for various reasons such as stabilization as well as improvement of their luminescence properties.

2.1.2 Advantages of quantum dots over conventional semiconductors

Conventional semiconducting materials such as germanium, gallium arsenide, silicon carbide, and silicon among others are often used in electrical circuits. However, they have limited ranges of tolerance for the frequency of the current they carry. The low tolerance of conventional semiconductors often poses a problem to circuits and many of its applications. On the other hand quantum dots, owing to their artificial fabrication can be made to tolerate different current frequencies over a much larger range of frequency than the conventional semiconductors. This gives the user more control over the flow of current. Cellular and molecular imaging, cell labelling and tracking, multiplex analyses and DNA detection are the specific conventional biological applications that employ fluorescence. Fluorescence resonance energy transfer (FRET), which involves a non-radiative transfer of excitation energy from a donor molecule (D)

to a proximal ground state acceptor molecule (A) presents a powerful tool for probing a variety of biological processes [4]. FRET uses fluorophores to probe the biological processes that result from events such as protein-protein interactions, ligand-receptor binding and changes in protein and oligonucleotide conformation in response to some biological stimulus. An ideal fluorescence marker for single colour applications should be bright, biocompatible, photo stable and non-toxic to the sample. Besides these characteristics, multicolour fluorescent experiments also require fluorophores to exhibit spectrally resolvable emission profiles with narrow symmetric emission spectra. Organic fluorophores such as organic dyes (Cyanine 7 - Cy7, oxazine 750, indocyanine green [60]), fluorescent proteins, chemiluminescent substrates and fluorescent polymers do not possess all these properties and therefore their application in multicolour fluorescence experiments can be problematic and limit the extent to which they can be applied for fluorescent labelling of biomolecules. Organic fluorophores are particularly associated with broad emission spectra, narrow excitation range and short fluorescence times [53-54, 61]. The broad emission spectra of these organic fluorophores create overlapping detection ranges that make multiplex analysis challenging [58]. Besides these, conventional fluorophores that are prone to chemical and photo-degradation, with low quantum yields and sensitive to pH present added limitations to the degree of their application in fluorescence studies. Particularly, indocyanine green which is mostly used as a near infrared dye has a quantum yield of 1.2% [62]. On the other hand, quantum dots have larger surface area compared to most conventional fluorophores, especially monovalent dyes. This permeates multiple functionalizations, which in turn gives rise to multireactive binding sites. Several biomolecules can therefore be attached to a single quantum dot, enhancing target affinity and energy transfer efficiency. Quantum dots are estimated to be more than 20 times brighter and more stable than traditional fluorophores [63-64]. This allows

for ultrasensitive detection, long term imaging and rapid detection applications such as flow cytometry [65]. Compared to existing labels, nanoparticles in general and quantum dots especially, are cheaper. They allow more flexibility, faster binding kinetics (similar to those in a homogeneous solution), high sensitivity and high-reaction rates for many types of multiplexed assays, ranging from immunoassays to DNA analysis [50]. Quantum dots exhibit broad absorption spectra, very high photostability, long fluorescence life time and very narrow emission spectra [66]. Further to these, the optical and electronic properties of quantum dots can be controlled to suit particular applications by varying the nanocrystal size, composition as well as post synthesis functionalization. Quantum dots therefore possess excellent optical and electronic properties that offer more promising alternatives to conventional semiconductors and fluorophores, thus attracting a lot of interest in scientific research [6]. This has in turn resulted in a shift from use of conventional semiconducting materials to quantum dots. For instance, quantum dots have recently replaced traditional fluorophores in applications that involve labelling and fluorescence imaging of protein molecules [6]. In spite of the excellent properties that quantum dots posses compared to conventional semiconductors and fluorophores, quantum dots possess properties such as water insolubility, non-specific binding, photo bleaching, aggregation or agglomeration of the nanocrystals, low quantum yield, intermittent blinking and toxicity that limit the extent of their applications.

2.1.3 Properties of quantum dots that pose challenge to their applications

2.1.3.1 The toxicity of quantum dots

The cytotoxicity of the quantum dots is probably the most cited limitation for in vivo applications. Although not many toxicity studies have been done, great concern has been raised over use of quantum dots in live cells and animals. Toxicity of quantum dots arises mainly from their composition [67]. The reason for this is that quantum dots mostly contain heavy metal atoms such as cadmium, mercury, lead and arsenic which are toxic [67]. The metal in the core shell of some quantum dots is therefore believed to be responsible for extra cellular cytotoxicity. Particularly, cadmium based quantum dots have been reported to show some cytotoxicity, emanating from release of cadmium ions (Cd^{2+}) upon exposure to air or UV radiation [68] . Cd^{2+} ions are able to bind to thiol groups on critical molecules in the mitochondria leading to enough stress and damage to cause significant cell death [58]. Small sized quantum dots, with green emission have more harmful effects than large red emitting quantum dots [69], implying that the size of the quantum dots affects their toxicity too. The surface capping and functionalizing materials as well as their concentrations could also affect the extent of the cytotoxicity of quantum dots. Hoshino et al. [70] investigated the cytotoxicity of differently capped quantum dots using a number of techniques which included comet assay and flow cytometry. Studies by these authors suggested that the ligand used to cover the quantum dots was responsible for the cytotoxicity effect and not the nanoparticle itself. The lowest cytotoxicity was observed by these authors with thioglycerol-coated quantum dots compared to carboxylic acid and amine-coated quantum dots. Besides extra cellular cytotoxicity, reports by Chang et al established that

quantum dots could also cause endo cellular cytotoxicity, especially when they enter the cells by endocytosis [71]. The authors further suggested that, irrespective of the surface coating of quantum dots, cell death is highly related to the amount of quantum dots' uptake into the cells. Once in the cell, quantum dot metabolism and degradation is largely unknown and accumulation of quantum dots in the kidney, spleen and the liver has been reported in several studies [56]. Also it is unknown whether the quantum dots can be cleared from the body [56].

Researchers in the recent past have proposed silicon based quantum dots as alternative to potentially toxic quantum dots [72]. These quantum dots, like many others can allow for surface modification. An even friendlier alternative to heavy metals for synthesis of quantum dots is zinc. Zinc is one of the most important minerals that are found naturally in our bodies and assists body functions in a number of ways. At cellular level, zinc helps in cell division and assists in liver functioning as well as expediting healing of wounds. It assists in other important functions such as carbohydrate metabolism, prevention of infections, synthesis of DNA and in male reproductive health. Zinc is mostly found in the muscle tissue and in the bone. The recommended intake of zinc per day is 7 mg for females and 9.5 mg for males. On average however, an adult ingests about 10-15 mg of zinc daily as a nutrient [73]. Of this, about 5 mg is absorbed into the body and this is considered a trace amount which is unhazardous to human body. Furthermore, zinc based quantum dots such as ZnSe when doped with manganese or copper can cover an emission range similar to that of CdSe quantum dots [9, 74]. They are also less sensitive to environmental changes such as chemical, thermal and photochemical disturbances. Zinc based quantum dots can therefore suitably replace the toxic and heavy metal based quantum dots since they pose no toxic risks to those involved in synthesis as well as those applying them.

2.1.3.2 Insolubility of quantum dots

Quantum dots are insoluble in polar solvents because the surface of their core shell is hydrophobic and in most cases, the surface coatings are also hydrophobic [75]. They are therefore only soluble in organic solvents. This restricts the extent to which they can be applied in biological uses and calls for modification of the surface chemistry of these nanocrystals. Without further modification, quantum dots would not be endocytosed, therefore limiting their use in biological experiments to studies using electroporation. If water soluble quantum dots are desired, the method chosen for the core shell synthesis has to allow for post synthesis modification of the surface to hydrophilize the quantum dots without significant loss of other properties of the nanocrystals.

2.1.3.3 Intermittent blinking

Quantum dots are known to switch between fluorescent and non fluorescent states with continuous illumination [64], a property commonly referred to as intermittent blinking. This arises from surface defects on the quantum dots, which acts as temporary “traps”, affecting electron-hole recombination [54]. Blinking of quantum dots is also associated with reduced quantum yield [54]. Whereas intermittent blinking of quantum dots may be interpreted as a limitation to application of quantum dots in some areas, especially those that require continuous illumination, it is seen as an added advantage in single molecule studies since the quantum dots can become periodically available for detection. The factors that are interpreted as limitations to

particular applications of quantum dots are therefore put into consideration when designing a method for synthesis.

2.1.3.4 Photo bleaching

This refers to the permanent destruction of fluorescence by light- induced conversion of a fluorophore to a chemically non fluorescent compound. Quantum dots show some degree of photo oxidation although they are much photo stable than organic dyes.

2.1.3.5 Non specific binding

Depending on the surface functionality, quantum dots have been reported to non specifically bind to biomolecules such as tissues and cells. This nonspecific binding problem causes a high level of background fluorescence that degrades the signal-to-noise ratio and limits tagging specificity and detection sensitivity. Coating of quantum dots with ligands containing methoxy groups, e.g. polyethylene glycol (PEG^{5000}) where 5000 represents the molecular weight (g) have been reported to reduce non specific binding.

2.1.3.6 Agglomeration of quantum dots

One of the typical features of quantum dots is their spontaneous self aggregation to form functional structures driven by the energetic of the system. Self aggregation occurs through non covalent interactions such as electrostatic forces, host-guest interaction, hydrogen bonding

interaction, charge transfer interaction, acid/base proton transfer, van der Waals forces as well as π-π interaction [76]. Aggregation of quantum dots is also reported when they are in biological environments, for instance inside the cells [77], during in situ hybridization [78] or when used as markers for molecular recognition cell surfaces [79]. This limits the biological applications of quantum dots to in vitro studies.

2.2 Synthesis of quantum dots

The shift from conventional semiconductors and fluorophores to quantum dots, and attempts to address limitations associated with their applications have witnessed extensive research on quantum dots and tremendous progress in the synthesis and modulation/understanding of their optical and electrochemical properties has been realized in the recent past [6]. Furthermore, studies involving surface modification of quantum dots to make them stable against oxidation, soluble, non-toxic and non aggregate have also been done and various ways of achieving one or more of these have been published recently. By controlled synthesis and post synthesis functionalization, researchers have addressed one or more of these challenges.

Most of the methods chosen for synthesis of quantum dots have been designed to include post synthesis procedures so as to address one or more of the above limitations and meet the desired applications of the synthesis products. These methods for synthesis of quantum dots have existed since 1980s [58, 80]. The pioneering work of synthesizing quantum dots by the research groups of Brus, Henglen and Gratzel involved liquid phase methods for synthesizing suspensions

of nanocrystals in solvents such as water and acetonitrile [80]. However, the first method to synthesize surface capped, size tuneable, regular in core structure and highly monodisperse was reported in 1993 by Murray et al [81]. Since then, there have occurred numerous modifications in the synthesis procedures of quantum dots in order to improve or change their properties and make them suitable for specific applications. For instance, quantum dots for biological applications need to be soluble, non-toxic to biomolecules and biocompatible. Synthesis of quantum dots for such applications will therefore involve a number of steps, which include core synthesis, shell growth or surface modification to make them soluble, biocompatible and non-toxic and eventually biomolecular conjugation [58].

2.2.1 Molecular beam epitaxy

This is a self organized and easy method of fabricating high quality quantum dots through a process known as Stanski-Krastanow [82]. In this process, certain chemicals are evaporated and then sprayed to condense into small objects on a heated crystalline substrate [83]. The main disadvantage of this method is that it is much harder to use quantum dots while they are still attached to the substrate. While they are all attached together on the substrate they act as one solid which almost defeats the purpose of creating the quantum dots. Other methods that fall under this include vapour phase epitaxy (VPE) and liquid phase epitaxy (LPE) [6].

2.2.2 Electron beam lithography

This method involves use of a focused beam of electrons to form a circuit pattern that deposits quantum dot materials on a substrate [84]. This process has some of the same shortcomings as epitaxy, mainly that the quantum dots are still connected to the substrate after synthesis. Additionally, scientists have found it difficult to create such small masks that need to have holes just nanometres in diameter. Lithography was originally a very popular process for creating quantum dots; however, this process creates many defects and is slow compared to the other processes.

2.2.3 Colloidal synthesis

Colloidal synthesis is a process that involves synthesizing quantum dots in a liquid. In this method, metallic or organometallic precursors (e.g. zinc, cadmium and mercury), and the corresponding chalcogen precursors (e.g. sulfur, selenium or tellurium) are injected into a hot solution containing organic solvents that are stable at high temperature such as trioctylphosphine oxide (TOPO) or trioctylphosphine (TOP). Quantum dot formation in this case involves the decomposition of metal-organic or organometallic precursors at elevated temperatures, mostly between 180 and 310 °C [59], depending on the selected precursors and solvents. Because of the high temperatures involved in this method, it is sometimes referred by some authors as organometallic thermolysis [50]. Nucleation of quantum dots start immediately after the injection of either metal organic or organometallic precursors at elevated temperatures [59]. Several properties of the quantum dots, especially the size can be fine tuned by varying the amount of

precursors, temperature as well as the synthesis time. The temperature plays the size dependent role because the nucleation of the seed crystal and deposition of new materials on existing materials take place depending on the respective temperature of the solvent. By taking samples from the reaction mixture at some intervals and exposing them to spectroscopic studies, the size of the particles can be monitored. The temperature of the reaction system is then lowered to quench growth once the desired size of the quantum dots is obtained. Jin et al [60] reported successful control of emission maximum range from700 to 850 nm for CdSeTe/CdS by varying the reaction time as well as the injection temperature of Se-Te precursor. Colloidal synthesis is usually carried out under inert conditions because the precursor species are highly reactive to oxygen. However, the quantum dots themselves are in most cases stable in air and post synthesis modifications can be performed in the open. The organic solvents coordinate the precipitated quantum dots making them stable, soluble in organic solvents and single non-aggregate particles. Surface coating and stabilization can also be achieved by capping the core shell material e.g CdSe with another inorganic layer such as ZnS. For the case of coating quantum dots with additional inorganic semiconductor material, the capping material precursor mixture is best introduced into the reaction mixture drop wise, especially during the annealing step. This is because, injection of capping material precursor mixture at the same temperature as that of the core shell synthesis will lead to nucleation of new nanocrystals, rather than epitaxial deposition of the capping ligand. The choice of the capping ligand can also influence the luminescence properties of the quantum dots since it interacts with quantum dot surface [85]. For instance, when capped with zinc sulphide (ZnS), cadmium selenide (CdSe) quantum dots show high fluorescence quantum yield [66]. Colloidal synthesis is the best and most preferred technique for the formation of quantum dots because the process can occur under “benchtop conditions,” or in

a normal laboratory setting. An extensive research on colloidal synthesis has witnessed development of modified methods for synthesis of these nanocrystals at much lower temperature. Li et al [86] reported a solvothermal reaction between zinc acetate [$Zn(CH_3COO)_2.2H_2O$] and thiourea (CSN_2H_4) at 120 °C resulting to ZnS quantum dots of particle size less than 3 nm and photoemissions at 365 (λ_{ex}=280 nm), 325 and 333 nm (λ_{ex}=222 nm). Synthesis of ZnS nanoparticles was in another report by Zeng et al [87] achieved at 80 °C for two h. They obtained cubic particles with a narrow size distribution and average diameter of 50 nm. Generally a lot has been done in quantum dot synthesis to even obtain nanocrystals at room temperature. In one such an example, Zhang et al synthesized mercapto acetic acid functionalized ZnS quantum dots at room temperatures and the colloid obtained in their experiment was stable at room temperature for 2 weeks [88].

Colloidal synthesis of quantum dots, just like other methods has some challenges associated with it. Firstly, the presence of organic coordinating solvents in the synthesis solution implies that the quantum dots obtained contain an outer layer comprising of one or more organic ligands. The size of the quantum dot obtained is therefore bigger than it would otherwise be. Whether an organic solvent or an extra inorganic shell is added to the surface of the core shell quantum dot, the particles obtained are insoluble in polar solvents since the surface coatings are themselves hydrophobic. Further surface modification are therefore necessary if the desired quantum dots are to be soluble in aqueous solvents. Various methods of solubilizing quantum dots have been identified and will be discussed later in this text. Furthermore, the high surface area of quantum dots makes their colloidal solutions unstable and proper surface functionalization with suitable ligands is necessary. Although most biochemical applications of

quantum dots require that they be in solution (colloidal form), Bodas et al have emphasized the importance of fabricating these nanocrystals on solid surfaces [89]. Electrochemical deposition of quantum dots on solid surfaces therefore presents a potential method for fabricating quantum dot based modified electrodes. Penner et al [80] developed a three step (electrochemical/chemical) method for deposition of synthesizing zinc oxide (ZnO), copper (I) iodide (CuI) and cadmium selenide (CdS) quantum dots on graphite surfaces. The method was based on electrochemical deposition of nanoparticles of the metal (M^o) from a solution of the metal (M^{n+}) followed by electrochemical oxidation of the metal nanoparticles to form $M_{n/2}$ and eventual displacement of the oxygen from the $M_{n/2}$ using compounds of the form HX, where X is the anion in the desired quantum dot product.

2.3 Surface capping and functionalization of quantum dots

Surface capping and functionalization of quantum dots involve introduction of additional layer(s) or coating(s) on the core shell structure. The process is intended to make the nano crystals stable, reduce or eliminate toxicity, avoid agglomeration as well as to improve their luminescence properties. In the process of functionalization, particular groups are introduced on the surface of the quantum dot material to suit particular applications. For instance, a carboxylic acid group can be introduced on the surface of a quantum dot to confer solubility properties. There is a huge diversity of different surface modifications and these give rise to quantum dots of very different optical and chemical properties. This diversity of surface modifications allows for multiple applications of the nanocrystals. However, the surface coatings of quantum dots affect two key aspects of the properties of quantum dots. These are photophysical and physicochemical

aspects. The particular photophysical characteristics affected are emission, wavelength, quantum yield and photostability whereas the physicochemical characteristics are size, charge as well as the aggregation stability of the particle suspension in biological systems. The most commonly used surface functionalizing/stabilizing compounds for quantum dots are organic polymeric materials and small inorganic ligands. Whether organic polymeric materials or small inorganic ligands, two approaches are mostly used to modify quantum dots in various ways. These approaches are ligand exchange reactions of hydrophobic surfactant molecules for hydrophilic bifunctional ones [64] or phase transfer methods using amphiphilic molecules. In both surface exchange reactions and phase transfer mechanisms, two main approaches are employed to functionalize quantum dots. In one of these methods, a previously synthesized functionalizing polymeric ligand with the desired groups is grafted onto the surface of the quantum dots. The second method involves initiating growth of the desired functionalizing polymeric ligand on the surface of the quantum dot when the nanocrystals are nucleating. This approach will call for balancing between nanocrystal growth conditions and polymerization conditions. Many polymerization conditions are incompatible with nanocrystals. For example, during polymerization, radicals that initiate the polymerization process may damage the nanocrystals. Therefore, controlled radical polymerization mechanisms have to be designed so that nanocrystal growth and polymerization can take place simultaneously in the same solution. This approach is therefore cumbersome and not commonly applied in quantum dot synthesis, capping and functionalization procedures. On the other hand, the first approach is a convenient route for introducing macromolecules onto the quantum dot surface and directs them out towards the environment for solubilization or bioconjugation. Using this approach, quantum dot

functionalization can be done during or after synthesis, thus making it a convenient method for functionalizing commercially available quantum dots.

2.3.1 Surface exchange reactions

Surface exchange reactions involve complete replacement of the surface bound ligands that result from quantum dot synthesis. Ligands such as TOPO, TOP, Tetradecylphosphoric acid (TDPA) [90], oroleic acids [91] on the surface of a quantum dot can be exchanged for amphiphilic bifunctional molecules such as marcapto carboxylic acids [HS-(CH_2)*n*-COOH, *n*=1-15] [92], 2-aminoethanethiol [93], Dithiothreitol [94], oligomeric phosphines [95], peptides [96],as well as crosslinked dendrons [97]. Amphiphilic compounds contain a hydrophobic end that can interact with the hydrophobic surface of the quantum dot and a hydrophilic end that extends to polar solvents (e.g. a water molecule), conferring solubility properties. A number of approaches are available for achieving surface exchange reactions. In one of the approaches reported by Gerion et al [98] a silica coating was deposited into an already TOPO coated CdSe/ZnS quantum dots. The silica coating displaced the TOPO from the surface to create a silica shell. Subsequently, phosphonate and ammonium containing monomers, (trihydroxysily)propyl methylphosphonate and chlorotrimethylsilane respectively were added along with the thiol containing monomers to increase the shell thickness. A quantum yield of 60 to 80% was achieved by these authors. In a similar approach, Jin et al [60] coated CdSeTe/CdS quantum dots with glutathione (GSH) by dispersing TOPO and hexadecylamine (HDA) in tetrahydrofuran, followed by addition of GSH and allowing surface exchange reactions to proceed at 60 °C. GSH is a tripeptide [γ-L-glutamyl-L-cysteinylglycinein] harmless compound

that exists in most organs and posses chelating properties and can detoxify Cd^{2+} ions besides other important roles mentioned above for peptides. The resulting quantum dots showed broad absorption spectrum from visible to near infrared (700 – 800 nm) and a quantum yield of 36%. Most quantum dots coated using this approach of surface exchange reaction are stable but large amounts of quantum dots are difficult to get [99]. In another surface exchange approach, TOPO molecules can be displaced by the intended bifunctional molecules by incubating the quantum dots in a solution containing the bifunctional linker.

Surface exchange reactions however affect the luminescence properties of the quantum dots and in most cases decrease the luminescence quantum yields. Furthermore, mercapto containing bifunctional ligands may form disulfides and fall off the quantum dot surfaces thus making them prone to aggregation and precipitation out of water. Complete replacement of the original capping ligand may also lead to incomplete surface covering when a new coating is introduced [59]. This exposes the quantum dot to surface photo-oxidation and cause shift of the emission wavelengths towards the blue colour [100]. Surface oxidation of a nanocrystal also leaves behind a smaller core semiconductor which leads to shifts of wavelengths to higher energies and thus smaller wavelengths [101].

2.3.2 Polymer coated quantum dots

The type, amount and method of introducing polymeric compounds on the surface of quantum dots, either directly or indirectly is usually influenced by or explored in the context of application of the product of functionalization. Generally, polymer coated quantum dots are user

friendly because, they are thought to be more stable than quantum dots coated with small organic ligands [59]. Secondly, multiple and diverse functionalities can be introduced at the surface of the quantum dot by using polymers. Polymers at the surface may play an interfacing role between the quantum dot surface and the surrounding matrix. For instance, electron transfer processes between quantum dots and the surrounding matrix are essential for a number of optoelectronic devices such as solar cells. Functionalization of quantum dot surface with electro active polymers is therefore explored with an aim of facilitating the charge transfer across the quantum dot/polymer interface. It is however worthy to note that, commonly used surface coating ligands such as decane, TOPO, TOP, among others, can be toxic to cells [66]. Peptides and polymeric peptides can coat quantum dots, overcoming most of the limitations associated with the above mentioned polymers. Furthermore, peptides have additional advantages which include their ability to mimic the biological environment and stability at physiological pH. Their reactive groups such as amines, carboxyl, thiol, and peptide tags can be dialed into the hydrophilic domain of the peptide sequence and enable enzymatic or standard conjugation chemistry to obtain biomolecules of interest. Molecular evolution strategies to randomize peptides can be adapted to select high affinity binders to the quantum dot surface. There is the possibility of creating multifunctional quantum dots by mixing peptide sequence in certain molar ratios in a single step for in vivo and in vitro studies (e.g. a quantum dot with biotin and polyethylene glycol (PEG), conjugating receptor ligand and PEG, etc). A number of methods have therefore been developed to obtain polymer coated quantum dots. These methods may either involve surface exchange reactions in which case a hydrophobic ligand on the surface of a quantum dot is replaced with a hydrophilic polymer or direct synthesis of polymer coated quantum dots. The strategies include coating quantum dots with end-functionalized polymers,

multidentate polymeric ligands, coating with amhiphilic polymers as well as encapsulation of quantum dots in dendrimers [85].

2.3.3 Amphiphilic polymer coated quantum dots

It has already been mentioned in this text that most methods used for quantum dot synthesis result in products that are insoluble in aqueous solvents, yet most of their applications require their solubility in such solvents. Surface stabilizing ligands of quantum dots, which often contain alkyl chains only confer low solubility to the quantum dots. To solubilize the insoluble surface stabilized quantum dots, reactions can be initiated on the surface of the quantum dot that lead to exchange of the insoluble ligands for soluble ones. Alkyl amines, phosphines and other surface active ligands, usually used to coat CdSe/ZnS quantum dots can be replaced with thiols covalently linked with hydrophilic groups. Mono and dithiols are reported to bind stably with ZnS shells and the resulting quantum dots can remain stable upto a year without aggregation or significant loss of functionality [102]. Research has made efforts to develop alternative methods that will produce water soluble quantum dots without performing exchange reactions. The most successful method so far involves use of amphiphilic polymers. Amphiphilic polymers are polymeric materials that contain both hydrophobic and hydrophilic groups in their structure. The hydrophobic part of the amphiphile interacts with the hydrophobic part of the quantum dot while the hydrophilic part extends to a water molecule, providing solubility as well as chemical functionality. Jin et al [103] synthesized CdSe/ZnS quantum dots by capping them with TOPO followed by surface exchange reactions in which case, the TOPO surface was replaced with p-sulfonatocalix[4]arene to form water soluble quantum dots. The quantum dots obtained showed a

very weak emission and formed a precipitate in water after several h. Although the authors did not suggest a reason for the weak emission and unsustainable solubility recorded in the p-sulfonatocalix[4]arene coated quantum dots, there is a possibility that surface exchange reactions resulted in incomplete coverage of the quantum dots, something that could affect the photophysical and solubility properties of the quantum dots. Mercapto containing bifunctional ligands are the other class of ampiphilic compounds that are extensively studied for surface modification of quantum dots. They include mercapto alcohols, mercapto- sulfonic acids, mercapto amines and mercapto amino acids [104]. Mercapto containing bifunctional ligands are mostly used as amphiphilic compounds for hydrophilizing quantum dots because these compounds can be introduced to the surface of quantum dots without surface exchange reactions. Liao et al [105], for instance synthesized CdSe quantum dots capped with mercapto acetic acid for determination of edaravone, a free radical that prevents brain edema after ischemia. Mercapto acetic acid was used for hydrophilization of the CdSe nanorystals and makes them water soluble. Obtaining a maximum emission at a wavelength of 535 nm and an absorption spectrum of CdSe quantum dots with a shoulder centred at 436 nm, the authors suggested that the prepared quantum dots were nearly mono disperse and homogenous. Oluwafemi et al [106] synthesized the same quantum dots (CdSe) but capped them using cysteine. Besides hydrophilizing and stabilizing the CdSe quantum dots, the cysteine also acted as a platform for bioconjugation with biomolecules. This was made possible by the presence of free ammonium and carboxylate groups in the cysteine which allows for covalent coupling with biomolecules such as amino acids, proteins and nucleic acids.

2.3.4 Encapsulated quantum dots

Surface coating of quantum dots can also be achieved by encapsulating them in hyper branched macromolecular polymeric materials called dendrimers. Dendrimeric materials are monodispersed and have a well defined structure (three dimensional), a property that can be used for controlled synthesis of nanocrystals [107]. This is because, the optical properties of the dendrimer encapsulated quantum dots depend on the dendrimer type, functionality, solvent used, reagent concentration, and the pH of the reacting solution. Encapsulation of nanocrystals in dendrimeric materials can be achieved via either intradendrimer synthesis or interdendrimer synthesis. In intradendrimer synthesis, the quantum dots are synthesized at the periphery of the dendrimer whereas in interdendrimer synthesis, they are synthesized in the dendrimer interior. The most commonly used dendrimeric materials for quantum dots encapsulation are functionalized poly(amidoamine)-PAMPAM polymers [108]. PAMPAM polymers contain both primary and tertiary amine groups at the surface and interior branches of the molecule, which possess chelating properties that capture the growing nanocrystals. The amine groups also allow for DNA complexation and can as well graft to the quantum dot surfaces while at the same time improving the fluorescent properties of the nanocrystal. PAMPAM dendrimers are also permeable to cell walls, a property that allows for commercial use of PAMPAM as transfection agents [108]. Cell permeability of PAMPAM dendrimers is known to increase with increase in the branching of the dendrimer (dendrimer generation). Lemon et al, [109] for instance synthesized dendrimer encapsulated CdS quantum dots using hydroxyl terminated PAMPAM of different generations (G4-OH, G6-OH and G8-OH). The size of the quantum dots obtained increased with increasing degree of branching of the dendrimer i.e dendrimer encapsulated

quantum dot diameters of 1.3 nm, 1.8 nm and 2.3 nm for G4-OH, G6-OH and G8-OH respectively. Furthermore, the respective absorbance bands and emission peaks for G4-OH, G6-OH and G8-OH were 280 nm and 320 nm, 350 nm and 470, and 370 nm and 510 nm. This implies that the size-depended photophysical properties of quantum dots can be tuned by varying the dendrimer generation rather than the reaction conditions. The disadvantages of PAMPAM polymer encapsulated quantum dots are that the amine groups only possess poor affinities to nanocrystal surfaces and do not fully stabilize the quantum dots against aggregation owing to their charged groups. Further surface modifications, using thiols are therefore required to improve the stability of the quantum dots. Wisher et al [108] encapsulated CdSe/ZnSe quantum dots in PAMPAM dendrimers by ligand exchange of TOPO for PAMPAM. The researchers could not reproducibly replace the TOPO ligands for PAMPAM due to low affinity of the amine groups to the CdSe particles. However, when a small number of thiol groups were introduced in the dendrimer structure, the thiol functionalized PAMPAM dendrimer thus obtained had improved binding affinity to the CdSe nanocrystals.

2.4 Applications of quantum dots

2.4.1 Optical biosensors based on quantum dots

The luminescence properties of quantum dots are very sensitive to changes in their surface chemistry. Therefore, when certain chemicals interact with the surface of the quantum dots, changes in the efficiency of the electron-hole combination occurs [110]. It is on this basis that optical sensors for detection of small molecules and ions have been developed. The addition

of Mn^{2+} ions to colloidal solutions of CdS can for instance induce photoluminescence effects of the quantum dots [111]. A large number of metallic ions have thus been detected based on this behaviour. Metal ions are also known to quench the luminescence properties of quantum dots. This has been proposed for optical sensing of ions. Sensors that use fluorescence quenching as the detection signal include those developed for detection of Cu(II) [112-115], Ag(I) [116] and CN^- [117-118] among others.

The photoluminescence features of quantum dots, together with the efficient and specific bioreactions have also presented potential applications in biosensors. Quantum dot-biomolecule hybrid systems have been explored for specific determination and quantification of specific analytes. In cases where quantum dots are used for biosensors, the interaction between the biomolecule and the target analyte produce events that change the intensity of the photoluminescence of the quantum dots. The events could be fluorescence resonance energy transfer (FRET) from the quantum dot to enzyme substrate reactions, antibody-antigen reactions or DNA hybridization, change of pH following some reactions between the biomolecule and the target analyte production of specific molecules from substrate-enzyme reactions. Chemical compounds such as hydrogen peroxide or benzoquinone are highly detected by quantum dots, causing change in the photoluminescence intensity of such quantum dots. It is such changes that are behind the success of several glucose biosensors previously reported using quantum dots. Duong et al [119] used mercaptopropionic acid capped CdSe/ZnS as energy transfer donors for detection of glucose. The enzymes glucose oxidase and horseradish peroxidase served as electron acceptors following the enzymatic oxidation reactions of glucose by glucose oxidase and subsequent reduction of hydrogen peroxide or oxygen. The rapid exchange of electrons between the substrates (glucose, hydrogen peroxide and oxygen) and the two enzymes as well as

the quantum dots resulted in non radiative energy transfer from the quantum dots to the enzymatic reactions. These rapid events caused change in the intensity of CdSe/ZnS photoluminescence (photoluminescence quenching), corresponding to the increasing concentration of glucose oxidase. The detection limit of the biosensor in this case was 0.1 mM. Yuan et al in 2008 [120] sought to improve the detection of glucose using commercially synthesized CdTe quantum dots and the enzymes horseradish peroxidase and glucose oxidase. The detection of glucose relied on the quenching of the photoluminescence of CdTe by benzoquinone. The catalytic reaction of glucose by glucose oxidase produced gluconic acid and hydrogen peroxide. The reaction of hydrogen peroxide with hydroquinone in presence of horseradish peroxide produced benzoquinone. The detection limit was 10 nM. Huang et al [121] used mercaptosuccinic acid-capped CdSe/ZnS quantum dots to detect glucose by monitoring changes in the photoluminescence of the quantum dots that resulted from pH changes. The change on pH was brought about by catalytic oxidation of glucose by glucose oxidase, producing gluconolactone and hydrogen peroxide, followed by subsequent hydrolysis of the gluconolactone to produce D-gluconic acid. Quenching of photoluminescence intensity of the CdSe/ZnS quantum dots was observed to increase with increasing concentration of glucose. In a more recent development, Yuan et al [122], used glutathione-capped CdSe/ZnS quantum dots for detection of glucose. The biosensor described by these authors is similar to that described by Duong et al as mentioned above except for three things. Whereas Duong et al used mercaptopropionic acid to cap/functionalize CdSe/ZnS quantum dots; Yuan et al chose glutathione as the capping ligand. Furthermore, whereas the quenching of CdSe/ZnS in the case of Duong et al resulted from FRET from the quantum dots to the bienzymatic reactions, that for Yuan et al relied on quenching of photoluminescence intensity of the CdSe/ZnS by hydrogen

peroxide. The hydrogen peroxide was produced from catalytic oxidation of glucose by glucose oxidase. The biosensor by Duong et al was a bienzyme system, involving glucose oxidase and horseradish peroxidase while that of Yuan et al was a mono enzyme system (used glucose oxidase only). The detection limit obtained by Yuan et al was 0.1 µM, a thousand times less than that obtained by Duong et al. The use of glutathione for capping rather that marcaptopropionic acid seemed to have improved detection of glucose, possibly because glutathione can detoxify Cd^{2+} and thus offering better biocompatibility than mercaptopropionic acid.

Several studies have also reported detection of some protein molecules of clinical importance by monitoring analyte induced changes of photoluminescence intensity of quantum dots or FRET. An ultrasensitive nanobiosensor based on FRET can detect very low concentrations of DNA and does not require separation of unhybridized DNA [123]. In such biosensors, quantum dots are linked to specific DNA probes to capture target DNA, which binds to a fluorophore (fluorescent dye) labeled reporter strand thus forming a FRET donor-acceptor assembly. The small size of the quantum dots also serves to concentrate the signal since several targets are confined at nanoscale domain. Garon et al [124] reported effective labelling of hematologic cells when reporter proteins were attached to quantum dots. They demonstrated that quantum dots have the ability to bind to specific cells of interest and be taken up by diverse range of hematologic cells and followed through many divisions and through differentiation. Sun et al [125] described a sensitive detection method for pyridoxine hydrochloride (vitamin B6) based on fluorescence quenching of CdTe quantum dots, achieving detection limit of 0.15 µg/mL. In their study, vitamin B6 was found to quench the fluorescence of CdTe quantum dots in a concentration dependent manner. Xu et al [126] described a FRET based biosensor for detection of β-lactamase. They achieved this by labeling a biotinylated β-lactamase substrate

with a carbocyanine dye, Cyanine 5 (Cy5) and immobilized the same on a quantum dots' surface through binding of biotin to streptavidin, pre-coated on the quantum dots. Resulting from FRET, the authors achieved up to 95% efficiency in fluorescent quenching of the emission from the quantum dots.

Changes in photoluminescence intensity of quantum dots induced by hybridization reactions also allows for detection of different biomolecules including DNA, proteins and RNA. This follows from surface functionalizing of quantum dots with different probe molecules such as oligonucleotides, peptides and antibodies. There are quite a number of studies that have reported successful conjugation of quantum dots with oligonucleotide sequences for DNA or mRNA detection. Yen et al [127] developed a sequence specific biosensor based on two systems all of which used two target specific oligonucleotide probes. One of the systems (quantum dot cross-linking system) was based on cross-linking of two quantum dots with distinct emission wavelengths (525 nm and 605 nm) caused by probe-target hybridization. In the other one (quantum dot organic fluorophore coupling system), quantum dots were used as fluorescent tags as well as nanoscalffolds that capture multiple fluorescently labeled hybridization products, resulting in amplified target signals. The detection of the target analyte was permeated by emission of 2 different fluorescent signals by the quantum dot/DNA/ probe complex.

2.4.2 Electrochemical biosensors based on quantum dots

Quantum dots have been used in electrochemical biosensors in various ways as described in the subsections given below.

2.4.2.1 Enzyme based electrochemical biosensors.

Although quantum dots show excellent electrochemical properties when properly functionalized, their use in enzyme based electrochemical biosensor has not been fully explored. This is confirmed by the fact that only two biosensors, one for uric acid by Zhang et al [88] and another one for hydrogen peroxide by Wang et al [128], have used quantum dots in association with enzymes. In the first ZnS quantum dots based reagentless uric acid biosensor; Xian et al functionalized ZnS quantum dots with mercaptoacetic acid, offering free carboxyl groups for electrode attachment as well as bioconjugation. The carboxyl groups of the mercapto acetic acid bonded covalently with a previously l-cysteine modified gold electrode. The functional groups of the mercaptoacetic acid also allowed for uricase enzyme cross linking in presence of 1-ethyl-3-(3-dimethylaminopropyl) carbodiimide (EDC). The presence of ZnS quantum dots in the biosensor was found to lower the electrocatalytic oxidation potential of the enzyme electrode by 169 mV (from 550 mV to 381 mV), compared to a similar biosensor without ZnS quantum dots. Furthermore, the peak current was amplified 7.25 times higher than that obtained with a similar biosensor without ZnS quantum dots. The biosensor obtained by these authors was further characterized by its extremely low detection limit (2.0×10^{-6} M), linear range of 5.0×10^{-6} to 2.0×10^{-3} M, good stability (retained 80.5 % of its activity after 20 days) and reproducibility (lost only 4.5 of its initial activity after more than 10 successive measurements). The presence of mercaptoacetic acid functionalized quantum dots in this biosensor therefore seemed to confer high enzyme loading capacity, biocompatibility and high conductivity. Important to note in this biosensor fabrication is the fact that quantum dot functionalization did not involve surface

exchange reactions. The initial properties of the quantum dots were therefore preserved as much as possible and surface functionalities served to improve these properties. This is unlike in surface exchange reactions whereby some initial properties of the quantum dot are either lost or compromised at the expense of new ones introduced.

In the second reported use of quantum dots in enzyme based electrochemical biosensors, Wang et al [128] used CdSe/ZnS quantum dots not only as surfaces or platforms for deposition of horseradish peroxidase (HRP) but also to facilitate direct electron transfer from the enzyme to a glassy carbon electrode surface. The CdSe/ZnS quantum dots were synthesized by these authors in TOPO, Hexadecyl amine (HDA) and TOP and no further functionalization was made to make them soluble. They were soluble in chloroform and were deposited on a HRP modified electrode by suspending it slightly above a quantum dot solution overnight (vapour deposition). The authors compared the performance of vapour deposited quantum dots onto a HRP modified electrode with drop coated quantum dot/HRP electrode and found that vapour deposition being a slow process results in good combination of the HRP with CdSe/ZnS quantum dots. For instance, the scanning electron micrographs of the two (vapour deposited and drop coated quantum dots) showed formation of a porous membrane when vapour deposition was chosen to introduce the CdSe/ZnS quantum dots on the electrode. The porous structure could favour electrochemical reactions. Furthermore, whereas the drop coated HRP-quantum dot electrode showed weak redox curves under cyclic voltammetry, the vapour deposited quantum dots gave a well resolved and defined quasi reversible peak. The researchers also noted that both the chemistry and structure of the HRP were retained as evidenced by electrochemical and spectroscopic studies of the HRP with vapour deposited CdSe/ZnS quantum dots. Catalytic peak was only observed at -400 mV for the vapour deposited enzyme electrode implying that the catalytic properties of the HRP were

retained when CdSe/ZnS were vapour deposited onto a HRP modified electrode and not when both the enzyme and CdSe/ZnS quantum dots were drop coated on the glassy carbon electrode. The analytical characteristics of the biosensor were a linear range of 5.0×10^{-6} to 1.0×10^{-5} M, a detection limit of 2.84×10^{-7} M and Michaelis-Menten constant (K_m^{app}) of 0.152 mM. It terms of reproducibility nine successive measurements gave a fairly good reproducibility with a standard deviation of 2.9% and the enzyme electrode retained 89% of its activity after one week, further confirming good stability.

A rather interesting use of quantum dots in an otherwise enzyme based electrochemical biosensor was illustrated by Xu et al [129]. In their work, Xu et al modified haemoglobin (hb) with CdS quantum dots. The modified haemoglobin was used to initiate direct electron transfer between hydrogen peroxide and graphite electrode, thereby eliminating the need for horseradish peroxidase which is usually used in biosensors for hydrogen peroxide determination. The chemical interaction between CdS quantum dots with haemoglobin gave a stable electrode which exhibited direct electron transfer and was sensitive to hydrogen peroxide. The Michaelis-Menten constant (K_m^{app}) obtained by this group was 112 µM, far much smaller than 230 µM obtained by Xiao et al [130] for a HRP/Au colloid self assembled monolayer electrode implying a higher affinity for hydrogen peroxide by the CdS/hemoglobin graphite electrode. Other analytical characteristics of the biosensor included a linear range of 5.0×10^{-7} to 3.0×10^{-4} M with a detection limit of 6.0×10^{-8} M. 91% of the biosensor activity was retained after 5 days. Spectroscopic studies of the CdS modified haemoglobin showed no conformational changes of the haemoglobin. The results obtained in case were interpreted by the authors to mean that the CdS quantum dots could provide a favourable microenvironment for the haemoglobin because of

its biocompatibility. It is also possible that modifying the haemoglobin with CdS offers a more spatial freedom to the hemoglobin for electron transfer. The three experiments described so far leave no doubt that quantum dots have a lot of unexploited potential in biosensors that use redox proteins.

2.4.2.2 Electrochemical DNA biosensors (Genosensors)

Genosensors (or DNA biosensors) are devices that combine a biological recognition agent (ssDNA, also called a probe) that confers selectivity, and a transducer that provides sensitivity and converts the recognition event into a measurable electronic signal [131]. Electrochemical DNA devices have recently received considerable attention in the development of sequence specific DNA biosensors through combination of two complimentary single nucleic acids into a single molecule (hybridization). Electrochemical biosensors for DNA rely on the conversion of the Watson-Crick base pair recognition events into quantifiable electrical signal. In DNA hybridization, the target gene sequence is identified by a DNA probe that can form a double stranded hybrid (dsDNA) with its complementary nucleic acid (target sequence) with high efficiency and extremely high specificity in the presence of a mixture of much different, non-complementary nucleic acid.

Generally, a DNA biosensor is prepared by immobilizing a single stranded oligonucleotide probe onto a transducer surface which recognizes its complementary (target). The main goal of preparation of the sensing surface is to ensure proper molecular orientation of the probe single strand DNA and its high accessibility to the target DNA fragment. In electrochemical genosensor fabrication, the immobilization of the probe DNA onto the

transducer surface plays a major role in the overall performance of the sensor [132]. For maximum sensitivity and selectivity, it is highly desirable for the genosensor to be designed such that it allows for optimum hybridization with least non-specific adsorption, if any. Proper tailoring of the electrode's surface chemistry and coverage is essential for assuring high reactivity, orientation/accessibility, and stability of the surface-bound probe, as well as for avoiding non-specific binding/adsorption events. Typically, short oligonucleotides, in the range 18 to 40 bases assure a high selectivity and sensitivity since they form a well ordered and dense orientation on the electrode surface, allowing high accessibility and subsequent hybridization with specific and unique regions of the target nucleotide sequence [133]. Previous reports [134] have for instance pointed out that, the density of immobilized probe ssDNA can greatly alter the hybridization thermodynamics and improve the selectivity of DNA biosensors. It is also important to understand the surface environment of the genosensor in relation to the desired analytical signal. Several methods have been explored for immobilization of the single strand DNA onto the sensing surface. These methods include adsorption, covalent binding and avidin-biotin complexation.

i. DNA immobilization by adsorption

This method is the simplest immobilizing strategy since it does not require special reagents or special modification of the nucleic acids. It may further be divided into physical adsorption and electrochemical adsorption. In physical adsorption, the required amount of probe single strand DNA solution is drop coated on the surface of the transducer and allowed to dry [135]. Physical adsorption may also be accomplished by dipping the electrode in ssDNA probe

solution and allowing it to dry [131]. The weakly adsorbed oligonucleotides are washed gently after which hybridization reactions are carried out. The hybridization may, and in most cases follows a similar procedure. Disadvantage of this method is that it leads to non-specific adsorption of oligonucleotides on the surface of the transducer, resulting to poor hybridization efficiency. Physical adsorption also suffers from desorption of the nucleic acid molecules. To address these issues, researchers have had to modify electrodes using biocompatible materials such as conducting polymers [136-137], dendrimers [138-139], functionalized metal complexes [140] and hydrogels [141] among others. These materials have been reported to provide good signal transduction, enhanced sensitivity, selectivity, durability, biocompatibility, direct electrochemical synthesis, and flexibility for the immobilization of the probe DNA [142]. Once modified, the chemistry on the surface of the electrode is altered and favourable reactions between the electrode modifier and directed sites of the probe DNA may be allowed such that the hybridization sites remain unaltered after immobilization.

Electrostatic adsorption entails creation of charges on the electrode surface, opposite to the charges on the probe DNA such that electrostatic interaction occurs when the two are brought into close proximity. First, the bare electrode is anodically pre-treated at a constant potential, giving rise to a hydrophilic rough surface. This is followed by dipping the electrode in an electrolyte solution containing the probe DNA and applying a potential negative to that of electrode pre-treatment under continuous stirring. The stability of the immobilized probe DNA is in this case enhanced by its negatively charged hydrophilic sugar backbone and the positively charged surface of the electrode surface. Furthermore, the hybridization sites (the DNA bases) are oriented toward the solution, providing access to the target DNA for hybridization. Electrochemical adsorption is also achievable with suitably modified electrodes. An example is

the use of polypyrrole modified electrode for immobilization of single strand DNA molecules. In their oxidized state, the polypyrrole polymeric film of the electrode surface provides a positive charge density, which exhibits electrostatic interaction with the negatively charged phosphate backbone of the probe DNA [143]. Other researchers have also proposed an electrochemically directed copolymerization of polypyrrole and the probe DNA in the same solution such that, electrode modification and probe immobilization are achieved in one step [143]. Although this method is simple and rapid, the orientation of the probe DNA on the electrode surface and its access to the target DNA are not guaranteed. Also, the polymerization conditions of polypyrrole may not be in agreement with the physiological requirements of the probe DNA. Since DNA, as a biomolecule maybe denatured on rendered inactive by polymerization conditions outside its optimum physiological set up, it is, in this case recommended that nucleic acid be used as a polyelectrolyte. Genosensors fabricated this way are also not easily reusable under denaturing conditions mostly used (heating and use of urea) [131].

ii. DNA immobilization by covalent coupling

For purposes of stabilizing the immobilized probe DNA on the surface of the transducer, it is necessary to covalently attach it through a linker bound to one of its ends. To achieve this, the probe DNA and the surface onto which the DNA is to be immobilized may be modified by introducing reactive functional groups that will allow for covalent coupling [144]. Several functionalities on either the electrode or the probe ssDNA have thus been reported for stable anchoring of the probe on the electrode surface. Commonly used reactive functional groups

include thiols, carboxyls and amino groups among others [145]. Covalent coupling via functionalized probe or electrode surfaces are usually accompanied by chemical activation steps, which have also been developed according to the combination of the introduced functional groups [146].

iii. The thiol and amine reactive functional groups.

A thiol group bound to one end of the probe DNA will covalently attach onto the surface of a gold electrode, giving rise to a well ordered orientation of the probe DNA on the surface of the electrode. This method makes use of the well established thiol-gold chemistry and takes place via chemisorption reactions between the thiol molecules on the DNA probes and transducer gold surfaces. Such a configuration is stable, allows for conformational changes and increases specific hybridization without leaking of the nucleic acids from the transducer [131]. For impedimetric detection techniques, the lengths of the carbon chain in the thiol arguably influence the detectable signal, depending on whether faradic or non faradic measurements are done. In non faradic impedance where changes in capacitance are taken as the analytical signals, the use of long chained thiols is prevalent. This is because, non faradic impedimetric measurements require a tightly packed self assembled monolayer, unlike in faradic impedimetric measurement where access of the redox probe to the electrode surface is highly desirable [147]. Self assembled thiol monolayers with carbon chains longer than 11 are known to form more dense monolayers than short chained thiols due to hydrophilic interactions of the chains. It should be remembered that thiols themselves are electrical insulators and will exhibit resistance to flow of current over a window of direct current bias voltages [148]. This however depends on

the terminal group and the chain length. For instance, the self assembly of long chained thiols (16 carbon atoms in the chain), with hydrophilic terminal groups on gold electrodes have been reported to show direct current conduction at potentials as low as 0 mV versus Ag/AgCl (3 M NaCl) even in the absence or a redox species [149]. This phenomenon was attributed to voltage induced structural rearrangement of the monolayer, resulting in pinholes or permeation of the monolayer with ions or water [150].

On the other hand, faradic impedimetric measurements rely on interfacial charge transport. Access of the redox probe to the electrode surface is highly desired during electrode fabrication so that changes in interfacial charge transfer after probe-target binding may solely be attributed to the target. For this reason, short chained thiols are preferred. Short chained thiols molecules such as alkanethiols [151] have been reported to be attractive in fabrication of highly reproducible probe modified surfaces with high hybridization activity [133]. 6-mercapto- 1-hexanol has also been reported to very well control the surface properties of DNA probes [152]. In fact, 6-mercapto- 1-hexanol not only serves as spacers that finely modulate surface density of DNA probes but also effectively prevents nonspecific DNA-gold interactions. The main advantage of this method is that it does not require introduction of additional functionalities to the gold electrode surface and thus it can be achieved with ease. However, this method does not always lead to stable configuration in other electrodes.

Another strategy for covalent coupling involves the use of condensation reactions between primary amine and carboxylic acid. In this case, the probe DNA may be modified with carboxylic acid while the electrode surface is modified with an amino group, or vice versa. To attach the probe DNA oligomers covalently on the amino functionalized surface, the solid

surface modified with amino groups are subsequently subjected to chemical activation by use of homobifunctional linkers such as disuccinimidyl glutarate (DSG) or phenylene diisothiocyanate (PDC) [153]. Although this surface activation protocol is commonly adopted for formation of covalent bonding in micro array fabrication, it is associated with some drawbacks. First, the activated surface does not live long and the surface should therefore be activated just prior to use, and during the cross-linking reaction, undesirable by-products remain on the surface [145]. It is also possible that the activated groups react with free amino groups on the same surface or free amino groups on the DNA nucleobases, leading to inactivation of the immobilized probes.

If the probe DNA is functionalized with a carboxyl group, its attachment on the surface of an amino functionalized electrode is often achieved in the presence of water soluble 1-ethyl-3-(3-dimethylaminopropyl) carbodiimide hydrochloride (EDC) and N-hydroxysuccinimide (NHS). 1-Ethyl-3-[3-dimethylaminopropyl]carbodiimide hydrochloride (EDC) is a zero-length cross linking agent used to couple carboxyl groups to primary amines. This cross linker has been used in diverse applications such as forming amide bonds in peptide synthesis, attaching haptens to carrier proteins to form immunogens, labeling nucleic acids through 5’ phosphate groups and creating amine-reactive NHS-esters of biomolecules. EDC reacts with a carboxyl to form an amine-reactive *O*-acylisourea intermediate. If this intermediate does not encounter an amine, it will hydrolyze and regenerate the carboxyl group. In the presence of *N*-hydroxysulfosuccinimide (Sulfo-NHS), EDC can be used to convert carboxyl groups to amine-reactive Sulfo-NHS esters. This is accomplished by mixing the EDC with a carboxyl containing molecule and adding Sulfo-NHS.

Such probe-activation strategies, however, have several fundamental problems in DNA microarray fabrication. Since most of the DNA microarray fabrications are based on robotic-spotting process, the probe should be prepared as a reproducible or controllable form for obtaining stable and reliable immobilization performance. However, activated carboxyl groups do not have a sufficiently long half-life in aqueous conditions, because the attached activator group is easily hydrolyzed [144] so that the activated DNA probes are inactivated. In addition, an excess amount of the dehydration reagent is required compared to the probe DNA, and therefore, by-products are formed. Also, the sample solution containing only the activated probe DNA, which would be ideal, cannot be obtained easily by general purification methods [154]. As mentioned above, in the processes of DNA microarray fabrication, activation strategies, which have been used widely for covalent bond formation between the probe and surface, still possess technical problems. Consequently, simple and direct covalent bonding fabrication method, which does not require additional activation steps and leaves no by-products, is preferred. This notwithstanding, and for fabrication of single use genosensors using solid disk electrodes, EDC-NHS activation strategies so far remain the best covalent coupling strategy, that assures retention of the immobilized DNA on the electrode surface throughout the measurement.

iv. Biotin –avidin Complexation

Avidin is a highly cationic glycoprotein with an isoelectric point of 10.5 [155]. It contains positively charged residues and oligosaccharide components with heterogeneous structures that consist mainly of mannose and N-acetylglucosamine. Biotin, also known as vitamin H is a small molecule found in tiny amounts in all living cells. Avidin extraordinarily exhibits high affinity

for biotin [156]. The strong interaction between avidin and biotin is frequently exploited to immobilize biological molecules. In fact early histochemical applications in mid 1970's exploited the high affinity of avidin for biotin. Since then, avidin has become a standard reagent for diverse detection schemes. In their simplest form, the methods involve applying a biotinylated probe to the sample and then detecting the bound probe with a labelled avidin. Biotin avidin binding schemes are commonly used to immobilize antigens in cells and tissues as well as to detect biomolecules in immunoassays and DNA hybridization techniques. Traditionally, the binding capacity of avidin or related molecules has been established in terms of moles of biotin bound per volume of resin or, at best, in terms of moles of a biotin-labelled model protein, such as bovine serum albumin or an antibody. The chemical or enzymatic incorporation of biotin labels into nucleic acids is also popular for immobilizing nucleic acids onto a solid surface or matrix for downstream applications such as protein-DNA interaction studies [157] DNA-mediated affinity chromatography [158] and solid-phase sequencing. Because binding capacity is influenced sterically by the size and geometry of the captured ligand, it is not always straightforward to extrapolate from moles of bound protein to moles of nucleic acid.

2.4.3 The electrochemical DNA detection methods that make use of quantum dots.

2.4.3.1 Differential Pulse anodic stripping voltammetry (DPASV)

In a classic format, DNA probes are single-stranded DNA (ssDNA) labelled to provide detectable signals for DNA hybridization. To achieve electrochemical transduction of

hybridization events, electrochemical indicators/intercalators are commonly used. The use of nanoparticles as tracers has emerged as a new technology for electrochemical detection of hybridization and offers unique opportunities for electrochemical transduction of DNA sensing events. Therefore, the current and mostly used electrochemical detection of DNA involves labelling of the DNA oligonucleotide probes with suitable redox probes. Properly synthesized and suitably functionalized biocompatible quantum dots have found some applications as tags for attachment of probe DNA. In such cases, the probe DNA, labelled with a quantum dot is exposed to hybridization reactions, followed by dissolution of the metal tracer in the quantum dots. Electrochemical stripping techniques are used to quantify the metal tracer. Stripping voltammetry is a powerful electro analytical technique for trace metal analysis [159]. The high sensitivity achieved in electrochemical stripping voltammetry results from preconcentration step whereby the target metals are accumulated or deposited on the surface of the working electrode. The detection limits resulting from stripping voltammetric techniques are three to four orders of magnitude lower than those of pulse-voltammetric techniques, also used for monitoring DNA detection. Several authors have demonstrated successful use of nanoparticle tags for oligonucleotide labelling and eventual analysis by electrochemical stripping techniques. In one such an example, Wang et al [160] used cysteamine/thioethanesulfonate capped CdS nanoparticles for detection of DNA hybridization. The modified CdS nanoparticles were tagged with thiolated oligonucleotide probe whereas streptavidin-coated magnetic beads were linked to biotinylated target oligonucleotide. After hybridization, the CdS was dissolved in nitric acid and chronopotentiometric stripping measurements of the dissolved cadmium ions were performed on a mercury-film electrode. A detection limit of 100 femtomole (fmol) was achieved in this method. Lead based quantum dots have also attracted applications in electrochemical DNA

sensors. This is because, lead shows a well defined oxidation potential and this gives well resolved and sharp stripping voltammetry signals. Several authors have therefore demonstrated successful fabrication of electrochemical DNA sensors based on measurement of lead ions. They include Wang et al who used PbS nanoparticles as tracers on electrochemical assays for multitarget detection [14] and Zhu et al who described a method for detection of DNA hybridization using PbS nanoparticle tags and electrochemical stripping of the lead ions [161], achieving a detection limit of 0.3 pM of the target oligonucleotide. Sun et al also reported application of PbS tagged DNA probes in electrochemical biosensors with a detection limit of 4.38 pM [162]. Du et al fabricated a DNA sandwich electrochemical biosensor using nano PbS and nano gold tags on magnetic microbeads and achieved a detection limit of 5.0×10^{-15} M and a linear range 2.0×10^{-14} to 1.0×10^{-12} M [163]. The protocol involving use of PbS as DNA tags in electrochemical detection of DNA was proposed by Hu et al [164] and achieved a linear range of 9.0×10^{-16} to 7.0×10^{-14} M and a detection limit of 2.6×10^{-16} M. The excellent performance of quantum dot based DNA sensors has in the recent past attracted attention in analysis of genetically modified organisms.

In general, the high sensitivity, small dimensions, low cost, and compatibility with micro fabrication technology nature of electrochemical DNA biosensors, compounded with other excellent properties described in section 2.1.6.2.2 has attracted the interest of researchers in analysis of GMOs. Two reports have thus described successful fabrication of electrochemical DNA sensors, using quantum dots for GMO analysis. In one such a report on electrochemical detection of DNA, Sun et al [165] used mercaptoacetic acid-capped CdS quantum dots as oligonucleotide labels for electrochemical detection of nopaline synthase (NOS) terminator. The NOS terminator is a regulatory gene sequence from the nopalin-synthase gene from the

Agrobacterium tumefaciens and is often used during the construction of genetically modified plants. In their approach, the NOS oligonucleotide was modified with $-NH_2$ to allow for covalent binding with the free carboxyl groups on the surface of the mercaptoacetic acid functionalized CdS quantum dots. By functionalizing a gold electrode with mercaptoethanol through self-assembly approach, the authors covalently linked the target single strand DNA (ssDNA) to the modified electrode. Hybridization of the target DNA with the probe DNA was accomplished on the electrode surface. By dissolving the CdS quantum dot hybrids in nitric acid and quantifying them using differential pulse anodic stripping voltammetry, a detection limit of 2.75×10^{-12} M and a linear range from 8.0×10^{-12} to 4.0×10^{-9} M were obtained Huang et al [166] developed an electrochemical method for detection of sequence specific DNA of 35S promoter of cauliflower mosaic virus gene using CdSe quantum dots.

Although the stripping voltammetric technique is associated with low detection limits as described above, it portrays a technique that largely relies on labelling. It is commonly acknowledged that labelling can enhance selectivity (e.g. using the sandwich approach with second probe) and sensitivity (e.g. using a label that greatly enhances signal transduction). Labelling can however change the binding properties of the probe DNA drastically, yielding analytical signals that are not proportional to the target. The fabrication and analysis is expensive, involves more steps, extra time, sample handing (due to labelling procedures) and is accompanied by use of toxic mercury compared to other electrochemical techniques. It is the desire of every analytical chemist that, high detection limits, high sensitivity and applicable linear analytical ranges be achieved with less analytical steps, short response time and less exposure to toxic substances or no exposure at all. Research seeking to improve the analytical performance of electrochemical analysis techniques such as square wave voltammetry,

differential pulse voltammetry and electrochemical impedance voltammetry would be a step towards achieving the goals of the analytical chemists in the present world.

2.4.3.2 The impedimetric genosensors.

A DNA sensor based on electrochemical impedance spectroscopy (impedimetric genosensor) is a device that transduces changes in interfacial properties between the electrode and the electrolyte solution induced by DNA hybridization, conformational changes or DNA damage into an electrical signal. Whereas stripping voltammetric measurements require labelling of the target DNA, impedimetric genosensors do not necessarily require labelling. In fact, the major driving force for studying impedimetric genosensors is their ability to perform label free detections [148, 167]. In impedimetric genosensor, the presence of the target molecule causes electrical changes (e.g. capacitance or resistant changes) on the sensing surface. Label free genosensors also allow for real time detection of the target probe, which is not possible with labelled detection protocols. Real time sensing in turn offers added advantages such as improved measurement accuracy and determination of binding constants from a curve fitted sensor output versus time plot.

Nanomaterials have facilitated the development of ultrasensitive electrochemical DNA sensors because of their high surface area, favourable electronic properties, charge sensitive conductance, non toxicity as well as their high electrocatalytic activity [168]. Owing to their nanometer size and physiochemical characteristics, nanomaterials show good biocompatibility [33]. Nanoparticles have found applications in impedimetric genosensors either as

nanostructured sensing platforms or labelling of the target DNA for signal amplification. It should be noted that, due to the enhanced sensitivity and selectivity associated with labelling, some impedimetric genosensors still use labels. For label free impedimetric genosensors, presence of nanoparticles may generate sterical hindrance or electrostatic repulsion which strongly influences impedimetric response in faradic based impedimetric genosensors. Various types of nano structured materials have been used as platforms to enhance the detection. These include single and multi walled carbon nanotubes, nanostructured polymers, gold nanoparticles and nano electrodes, nanostructured silicon, nanomeric composites and nano membranes among others.

Xu et al., used multi walled carbon nanotubes (MWCTNs) copolymerized with polypyrrole on a glassy carbon electrode and detected target DNA in presence of a redox marker [169-170]. Detection limits in the order of a 10^{-12} M were obtained using this protocol. A recent report by Bonanni et al described the use of screen printed electrodes modified with MWCNTs for impedimetric detection of H1N1 influenza with a detection limit in the pico molar range [171]. Carboxylic acid functionalized single walled carbon nanotubes were used by Caliskan et al to modify graphite electrodes for electrochemical detection of DNA related to Hepatitis B virus [172]. For impedimetric detection of transgenic DNA, the carbon based platforms include a polylysine/single walled carbon nanotube modified electrode for detection of transgenic fragments [173] and screen printed electrodes modified with MWCNTs for impedimetric detection of transgenic insect resistant Bt maize [167].

(a) Nanostructured polymers and polymeric composite materials

The surface of the transducer electrode can grossly be altered through electropolymerization of suitable monomers in presence of structure directing molecules to obtain well ordered nanostructured polymeric surfaces. The conductivity of these electrodeposited polymeric surfaces can easily be modulated by changing the electrochemical potential, doping and/or dedoping, changing the pH as well as the electrolyte. Nanostructured conducting polymers such as polyaniline, polythiophene, polypyrrole and their derivatives contain conjugated π bonds that render them sensitive to small changes at the electrode-electrolyte interface. Moreover, most of these polymers can be variably modified to make them biocompatible and allow for immobilization of probe DNA via either covalent linking or electrostatic interactions. Because of these desirable characteristics, nanostructured polymers, their derivatives and polymeric composites have found applications as platforms for attachment of probe DNA for impedimetric genosensing.

One such an important polymeric material in impedimetric genosensing is polypyrrole and its derivatives. The electrostatic attraction between electrochemically oxidized polypyrrole and the negatively charged backbone of nucleotides was explored for direct immobilization of DNA on a polypyrrole modified electrode [174]. Peng et al physically entrapped the target DNA on a polypyrrole films and used CdS tagged probe DNA to enhance the charge transfer resistance upon hybridization [175-176]. These genosensors were characterized by random attachment of the oligonucleotides on the polymer surface and showed low hybridization efficiencies. Ghanbari et al 2008 proposed another genosensor using electrochemically fabricated polypyrrole nanofibre platform [177]. They immobilized the dsDNA by physisorption and the genosensor exhibited

low detection limit due to increased electroactivity arising from high specific surface area. In another nanostructured polypyrrole platform, a poly[pyrrole-co-4-(3-pyrrolyl) butanoic acid was used as a DNA immobilization platform and enhanced increase in the charge transfer resistance with increasing concentration of the target DNA was realized [178]. Further studies by the same authors sought to investigate the effect of the length of the conjugated polypyrrole chains on the hybridization efficiency. They used 3-pyrrolylacrykic acid, 5-(3-pyrrolyl)-2,4-pentadienoic acid and 3-pyrrollyl pentanoic acid as platforms for immobilization of probe DNA [179]. They observed that nanostructured polyoyrrole and polypyrrole copolymer platforms containing more conjugated chains allowed conjugation of more probe DNA molecules and increased the hybridization efficiency.

Besides polypyrrole, nanostructured polyaniline, polyaniline derivatives, copolymers and composites make the other class of polymeric materials commonly used as platforms for immobilization of DNA. A composite of gold nanoparticles and polyaniline nanotube membrane was used by Feng et al for DNA immobilization and hybridization [180]. The impedimetric response was characterized by a wide dynamic range and low detection limit. In a more recent development, Zhou et al used polyaniline nanofibres on a carbon paste electrode for impedimetric detection of amplified sequences of transgenetically modified beans [181]. DNA loading was found to be greatly enhanced on this platform, translating to a high sensitivity and a detection limit of 5.6×10^{-13} M.

Other fairly reported nanostructured polymeric materials and composite platforms are those of pyridine propylene based dendrimers and metallodendrimers. Yang et al explored a rather uncommon polymer in DNA sensing [182]. They used poly-2,6-pyridinedicarboxylic acid

film on the surface of a glassy carbon electrode. Addition of gold nanoparticles on the sensing layer enhanced the probe DNA immobilization as well as changes in the charge transfer resistance. The platform was used for detection of sequence specific DNA related to PAT gene in transgenic plants and resulted to a detection limit of 2.4 $x10^{-11}$ M. A multinuclear nickel (II) salicylaldimine metallodendrimer platform on a glassy carbon electrode was reported for deposition of probe DNA and thereafter used for impedimetric and voltammetric detection of target DNA [183]. The fabricated genosensor responded well to low concentrations of target DNA (5 nM). A more recent report by the same authors [184] described an electrodeposited poly(propylene imine) dendrimer as an immobilization layer for probe DNA immobilization. The genosensor gave a detection limit of 9.43 $x10^{-12}$ M and a linear range of 1.0 x 10^{-11} to 5.0 x 10^{-9} M.

(b) Gold nanoparticles

Gold nanoparticles possess excellent properties such as high catalytic and redox activity as well as high surface area owing to their nanoscopic size. These properties are essential in improving surface immobilization of probe DNA and enhancing the rate of electrical communication between the redox active sites and the electrode. The application of gold nanoparticles in impedimetric genosensing thus includes their use as platforms for DNA as well as labels for signal amplification. Gold nanoparticle platform for DNA immobilization include a fabricated platform reported by Fu et al using self assembling bilayer-two dimensional silane and gold nanoparticles on gold substrates [185]. These authors successfully immobilized thiolated

ssDNA on the gold nanoparticles. An increased surface area thus formed increased the number of DNA attachment points and improved the sensitivity of the label free detection of DNA hybridization.

Nanoporous silicon was used by Irina et al [186] and Vamvakakii et al [187] for impedimetric detection of target DNA and recorded high hybridization efficiency and reproducible impedance changes. As for nanomaterials as labels, gold nanoparticles are the most commonly used nanomaterials for impedimetric detection of DNA hybridization. They are used mainly to amplify the electrochemical signal; either capacitance or resistance. This is exemplified by gold nanoparticle labelled oligonucleotides reported by Moreno-Hagelsieb et al [188] and streptravidin coated gold nano particles for detection of biotinylated target DNA reported by Bonanni et al [189] among others. Recently, quantum dots have attracted attention as labels for amplification of the electrochemical signal resulting from DNA hybridization. These include CdS used by Peng et al [179] and Xu et al [190] to amplify the electrochemical detection of specific oligonucleotide sequence. Kjallman et al [191] used CdTe nanoparticles for the modification of the hairpin target probe and used impedimetric detection method achieving sensitivity in the order of a femtomolar.

2.4.3.3 DNA detection by square wave voltammetry.

The demand for detection of trace levels for substances of environmental, clinical and forensic importance is growing tremendously. Electrochemical techniques such as square-wave voltammetry (SWV) and differential pulse voltammetry (DPV) have been a powerful tool for

analytical purposes. Among them, the SWV is the most advanced technique both for elucidation of electrode mechanisms as well as for analytical applications, especially when adsorption of reactant or/and product occur [192]. The unique advantages of square-wave voltammetry such as fast scan rate, large frequency, large amplitude, short time required for measurements as well as the specific approach in the current sampling procedure rank this technique as one of the most advanced among the family of pulse voltammetric techniques [192].

In DNA detection, SWV is reportedly an attractive approach for rapid and inexpensive assays, and has been applied in detection of DNA damage on carbon electrodes [193], pyrolytic graphite electrodes [194] as well as on metallopolymer-coated electrodes [195]. In detection of DNA damage, it is assumed that minimal voltammetric signals are observed on a double stranded DNA due to inaccessibility of the electroactive bases. Denaturation or damage of DNA however exposes these bases to electrodes and reduction or oxidation signals can be observed on mercury or solid electrodes, respectively [193].

SWV is also used for detection of DNA hybridization based on the electrochemical signals of the purine bases, mainly guanine and adenine. At bare electrodes, their voltammetric peaks are poorly resolved and provide sensitivity for DNA analysis [174]. Some authors [196] however described the detection of DNA hybridization and avidin on transgenic maize on a carbon paste electrode using adsorptive transfer stripping SWV with a detection limit of 120 nM. Quite a few reports have described electrode modification or use of labels as a strategy to enhance the analytical signals and improve the sensitivity by square wave voltammetry technique. Sabzi et at [197] used methylene blue as an electroactive label on a pencil graphite

electrode for detection of Human Papilloma Virus (HPV) Target DNA by square wave voltammetry, achieving a detection limit of 1.2 ng μL^{-1}.

2.4.3.4 DNA detection by differential pulse voltammetry (DPV).

The detection of DNA hybridization or DNA damage in DPV follows the same principle as that of SWV in the sense that the analytical signal monitored emanates from oxidation of either guanine or adenine. In spite of the analytical advantages of SWV over DPV mentioned above, DPV appears to be more explored for detection of DNA hybridization compared to SWV. Caliskan et al [172] used carboxylic acid functionalized single wall carbon nanotubes modified graphite sensors for electrochemical monitoring of direct DNA hybridization related to specific sequence of Hapatitis B virus using DPV. Zhang et al [198] recently described label free detection of DNA on a gold nanoparticle/poly(neutral red) modified electrode, achieving a detection limit of 4.2×10^{-12} M for the complementary target DNA using DPV. In another report by Du et al, [199], colloidal gold nanoparticles and carboxyl group functionalized CdS nanoparticles were used for detection of DNA hybridization by DPV technique. In their approach, a redox active cobalt complex $[Co(phen)_2(Cl)(H_2O)]Cl.2H_2O$ was used as the hybridization indicator. From these reports, it is evident that the use of quantum dots as biocompatible platforms for attachment of probe DNA and detection of hybridization reactions without use of reporter molecules is largely under explored. Owing to their small sizes, biocompatible quantum dots could provide a large surface area and sufficient amount of binding

points for DNA immobilization and are envisaged to enhance the analytical signals without use of redox active labels.

It is evident from the discussion on the use of nanomaterials for detection of DNA hybridization that quantum dots have not been explored as platforms for attachment of the probe DNA while not much has been done on the use of quantum dots as probe DNA labels. It should be remembered that the size of quantum dots is far much smaller than that of the nanostructured materials. It is therefore envisaged to offer more binding points for attachment of the probe DNA, owing to their large surface area. High DNA loading, usually associated with enhanced hybridization efficiency is expected to improve the sensitivity, lower the detection limits and realize large detection ranges for voltammetric and impedimetric genosensors. With confinement of electrons within a very small 3 dimensional sphere in the quantum dots (due to quantum confinement effects), the electron transfer energetic are tuned [200] such that fast electron transfer rates between oxidized guanine and the electrode would be high, resulting to amplified electrochemical signals. In this study, mercaptopropionic acid functionalized quantum dots are used as platforms for attachment of probe DNA whose hybridization with the target DNA is detected by impedimetric (EIS) and voltammetric (SWV and DPV) methods.

2.4.4. Important analytical parameters in genosensors.

To demonstrate potential analytical utility, analytical devices (sensors and biosensors) must exhibit desirable analytical properties. These properties include selectivity, limit of detection, reproducibility, stability and dynamic range as discussed in the following subsections.

2.4.4.1 Selectivity

Selectivity, sometimes referred to as specificity is the ability of the sensor to respond to the target analyte and not to any other similar molecule or to discriminate between the target analyte and non targeted molecules. This property is very important especially if the analytical device is to be applied in real sample analysis where the concentration of the target molecule is much less than that of the non targeted molecules.

2.4.4.2 Limit of detection

This refers to that smallest amount of the target analyte that an analytical device can reliably detect. There exists no universal method for determining the detection limit and different authors quite often use different methods to determine the detection limits. In one method, the detection limit can be determined by measuring the sensor response to a dilution series and determining the target smallest concentration at which the sensor response is clearly distinguishable from the response to a blank solution [201]. In another method, the limit of detection is calculated from the slope of analyte concentration-analytical signal linear

relationship (sensitivity) and the standard deviation of the blank response as described by [202]. With different methods used to determine the detection limits, comparison of detection limits values of the same analyte obtained by different authors may not always make sense. Another challenge of these methods is that detection limits are almost always determined in the absence of coexisting nontarget molecules [33]. In real sample analysis, such pure samples rarely occur and reported limits of detection do not necessarily predict success in real sample analysis.

2.4.4.3 Reproducibility and stability

Reproducibility in biosensors is a measure of the scatter or drift in a series of observations or results performed over a period of time. It is usually determined for the analyte concentrations within the usable range [203].

2.4.4.4 Dynamic range

If the sensor is to be used to quantify the analyte concentration and not just detect its presence, the range of measurable concentrations is important. The dynamic range is the ratio of the largest measurable target concentration and the limit of detection [204]. The upper limit is almost invariably set by the saturation of the probe with target and thus is determined by the affinity step. Dynamic range can be extended on the upper end by simply performing measurements with dilution series of the sample. Real time measurements also can enhance dynamic range.

CHAPTER 3

Experimental

This chapter describes the various analytical techniques employed, detailed research methodology and general experimental procedures for the chemical synthesis of quantum dots and nanocrystals as well as electrochemical, microscopic and spectroscopic characterization of the synthesized quantum dots and nanocrystals. Also described in this chapter are procedures for the fabrication, characterization and application of voltammetric and impedimetric sensors and genosenors for detection of selected analytes; mainly dopamine and an oligonucleotide sequence related to 5-enolpyruvylshikimate-3-phosphate synthase, a common vector gene in glyphosate resistant transgenic plants.

3.1 Materials and reagents

Analytical grade Zinc nitrate hexahydrate (≥ 99.0 %), 3-mercaptopropionic acid (3-MPA) (>99 %), sodium hydroxide (≥ 99.0 %) , selenium powder (99.99 %), tellurium powder (99.997 %) , sodium chloride (≥ 99.5 %), sodium borohydrate, disodium hydrogen phosphate (> 98 %), sodium dihydrogen phosphate (>99 %), potassium hexacyanoferrate (III) (≥ 99.0 %), potassium hexacyanoferrate (II) (≥ 99.0 %), 1-ethyl-3-(3-dimethylaminopropyl) carbodiimide hydrochloride (EDC), N-hydroxysuccinimide (NHS) (98 %) and tris-ethylenediamine tetraacetic acid buffer (TE buffer) which comprised of 10 mM Tris-HCl and 1.00 mM EDTA, pH 8.00 ± 0.1, gallium (99.9995 %) and perchloric acid were all purchased from Sigma-Aldrich (Cape

Town, South Africa). 20 base oligonucleotide DNA sequences were purchased from Inqaba Biotechnical Industries (Pty) Ltd., Hatfield, South Africa. All chemicals were of analytical reagent grade and were used without further purification. An amine terminated DNA with the sequence NH_2-5′-CCC ACC GGT CCT TCA TGT TC-3′ was used as the probe DNA while the sequence 5′-GAA CAT GAA GGA CCG GTG GG-3′, which is a section of CP4 epsps gene of GMOs was used as the complementary sequence. The sequences for the non complementary and 3-base mismatch were 5′-CAT AGT TGC AGC TGC CAC TG-3′ and 5′-GAT CAT GAA GCA CCG GAG GG-3′, respectively. The oligonucleotide DNA stock solutions were prepared with TE buffer and stored in a freezer at -20 °C when not in use. Deionized water (18.2 MΩ cm) purified by a Milli-QTM system (Millipore) was used as reagent water for aqueous solution preparation. Phosphate buffer solution of 0.1 M was prepared by dissolving 3.5590 g of disodium hydrogen phosphate and 3.4023 g of potassium dihydrogen phosphate separately in 250 mL deionized water, then mixing the salt solutions according to Henderson- Hasselbalch equation to obtain the required pH values. The phosphate buffer saline (PBS) was refrigerated at 4º C. 5.00 mM $[Fe(CN)_6]^{3-/4-}$ was prepared from $K_4Fe(CN)_6$ and $K_3Fe(CN)_6$ in a 1:1 ratio. Analytical grade argon and nitrogen gases were purchased from Afrox Company, South Africa. Alumina polishing pads and powder (0.05, 0.3 and 1.0 μm) were obtained from Buehler, Illinois, USA.

3.2 Measurement and instrumentation

The synthesized quantum dots and nanocrystals were characterized using electrochemical, microscopic and spectroscopic techniques. The electrochemical techniques used were mainly cyclic voltammetry (CV) and electrochemical impedance spectroscopy (EIS). The microscopic techniques were high resolution transmission electron microscopy (HR-TEM) and atomic force microscopy (AFM) while the spectroscopic techniques were fluorescence spectroscopy (both 2 dimensional and 3 dimensional), utraviolet visible spectroscopy (UV-vis) and Fourier transform infra red spectroscopy (FTIR). For sensor and genosensor studies, electrochemical techniques were used. These techniques were mainly cyclic voltammetry, electrochemical impedance spectroscopy, square wave voltammetry, steady state-time based amperometry as well as differential pulse voltammetry. In the section that follows, a description of the principles, practical aspects as well as instrumentation of all the techniques used in this study is given.

3.3 Electrochemical techniques

Generally, electrochemical techniques give information on the reduction and/or oxidation processes taking place when an electric potential is applied to the system under study. An electrochemical system for voltammetric and impedimetric measurements comprises of a potentiostat, a computer and an electrochemical cell. A potentiostat is an electronic device that controls the voltage difference between the working electrode and the reference electrode. Both electrodes are contained in an electrochemical cell. The potentiostat implements this control by

injecting current into the cell through an auxiliary electrode. In almost all applications, the potentiostat measures the current flow between the working and auxiliary electrodes. The controlled variable in a potentiostat is the cell potential and the measured variable is the cell current. A potentiostat typically functions with an electrochemical cell containing three electrodes; the working, reference and the auxiliary or counter electrodes.

The working electrode: This is the electrode at which the electrochemical reactions being studied occur. The most commonly used materials for working electrodes include solid disk glassy carbon, platinum and gold electrodes. Screen printed electrodes of each of these materials are also used as working electrodes. Whereas solid disk working electrodes can be used over and over again with standard cleaning before and after use, screen printed electrodes are mainly "single use" electrodes.

The reference electrode: This is the electrode against which the potential of the working electrode is measured. A reference electrode should have a known constant electrochemical potential as long as no current flows through it. Commonly used reference electrodes for electrochemical measurements in aqueous solutions are the silver/silver chloride (Ag/AgCl) and the saturated calomel electrodes (SCE).

The auxiliary or counter electrode: This is a conductor that completes the cell circuit, acting as a sink for electrons so that current can be passed from the external circuit through the cell.

The cyclic voltammetry, time based steady state amperometry, square wave voltammetry and differential pulse voltammetry measurements were performed using a BAS100W integrated and automated electrochemical potentiostat from Bio Analytical Systems, Lafayette, USA. The voltammograms were recorded with a computer interfaced to the BAS 100W electrochemical

workstation. A 10 mL electrochemical cell with a conventional three electrode set up was used. The three electrodes consisted of a gold disk working electrode with an area of o.0201 cm^2, a Ag/AgCl (saturated 3 M NaCl) reference electrode and a platinum wire as the auxiliary electrode. Therefore, all potentials in this study are quoted with respect to Ag/AgCl (3M NaCl). The three electrodes and the corresponding three electrode cell configuration are shown in the figures below.

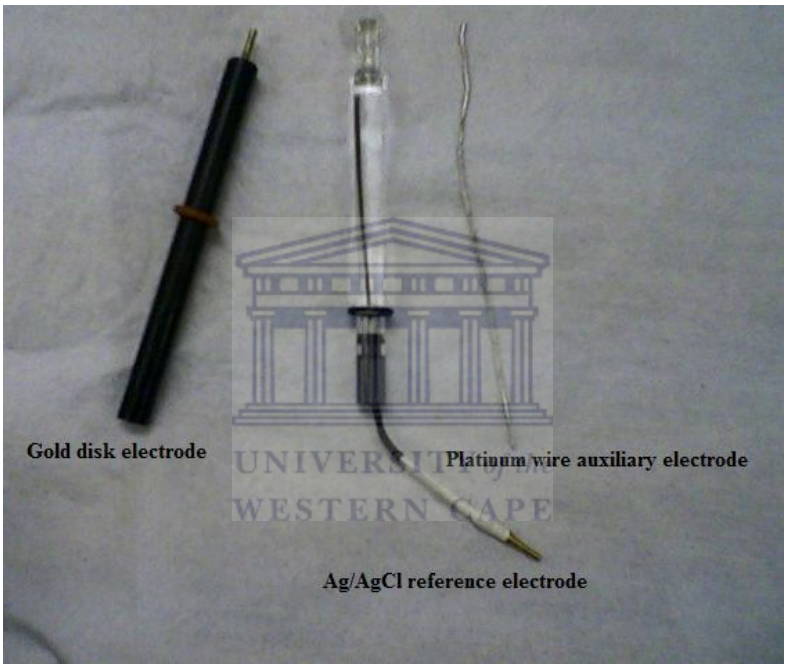

(a)

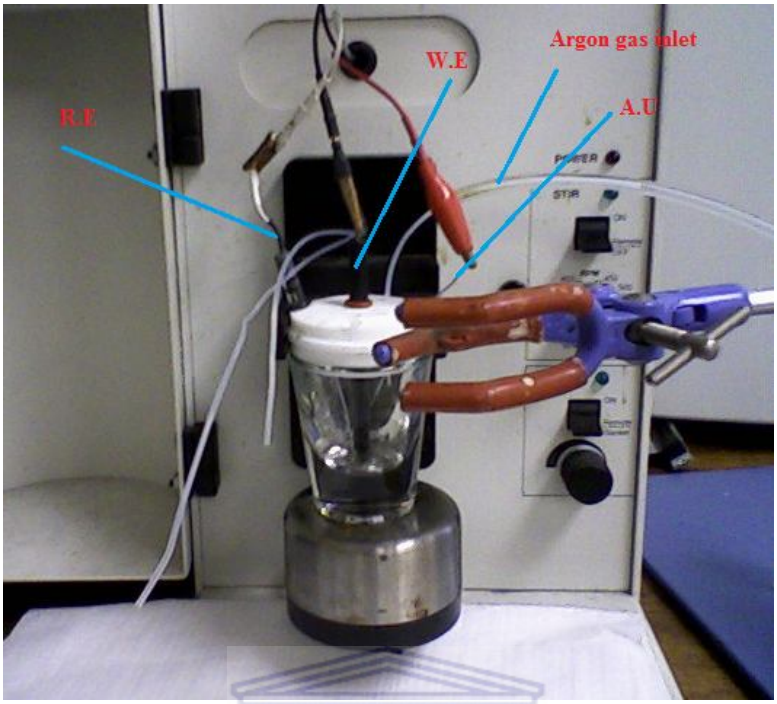

(b)

Figure 4: Digital images of (a) gold disk electrode, Ag/AgCl reference electrode and platinum auxiliary electrode; and (b) a three electrode cell configuration set up. The images were taken using a Panasonic Lumix DMC-LS80 digital camera.

All electrochemical impedance spectroscopy (EIS) measurements were done on a VoltaLab PGZ 402 from Radiometer Analytical (Lyon, France) using a three electrode configuration set up described above. The impedimetric data was recorded using a computer interfaced to the VoltaLab electrochemical work station.Prior to experiments, the bare gold disk electrode was cleaned by polishing with 1, 0.50 and 0.03 μM alumina slurries in glassy polishing pads respectively (2 min on each pad), followed by ultrasonication in distilled water and absolute ethanol respectively for 5 min each. The freshly polished gold was electrochemically cleaned in 0.50 M H_2SO_4 by potential scanning between −300 and 1500 mV until reproducible cyclic

voltammograms were obtained. The platinum auxiliary electrode was cleaned by burning in a flame for several minutes and the Ag/AgCl electrode was cleaned by rinsing with copious amounts of distilled water. Phosphate buffer saline solution (0.10 M PBS, pH 7.40) was used as the supporting electrolyte for all voltammetric measurements, except for the catalytic detection of dopamine in presence of excess ascorbic and uric acids which was done at a pH of 6.00. EIS measurements were done in 5.00 mM $[Fe(CN)_6]^{3-/4-}$. All experimental solutions were purged with high-purity argon gas for 10 min and blanketed with argon atmosphere during measurements. The experiments were carried out at controlled room temperature of 25 ºC.

3.3.1 Electrochemical impedance spectroscopy

Electrochemical Impedance spectroscopy (EIS) is a non-destructive and effective method for probing the features of surface-modified electrodes [205]. It offers a label free detection and allows for analysis of both resistance and capacitance properties of materials [206]. The measurement of EIS involves application of a sinusoidal voltage to an electrochemical cell, and measuring the current response. A frequency response analyzer generates time-invariant amplitude (A), phase (θ) and angular frequency (ω) voltage-current waves. The ratio of voltage (E) to current (I) gives the impedance and has the units of resistance (ohms), in accordance with the Ohm's law; Voltage (E) = Current (I) x Resistance (R). Impedance is run over a wide range of frequencies, giving rise to several electrochemical reactions at the electrode-electrolyte interface. The total impedance is therefore a function of frequency and is expressed in a complex form, with real and imaginary components as follows

$$Z(j\omega) = \frac{E(j\omega)}{I(j\omega)} = Z'(\omega) + jZ''(\omega) \qquad (1)$$

where $Z'(\omega)$ and $jZ''(\omega)$ are the real and imaginary terms respectively, $j = \sqrt{-1}$ and is an imaginary number while ω is the radial frequency (rad. s^{-1}) and equals $2\pi f$, f being the exciting frequency (Hz). Impedimetric data is graphically represented in various forms. The most common is the Nyquist plot whereby the imaginary part of the impedance (Zi) is plotted against the real part (Zr). The real part of the impedance represents the resistive component of the system while the imaginary part is due to insulating layers such as the double layer capacitance or any additional layers in the system [167]. In the Nyquist plot, the low frequency data is represented on the right side while the high frequency data is represented on the left side of the diagram. The figure below shows a typical shape of a Faradaic impedance spectrum (typical Nyquist diagram) and the corresponding Randle's circuit. It includes a semicircle region lying on the axis followed by a straight line. The semicircle portion, observed at higher frequencies, corresponds to the electron transfer-limited process, whereas the linear part is characteristic of the lower frequencies range and represents the diffusion-limited electrochemical process. In the case of very fast electron transfer processes, the impedance spectrum could include only the linear part whereas a very slow electron-transfer step results in a large semicircle region that is not accompanied by a straight line. The electron transfer kinetics and diffusion characteristics can be extracted from the spectra. The semicircle diameter equals to the electron transfer resistance R_{ct}.

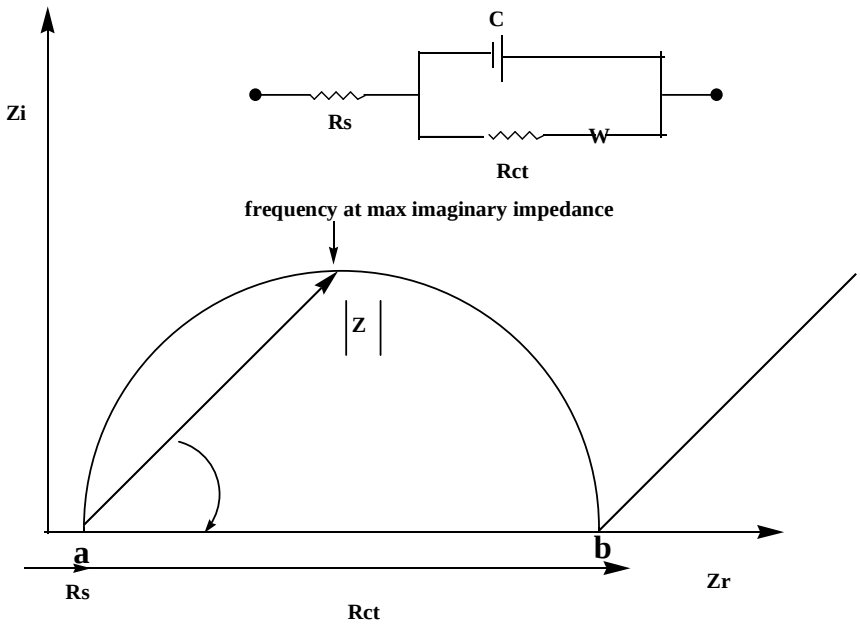

Figure 5: Nyquist plot and the corresponding Randles circuit

At high frequencies ω→∞, the real Z axis intercepts the semicircle and the intercept equals solution resistance (Rs) while at lower frequencies, the intercept between the real Z and the semicircle yields a value corresponding to Rs + R_{ct}. The frequency at maximum imaginary impedance (ω_{max}) of the semicircle in the Nyquist plot corresponds to Zim = 0.5 R_{ct} and relates to the R_{ct} and C_{dl} according to the following equation

$$\varpi_{max} = \frac{1}{R_{ct} \times C_{dl}} \qquad (2)$$

It is also related to the reciprocal of the time constant (τ) according to equation 3

$$\tau = R_{ct} \times C_{dl} \qquad (3)$$

The advantage of Nyquist plot is that it shows unique impedance arcs, characterized by activation –controlled processes with distinct time constants. Since the total electrode impedance consists of the contributions of the electrolyte, the electrode solution interface and electrochemical reactions taking place on the electrode, the shape of the impedance curves provides meaningful information regarding the different electrochemical transformations at the electrode-electrolyte interface. The total impedance is determined by several parameters: (1) electrolyte solution resistance (Rs) (2) the double layer capacitance (C_{dl}), (3) electron or charge transfer resistance (R_{ct}) (4) Warburg impedance (w). These parameters can be modelled by extracting components of the electronic equivalent circuits that correspond to the experimental impedance spectra. The Randles electronic equivalent circuit is commonly used to model interfacial phenomena and provides an effective simulation of the impedance characteristics of a fast charge transfer reaction at a planar electrode. All electronic characteristics of the equivalent circuit and the corresponding physical parameters of the real electrochemical system can be extracted from such analysis. Since the variable parameters of the system represent the functions of the modifying layer and its composition, they can be used to quantitatively characterize the layer. Analysis of the Zre(ω) and Zim(ω) values observed at different frequencies allows the calculation of the important parameters . Thus, the impedance spectroscopy represents not only a suitable transduction technique to follow the interfacial interactions of biomolecules, but it also provides a very powerful method for the characterization of the structural features of the sensing interface and for explaining mechanisms of chemical processes occurring at the electrode/solution interfaces.

3.3.1.1 The electrolyte solution resistance (Rs)

The solution resistance arises from the finite conductance of the ions in bulk solution. It is a significant factor in the impedance of an electrochemical cell. The resistance of an ionic solution depends on the ionic concentration, type of ions, temperature, and the geometry of the area in which current is carried. Although the solution resistance is compensated in a three electrode configuration by the counter and reference electrodes, some degree of solution resistance still exists between the reference and the working electrode. This resistance must be put into consideration when designing the Randles circuit since all of the current must pass through the uncompensated resistance of the electrolyte solution.

3.3.1.2 The double layer capacitance (C_{dl})

When an electrode is polarized relative to its solution, it attracts ions of the opposite charge. As ions from the solution accumulate on the electrode surface, a charge separation between the charged ions and the charged electrode develops. This tendency is countered by the randomizing thermal motion of the ions, but results in a local buildup of excess ions of opposite charge. This charge separation creates a capacitance called the double layer capacitance or diffuse layer capacitance. The double layer capacitance basically exists on the interface between an electrode and the surrounding electrolyte. It depends on the dielectric permittivity introduced into the double charged layer molecules (ε_{dl}) and should be smaller for less polar molecules as depicted by the equations below

$$C_{dl} = \frac{\varepsilon_{dl} A}{\delta} \qquad (4)$$

And

$$\varepsilon_{dl} = \varepsilon_0 \varepsilon_\rho \qquad (5)$$

Where ε_0 is the dielectric constant of the vacuum (8.85 x 10-12 F m^{-1}), ε_ρ is the effective dielectric constant of the layer separating the ionic charges and the electrode surface, A is the area of the electrode and δ is the thickness of the separating layer. The C_{dl} can be represented in the equivalent circuit as a sum of a constant capacitance of an unmodified electrode (e.g., for a polycrystalline Au electrode, C_{Au} is approximately 40 -60 µF cm^{-2} depending on the applied potential [207]) and a variable capacitance originating from the electrode surface modifier, C_{mod}, connected as series elements. Any electrode modifier of insulating features decreases the double-layer capacitance as compared to the pure metal electrode. Thus, the double-layer capacitance could be expressed by the equation below

$$\frac{1}{C_{dl}} = \frac{1}{C_{bare}} + \frac{1}{C_{mod}} \qquad (6)$$

The capacitance in solid electrodes is known to deviate from the normal capacitive behaviours [148] due to roughness or non-homogeneities [207] . For purposes of fitting impedimetric data, a constant phase element (CPE) is therefore used instead of a capacitor to take care of the electrode non-idealities [208].

3.3.1.3 The electron or charge transfer resistance (R_{ct})

The electron transfer resistance, R_{ct}, controls the electron transfer kinetics of the redox probe at the electrode interface. In the Nyquist plot, the semicircle diameter equals the electron transfer resistance and its value varies when different substances are adsorbed onto the electrode

surface. Thus, the insulating modifier on the electrode is expected to retard the interfacial electron transfer kinetics and to increase the electron transfer resistance. The electron transfer resistance at the electrode is given by the equation below

$$R_{ct} = R_{bare} + R_{mod} \qquad (7)$$

where R_{bare} and R_{mod} are the constant electron transfer resistance of the unmodified electrode and the variable electron transfer resistance introduced by the modifier, in the presence of the solubilized redox probe, respectively. These resistances are also connected as series elements in the equivalent electronic circuit. The electron transfer resistance can be translated into the exchange current (i_o) under equilibrium and the heterogeneous electron transfer rate constant (k^0), according to equations 8 and 9 below

$$R_{ct} = \frac{RT}{nFi_o} \qquad (8)$$

$$i_o = nFAk^0C^* \qquad (9)$$

A is the electrode area (cm^2), n is the number of electrons, F is the Faraday constant (96,584 C mol^{-1}), R is the gas constant (8.314 J mol^{-1} K^{-1}), T is the temperature (K), k^0 is the heterogeneous rate transfer constant (cm s^{-1}) and C^* is the bulk concentration of the electroactive probe. In the absence of any redox label in the electrolyte solution, only non-Faradaic impedance is operative. The electron transfer characterizing parameters, R_{ct} and W, become infinite, and the equivalent circuit can be simplified further.

3.3.1.4 The Warburg impedance

The rate of an electrochemical reaction can be strongly influenced by diffusion of a reactant towards or a product away from the electrode surface. This is often the case when a solution species must diffuse through a film on the electrode surface. This situation can exist when the electrode is covered with reaction products, adsorbed solution components, or a prepared coating. Whenever diffusion effects completely dominate the electrochemical reaction mechanism, the impedance is called the Warburg Impedance. For diffusion-controlled electrochemical reaction, the current is 45 degrees out of phase with the imposed potential. With this phase relationship, the real and imaginary components of the impedance vector are equal at all frequencies. In terms of simple equivalent circuits, the behavior of Warburg impedance (a 45 degree phase shift) is midway between that of a resistor (a 0 degree phase shift) and a capacitor (90 degree phase shift). There is no simple electrical equivalent for the Warburg impedance.

It is important to note that two components of the equivalent circuit (Rs and w) represent bulk properties of the electrolyte solution and diffusion of the applied redox probe, respectively. Thus, they are not affected by chemical transformations occurring at the electrode interface. The other two components of the circuit, C_{dl} and R_{ct}, depend on the dielectric and insulating features at the electrode/electrolyte interface.

3.3.1.5 The Bode plots

One of the most important parameters governing the EIS is the applied frequency. At low frequencies (f< 1 mHz) the impedance value is basically determined by the DC-conductivity of

the electrolyte solution. At very high frequencies (f> 100 kHz) inductance of the electrochemical cell and connecting wires could contribute to the impedance spectra. Thus, the analytically meaningful impedance spectra are usually recorded at frequencies where they are mainly controlled by the interfacial properties of the modified electrodes (10 mHz< f< 100 kHz). However, the Nyquist plots do not show the dependence of the impedance on the frequency applied; neither do they give direct information on frequency and phase angle. When the phase angle, θ, between the voltage applied and the current induced is zero, then a pure resistance is present. When a phase angle of 90^{o} is measured between the voltage and current at the same frequency, a pure capacitance is present. Angles between these values can mean a combination of a capacitor and resistors are present. It is therefore important to plot the impedance, usually the log of the impedance magnitude, as a function of frequency and in addition the phase angle as a function of frequency. Such a plot is known as the bode plot. In bode plots, the logarithm of absolute impedance (log |Z|) and the phase angle are plotted versus the logarithm of frequency (log f). The use of log frequency allows a very wide frequency range to be plotted on one graph. Of great significance in bode plot is its ability to distinguish between regions which are dominated by resistive elements such as solution resistance and charge transfer resistance, and regions that are dominated by capacitive elements. Resistive controlled regions are characterized by a zero slope while capacitive controlled regions have a slope of -1. Below is a Bode Plot for a Simple Electrochemical System. The plot of log |Z| versus log frequency yields the values Rs and R_{ct}.

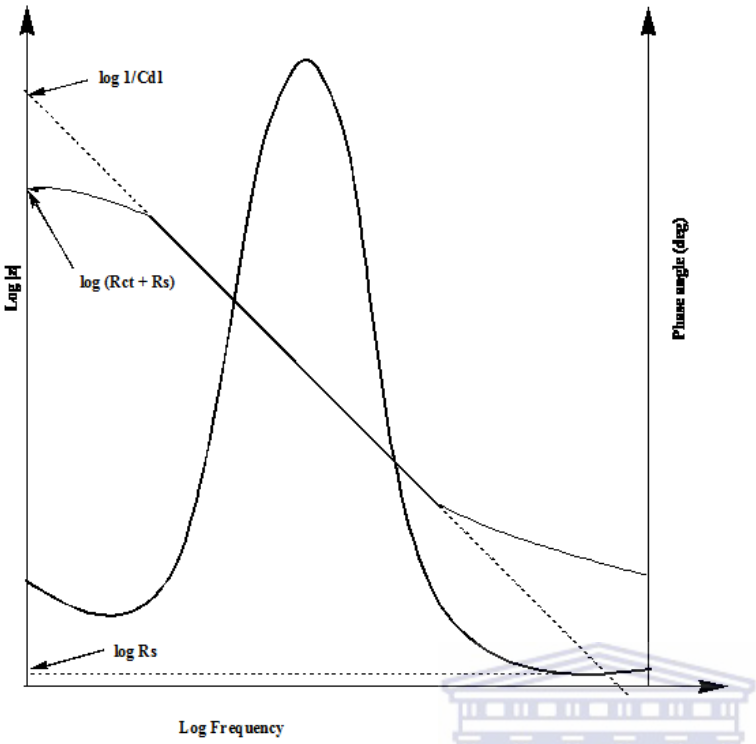

Figure 6: Bode Plot for a Simple Electrochemical System.

At the highest frequencies, solution resistance dominates the impedance and log Rs can be read from the high frequency horizontal plateau, as illustrated in the diagram above. At low frequencies, charge transfer resistance contributes to the impedance and the log (Rs + R_{ct}) can be read from the high frequency horizontal plateau, also illustrated in the diagram above. At intermediate frequencies, the curve should have a straight line with a slope of -1 as explained for a capacitive dominated region. If this straight line is extrapolated to the log |Z| axis where $\omega = 2\pi f = 1$, f equals 0.1591, log ω equals 0 and the value of C_{dl} can be evaluated from the equation

$$|Z| = \frac{1}{C_{dl}} \qquad (10)$$

The Bode plot format also shows the phase angle (θ). At the high and low frequency limits, where the behaviour of the Randles cell is resistor-like, the phase angle is nearly zero. At intermediate frequencies, the phase angle increases as the imaginary component of the impedance increases. The phase angle versus log frequency plot yields a peak at $\omega_{(\theta=max)}$, the frequency (in radians), at which the phase shift of the response is maximum. The double layer capacitance can in this case be determined using the equation:-

$$\varpi_{(\theta=\max)} = \sqrt{\left(\frac{1}{C_{dl} \times R_{ct}}\right)\left(1+\frac{R_{ct}}{Rs}\right)} \qquad (11)$$

The Bode plot thus provides a clearer description of the electrochemical system's frequency-dependent behaviour than does the Nyquist plot, in which frequency values are implicit rather than explicit.

In most applications however, analysis of both Bode and Nyquist plots is highly advised in order to conclusively study electrochemical processes at interfaces. The technique is rapidly developing for interrogating interfacial electrical properties, mechanisms of electrochemical reactions, transport properties of materials as well as exploration of the properties of porous electrodes [207, 209]. It has become an attractive electrochemical tool for numerous applications such as immuno [210-211] and genosensing [169, 179, 212], enzyme activity determination [213], studies of corrosion [214] and surface phenomena . It is therefore a suitable technique for the transduction of biosensing events at the surface of an electrode and in the recent years, EIS [205] has been widely used for the detection of DNA hybridization, occurring at a sensor surface [207, 215].

3.3.2 Voltammetry

3.3.2.1 Cyclic voltammetry

Cyclic voltammetry is one of the most widely applied techniques in modern electrochemistry due to its ability to allow probing of the mechanics of redox and transport properties of a system in solution. Cyclic voltammetry is usually performed using a three electrode configuration whereby the potential relative to some reference electrode is scanned at a workin*g* electrode while the resulting current flowing through a counter (or auxiliary) electrode is monitored in a quiescent solution. In the cyclic voltammetry experiment, an applied potential (E) is swept from an initial value (E_i) to a more oxidizing or reducing value (E_f) and then back to the initial value [216]. The potential at any time (t) and voltage scan rate (v) on the forward and reverse sweep can be calculated using the equation 11 and 12 below

$$E_{forward} = E_i + \nu t \qquad (12)$$

And

$$E_{reverse} = 2E_f + E_i - \nu t \qquad (13)$$

If the potential at the working electrode is more positive than that of an electroactive species in the solution, electrons move from the solution to the electrode and the electroactive species is oxidized. In the process, an anodic current is produced. In the International Union of Pure and Applied Chemistry (IUPAC) convention, the anodic current is positive while in polarographic convention, it is negative. Similarly, on the return scan, as the working electrode potential becomes more negative than the reduction potential of a redox couple, reduction (*i.e.* electrons

flowing away from the electrode) may occur to cause a cathodic current, which is negative in IUPAC convention and positive in polarographic convention. The magnitude of the observed faradaic current can provide information on the overall rate of the many processes occurring at the working electrode surface. As is the case for any multi–step process, the overall rate is determined by the slowest step. For an oxidation-reduction process induced at a working electrode, the rate determining step may be any one of the following individual step depending on the system: rate of mass transport of the electro-active species, rate of adsorption or de-sorption at the electrode surface, rate of the electron transfer between the electro-active species and the electrode, or rates of the individual chemical reactions which are part of the overall reaction scheme.

For an oxidation reaction of the form

$$M_{Reduced} \leftrightarrow M_{Oxidized} + ne^{-} \quad (14)$$

Where $M_{reduced}$ is the reduced species, $M_{oxidized}$ is the oxidized species and n is the number of electrons; the relationship between the potential and the concentrations of the reduced and oxidized species at equilibrium is described by the Nernst equation below;

$$E = E^{o} + \frac{0.059}{n} \log \frac{[M_{Oxidized}]}{[M_{Reduced}]} \quad (15)$$

where E is the applied potential and $E^{0'}$ the formal potential; $[M_{oxidized}]$ and $[M_{reduced}]$ represent surface concentrations at the electrode/solution interface, but not bulk solution concentrations. It is important to note that the Nernst equation may or may not be obeyed depending on the system or on the experimental conditions.

A typical cyclic voltammogram highlighting the key anodic and cathodic parameters is shown in figure 7 below. It shows a case where the scan starts at a slightly negative potential (A, where E_i = -400 mV) up to some positive switching value (B, where E_f = 700 mV) at which the scan is reversed back to the starting potential. The current is first observed to peak at $E_{p,a}$ (with value $i_{p,a}$) indicating that an oxidation is taking place and then drops due to depletion of the reducing species from the diffusion layer. During the return scan the processes are reversed (reduction is now occurring) and a peak current is observed at $E_{p,c}$ (corresponding value, $i_{p,c}$).

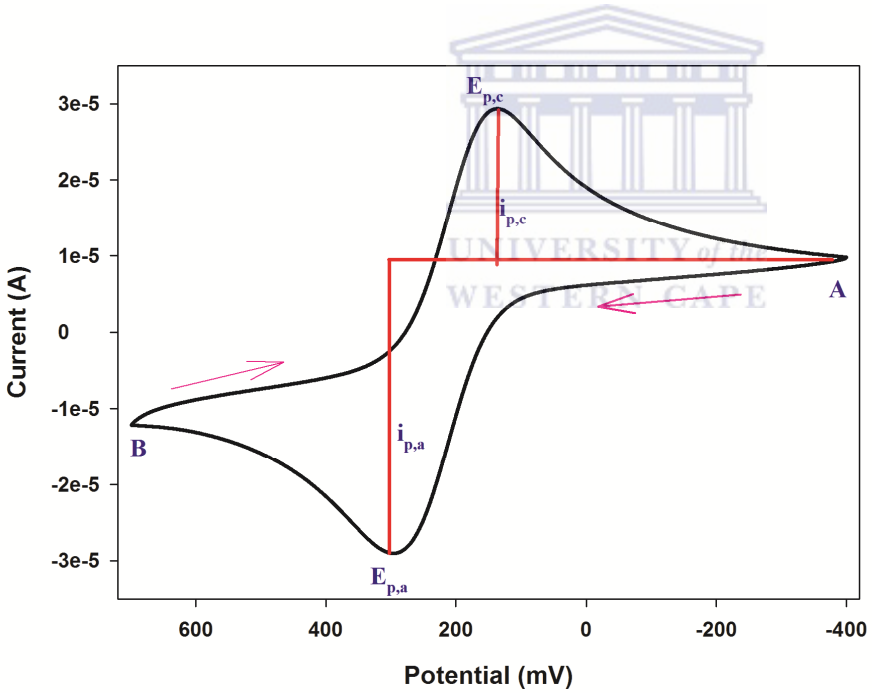

Figure 7: Typical cyclic voltammogram indicating some important anodic and cathodic peak parameters.

For a reversible charge transfer reactions where the redox products are stable within the time frame of the experiment, the peak parameters are characterized by the following:-

i. The ratio of the anodic and the cathodic current is unity ($i_{p,a}/ i_{p,c}= 1$),

ii. The corresponding peak potentials $E_{p,a}$ and $E_{p,c}$ are independent of scan rate and concentration,

iii. The formal potential E^0 is centred between $E_{p,a}$ and $E_{p,c}$, i.e $E^0= (E_{p,a} + E_{p,c})/2$.

iv. The peak separation (ΔE_p), given by $\Delta E_p = E_{p,a} - E_{p,c}$ always equals 59/n mV at all scan rates for n electrons transferred in the reversible redox process.

Due to uncompensated solution resistance, non linear diffusion and other experimental non idealities, the experimental peak separation generally yields a higher value than the theoretical 59/n mV. Larger values of ΔE_p, which increase with increasing scan rate, are characteristic of slow electron transfer kinetics. In accordance with part iv above, another peak parameter (half peak potential, $E_p/2$, where the current is half of the peak current) can similarly be deduced and be related to the half wave potential as in the equation below

$$E_{p/2} = E_{1/2} \pm \frac{29mV}{n} \qquad (16)$$

For multielectron-transfer (reversible) processes, the cyclic voltammogram consists of several distinct peaks, if the E^o values for the individual steps are successively higher and are well separated.

Cyclic voltammetric studies are usually heterogeneous in nature in the sense that the electrochemical processes occur at the interface between the electrode and the electroactive species in solution. It is worthy to note that cyclic voltammetry is carried out in unstirred solution and the electroactive species from the solution reach the electrode surface by diffusion due to concentration gradients created around the electrode surface. This process is called mass transport. The magnitude of the observed signal will be very much a function of these diffusion properties of the system. Intuitively, the current intensity (*i.e.* the flow of electrons) is expected to depend on the surface area of the working electrode and the concentration of the electro-active species. Also, one can expect the voltage scanning rate to affect the concentration profile around the electrode which itself directly affects the rate of charge transport, and for this matter the diffusion coefficient appears . The peak current (i_p) for a reversible system at 298 K is directly proportional to the square root of the scan rate as described by the Randles–Sevcik equation:

$$i_p = 2.69 \times 10^5 n^{3/2} A D^{1/2} \nu^{1/2} C \qquad (17)$$

where n is the number of electrons exchanged during the redox process, A (cm^2) the active area of the working electrode, D the diffusion coefficient ($cm^2\ s^{-1}$), C is the bulk concentration of the electroactive species (mol cm^{-3}) and ν is the voltage scan rate ($V\ s^{-1}$). A plot of the root of scan rate versus the peak current would in this case yield a linear plot with a zero intercept. Again due to uncompensated solution resistance and other factors mentioned previously in this section, deviations from the zero intercept are usually witnessed for experimental results.

Irreversible and Quasi-reversible Systems: Quasi reversible electrochemical processes exhibit sluggish electron transfer reactions and are characterized by significantly reduced peak sizes

which are widely separated. Totally irreversible systems are characterized by a shift of the peak potential with the scan rate and in most cases show either anodic or cathodic peak. The relationship between the peak potential and the scan rate for a quasi reversible system was described by Nicholson [217] according to the equation below

$$E_p = E^o - \left(\frac{RT}{\alpha nF}\right)\left[0.78 - \ln\frac{k^o}{D^{1/2}} + \ln\left(\frac{\alpha nF\nu}{RT}\right)^{1/2}\right] \qquad (18)$$

where α is the transfer coefficient and n is the number of electrons involved in the charge-transfer step. Thus, E_p occurs at potentials higher than E°, with the over potential related to k° (standard rate constant) and ν. Independent of the value k°, such peak displacement can be compensated by an appropriate change of the scan rate. The peak potential and the half-peak potential (at 25°C) will differ by 48/αn mV. Hence, the voltammogram becomes more drawn-out as αn decreases.

The peak current, given by:

$$i_p = 2.99x10^5(\alpha n)^{3/2} ACD^{1/2}\nu^{1/2} \qquad (19)$$

is still proportional to the bulk concentration, but will be lower in height (depending upon the value of α). Assuming α= 0.5, the ratio of the reversible-to-irreversible current peaks is 1.27 (*i.e.* the peak current for the irreversible process is about 80% of the peak for a reversible one). For quasi-reversible systems (with $10^{-1} > k° > 10^{-5}$ cm/s) the current is controlled by both the charge transfer and mass transport. The shape of the cyclic voltammogram is a function of the ratio $k°/(\pi\nu nFD/RT)^{1/2}$. As the ratio increases, the process approaches the reversible case. For small

values of it, the system exhibits an irreversible behaviour. Overall, the voltammograms of a quasi-reversible system are more drawn out and exhibit a larger separation in peak potentials compared to a reversible system.

For quasi-reversible reactions with a peak separation up to 200 mV a numerical approach brings values of function psi (Ψ) [218]. This well known kinetic parameter relates with the standard rate constant (k°) according to the equation below [219]:

$$\psi = k^{o}\left[\frac{\pi D n \nu F}{RT}\right]^{-1/2} \qquad (20)$$

The values depicting variation of the peak potentials with the kinetic parameter (Ψ) for cyclic voltammetry are given in the table below.

Table 2: Variation of the peak potentials with the kinetic parameter (Ψ) for cyclic voltammetry adopted from reference [217].

$\Delta E_p \, x \, n$ (mV)	61	63	64	65	66	68	72	84	92	105	121	141	212
Ψ	20	7	6	5	4	3	2	1	0.75	0.5	0.35	0.25	0,1

In view of the above discussion, both analytical chemists and non analytical chemists rely on cyclic voltammetry to investigate the electrochemical properties of a system. Important information about a system that can be obtained using cyclic voltammetry include whether the

system is electrochemically reversible, irreversible or quasi reversible, whether the electron transfer process is either slow or fast and whether it is diffusion or adsorption controlled. The number of electrons involved in a redox process can as well be determined by close analysis of a cyclic voltammogram. The redox potentials of a system under investigation further influence potential applications of the system. For instance, a system that exhibits reversible electrochemistry at low potentials may find suitable applications in electrochemical biosensor fabrication. This is because; such low potentials reduce or eliminate interference of the biosensor response by other redox active molecules that may be present in the sample under analysis. In particular, cyclic voltammetry have successfully been used for the investigation of energy levels in semiconductor NCs [220]. Cyclic voltammetric studies of CdTe [221] and CdSe [222] nanocrystals have shown some correlation between their optical properties (band gap and band positions, photoluminescence quantum yields, stability) and the appearance and shape of specific features in the corresponding cyclic voltammograms. The high sensitivity of cyclic voltammetry to the surface states of nanocrystals ushers in the possibility of distinguishing between electrochemical peaks relating to the conduction bands, valence bands as well as surface trap states.

3.3.2.2 Square wave voltammetry

Square wave voltammetry (SWV) has proved to be a suitable method to investigate redox reactions with overlapping waves. The excitation signal in SWV consists of a symmetrical square wave pulse of amplitude superimposed on a staircase wave form of step height ΔE. The forward pulse coincides with the staircase step. The net current (i_{net}) is obtained by taking the

difference between the forward and the reverse currents (i_{fwd}-i_{rev}) and is centred on the redox potential. In SWV, the peak height is directly proportional to the concentration of the electroactive species and direct detection limit as low as 10^{-8} M is possible. SWV is associated with some advantages over cyclic voltammetry. These advantages include excellent sensitivity and rejection of back ground currents. The scanning speed in SWV is also high. This high speed coupled with computer control and signal averaging allows for experiments to be performed repetitively and this increases the signal to noise ratio. SWV is also applied in study of electrode kinetics with regard to preceding, following or catalytic homogeneous chemical reactions and determination of some species at trace levels.

3.3.2.3 Differential pulse voltammetry

Differential pulse voltammetry (DPV) has progressively attracted the attention of electroanalysts, becoming one of the most popular tools for electroanalysis. In differential pulse voltammetry, a series of periodical constant pulse of potential is superimposed to a linear scan, yielding a consistent enhancement of the electrochemical signal. Current is then measured at two points for each pulse; first before the application of the pulse, and second at the end of the pulse. These sampling points are selected to allow for the decay of the nonfaradaic (charging) current. The difference between current measurements at these points for each pulse is determined and plotted against the base potential. This results in a peak shaped voltammogram.

3.3.2.4 Time based constant potential amperometry

The principle of amperometry is based on the measurement of the current between the working and counter electrode which is induced by a redox reaction at the working electrode. The conditions are chosen in such a way that the current is directly proportional to the concentration of a redox active species in the analyte solution. The electrical potential of the working electrode versus the measured solution is achieved by a separate reference electrode and is controlled by a potentiostat electronic system.

3.4 Microscopic techniques

3.4.1 High resolution transmission electron microscopy

High resolution transmission electron microscopy (HRTEM) is a powerful technique that gives the surface morphology and crystallographic information of particles of atoms in a material. HRTEM allows the direct imaging of nanoparticles and provides more information on the quality of individual particles. Useful information about the morphology of a material include its size, shape and the arrangement of the particles which make up the specimen as well as their relationship to each other on the scale of atomic diameters. The crystallographic information includes the arrangement of atoms in the specimen and the degree of order and detection of atomic scale defects in areas a few nanometers in diameter. This technique can therefore be used to determine whether particles that make up the specimen are either dispersed or agglomerated. Coupled with energy dispersive spectrometric technique, HRTEM can further give the elemental composition of a sample and their respective ratios. Quantum dots are known to agglomerate if

no surface coatings are introduced to prevent this. In the synthesis of quantum dots, 3-mercaptopropionic acid was used as a capping agent to prevent among other things the possible agglomeration of the quantum dots. The aim of carrying out HRTEM analysis on quantum dots in our synthesis was therefore to confirm the size of the nanocrystals, check if they are agglomerated or dispersed as well as their chemical composition.

3.4.2 Atomic force microscopy (AFM)

The atomic force microscope is an instrument that can analyze and characterize surfaces of samples at a microscope level (from 100 µm to < 1 µm). The instrument was invented by Gerd Binnig in 1986 to overcome the main limitation of scanning tunnelling microscope that it could only image materials that conduct tunnelling current. In AFM imaging, a sharp tip, usually a few microns long and less than 100 Å is brought into contact or in a very close proximity with the sample being imaged. The tip, normally located at the end of a 100 t0 200 µm long cantilever scans the sample beneath it. During scanning, some forces either attracts of repel the tip, causing deflections that are recorded and processed using imaging software. The resulting image is a topographical representation of the sample being imaged. The main advantage of AFM is that it can measure a number of characteristic properties of a sample that other forms of microscopy cannot give. For instance, AFM provides extraordinary topographic contrast height measurements with unobstructed surface feature as opposed to scanning electron microscope. Whereas HRTEM gives 2 dimensional profiled images viewed from cross-sectioned samples, AFM yields 3 dimensional images with in-depth information without expensive sample preparation. Unlike scanning tunnelling microscopy, SEM and HRTEM, AFM does not require

the sample to be conductive. AFM can also be used to study a very wide variety of samples including plastics, metals, glasses, semiconductors as well as biological samples such as cell walls and bacteria.

3.5 Spectroscopic techniques

3.5.1 Ultraviolet –visible spectroscopy (UV-vis)

UV-vis spectroscopy is a technique to study the electronic transition of materials with transition energy in the approximate range between10^2 and 10^3 kJ mol^{-1}, which span the near IR through the visible to the UV region of electromagnetic spectrum. For most semiconductors, the energy required for promotion of an electron from valence band to conduction band is in the same energy region, and thus UV-vis spectroscopy is a powerful technique to study the interband electronic transition in semiconductors. The study of optical absorption is therefore important to understand the behaviour of semiconductor nanocrystals. A fundamental property of semiconductors is the band gap-the energy separation between the filled valence band and the empty conduction band. Optical excitation of electrons across the band gap is strongly allowed, producing an abrupt increase in absorption at the wavelength corresponding to the band gap energy. The absorption of light at a particular wavelength is determined by the ratio of transmitted light and incident light (I/Io). Therefore absorbance can be expressed as:

$$A = -\log\left(\frac{I}{I_0}\right) \qquad (21)$$

Each molecule in a solution absorbs a certain amount of light. Beer's Law quantifies the absorbance of each molecule at a wavelength to its concentration and the length of the light path.

$$A_\lambda = \varepsilon_\lambda cl \qquad (22)$$

where ε_λ is the molar extinction coefficient at wavelength λ, c is the concentration and l is the length of light path. Typically the light path is a constant equal to the quartz cell length of 1cm, while the concentration may vary. Based on experimentally measured absorbance, it is possible to determine ε_λ or *c* if one of the values is known. UV-vis absorption spectroscopy is also an effective technique used to study particle growth of nanocrystals [223]. According to the effective mass model, the radius of the particle is related to the absorption band [224]. UV-vis characterization gives an idea about the size of the particles under investigation since the band edge depends on the particle size. Absorption peak occurring at lower wavelengths imply a blue-shifted absorption edge resulting from quantum confinement of the excitons present in the sample. The excitons present in the sample cause a more discrete energy spectrum of the individual nanoparticles. If no visible absorption is seen in the visible region, the system can be said to be a non-linear optical (NLO) material.

3.5.2 Fluorescence spectroscopy

Fluorescence is the emission of light by a molecule (fluorophore) that occurs within microseconds after the absorption of light (excitation) of shorter wavelength [225]. Semiconductors contain a conduction band, a band gap, as well as a valence band. The interaction of all three components imparts optical properties of the quantum dot [61]. Under normal conditions of room temperature, the electronic state of a quantum dot will be in its lowest

possible energy state, known as the ground state (S_0). Once exposed to a visible or ultraviolet light, a quantum dot will absorb a photon and one or more electrons of the quantum dot will jump from the valence band to the conduction band [61]. This leaves a hole in the valence band where the electron originally was found and an electron-hole pair known as an exciton is produced [54]. An excited quantum dot acquires several energy levels known as singlet states, denoted as S_1, $S_{2, ..., }$ S_n also arise. In the a singlet excited state, the electron in the higher energy orbital has the opposite spin orientation relative to electron in the lower orbital.

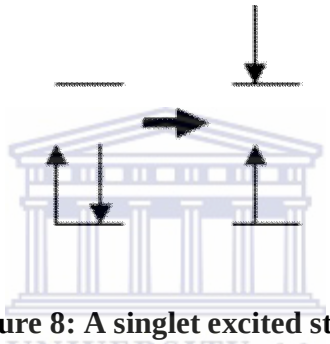

Figure 8: A singlet excited state.

From the excited state, the hole and the electron recombine bringing the quantum back to the ground state. This process may take place via non-radiative transition or a radiative decay from a singlet excited state to the ground state.

(a) The non-radiative transition of an excited molecule

The non-radiative electron-hole recombination paths include internal conversion or a transition to an excited triplet state (intersystem crossing). Triplet excited state occurs via

inversion of the spin of the excited electron (spin flip resulting in two unpaired electrons with the same spin orientation, resulting in a state with Spin=1 and multiplicity of 3 (triplet state).

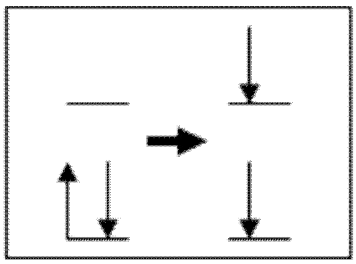

Figure 9: A triplet excited state.

The various energy levels of triplet states are denoted as T_1, T_2,T_3, etc.

(b) The radiative transition of an excited molecule.

From a triplet excited state, a molecule may undergo a radiative transition to the ground state. This is accompanied by a spontaneous emission of (photon) light and the process is called phosphorescence. A radiative electron-hole recombination may also occur, causing a direct transition from a singlet excited state to the ground state [54, 61]. This produces a photon emission spectrum and the process is called fluorescence. The photon energies produced in both fluorescence and phosphorescence reflect the various energy states that are present in the quantum dot. These different energy states are produced by different defects as well as the many different ways though which impurities are incorporated into the lattice.

Typically, fluorescence results from a transition between the lowest energy level of the first excited singlet state and some vibrational level of the ground state. The delay between absorption and emission in fluorescence is of the order of 10^{-8} seconds or less whereas it is much longer in phosphorescence [226]. The emission delay in phosphorescence is believed to result from the presence of vacant lattice sites (trap states), impurities, lattice defects, and/or irregularities in the host lattice that detain or trap the charge carriers (electrons/holes) before their radiative recombination with the luminescent centres. Fluorescence therefore exhibits shorter life time than phosphorescence, a property that allows for fast analysis. The use of fluorescence as an analytical probe tool was inspired by J.B Birk's work (1960) who used fundamental fluorescence to study the photophysical properties of simple aromatic molecules in solution [227]. Since then, fluorescence spectroscopic studies have been extended to more complex systems. Today, fluorescence spectroscopy has been established as a sensitive, selective, non-destructive, and versatile tool for probing various systems such as solutions, colloids, organic and inorganic solids, and polymers [228-229].

In characterization of colloidal quantum dots, fluorescence emission spectrum provides information about the nature of a point defect of a material by determining not only the presence, but also the type of vacancies, interstitials, and impurities in the lattice. It is however important to mention that, single-wavelength emission spectrum can be limited for the analysis of complicated multicomponent samples, or even a simple mixture which contains grossly overlapping emission and/or excitation spectra. This is because conventional fluorescence spectra reveals the fluorescence of a sample within one spectral region, and may not provide enough data to distinguish between two or more closely related emitting molecules. Advanced fluorescence measurements known as three-dimensional excitation–emission matrix (EEM)

fluorescence spectroscopic analyses are therefore necessary for analysis of quantum dot point defects, trap states, types of vacancies, interstitials and impurities in the lattice. EEM produces fluorescence spectra at many excitation wavelengths providing an overall view of all features existing within the selected spectral range. It has been proven to be a useful technique to differentiate the changes and transformations of organic matters in natural environments [230-232]. The prominent advantage of the EEM fluorescence spectroscopy is that the information regarding the fluorescence characteristics can be completely obtained by changing the excitation wavelength and emission wavelength simultaneously. By analyzing different spectral regions, EEM could be also used to distinguish the fluorophores present in colloidal quantum dot samples [233].

3.5.3 Fourier transforms infrared spectroscopy (FTIR)

Fourier transform infrared spectroscopy (FTIR) is a powerful technique that provides information about the chemical bonding or molecular structure of materials. FTIR works on the principle that bonds and groups of bonds vibrate at characteristic frequencies. Upon exposure of a molecule to infrared rays, the molecule absorbs infrared energy at frequencies that are characteristic to that molecule. During FTIR analysis, a spot on the specimen is subjected to a modulated IR beam. The specimen's transmittance and reflectance of the infrared rays at different frequencies is translated into an IR absorption plot consisting of reverse peaks. The resulting FTIR spectra is then analyzed and matched with known signatures of identified materials in the FTIR library. In our synthesis of quantum dots, 3-mercaptopropionic acid was incorporated as an amphiphilic molecule. It was expected that the thiol group (HS-) of the 3-

mercaptopropionic acid which is hydrophobic would covalently bind with the hydrophobic surface of the quantum dot while the carboxylic acid group (-COOH) extends to a water molecule to make the quantum dot soluble. It was therefore necessary to analyze the quantum dots to check if the 3-mercaptopropionic acid was truly retained on the quantum dot surface. The FTIR was thus carried out to mainly check the presence of 3-mercaptopropionic acid in the synthesized quantum dots.

3.5.4 X-ray diffraction spectroscopy (XRD)

X-ray diffraction spectroscopy is a versatile non destructive technique that reveals detailed information about the chemical composition and crystallographic structure of natural and synthetic compounds. A crystalline lattice is a regular three dimensional distribution (cubic, rhombic) of atoms in space. The atoms are arranged in such a manner that they form a series of parallel planes separated from one another by a distance (d), which varies according to the nature of the material. When a monochromatic x-ray beam with a wavelength lambda (λ) is projected onto a crystalline material at an angle theta (θ), diffraction occurs only when the distance travelled by the rays reflected from successive planes differs by a complete number of wavelengths.

3.6 Procedures

3.6.1 Synthesis of selenide quantum dots

3.6.1.1 Mercaptopropionic acid-capped zinc selenide quantum dots (ZnSe-3MPA).

ZnSe-3MPA quantum dots were prepared according to method described by Andrade et al 2009 [234] with some modification.

Preparation of Se^{2-}

In normal atmospheric conditions, selenium reacts quickly, vigorously and isothermally with sodium borohydride in aqueous solution to produce sodium hydrogen selenide according to the stoichiometry of equation (23) below.

$$4NaBH_{4(s)} + 2Se_{(s)} + 7H_2O_{(l)} \rightarrow 2NaHSe_{(aq)} + Na_2B_4O_{7(aq)} + 14H_{2(g)} \quad (23)$$

The first step in the synthesis of ZnSe-3MPA involved reduction of selenium powder by $NaBH_4$ to obtain Se^{2-} ions. This was achieved by mixing 0.1579 g of Se powder with 0.1513 g of $NaBH_4$ in a round bottomed flask and adding de-ionized water to make 100 mL solution, resulting to 0.02 M and 0.04 M of Se and $NaBH_4$ respectively. The mixture was then stirred continuously at room temperature under nitrogen saturation for 25 minutes after which a dark yellow solution was formed.

Preparation of Zn^{2+}

The second step was to separately obtain Zn^{2+} ions. In this step, 0.01 M of zinc nitrate hexahydrate was prepared by dissolving 0.2975 g of the salt in de-ionized water and making it into a 100 mL solution. 696 µL of 3-mercaptopropionic acid (3-MPA) was added to the zinc nitrate solution to make 0.04 M of the capping agent in a total reaction volume of 200 mL. The pH of the resulting solution was adjusted to 12.12 by adding 0.5 M of NaOH. Under basic conditions, the zinc ions interact with the thiol group of the capping agent while the dehydrogenated carboxyl groups stabilize the quantum dots through electrostatic repulsion. The mixture was saturated with nitrogen gas for 30 minutes.

The third step involved drop wise addition of the freshly prepared Se^{2-} ions into the nitrogen saturated zinc nitrate/3-MPA solution. The reaction was allowed to take place under nitrogen saturation with continuous stirring at room temperature. After 40 minutes, a pale yellow solution was formed. The reaction was then quenched by immediately moving the reaction flask into a fridge at -20 °C after the 40^{th} minute.

3.6.1.2 Mercaptopropionic acid-capped gallium selenide quantum dots (Ga_2Se_3-3MPA).

Preparation of Ga^{3+}

The element gallium belongs to group 13 of the periodic table. The valence shells of the members of this group have an electronic configuration of the form ns^2np^1. It is therefore expected that majority of compounds of the elements of this group would contain elements in

oxidation state +3. However, all the metals of this group, except boron and aluminium exhibit an additional oxidation state of +1 [235]. This is attributed to the inert pair effect, whereby, after the removal of one electron from p-orbital, the remaining ns^2 (e.g. $6s^2$) electrons behave like stable noble gas and do not take part in ion formation. This reluctance of the s-electron pair to take part in chemical combination is called inert pair effect. Whereas compounds of gallium in its univalent oxidation state have been reported[235], details of cationic existence of Ga^{3+} are scanty. In fact, there is no evidence for the existence of simple Ga^{3+}. Oxyacid salts of gallium, which probably contain the metal as an aqua-complex are deliquescent and crystallize with water of crystallization. They present important sources of water soluble ionic Ga^{3+} precursors for synthesis procedures. Hot perchloric acid is an example of an oxyacid which reacts with gallium metal to precipitate hydrated gallium (III) perchlorate according to the equation (24)

$$2Ga_{(s)} + 6HClO_{4(l)} + 6H_2O_{(l)} \rightarrow 2Ga(ClO_4).6H_2O_{(s)} + 3H_{2(g)} \qquad (24)$$

In our preparation, 4.87 g of Ga metal was weighed into a round bottomed flask and 2 mL of concentrated $HClO_4$ added. The mixture was refluxed under constant stirring for 4 h at 120 °C, after which, a white precipitate of $GaClO_4.6H_2O$ was formed. 1.900 g of the gallium salt was dissolved in 100 mL of distilled water and 696 µL of concentrated MPA added. The pH of the solution was adjusted to 12.12 using NaOH and saturated with N_2 for 30 min. Selenium ions were prepared as described previously (see preparation of ZnSe-3MPA quantum dots). Freshly prepared Se^{2-} was added drop wise into the nitrogen saturated $Ga(ClO_4)_3$/3MPA solution. After 10 min a brown solution was formed and the reaction was quenched by immediately placing the reaction flask in a freezer at -20 °C.

3.6.1.3 Mercaptopropionic acid-capped zinc-gallium selenide quantum dots ($Zn_2Ga_2Se_5$-3MPA).

$Zn^{2+,}$ Ga^{3+} and Se^{2-} were prepared as described previously. 25 mL of Nitrogen saturated $Ga(ClO_4)_3$/3MPA solution was added drop wise to an equal volume of nitrogen saturated zinc nitrate/3-MPA solution. The mixture was continuously stirred under nitrogen saturation for 10 minutes. 50 mL of freshly prepared Se^{2-} was added drop wise into the nitrogen saturated $Ga(ClO_4)_3$/3MPA- zinc nitrate/3-MPA mixture. The reaction mixture was stirred for 40 min and quenched by immediately placing the reaction flask in a freezer at -20 °C.

3.6.2 Synthesis of telluride quantum dots

3.6.2.1 Mercaptopropionic acid-capped zinc telluride quantum dots (ZnTe-3MPA).

Preparation of Te^{2-}

Tellurium metal was reduced by adding 0.0255 g of the metal to 3 mL of concentrated hydrazine hydrate in a round bottomed flask. The mixture was then stirred continuously at room temperature under nitrogen saturation for 2 h after which a bluish solution was formed. The solution was diluted to 10 mL using deionized water. A nitrogen saturated zinc nitrate/3-MPA solution was prepared as previously described and acted as the source of Zn^{2+}. To a freshly prepared nitrogen saturated zinc nitrate/3-MPA solution, freshly prepared telluride solution was added drop wise under nitrogen saturation with constant stirring. The reaction was allowed to take place under nitrogen saturation with continuous stirring at room temperature. After 10

minutes, a purple-blue solution was formed. The reaction was then quenched by immediately moving the reaction flask into a fridge at -20 °C after the 10th minute.

3.6.2.2 Mercaptopropionic acid-capped gallium telluride quantum dots (Ga_2Te_3-3MPA).

Nitrogen saturated $Ga(ClO_4)_3$/3MPA solution was prepared as previously described for the preparation of Ga_2Se_3-3MPA while Te^{2-} was prepared as described for the preparation of ZnTe-3MPA. Freshly prepared Te^{2-} was added drop wise into the nitrogen saturated $Ga(ClO_4)_3$/3MPA solution. The reaction was allowed to take place under nitrogen saturation with continuous stirring at room temperature for a further 10 minutes after which it was quenched by immediately moving the reaction flask into a freezer at -20 °C after the10th minute.

3.6.2.3 Mercaptopropionic acid-capped gallium telluride quantum dots ($Zn_2Ga_2Te_5$-3MPA).

Zn^{2+}, Ga^{3+} and Te^{2-} were prepared as described previously. 25 mL of Nitrogen saturated $Ga(ClO_4)_3$/3MPA solution was added drop wise to an equal volume of nitrogen saturated zinc nitrate/3-MPA solution. The mixture was continuously stirred under nitrogen saturation for 10 minutes. 50 mL of freshly prepared Te^{2-} was added drop wise into the nitrogen saturated $Ga(ClO_4)_3$/3MPA- zinc nitrate/3-MPA mixture. The reaction was allowed to take place for with constant stirring under nitrogen saturation for10 minutes. The reaction was then quenched by immediately moving the reaction flask into a freezer at -20 °C after the10th min.

3.6.3 Electrochemical characterization

To study the electrochemistry of the quantum dots and nanocrystals in solution, 5 mL of each of the freshly prepared quantum dot or nanocrystal solution was put in a 10 mL electrochemical cell and de-aerated with argon for 10minutes. The voltammograms (CV, SWV or DPV) were recorded under argon atmosphere. The electrochemistry of the quantum dots and nanocrystals immobilized on the surface of the gold electrode was done as follows. For each material, a thoroughly cleaned gold electrode was immersed in its solution for a specific period of time in the dark. The immobilization time for each material was different and was chosen from optimized experiments, basing on the surface coverage of the quantum dot or nanocrystal on the electrode surface. The optimized immobilization times were 24 h (ZnSe-3MPA), 12 h (Ga_2Se_3-3MPA), 12 h ($Zn_2Ga_2Se_5$-3MPA) and 16 h for all telluride quantum dots. The voltammetric measurements of the modified electrodes were done in 5 mL of 0.1 M phosphate buffer saline solution of pH 7.40. Impedimetric measurements of the modified electrodes were done in 5 mL of 5.00 mM of $Fe(CN)_6^{4-/3-}$ solution in the frequency range 50 kHz to 100 mHz at an amplitude of 10 mV and a potential of 200 mV.

3.6.4 Spectroscopic characterization of the quantum dots and nanocrystals

3.6.4.1 Utraviolet–visible spectroscopy

Freshly prepare samples were used for UV-vis analysis. UV–visible (UV-vis) absorption measurements of samples were obtained in quartz cuvettes using a Nicolet Evolution 100 UV–visible spectrometer (Thermo Electron, UK)

3.6.4.2 Fluorescence spectroscopy

Fluorescence spectra of liquid samples were recorded using Horiba NanoLog™ 3-22-TRIAX (USA), with double grating excitation and emission monochromators at a slit width of 5 nm.

3.6.4.3 Fourier transforms infra red spectroscopy (FTIR).

Before analysis, liquid samples of quantum dots or nanocrystals from the mother solution were preconcentrated by centrifuging at 14000 rpm for 30 minutes. The preconcentrated sample of each quantum dot was mounted on a NaCl pill with the aid of nujol. The FTIR spectra were recorded spectrum 100 FT-IR spectrometer (PerkinElmer, USA) in the region 400 to 4000 cm^{-1}.

3.6.4.4 X-ray diffraction spectroscopy (XRD).

Before analysis, liquid samples of quantum dots or nanocrystals from the mother solution were preconcentrated by centrifuging three times at 14000 rpm, each for 30 minutes. The preconcentrated quantum dot samples were then precipitated in absolute ethanol followed by a further 30 minute centrifuging at 14000 rpm. Nitrogen gas was gently bubbled through the precipitate until all solvent was driven out. The XRD of the powdery samples was recorded in the range 20 – 70 degrees using a Bruker AXS D8 Advance diffractometer from BRUKER-AXS Germany at 40 KV voltage and 40 mA current.

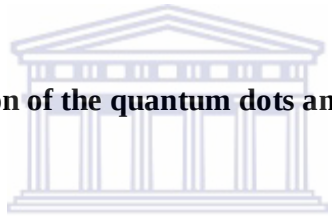

3.6.5 Microscopic characterization of the quantum dots and nanocrystals

3.6.5 .1 High resolution transmission electron microscopy (HRTEM)

Before analysis, liquid samples of quantum dots or nanocrystals from the mother solution were preconcentrated by centrifuging at 14000 rpm for 30 min. The preconcentrated samples were dispersed in ethanol and ultrasonicated for 5 minutes. A small drop of a dilute solution of the quantum dots in ethanol was placed on a copper coated HRTEM grid and the solvent was left to dry. HRTEM analysis of the mounted quantum dots or nanocrystals was done using a Tecnai G2 F20X-Twin MAT 200 kV Field Emission Transmission Electron Microscope from FEI (Eindhoven, Netherlands).

3.6.5 .2 Atomic Force microscopy (AFM).

The preparation of samples for AFM analysis was as follows: 10 µL of liquid quantum dot sample was dropped on a screen printed gold electrode and left covered in the dark overnight for the liquid to evaporate. The samples were scanned with a silicon tip at a spring constant of 1-5 N/m and resonance frequency of 60-100 kHz. The scanned AFM images were taken using a Veeco NanoMan V model (Cambridge, USA).

3.6.6 Application procedure 1- A potential masking approach in the detection of dopamine on 3-mercaptopropionic acid capped ZnSe quantum dots modified gold electrode in the presence of interferences

3.6.6.1 Preparation of ZnSe-3MPA quantum dot modified gold electrode.

A thoroughly cleaned electrode was immersed in a quantum dot solution for 24 h in the dark. The modified electrode was then removed from the quantum dot solution and gently rinsed with de-ionized water to remove and physically or weakly adsorbed quantum dots. This electrode will be abbreviated in this work as Au/ZnSe-3MPA. A freshly prepared electrode was used in all electrochemical measurements. Stock solutions of dopamine, uric acid and ascorbic acid were prepared in the working buffer and stored at 4°C when not in use and were diluted using the working buffer during analysis. The working buffer was 0.1 M phosphate buffer saline solution of pH 6.0.

3.6.7 Application procedure 2: Impedimetric response of a label-free genosensor prepared on a 3-mercaptopropionic acid capped gallium selenide nanocrystal modified gold electrode.

3.6.7.1 Preparation of electrode.

A gold disk electrode was thoroughly cleaned by polishing it on a soft polishing pad using 1.00, 0.30 and 0.05 μM slurries of alumina respectively, rinsing with de-ionized water after each polish. This was followed by ultrasonication in de-ionized water for 5 min. The freshly polished gold was electrochemically cleaned in 0.50 M H_2SO_4 by potential scanning between −300 and 1500 mV until reproducible cyclic voltammograms were obtained. The gold electrode was immersed in a Ga_2Se_3-3MPA solution for 12 h in the dark, to obtain an Au|Ga_2Se_3-3MPA electrode. The modified electrode was then removed from the Ga_2Se_3-3MPA solution and gently rinsed with de-ionized water to remove any physically or weakly adsorbed nanocrystals. The Au|Ga_2Se_3-3MPA electrode was then immersed in a mixture of 5.0 mM EDC and 8.0 mM NHS in pH 7.40 PBS for 30 min to obtain an active surface. The surface activated electrode was again rinsed gently with de-ionized water. 10 μL of 20 μM probe ssDNA solution was dropped on the modified solution and left to immobilize for 12 h at 25 °C, to give Au|Ga_2Se_3-3MPA|ssDNA (biosensor).

3.6.7.2 Hybridization and electrochemical detection

Hybridization reaction was electro statically performed by dipping the biosensor in a stirred solution (0.10 M PBS, pH 7.40) containing different concentrations of the target

(complementary) DNA at a potential of 500 mV for 10 min. The hybridized electrode was washed twice with the same buffer solution. The same procedure was repeated using the non-complementary or the 3-base mismatched oligonucleotide instead of the complementary DNA. Electrochemical detection was done using EIS in presence of 5.00 mM $[Fe(CN)_6]^{3-/4-}$ (ratio, 1:1) as the redox probe. The impedimetric spectra were recorded on a VoltaLab PGZ 402 at the frequency range 50 kHz to 100 mHz at an amplitude of 10 mV and a potential of 200 mV.

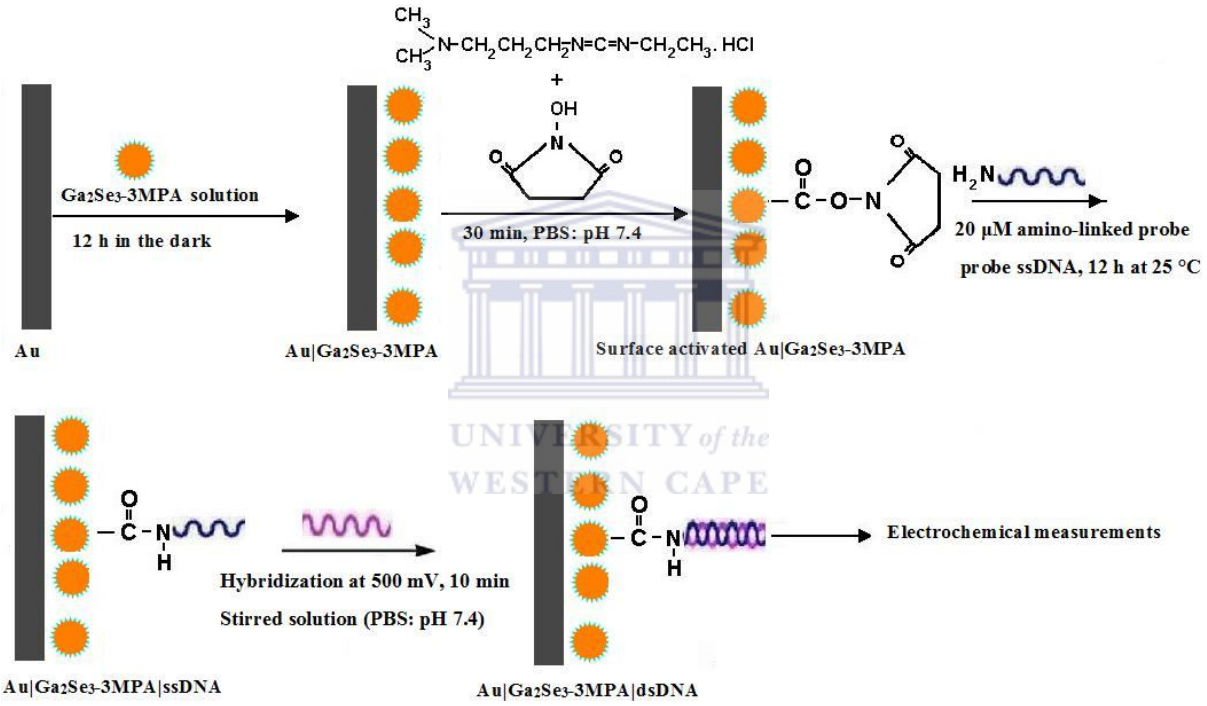

Figure 10: Scheme for the preparation and hybridization of DNA on a label free based on a 3-mercaptopropionic acid capped gallium selenide nanocrystal modified gold electrode.

3.6.8 Application procedure 3: Voltammetric response of a label-free genosensor prepared on a 3-mercaptopropionic acid capped zinc selenide quantum dot modified gold electrode.

3.6.8.1 Preparation of electrode.

A gold disk electrode was cleaned a described earlier. The gold electrode was immersed in a quantum dot solution for 12 h in the dark, to obtain an Au/ZnSe-3MPA electrode. The modified electrode was then removed from the quantum dot solution and gently rinsed with de-ionized water to remove any physically or weakly adsorbed nanocrystals. The Au/ ZnSe-3MPA electrode was then immersed in a mixture of 5.0 mM EDC and 8.0 mM NHS in pH 7.4 PBS for 30 min to obtain an active surface. The surface activated electrode was again rinsed gently with de-ionized water. 10 µL of 20 µM probe ssDNA solution was dropped on the modified solution and left to immobilize for 12 h at 25 °C, to give Au/ZnSe-3MPA/ssDNA (genosensor).

3.6.8.2 Hybridization and electrochemical detection

Hybridization reaction was electro statically performed by dipping the biosensor in a stirred solution (0.1 M PBS, pH 7.4) containing different concentrations of the target (complementary) DNA at a potential of 500 mV for 10 min. The hybridized electrode was washed twice with the same buffer solution. The same procedure was repeated using the non-complementary or the 3-base mismatched oligonucleotide instead of the complementary DNA. Electrochemical detection using SWV and DPV in a 10 mL electrochemical cell containing phosphate buffer saline of pH 7.40. Impedimetric measurements were also done in presence of 5.00 mM $[Fe(CN)_6]^{3-/4-}$ (ratio, 1:1) as the redox probe.

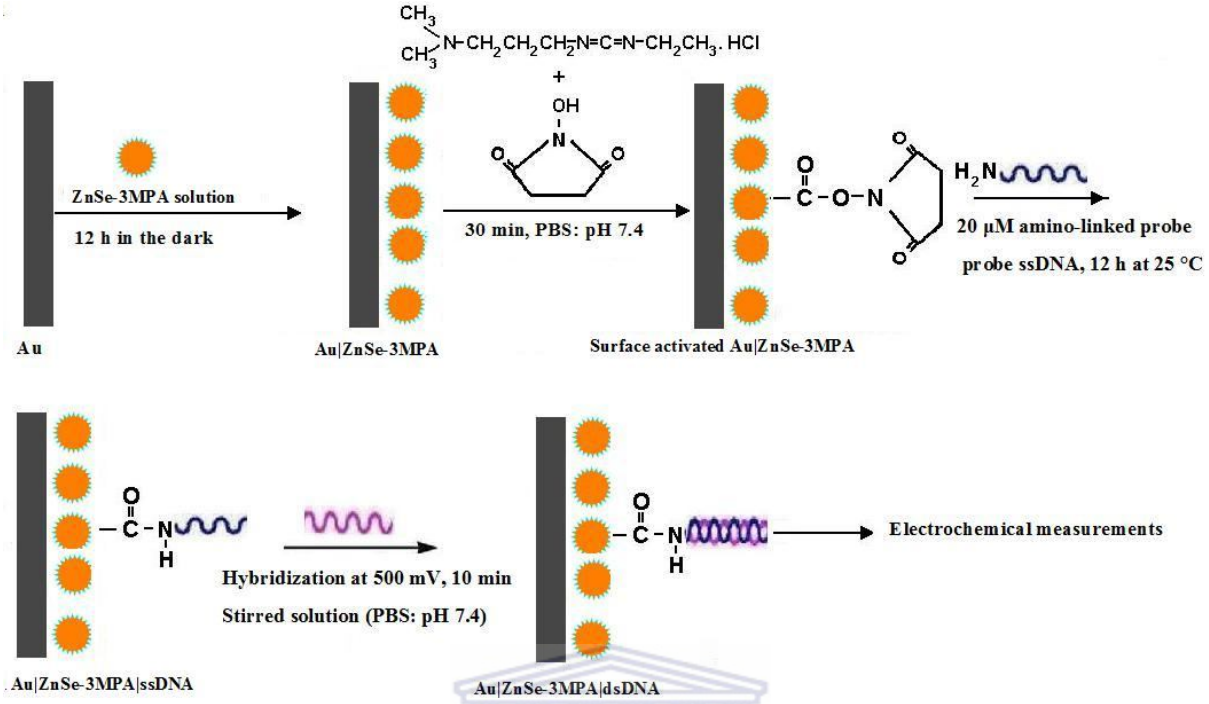

Figure 11: Scheme for the preparation and hybridization of DNA on a label free based on a 3-mercaptopropionic acid capped zinc selenide quantum dot modified gold electrode.

3.6.9 Application procedure 4-Telluride quantum dot-impedimetric genosensors.

The fabrication of telluride quantum dot genosensors followed a protocol similar to that described in section 3.3.6 except that the Ga_2Se_3-3MPA were replaced with either ZnTe-3MPA, Ga_2Te_3-3MPA or $Zn_2Ga_2Te_5$-3MPA. A general electrode preparation scheme is thus given in the figure below.

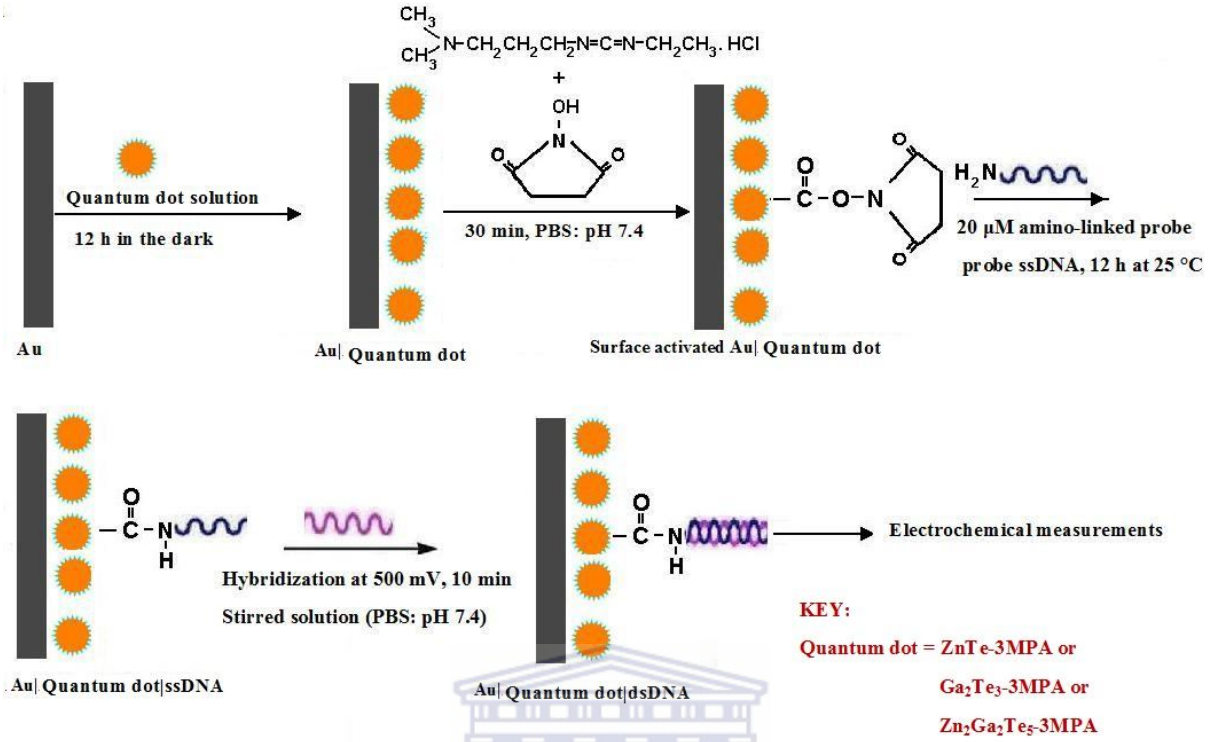

Figure 12: Scheme for the preparation and hybridization of DNA on a label free based on 3-mercaptopropionic acid capped telluride quantum dot- modified gold electrodes.

Similarly, the hybridization and detection procedures followed the same steps as for section 3.3.6.

CHAPTER 4

Results and Discussion 1: Characterization of binary and ternary selenide quantum dots and nanocrystals.

4.1 Introduction

The investigation of the electronic structure of semiconductors has recently become an area of great interest. This has been inspired by the possibility of fabricating novel materials whose magnetic and electronic properties can easily be adjusted. Chalcogenide quantum dots, depending on the composition of the transitionmetal may exhibit structural vacancies that give rise to numerous electronic, structural and optical properties [236]. For instance, semiconductors consisting of group II and VI elements are typically characterized by sp^3 hybridized bonding, accommodating all eight electrons in each cation-anion pair. These semiconductors therefore exhibit valence match and crystallize to form either zinc blende or wurzite structures. For semiconductors consisting of group III and VI however, the sp^3 hybridized bonding is difficult to form and their crystalline structure stabilizes by forming structural vacancies. In Ga_2Se_3 for example, there exists nine electrons per a gallium-selenium pair, resulting in a valence mismatch semiconductor system that crystalizes in a defected zinc blende structure. In its structure, a third of the gallium sites are vacant. The structural vacancies are important sources of desired structural, optical and electronic properties of the semiconductor crystals. Semiconductors whose elements exhibit valence matching can be modulated to exhibit structural vacancies by introducing impurities through doping or alloying. Introduction of chemical impurities (doping) can result in vacancy generation as the crystal seeks equilibrium between local charge balance,

bonding coordination, and valence around the impurity and thermal energy can create vacancies even in ultrapure materials at temperatures above absolute zero. Semiconductor doping involves addition of an extra element, either a transition metal or a chalcogen. This forms ternary semiconductor systems that are classified into two. The first type consists of two chalcogens and one transitional element while the other type consists of two transitional elements and one chalcogenide [237].

The electrochemical and optical properties of quantum dots are highly sensitive to their surface structure due to their large surface area to volume ratio [238]. Upon application of electrical potential in cyclic voltammetry, the Fermi level of the electrode and that of the adsorbed quantum dots are shifted either lower or higher energies leading to oxidation or reduction respectively. A Fermi level equivalent to the band edge of the quantum dot causes an electron transfer between the quantum dot and the electrode, generating some current. The peak current thus corresponds to band energy of either the conduction or valence band and the peak separation is a measure of the band gap energy. The study of the electrochemistry of quantum dots can therefore reveal information regarding various electronic transitions and possible decomposition during oxidation or reduction. Since the energy levels of surface traps of quantum dots are difficult to predict [221], it is important to establish the correlation between the electrochemical and optical band gaps. It has been already established that [239-241] the potentials related to the cathodic and anodic curves obtained from cyclic voltammetry can be used evaluate ionization energy (Ip) and the electron affinity (Ea), as well as the difference between the highest occupied molecular orbital (HOMO) and the lowest un occupied molecular orbital (LUMO). This difference is called the band gap (Eg). Furthermore, quantum chemical calculations by Bredas et al reported a linear correlation between Ip and Ea, as well as between

Ea and reduction potentials (E_{red}) [242]. All these parameters are related according to the equations below [239]

$$Ea = \left(E'_{red} + 4.4\right)eV \qquad (25)$$

$$Ip = \left(E'_{ox} + 4.4\right)eV \qquad (25)$$

$$Eg = Ip - Ea \qquad (27)$$

Where E'_{red} and E'_{ox} are the respective onset reduction and oxidation potentials versus Ag/AgCl reference electrode.

4.2 Electrochemistry of ZnSe-3MPA quantum dots

4.2.1. ZnSe-3MPA quantum dot solution

The cyclic voltammetry of ZnSe-3MPA quantum dot solution on gold electrode was studied at a potential range of -200 to +800 mV and the results are shown in the figure below. Two anodic peaks are observed in the potential region of 300 mV to 400 mV and 510 mV to 680 mV. In the reverse scan, only one cathodic peak occurs in the potential region of 130 mV to 160 mV. Peaks B_2 and B_3 shifted significantly to more positive potentials while peak B_4 shifted to more negative potentials with increasing scan rate. This is an indication that the reactions responsible for these peaks are irreversible and points to an electrochemical decomposition of the ZnSe-3MPA quantum dots. A plot of scan rate versus peak current for peak B_2 was non linear

but a linear relationship was found between the peak current and the square root of scan rate. This suggests that peak B_2 resulted from diffusion controlled irreversible reaction and was attributed to oxidation of selenium according to the equation below.

$$Se^{2-} \rightarrow Se^{0} + 2e^{-} \qquad (28)$$

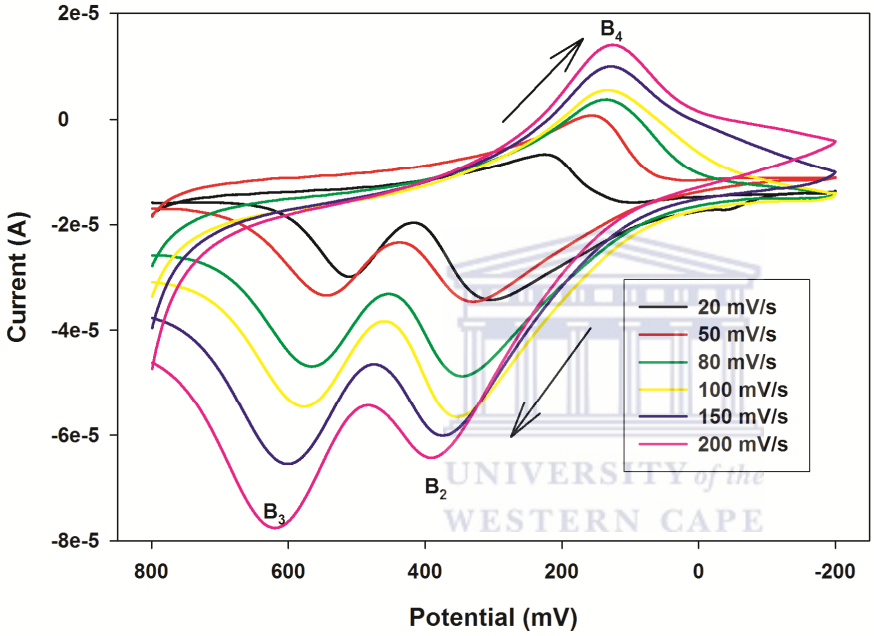

Figure 13: Cyclic voltammograms of ZnSe-3MPA solution.

The peak currents for peaks B_3 and B_4 were linearly dependent on scan rate but non-linearly dependent on the square root of scan rate. This suggests that the electrochemical reactions responsible for these peaks were surface confined. Peak B_3 was attributed to anodic dissolution of selenium according to the equation

$$Se^{2-} \rightarrow Se^{4+} + 6e^{-} \qquad (29)$$

while peak B_4 was attributed to electro deposition of selenium on the gold electrode according to the equation

$$Se^{4+} \rightarrow Se_{ads} + 4e^{-} \qquad (30)$$

Using peak B_3 and B_4, the evaluated electrochemical band gap was 0.53 eV.

4.2.2 Electrochemistry of Au|ZnSe-3MPA in phosphate buffer solution.

The electrochemical behaviour of ZnSe-3MPA immobilized on a gold electrode was investigated in phosphate buffer solution of pH 7.40 as well as in 5.00 mM $Fe(CN)_6^{3-/4-}$ using cyclic voltammetry and electrochemical impedance spectroscopy. Near symmetrical anodic and cathodic waves are clearly observed, characterizing adsorbed electrochemistry of the ZnSe-3MPA quantum dots. To confirm this, linear relationship between the peaks current and scan rate was investigated. The cathodic and anodic peak currents were linear functions of the scan rate in the range 80 mV/s to 450 mV/s and their linear regressions were $I_{p,a} = -8.3985 \times 10^{-5}\nu + 5.094 \times 10^{-9}$ ($r^2 = 0.999$) and $I_{p,c} = 1.0024 \times 10^{-4}\nu - 3.999 \times 10^{-6}$ ($r^2 = 0.989$). These results indicate that the electron transfer reaction in the buffer was controlled by adsorption of ZnSe-3MPA quantum dots on the surface of gold electrode. To determine the number of electrons transferred as well as the surface concentration of the adsorbed ZnSe-3MPA quantum dots on the surface of the gold electrode, equation 31a [243] and equation 31b [244] were re-expressed to give equation 31c;

$$i_p = \frac{n^2F^2A\Gamma\nu}{4RT} \qquad (31a)$$

$$Q = nFA\Gamma \qquad (31b)$$

$$i_p = \frac{nFQ\nu}{4RT} \qquad (31c)$$

Where Γ is the surface concentration of the electrode material (ZnSe-3MPA, mol cm^{-2}), A is the electrode area ($0.0201cm^2$), i_p is the peak current (A), Q is the quantity of charge (C) calculated from the reduction peak area of the voltammograms, n is the number of electrons, F is the Faraday constant (96,584 C mol^{-1}), R is the gas constant (8.314 J mol^{-1} K^{-1}), T is Kelvin temperature (298 K) and v is the scan rate (V s^{-1}). The number of electrons transferred calculated from equation 31c for both anodic and cathodic processed were 5.6281 and 5.7892 respectively. This suggests six electron transfer process. On average, a surface concentration of 2.5215 $x10^{-10}$ mol cm^{-2} was calculated. This surface concentration lies within the order of a monolayer and characterized MPA induced self assembled monolayer [245].

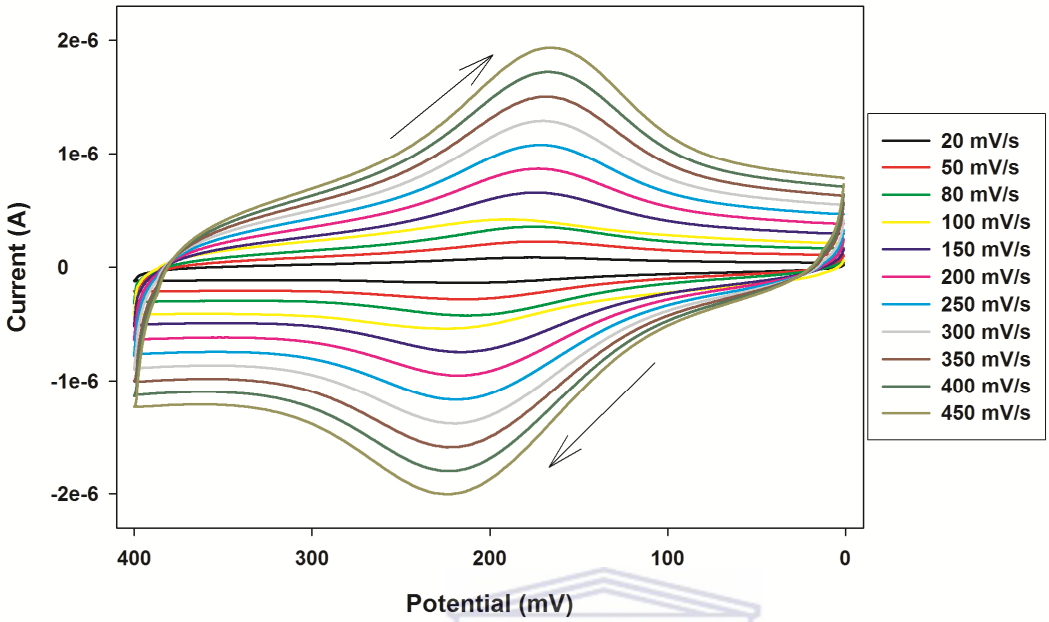

Figure 14: Cyclic voltammograms of Au|ZnSe-3MPA in 0.10 M phosphate buffer of pH 7.40.

On varying the scan rate, the formal potential $\{E^0 = (E_{p,a} + E_{p,c})/2\}$ was found to be fairly constant ≈ 200 mV (SD = 1.35 x10^{-4} for 11 scan rates). This is an indication that the electron transfer coefficients, α_a and α_c for anodic and cathodic processes, respectively, are similar ($\alpha_a \approx \alpha_c \approx 0.5$).

The dependence of peak potentials (both cathodic and anodic) on the natural logarithm of scan rate was linear at high scan rates (from 100 mV/s to 450 mV/s) but non linear at scan rates below 100 mV/s. According to Laviron's equation [246] and the steady state theory [247], the anodic peak potential and the cathodic peak potential are related with the natural logarithm of the scan rate as shown in the equations below.

$$E_{p,c} = E^{0'} - \frac{RT}{\alpha nF} \ln \frac{\alpha nF\nu}{RTk_s} \qquad (32a)$$

$$E_{p,a} = E^{0'} + \frac{RT}{(1-\alpha)nF} \ln \frac{[(1-\alpha)nF\nu]}{RTk_s} \qquad (32b)$$

Where $E_{p,c}$ and $E_{p,a}$ are cathodic and anodic peak potentials (V) respectively, $E^{0'}$ (≈0.20 V) is the formal potential, α is the electron transfer coefficient (≈0.5), k_s is the standard rate constant (s^{-1}) and n, F, R and T have their usual meanings as defined previously. The linear regressions for the cathodic and anodic processes were $E_{p,c}$=0.0147lnν + 0.1623 (r^2 = 0.9632) and $E_{p,a}$=0.0084lnν + 0.2207 (r^2=0.9986), respectively. From the slope of anodic plot, the number of electrons transferred was estimated to be six (6) and the electron transfer rate estimated from its intercept was 6.1094 s^{-1}. This multi-electron transfer was attributed to complete oxidation of the ZnSe-3MPA quantum dots according to the equation below.

$$ZnSe \rightarrow Zn^{2+} + Se^{4+} + 6e^{-} \qquad (33)$$

A similar electrochemical oxidation of ZnSe nanocrystals was reported at potentials more positive than 700 mV [248]. The low oxidation potentials and rapid multi-electron transfer rate observed in this project may be attributed to orientation of a large number of closely packed nanostructured ZnSe-3MPA quantum dots on the surface of the gold electrode. From Faraday law, current is directly proportional to the amount of the material undergoing an electrochemical reaction. A high amount of quantum dots adsorbed on the surface of the electrode therefore increases the rate of electron transfer, greatly lowering the redox potentials [249-250]. The quantum confinement effects of the ZnSe-3MPA quantum dots also confine electrons within a

very small three dimensional space, bringing them to a very close proximity with the electrode. The cumulative effect of these factors is the high standard rate constant observed.

4.2.3 Electrochemistry of Au|ZnSe-3MPA in $Fe(CN)_6^{4-/3-}$ solution.

The oxidation of ferrocyanide to ferricyanide involves a single electron transfer and quite often serves as a probe reaction in fundamental electrochemistry [251]. This is because; its electrochemical reaction involves a single electron transfer with a characteristic ideal quasi-reversible outer sphere kinetic behaviour. Its cyclic voltammetric quasi-reversible electron transfer profiles have been used for quantitative mathematical analysis [217]. In $[Fe(CN)_6]^{3-/4-}$ solution, a wider redox peak separation (from 137 mV to 349 mV) and lower currents both of which indicates a more sluggish electron transfer rate, can be observed at the Au/ZnSe-3MPA interface when compared to that of bare gold electrode. Since $[Fe(CN)_6]^{3-/4-}$ and the ZnSe-3MPA quantum dots are negatively charged, the charge repulsion caused the reduction in the rate of electron transfer.

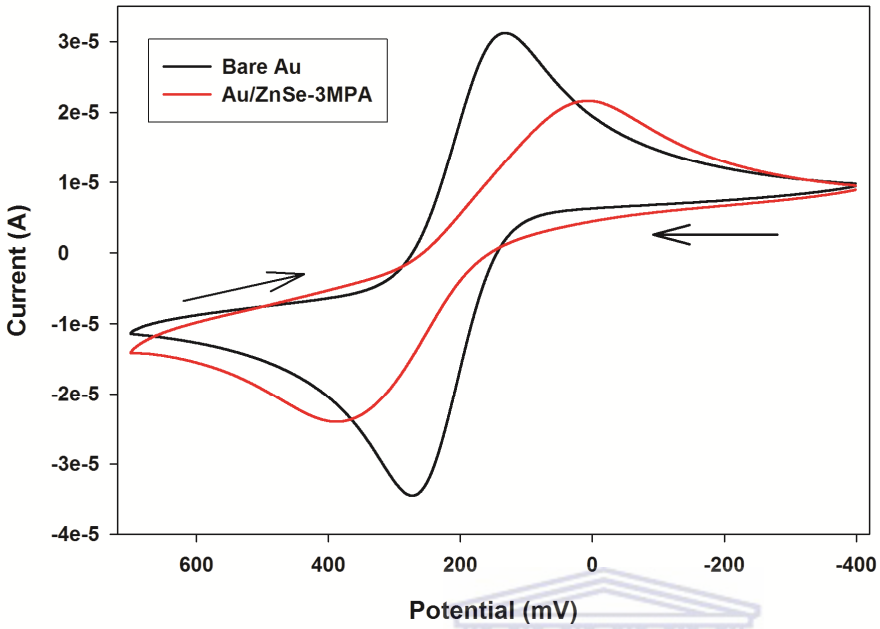

Figure 15: Cyclic voltammograms of bare Au and Au/ZnSe-3MPA electrodes in 5 mM of $Fe(CN)_6^{3-/4-}$ at a scan rate of 100 mV/s.

The modification of the electrode with the ZnSe-3MPA quantum dots changes the capacitance and the interfacial electron transfer resistance of the electrode. These changes were investigated using EIS in a $[Fe(CN)_6]^{3-/4-}$ redox probe. The impedimetric data was fitted using a simple Randle equivalent circuit (see inset in the figure below). The parameters of the equivalent circuit included the solution resistance (R_s), the Warburg impedance (W) resulting from the diffusion of the redox probe and charge transfer resistance (R_{ct}). R_{ct} and CPE represent interfacial properties of the electrode which are highly sensitive to surface modification. The double layer capacitance (C) is substituted with constant phase element (CPE) as previously explained so as to take into account the electrode non-idealities. In the Nyquist diagram the semi circle observed at higher frequency, corresponds to the electron limited process whereas the

linear part is the characteristics of the lower frequency range and represents the diffusion limited electron transfer process. The Nyquist diagram below shows a small semicircle for the bare Au with a R_{ct} of 718.80 Ω. On modifying the electrode with ZnSe-3MPA quantum dots, the Au/ZnSe-3MPA obtained showed a large semicircle with the R_{ct} increasing to 6924 Ω.

.

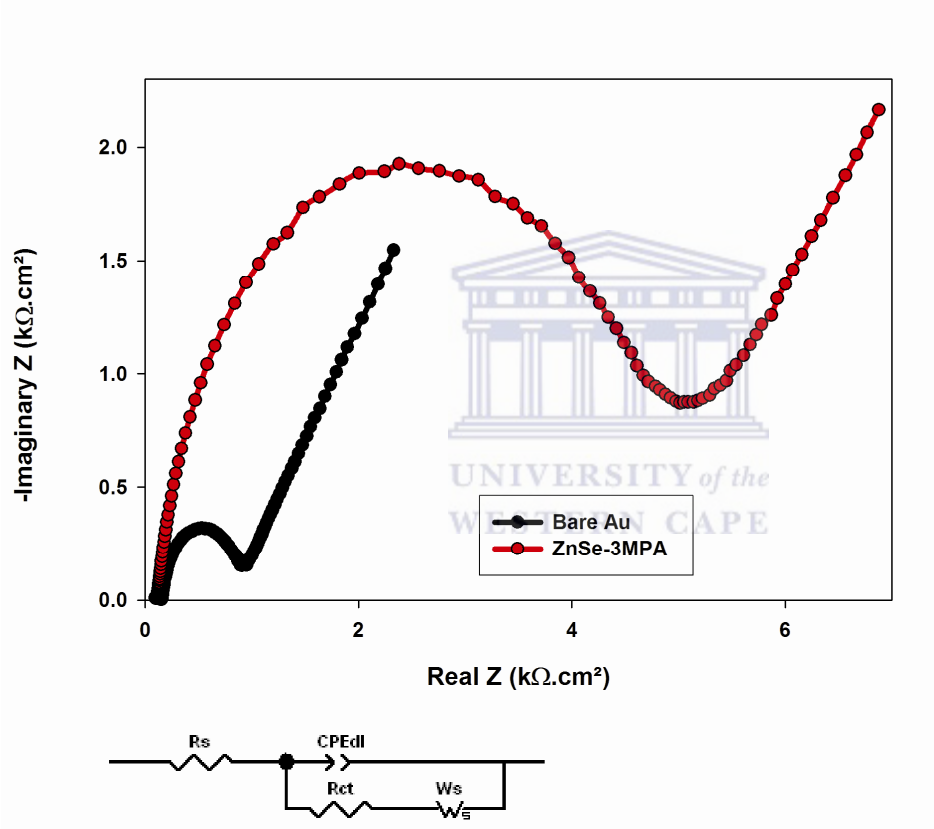

Figure 16: Nyquist plot of bare Au and Au|ZnSe-3MPA in 5.00 mM $Fe(CN)_6^{3-/4-}$, with Randles equivalent circuit.

These results corroborate the observation made under cyclic voltammetry whereby, the negatively charged quantum dots impeded electron transfer from the redox probe to the surface

of the gold electrode. A comparative analysis of the interfacial heterogeneous electron transfer rate of the bare Au and the Au|ZnSe-3MPA electrodes was done using equations 8 and 9 [205], also described previously:

$$R_{ct} = \frac{RT}{nFi_o} \qquad (8)$$

$$i_o = nFAk^0C^* \qquad (9)$$

where n, F, R, T and A are as defined previously while $\mathbf{i_o}$ is the standard exchange current (A), k^0 is the heterogeneous rate transfer constant (cm s^{-1}) and C^* is the concentration of $Fe(CN)_6^{3-/4-}$ (5.00 mM). The values of i_o for the bare Au and Au|ZnSe-3MPA electrodes were 3.5724 x 10^{-5} A and 3.7086 x 10^{-6} A, respectively and the corresponding k^0 values were 3.6841 x 10^{-3} cm s^{-1} and 3.8988 x 10^{-4} cm s^{-1}. The larger value of k^0 for Au electrode supports the theory that the semi-conducting ZnSe-3MPA impeded the charge transfer of the $Fe(CN)_6^{3-/4-}$ redox probe and corroborates the electrostatic repulsion phenomenon observed in EIS.

Time constant (τ) is another important kinetic parameter for interrogation of interfacial charge transfer. This parameter can be calculated from the frequency at maximum imaginary impedance (ω_{max}) of the semicircle in the Nyquist plot according to the following equations:-

$$\varpi_{max} = \frac{1}{Rct \times Cdl} \qquad (2)$$

and

$$\tau = Rct \times Cdl \qquad (3)$$

where C_{dl} is the double layer capacitance and $\omega_{max} = 2\pi f$, f being the exciting frequency (Hz) while R_{ct} is as defined previously (charge transfer resistance). It is evident from these equations that the time constant is directly proportional to the charge transfer resistance but inversely proportional to frequency. Low values of time constants would therefore depict high charge transfer kinetics and vice versa. Taking frequencies from the Nyquist plot for calculations, the time constants for bare and Au|ZnSe-3MPA were found to be 2.1791 x 10^{-4} s rad^{-1} and 2.7344 x 10^{-3} s rad^{-1} respectively. The time constant for the Au|ZnSe-3MPA is one order of magnitude higher than that of the bare electrode, indicating high impedance to charge transfer across the interface.

Besides the surface concentration of the ZnSe-3MPA quantum dots calculated previously, another important attribute of a modified electrode is the percentage coverage or the surface coverage of the electrode by the modifier. This attribute is sometimes expressed as a ratio of the surface of the electrode covered by the modifier to the whole electrode surface. It offers important insights regarding the surface state of the electrode; the charge resistance related to it as well as the expected extent of bio conjugation if the electrode modifier is biocompatible. The surface coverage (θ) of ZnSe-3MPA on gold electrode was calculated from equation 34 [252-253] and found to be 0.91.

$$\theta = 1 - \frac{R_{ct}^{Bare}}{R_{ct}^{Au/ZnSe-3MPA}} \qquad (34)$$

(where R_{ct}^{Bare} and $R_{ct}^{Au/ZnSe-3MPA}$ are the charge transfer resistance of the bare Au and Au/ZnSe-3MPA electrodes respectively). Since the quantum dots attached to the gold electrode are

biocompatible, the 0.91 surface coverage is envisaged to an equal coverage of the electrode by the biomolecule, in this case the DNA.

4.3 Electrochemistry of Ga_2Se_3-3MPA nanocrystals.

4.3.1 Electrochemistry of Ga_2Se_3-3MPA nanocrystals in solution

The results of cyclic voltammetry of Ga_2Se_3-3MPA nanocrystals solution on gold electrode studied in the same potential window as that of ZnSe-3MPA (-200 to +800 mV) are shown in Figure 17. An anodic peak (A_1) whose potential shifts inconsistently with scan rate is observed. This peak was absent in ZnSe-3MPA. A significant structural difference between Ga_2Se_3-3MPA and ZnSe-3MPA is that, whereas ZnSe-3MPA exhibits valence match between zinc and selenium (zinc and selenium are both divalent), Ga_2Se_3-3MPA exhibits predominant valence mismatch due to the trivalent nature of the gallium. As a result of this, a third of the gallium atoms in the Ga_2Se_3-3MPA contains structural vacancies [254]. This gives rise to gallium and selenium related defects in the Ga_2Se_3-3MPA lattice. The peak A_1 may therefore be due to oxidation of surface defects of Se forming intra band surface states [248].

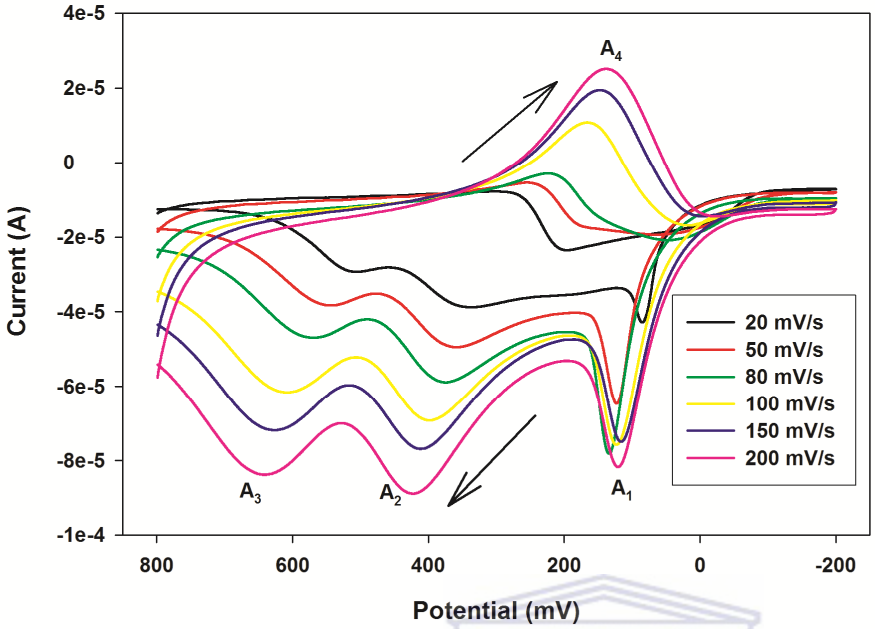

Figure 17: Cyclic voltammograms of Ga_2Se_3-3MPA solution.

The anodic peaks A_2 and A_3 shifted to more positive potentials with increasing scan rate, suggesting an irreversible behaviour of the processes responsible for these peaks. Peak A_2 results from anodic stripping of elemental Se, arising from electro oxidation of Se-related surface states [255]. The electrochemical band gap calculated using peak A_3 and A_4 was 0.53 eV, similar to that obtained for ZnSe-3MPA.

4.3.2 Electrochemistry of Au| Ga_2Se_3-3MPA in phosphate buffer solution.

The electrochemical behaviour of Ga_2Se_3-3MPA immobilized on a gold electrode was investigated in phosphate buffer solution of pH 7.40 as well as in 5.00 mM $Fe(CN)_6^{3-/4-}$ using cyclic voltammetry and electrochemical impedance spectroscopy. Figure 18 shows the cyclic

voltamogramms of the Au|Ga_2Se_3-3MPA in 0.10 M PBS of pH 7.40. Near symmetrical cathodic and anodic curves whose peak separation range from 20 mV (for 20 mV/s scan rate) to 63 mV (for 450 mV/s scan rate) can clearly be seen. The near symmetry shape of the voltamogramms is an indicator of surface confined electrochemical reactions of the adsorbed Ga_2Se_3-3MPA. Usually, surface confined electrochemical reactions exhibit a peak separation of zero [256]. The deviation from this phenomenon maybe attributed to densely packed electro inactive organic chains of the 3MPA along which electrons diffuse from the quantum dot to the electrode surface. To further verify surface electrochemistry of the Ga_2Se_3-3MPA, the logarithmic linear relationship between the peak currents and scan rates was investigated. The value of the slope of the linear plot of log *v* versus log i_p can be used to elucidate the nature of the processes influencing the electrochemistry of the surface confined material. Slopes with values of 1.0 and 0.5 refer to adsorption-controlled and diffusion-controlled electrochemical processes, respectively. Intermediate values for the slope indicate mixed diffusion/adsorption-controlled processes [257]. In this work, the plots of log *v* versus log i_p (not shown) gave slopes of 1.04 and 1.14 for the anodic and cathodic peaks, respectively which confirmed the occurrence of adsorption-controlled electrochemistry of the Ga_2Se_3-3MPA system.

The ΔE_p values were also found to be linear with the square root of scan rate (r^2 = 0.99), indicating a quasi-reversible electrochemistry of the Ga_2Se_3-3MPA in the buffer solution [218].

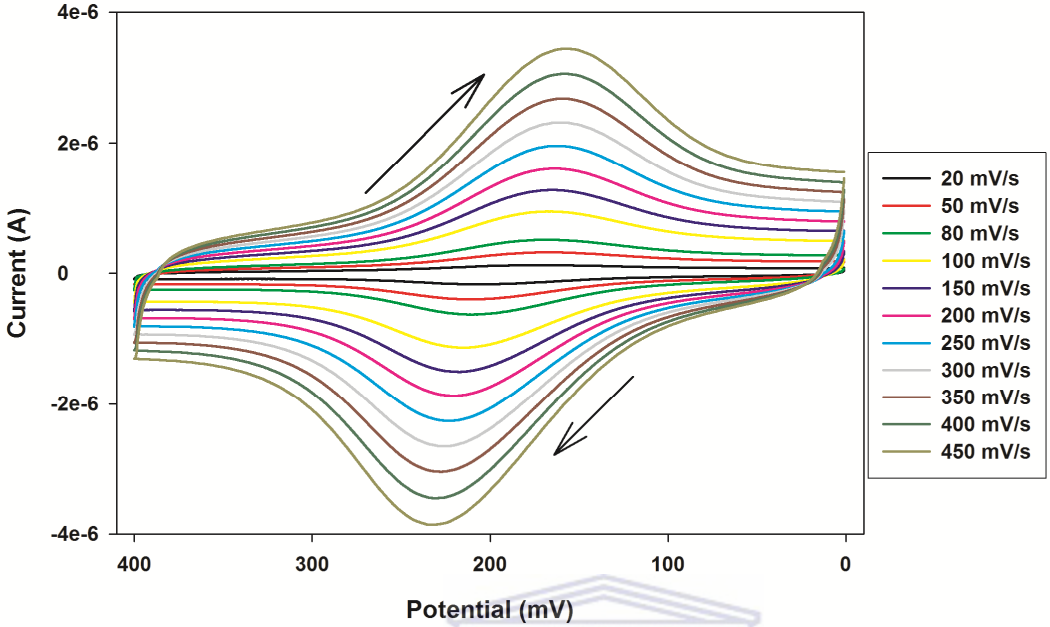

Figure 18: Cyclic voltammograms of Au|Ga_2Se_3-3MPA in 0.10 M phosphate buffer of pH 7.40.

The average value for the ratio of cyclic voltammetric anodic to cathodic peak currents of Au|Ga_2Se_3-3MPA in buffer was 1.29, which indicates a one-electron quasi-reversible electrochemistry [258]. To further confirm this (number of electrons transferred), equations 31a, 31b and 31c were applied as used for ZnSe-3MPA.

From the slopes of the i_p versus *v* plots, n was calculated to be 0.98 and 1.14 for the anodic and cathodic processes, respectively, indicating that Ga_2Se_3-3MPA nanocrystals undergo a one-electron redox reaction at the Au electrode in phosphate buffer. The surface concentration of Ga_2Se_3-3MPA, calculated from equation 31b, was 6.1426 x 10^{-10} mol cm^{-2}. The formal potential (defined previously) was unaffected by the scan rate (SD = 1.21 x10^{-3} for 11 scan

rates), indicating that the electron transfer coefficients, α_a and α_c for anodic and cathodic processes, respectively, are similar ($\alpha_a \approx \alpha_c \approx 0.5$).

4.3.3 Electrochemistry of Ga_2Se_3-3MPA in $Fe(CN)_6^{4-/3-}$ solution.

Cyclic voltammetry of the Au|Ga_2Se_3-3MPA electrode in $Fe(CN)_6^{3-/4-}$ (Fig. 19) showed a wider redox peak separation (ΔE_p) than for Au (from 137 mV for Au to 324 mV for Au|Ga_2Se_3-3MPA) and a 49 % decrease in peak currents. The cyclic voltammetric behaviour of the modified electrode indicates a more sluggish electron transfer rate at the Ga_2Se_3-3MPA|$Fe(CN)_6^{3-/4}$ interface compared to Au|$Fe(CN)_6^{3-/4}$.

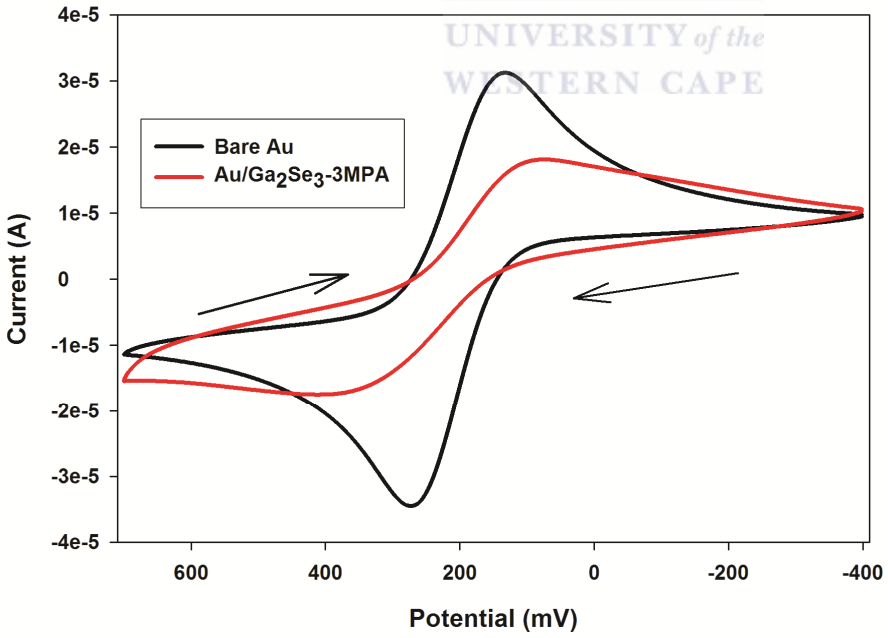

Figure 19: Cyclic voltammograms of bare Au and Au|Ga_2Se_3-3MPA in 5.00 mM $Fe(CN)_6^{3-/4-}$ at 100 mV/s.

Since $[Fe(CN)_6]^{3-/4-}$ and the Ga_2Se_3-3MPA quantum dots are negatively charged, the charge repulsion caused the reduction in the rate of electron transfer.

Electrochemical impedance spectroscopy is a well known technique for interrogating interfacial electrical properties of surface modified electrodes. Figure 20 below depicts the Nyquist plots for bare Au and Au|Ga_2Se_3-3MPA in 5.00 mM $Fe(CN)_6^{3-/4-}$. The figure also shows the corresponding Randle's equivalent circuit consisting of a solution resistance (R_s), charge transfer resistance (R_{ct}), Warburg impedance (Z_w) and constant phase element (CPE_{dl}). R_{ct} represents the resistance to the charge transfer between the electrolyte and the electrode and contains information on the electron transfer kinetics of the redox probe at the electrode interface. The R_{ct} values of bare Au and Au|Ga_2Se_3-3MPA electrodes were 718 ± 1.74 Ω and 3338 ± 0.66 Ω, respectively. This represents a four-fold increase in R_{ct} value when Au electrode was modified with Ga_2Se_3-3MPA nanocrystals. The increase in R_{ct} value could be due to the electrostatic repulsion between the Ga_2Se_3-3MPA and $Fe(CN)_6^{3-/4-}$ redox probe which are both negatively charged. The surface coverage (θ) of Ga_2Se_3-3MPA on gold electrode was calculated from equation 35 [252, 259] and found to be 0.78.

$$\theta = 1 - \frac{R_{ct}^{Bare}}{R_{ct}^{Au/ZnSe-3MPA}} \qquad (35)$$

where R_{ct}^{Bare} and $R_{ct}^{Au/ZnSe-3MPA}$ are the charge transfer resistance of the bare Au and Au|Ga_2Se_3-3MPA electrodes, respectively.

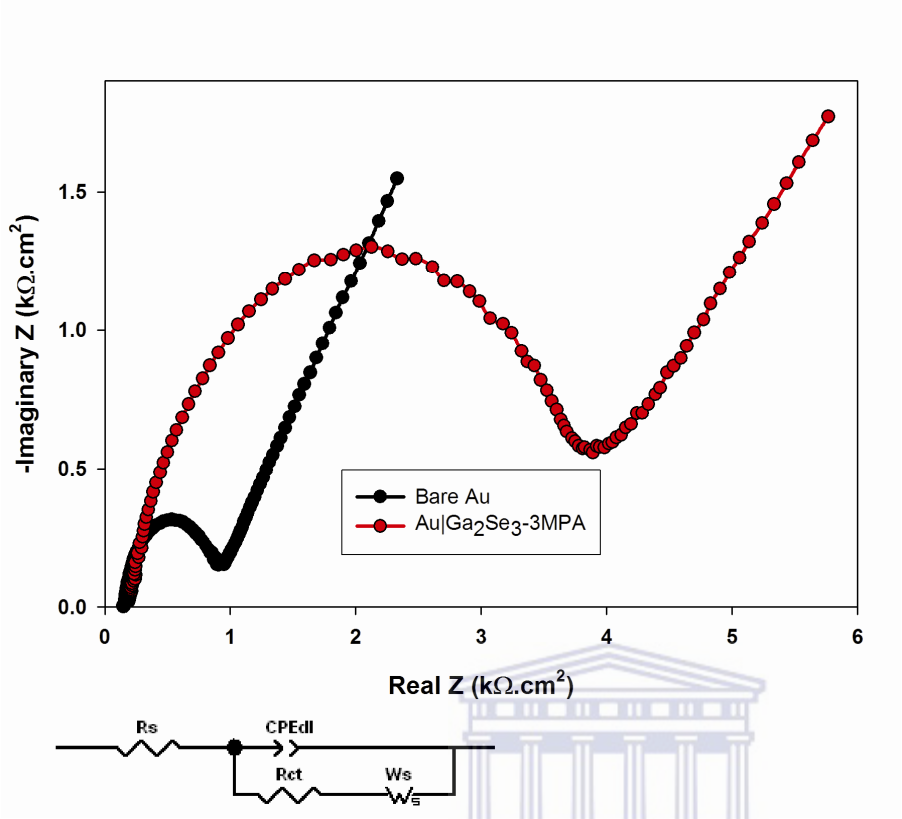

Figure 20: Nyquist plot of bare Au and Au|Ga_2Se_3-3MPA in 5.00 mM $Fe(CN)_6^{3-/4-,}$ with Randles equivalent circuit.

A comparative analysis of the interfacial heterogeneous electron transfer rate of the bare Au and the Au|Ga_2Se_3-3MPA electrodes was done using equations 8 and 9 as done for Au|ZnSe-3MPA. The value of i_o for Au|Ga_2Se_3-3MPA electrode was and 7.6934 x 10^{-6} A, and the corresponding k^0 value was 7.9321 x 10^{-4} cm s^{-1}. Since the same bare electrode was used, the i_0 and k^0 values for the bare Au were taken as 3.5724 x 10^{-5} A and 3.6841 x 10^{-3} cm s^{-1} (calculated previously). Again, the k^0 value for the bare Au electrode was larger than that of the Au| Ga_2Se_3-3MPA electrode, an indication that semi-conducting Ga_2Se_3-3MPA impeded the charge transfer of the

$Fe(CN)_6^{3-/4-}$ redox probe and corroborates the electrostatic repulsion phenomenon observed in EIS.

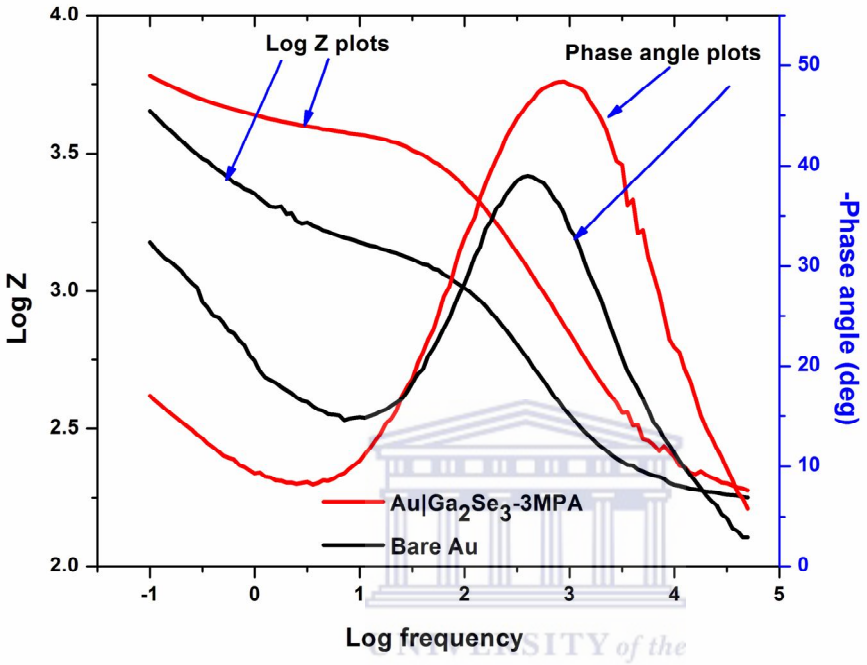

Figure 21: Bode plots of bare Au and Au|Ga_2Se_3-3MPA in 5.00 mM $Fe(CN)_6^{3-/4-,}$ with Randles equivalent circuit.

The Bode plot gives direct information on the frequency and phase angle. In the figure above (Fig 21), the Bode plots also show remarkable differences in the electrochemistry of the bare Au-$Fe(CN)_6^{3-/4-}$ and Au|Ga_2Se_3-3MPA -$Fe(CN)_6^{3-/4-}$ interfaces. The absolute phase angle increases from 39° (for bare Au) to 50° (Au|Ga_2Se_3-3MPA). This indicates decrease in conductivity at the Au|Ga_2Se_3-3MPA-$Fe(CN)_6^{3-/4-}$ interface.

4.4 Electrochemistry of $Zn_2Ga_2Se_5$-3MPA quantum dots.

4.4.1 Electrochemistry of $Zn_2Ga_2Se_5$-3MPA quantum dot solution

The electrochemistry of $Zn_2Ga_2Se_5$-3MPA quantum dots was studied within the same potential window as that of Ga_2Se_3-MPA and ZnSe-3MPA in solution and the results are shown in the figure below. A significant difference between the cyclic voltammograms of Ga_2Se_3-MPA and $Zn_2Ga_2Se_5$-3MPA is that, the inconsistent anodic peak A_1 and the cathodic peak A_4 (in Ga_2Se_3-MPA) are largely absent in $Zn_2Ga_2Se_5$-3MPA quantum dots. Peak C_2 is observed to occur at a potential similar to that of B_2 in ZnSe-3MPA quantum dots (Fig. 13). However, whereas peak B_2 shifted consistently towards more positive potentials with increasing scan rate, peak C_2 shows an inconsistent shift with increasing scan rate. Since the inconsistence of peak C_2 is similar to that of peak A_1 in Ga_2Se_3-3MPA, it can be ascribed to oxidation of surface defects of Se forming intra band surface states [248].

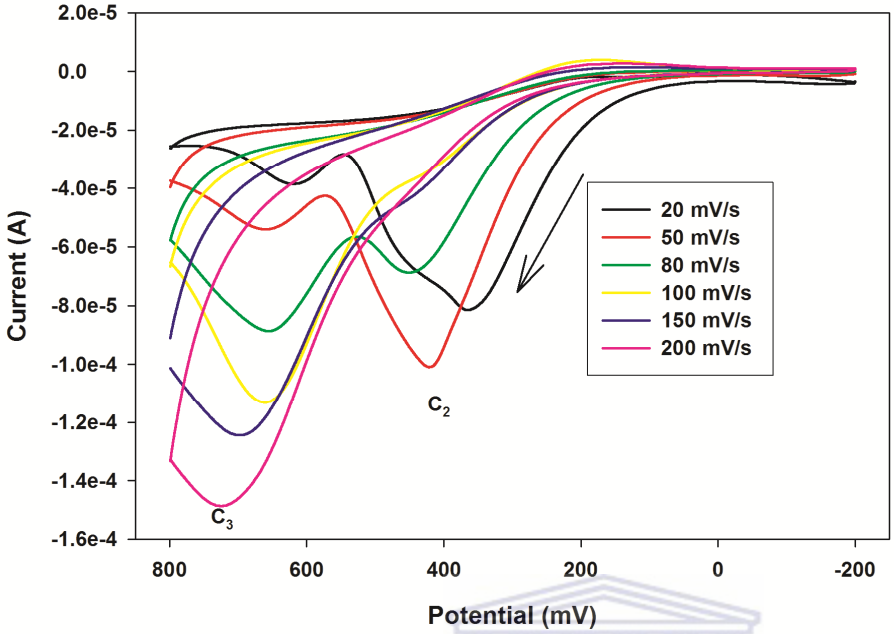

Figure 22: Cyclic voltammograms of $Zn_2Ga_2Se_5$-3MPA solution.

It has already been mentioned that Ga_2Se_3-MPA exhibits a predominant valence mismatch. In $Zn_2Ga_2Se_5$-3MPA quantum dots, the valence mismatch is expected to be more pronounced than it is in Ga_2Se_3-MPA due to existence of trivalent gallium and divalent zinc cations against only divalent selenium anions. The zinc and gallium related vacancies in $Zn_2Ga_2Se_5$-3MPA are, for this reason expected to be more dominant than in Ga_2Se_3-MPA. This could possibly be the reason for the shift in the peak potential for oxidation of surface defects of Se from around 100 mV (in Ga_2Se_3-MPA) to around 400 mV (for $Zn_2Ga_2Se_5$-3MPA). Peak C_3 is occurring at similar potential to that of A_3 (in Ga_2Se_3-MPA, Fig. 17) and peak B_3 (in ZnSe-3MPA, Fig 13). This may as well be ascribed to anodic dissolution of selenium as mentioned for ZnSe-3MPA. The existence of zinc and gallium related vacancies in $Zn_2Ga_2Se_5$-3MPA could possibly form a

self compensated system whereby electronic transitions take place between localized donor and acceptor species. Instead of electrodeposition of selenium on the surface of the gold electrode as observed in peak B_4 (ZnSe-3MPA), it is possible that electronic transitions occurred between the selenium and the gallium or zinc vacancies, without necessarily engaging the electrode in the reaction. This could probably explain the absence of the reductive peak in the $Zn_2Ga_2Se_5$-3MPA quantum dot system. Since the $Zn_2Ga_2Se_5$-3MPA didn't show a cathodic peak, it was impossible to determine its electrochemical band gap.

4.4.2 Electrochemistry of Au|$Zn_2Ga_2Se_5$-3MPA in phosphate buffer solution

Like for ZnSe-3MPA and Ga_2Se_3-3MPA, the electrochemical behaviour of $Zn_2Ga_2Se_5$-3MPA immobilized on a gold electrode was investigated in phosphate buffer solution of pH 7.40. The cyclic voltammograms in figure 23 show an almost symmetrical system with nearly equal charges for reduction and oxidation processes. A plot of peak current versus scan rate for both cathodic and anodic processes yielded straight lines with slopes 3.7762×10^{-5} (cathodic,R^2= 0.99) and -7.3892×10^{-5} (anodic, R^2 = 0.99). These results are in agreement with surface confined electrochemistry. To further confirm this, plots of log peak current versus log scan rate gave slopes of 0.99 for cathodic and 0.90 for anodic process. These values are close to 1 as expected for a species undergoing surface confined electrochemistry [257].

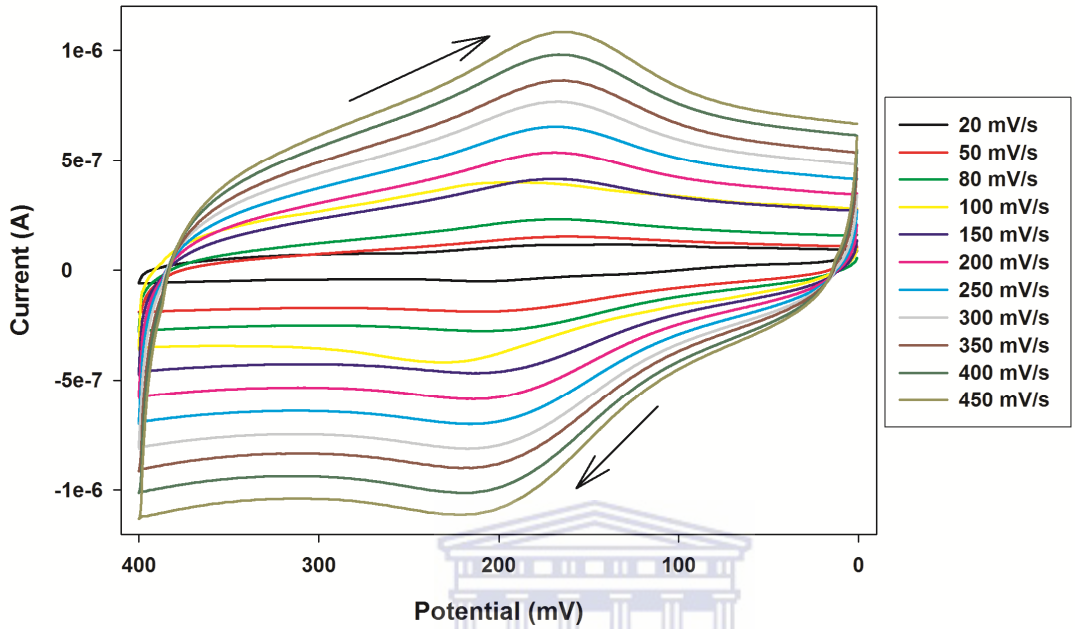

Figure 23: Cyclic voltammograms of Au|$Zn_2Ga_2Se_5$-3MPA in 0.10 M phosphate buffer of pH 7.40.

From the slopes of the plots of peak current versus scan rate, and the amount of charge (Q), calculated from integration of anodic and cathodic voltammograms, equation 31c (Refer to section **4.2.2)** was used to calculate the number of electrons transferred. The number of electrons calculated was 2.9571 for anodic and 2.8163 for cathodic, implying that the surface confined electrochemistry of $Zn_2Ga_2Se_5$-3MPA was a three electron transfer process. The immobilization of the $Zn_2Ga_2Se_5$-3MPA quantum dots is envisaged to have brought them into close proximity with the gold electrode. The three electron transfer process can therefore be attributed to electronic transitions involving the gallium related vacancies according to the equation 36 below

$$Ga^{3+}_{(aq)} + 3e^{-} \leftrightarrow Ga_{(s)} \qquad (36)$$

The surface concentration of the immobilized $Zn_2Ga_2Se_5$-3MPA quantum dots was calculated from equation 31c (refer to section **4.1.1.2)** and was found to be 1.3778 x 10^{-10} mol cm^{-2}.

4.5 Comparative electrochemistry of ZnSe-3MPA, Ga_2Se_3-3MPA and $Zn_2Ga_2Se_5$-3MPA quantum dot solution

In order to compare the electrochemical behaviour of the binary and ternary selenides, multigraph plots of the three were made in both solution and buffer solution. Besides the different number of peaks observed for each material, figure 24 shows that the current generated by the binary ZnSe-3MPA and Ga_2Se_3-3MPA was similar while that generated by the ternary $Zn_2Ga_2Se_5$-3MPA was much higher. This depicts that the $Zn_2Ga_2Se_5$-3MPA quantum dots in solution are more conductive than the ZnSe-3MPA and Ga_2Se_3-3MPA. This is attributed to gallium-induced structural vacancies in the $Zn_2Ga_2Se_5$-3MPA crystal lattice.

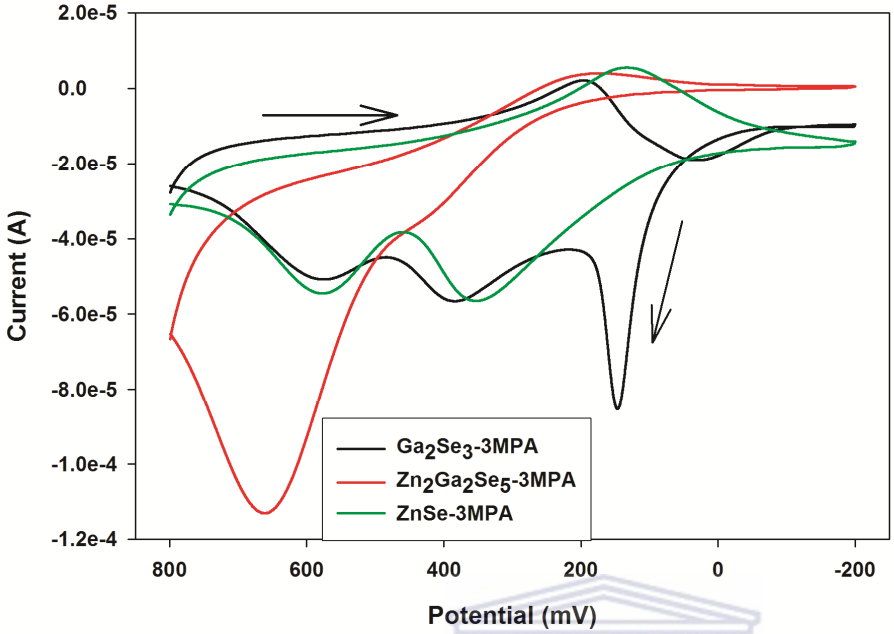

Figure 24: Multigraph of the cyclic voltammograms of $Zn_2Ga_2Se_5$-3MPA, ZnSe-3MPA and Ga_2Se_3-3MPA, all in solution at 100 mV/s.

A common property of all the $Zn_2Ga_2Se_5$-3MPA, ZnSe-3MPA and Ga_2Se_3-3MPA semiconducting materials investigated here is that they are all soluble. Although the specific concentrations of each of the synthesized materials were not determined, it is envisaged that the ternary $Zn_2Ga_2Se_5$-3MPA quantum dots contain a higher amount of ions per unit volume compared to the other two. This means that the rate of ionic diffusion is to the electrode is higher in $Zn_2Ga_2Se_5$-3MPA that in both ZnSe-3MPA and Ga_2Se_3-3MPA. It is also known that the amount of current generated in an electrochemical process is directly proportional to the amount of material undergoing reaction. A high accumulation of $Zn_2Ga_2Se_5$-3MPA quantum dots on the surface of gold electrode per unit time therefore increases the rate of reaction and hence high currents are generated.

When immobilized however, the figure below shows a reversed trend, i.e, least current is obtained with $Zn_2Ga_2Se_5$-3MPA quantum dots. In immobilized systems, diffusion plays a limited role in influencing the rate of reaction at the electrode. Instead, the rate of reaction and hence the amount of current is influenced largely influenced by the surface concentration of the adsorbed electroactive species.

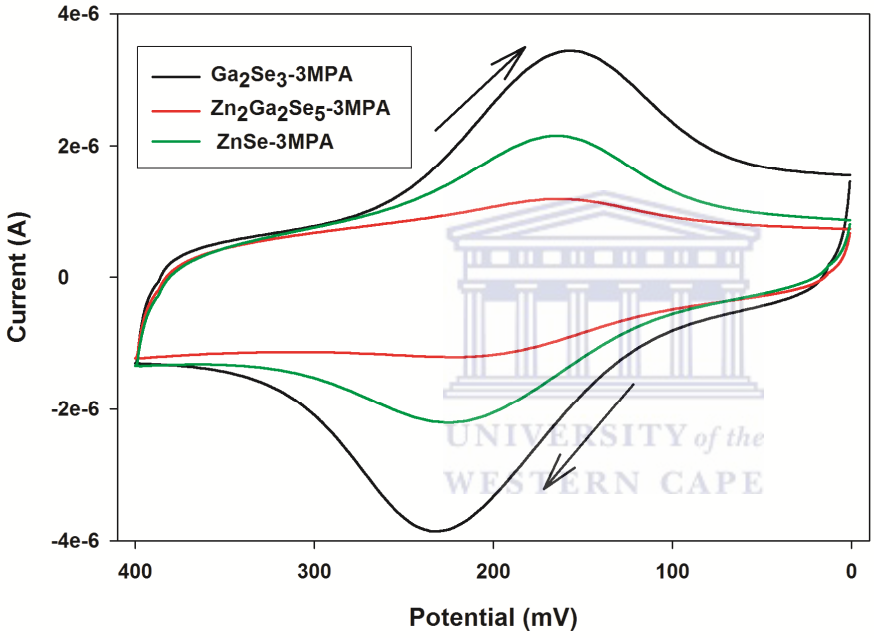

Figure 25: Multigraph of the cyclic voltammograms of gold electrode-immobilized $Zn_2Ga_2Se_5$-3MPA, ZnSe-3MPA and Ga_2Se_3-3MPA, all in 0.10 PBS, pH 7.40 at 500 mV/s.

The surface concentrations of $Zn_2Ga_2Se_5$-3MPA, ZnSe-3MPA and Ga_2Se_3-3MPA, already reported earlier were 1.3778 x 10^{-10} mol cm^{-2}, 2.5215 x 10^{-10} mol cm^{-2} and 6.1426 x 10^{-10} mol cm^{-2} respectively. Although these values lie within the same order of magnitude, Ga_2Se_3-3MPA which has a distinctively higher surface values also shows distinctively high current amplitude.

Likewise, $Zn_2Ga_2Se_5$-3MPA and ZnSe-3MPA whose surface concentration values are relatively close also exhibit relatively close current amplitudes. It is therefore reasonable to suggest that the amount of current generated by the adsorbed $Zn_2Ga_2Se_5$-3MPA, ZnSe-3MPA and Ga_2Se_3-3MPA is correlated with their relative surface concentrations.

4.6 Spectroscopy of the selenide quantum dots

4.6. 1 Ultraviolet –visible spectroscopy (UV-vis)

Usually, the nature of the interaction between the conduction and valence bands as well as the size of the band gap determines the optical properties of semiconducting nanocrystals. The absorption of a photon by a semiconductor causes electronic transition from the valence band to the conduction band, which creates an electron-hole pair known as an exciton in the valence band. The lowest-energy electron-hole pair (excitonic) state ($1S_{3/2}$-$1S_e$) is not usually observable in nanocrystals that are heterogeneous in size, shape and composition. However, more homogeneous nanocrystals exhibit characteristic sharp absorption peaks. The UV-vis absorption spectra of the ZnSe-3MPA (Fig. 26, black) shows a sharp absorption maxima at 350 nm, which is a blue shift from the featureless absorption edge of bulk ZnSe at 460 nm [260]. Such sharp absorption spectra with clear excitonic feature indicate narrow size distribution of the dots.

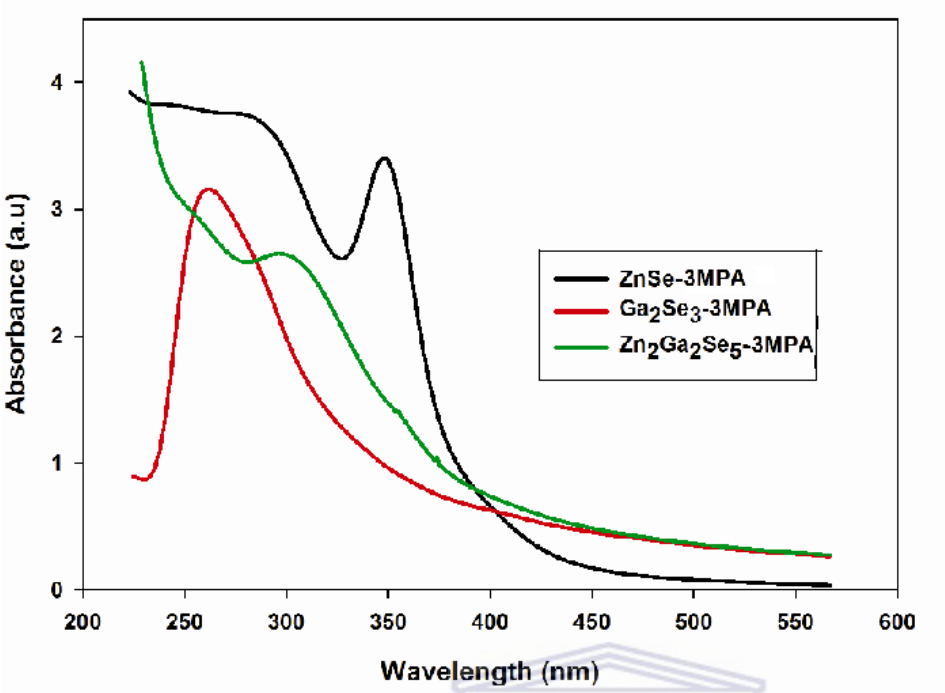

Figure 26: UV-vis spectra of ZnSe-3MPA, Ga_2Se_3-3MPA and $Zn_2Ga_2Se_5$-3MPA.

From the UV-vis absorption maxima (350 nm, equivalent to 3.54 eV), particle size can be calculated using the effective mass approximation model according to equation (37) [260]

$$Eg = \frac{h^2}{8a^2}\left(\frac{1}{m_e} + \frac{1}{m_h}\right) \qquad (37)$$

Where E_g is the band gap (eV), a is the particle size, h is the Planks constant, m_e is the electron mass = $0.17m_o$, m_h is the hole mass = $1.44m_o$ (m_o = 9.1095 x 10^{-31} kg, is the mass of a stationary electron). The size of ZnSe-3MPA calculated from this model was found to be 3.40 nm.

The $Zn_2Ga_2Se_5$-3MPA shows an absorption band at around 325 nm, which is mid way between the absorption bands of ZnSe-3MPA and Ga_2Se_3-3MPA. An in depth analysis of the $Zn_2Ga_2Se_5$-3MPA (HRTEM and fluorescence discussed later) showed that its properties were

more or less similar to those of ZnSe-3MPA than to those of Ga_2Se_3-3MPA. It should be remembered that during synthesis of $Zn_2Ga_2Se_5$-3MPA, the selenium ions were introduced to a nitrogen saturated mixture of gallium and zinc ions. Since zinc and selenium exhibit a valence match, a zinc-selenium reaction was probably more favourable than a gallium-selenium reaction. Moreover, zinc is more metallic than gallium and its reaction with selenium is expected to be more favourable that with gallium. Based on this explanation, the absorption band of $Zn_2Ga_2Se_5$-3MPA could be attributed to a blue shifted absorption edge of gallium doped ZnSe-3MPA (if gallium is considered a dopant or an impurity). These observations are consistent with previous explanation [261] that doping or introduction of transition metal impurities into quantum dots changes their band gap values. Generally, the wavelength of the exciton absorption band decreases with decreasing particle size as a result of quantum confinement of the photogenerated electron hole pairs [262]. The blue shift is therefore an indication that the size of $Zn_2Ga_2Se_5$-3MPA particles is smaller than that of ZnSe-3MPA. Since the band gap of bulk $Zn_2Ga_2Se_5$-3MPA is not established, it is impossible to use the effective mass model to estimate their size. The claim that the size of $Zn_2Ga_2Se_5$-3MPA particles is smaller than that of ZnSe-3MPA will be verified by HRTEM.

The UV-vis absorption spectrum of the Ga_2Se_3-3MPA (Fig. 26, red) shows a sharp absorption maxima at 260 nm, which is due to the presence of a zinc-blend-type defect in Ga_2Se_3-3MPA [263]. The excitonic feature of UV-vis maximum at 260 nm (Fig. 26, red) shows that Ga_2Se_3-3MPA nanocrystals are homogeneous in particle size distribution. It is also evident that the optical band gaps of ZnSe-3MPA (3.54 eV) and Ga_2Se_3-3MPA (4.63 eV) are significantly different from their electrochemical band gap calculated earlier (0.53 eV). This

difference may be attributed to the interface barrier between the quantum dot film and the electrode.

4.6.2 Fluorescence spectroscopy

The figure below shows the 2 dimensional fluorescence (emission and excitation) spectra of ZnSe-3MPA. In the excitation spectrum, an emission wavelength of 449 nm gave a sharp band in the region 380 – 400 nm, peaking at 390 nm. This was assigned to higher excited state transitions (S_1) of the quantum dots. When excited at 390 nm, two emission bands from 425 – 435 nm with maxima at 430 nm and from 440 – 465 nm with sharp maxima at 449 nm were observed. The main sharp emission at 449 nm is the exciton emission (band edge emission) resulting from direct electron-hole recombination transitions in the quantum dots.

.

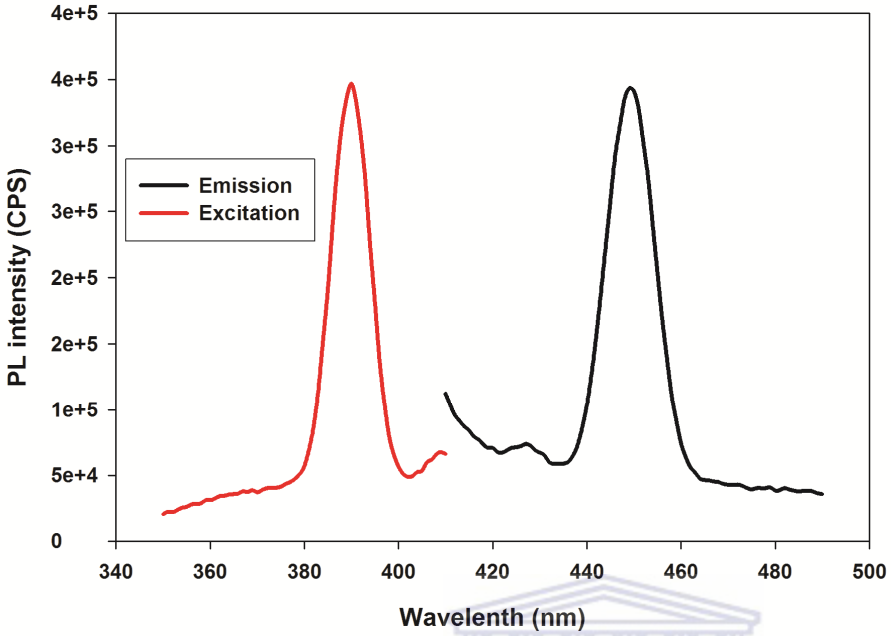

Figure 27: Fluorescence spectra of ZnSe-3MPA quantum dots.

Other possible sources of emissions in quantum dots are impurities, vacancies within the lattice, surface trap and interstitial states among others [264]. Surface trap emissions usually occur at wavelengths higher than the band edge emission wavelength [238]. Since Zn and Se in ZnSe-3MPA quantum dots are both divalent and exhibit valence match, Zn-related vacancies are less likely to cause the emission at 430 nm. The low intensity emission at 430 nm may therefore be attributed to self activated emissions of the quantum dots. The line width of the band edge emission (full width at half maximum) is about 10 nm, which indicates that the ZnSe-3MPA quantum dots have a very narrow size distribution [265]. The emission and excitation spectra are mirror images of each other, an aspect that further confirms S_0 to S_1 band edge-electronic transitions of the quantum dots.

The corresponding 3 dimensional excitation/emission matrix, both contour and topographic plots of the ZnSe-3MPA quantum dots are shown in figures 28 and 29 below. Analysis of the spectrum was done within an excitation from 350 to 400 nm and emission from 430 to 500 nm, all at 1 nm increments. $1S_{3/2}$-$1S_e$ excitonic spectral features of ZnSe-3MPA were observed in two regions. In one region is a high intensity peak at $\lambda_{exc}/\lambda_{emi}$ = 390 nm/450 nm, with a stokes shift of 60 nm. This is similar to $\lambda_{exc}/\lambda_{emi}$ = 390 nm/449 nm peaks observed in 2 d fluorescence and is attributed to band edge emissions.

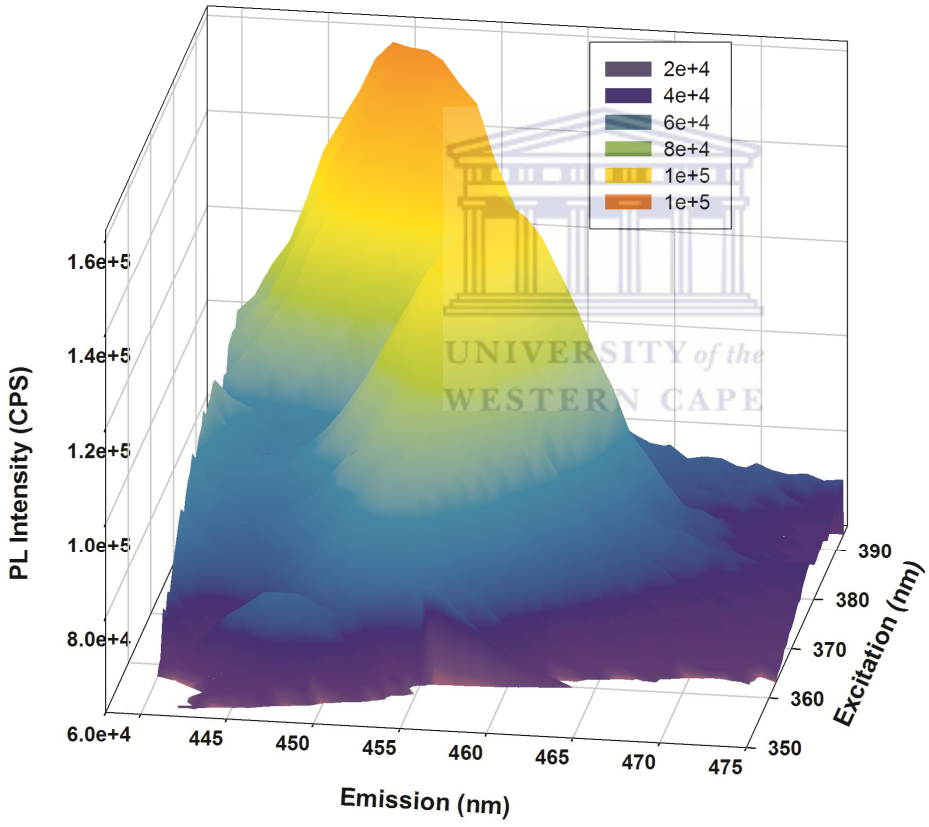

Figure 28: Topographic EEM plots of ZnSe-3MPA in aqueous solution.

The low intensity peak at $\lambda_{exc}/\lambda_{emi}$ 384 nm/455 nm is attributed to surface state emission. The stokes shift at this region is long (101 nm) probably due to the extension of exciton wave-function to the outer 3-MPA.

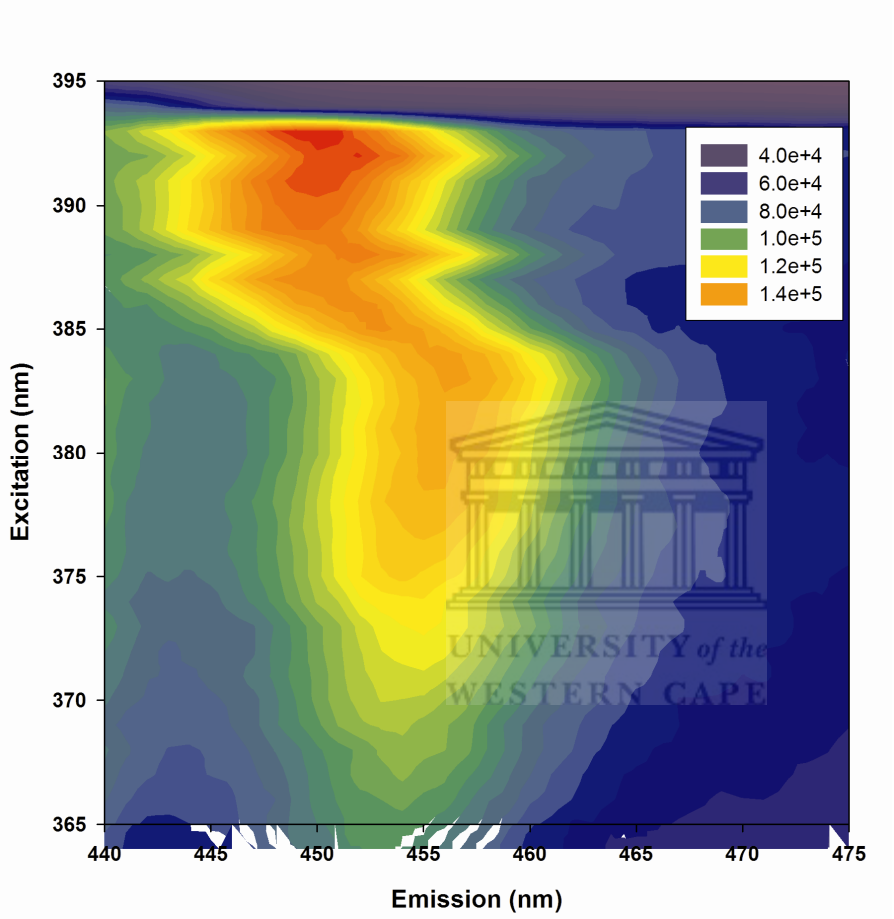

Figure 29: Contour EEM plots of ZnSe-3MPA in aqueous solution.

An analysis of the contour EEM spectra shows that the maximum emission in the two regions is not affected by the excitation wavelength.

As already mentioned before, the trivalent nature of cationic gallium in the Ga_2Se_3-3MPA creates a valence mismatch between the gallium and selenium, and hence structural

vacancies. These vacancies or trap states influence electron-hole recombinations when the excited Ga_2Se_3-3MPA radiatively returns back to its ground state. In the topographic EEM spectra of Ga_2Se_3-3MPA shown in the figure below, the electronic transition from an excited state to the lowest-energy electron-hole pair (excitonic) state ($1S_{3/2}$-$1S_e$) of Ga_2Se_3-3MPA was observed in only one region at $\lambda_{exc}/\lambda_{emi}$ = 397 nm/403 nm. These strong peaks characterize band edge emissions resulting from direct and radiative electron-hole transitions of the Ga_2Se_3-3MPA from excited state (S_1) to the ground state (S_0).

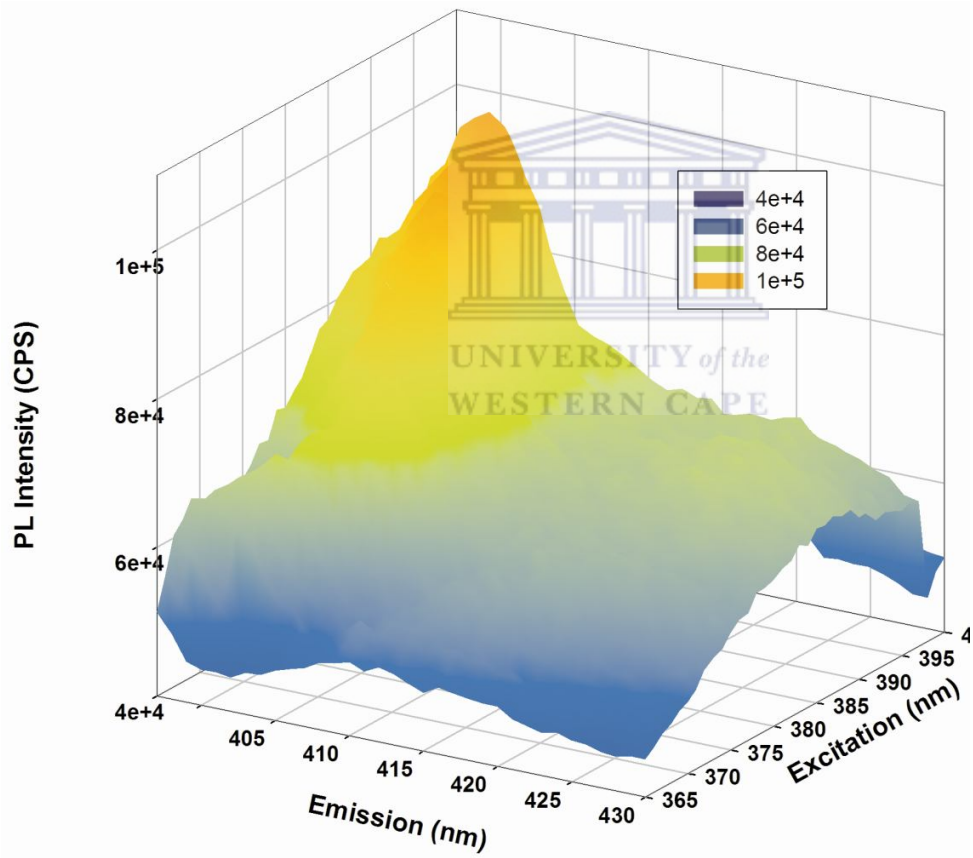

Figure 30: Topographic EEM plots of Ga_2Se_3-3MPA in aqueous solution.

It has been mentioned earlier that presence of vacant lattice sites (trap states), impurities, lattice defects, and/or irregularities a semiconductor delay emission, sometimes leading to phosphorescence rather than fluorescence. In quantum dots however, the quantum confinement effects reduce the donor - acceptor proximity, allowing a fast hole-electron recombination transition. In the case of the synthesized Ga_2Se_3-3MPA, an extremely narrow stokes shift of 6 nm was realized. This suggests that the Ga_2Se_3-3MPA exhibited self-compensated transitions whereby electrons made radiative transitions from a continuous gallium trap distribution to localized selenium acceptors.

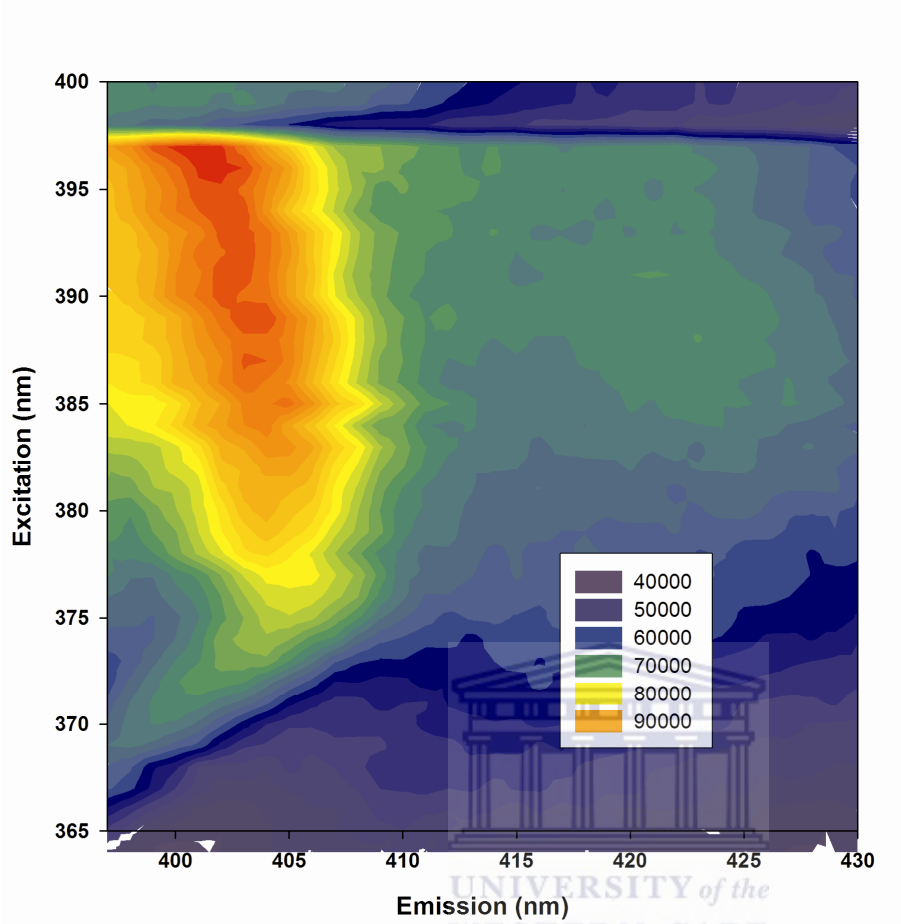

Figure 31: Contour EEM plots of Ga_2Se_3-3MPA in aqueous solution.

The valence mismatch $Zn_2Ga_2Se_5$-3MPA quantum dots is more pronounced than it is in Ga_2Se_3-3MPA quantum dots. $Zn_2Ga_2Se_5$-3MPA quantum dots are therefore expected to contain a large distribution of Zn and Ga -related vacancies. The topographic and contour EEM fluorescence spectra of $Zn_2Ga_2Se_5$-3MPA are shown in figures 32 and 33 below. Two fluorescence regions are observed at $\lambda_{exc}/\lambda_{emi}$ = 399 nm/397 nm and $\lambda_{exc}/\lambda_{emi}$ = 399 nm/420 nm. The first emission peak at 397 nm is quite unusual in the sense that it occurs at wavelength lower that the excitation wavelength (399 nm). Usually, emission wavelengths below the excitation

wavelength do not exhibit any fluorescence because the emitted energy is always lower than the excitation energy.

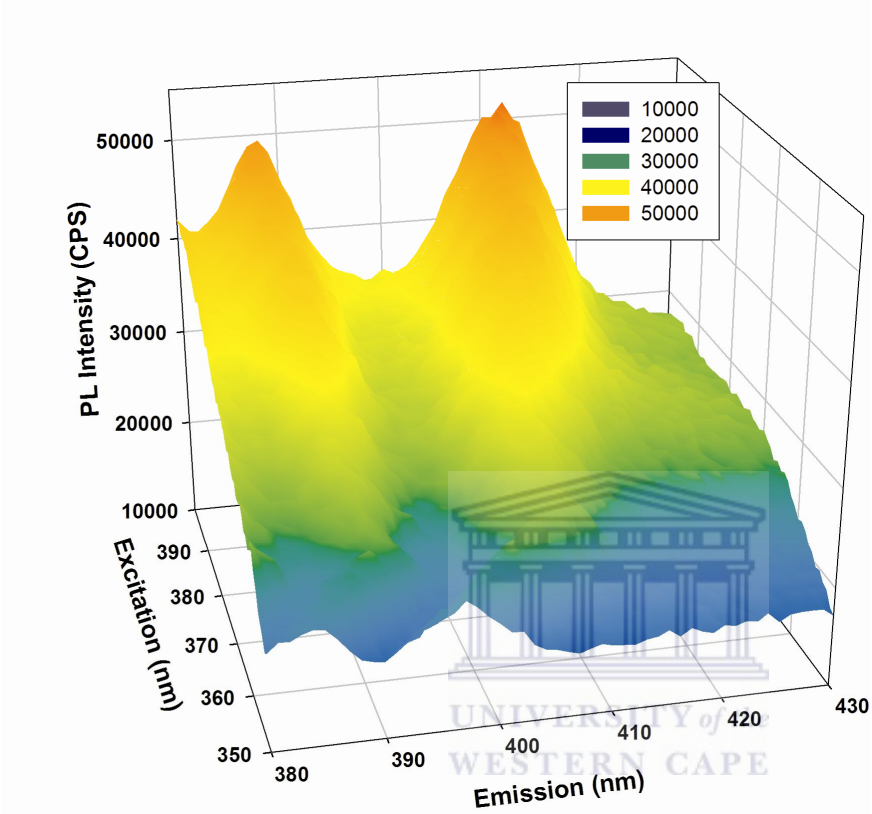

Figure 32: Topographic EEM plots of $Zn_2Ga_2Se_5$-3MPA in aqueous solution.

We therefore attribute the 397 nm emission peak to first order Raleigh scattering caused by deviation of light (by $Zn_2Ga_2Se_5$-3MPA quantum dots) from its original path to all directions.

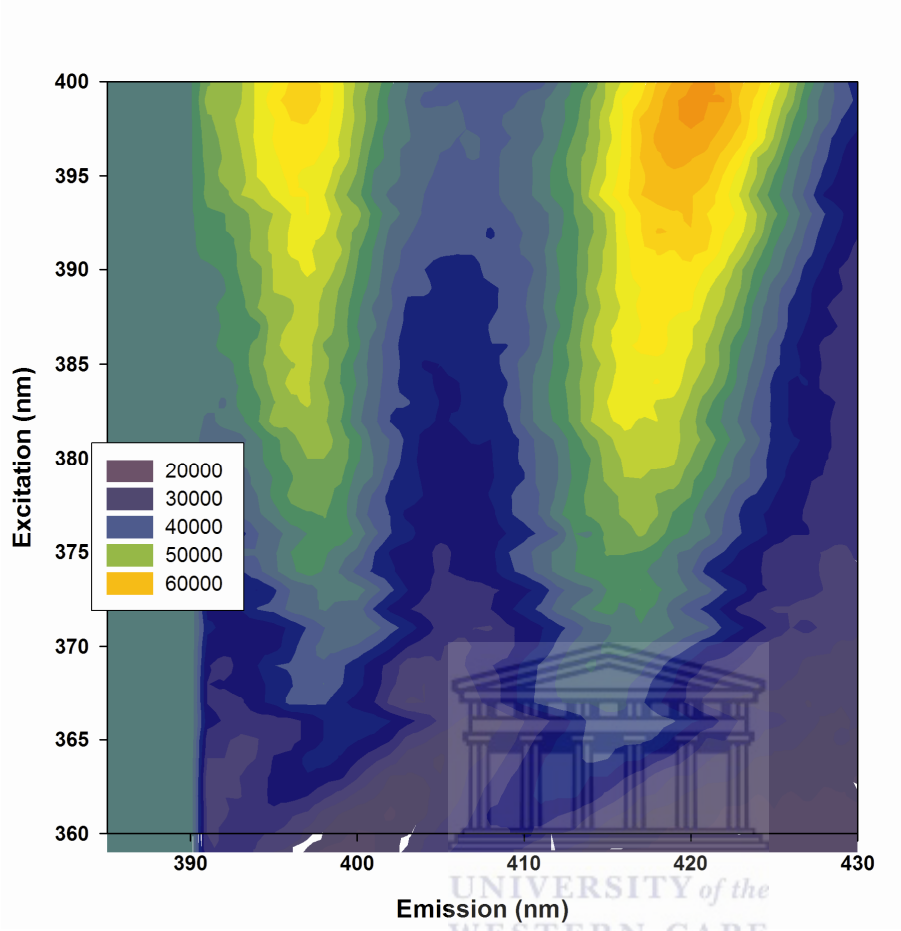

Figure 33: Contour EEM plots of $Zn_2Ga_2Se_5$-3MPA in aqueous solution.

The second fluorescence region ($\lambda_{exc}/\lambda_{emi}$ = 399 nm/420 nm) represents the band edge emission of the $Zn_2Ga_2Se_5$-3MPA. It was also observed that the second emission peak at 420 nm is approximately midway between the band edge emissions of ZnSe-3MPA (450 nm) and Ga_2Se_3-3MPA (403 nm). It is therefore reasonable to suggest that new $Zn_2Ga_2Se_5$-3MPA ternary quantum dots were successfully synthesized, but not matrix mixture of ZnSe-3MPA and Ga_2Se_3-3MPA.

4.6.3 Fourier transforms infrared spectroscopy (FTIR)

The FTIR spectra of ZnSe-3MPA, Ga_2Se_3-3MPA and $Zn_2Ga_2Se_5$-3MPA quantum dots in the region 800 cm^{-1} to 4000 cm^{-1} are shown in the figure below. All the three quantum dots show bands in the region 1365 cm^{-1} to 1475cm^{-1}. These bands arise from the rock and scissor-type bending vibrations of C-H groups in the 3MPA. The band at 1640 cm^{-1}, present in each spectra arises from the stretching vibrations of C=O bond in $–CH_2COO^-$ [266].

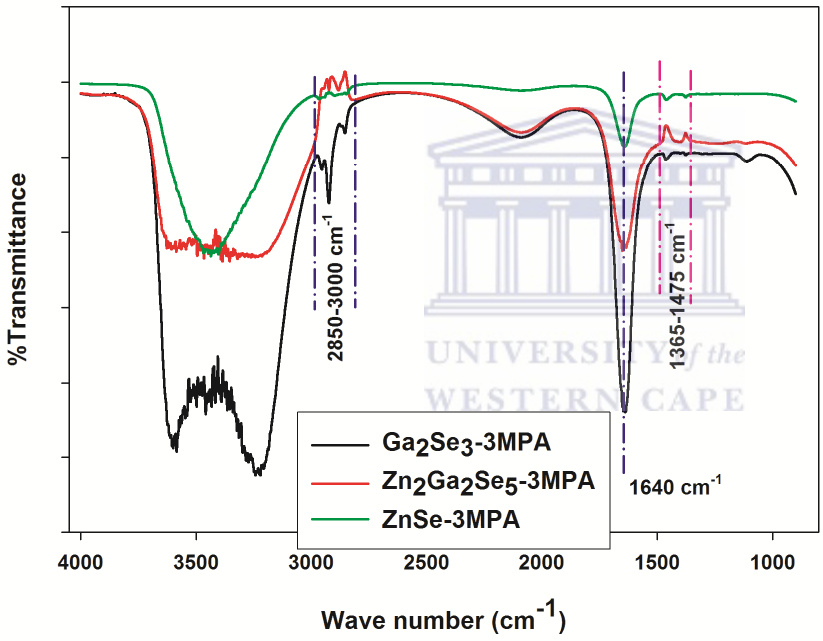

Figure 34: FTIR spectra of ZnSe-3MPA, Ga_2Se_3-3MPA and $Zn_2Ga_2Se_5$-3MPA quantum dots.

The split bands occuring in the region 2850 cm^{-1} to 3000 cm^{-1} represent the symmetric and assymetric stretching vibrations of C-H. ZnSe-3MPA quantum dots shows a well resolved and sharp band at 3435 cm^{-1}, attributed to stretching vibrations of the hydroxyl groups (-O-H) of the carboxylic acid part of the 3MPA [267]. In both Ga_2Se_3-3MPA and $Zn_2Ga_2Se_5$-3MPA quantum

dots, this band appeared to be broad and split, especially for Ga_2Se_3-3MPA. This could result from partial dehydrogenation of the carboxylic acid group in the 3MPA. These results show that the quantum dots were successfully encapsulated in the 3MPA.

4.6.4 X-ray diffraction spectroscopy (XRD)

The figure below shows the diffraction patterns of the ZnSe3-3MPA. Diffraction peaks were observed at 2θ = 27.33°, 31.70°, 34.36°, 36.20°, 47.54°, 56.60°, 62.76°, 66.34°, 67.82° and 68.96° which correspond to (111), (100), (002), (101), (102), (110), (103), (200), (112) and (201) respectively.

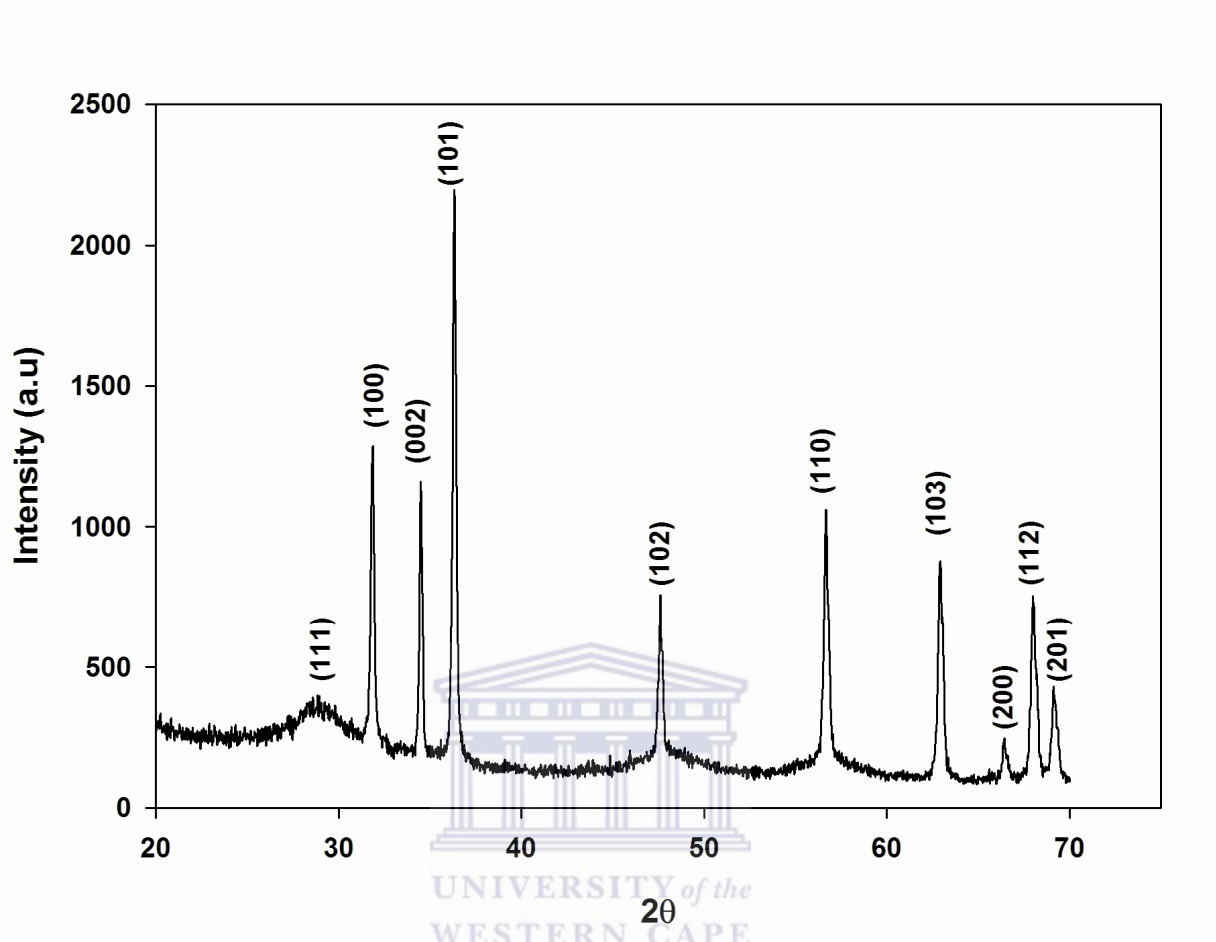

Figure 35: XRD patterns of ZnSe-3MPA quantum dots.

This indicates that the synthesized ZnSe-3MPA possessed a polycrystalline hexagonal wurtzite structure.

4.7 Microscopy of selenide quantum dots

4.7.1 High resolution transmission electron microscopy

The high resolution transmission electron micrographs of the selenide quantum dots and nanocrystals are shown in figures 36, 37 and 38 below. In all samples, high quality non-aggregated particles were formed. Non-aggregation of the quantum dots is believed to result from electrostatic repulsion of negatively charged dehydrogenated carboxyl groups present in the 3-MPA [67]. The average diameter for the ZnSe-3MPA quantum dots estimated from the micrographs was 3.60 nm, while that of $Zn_2Ga_2Se_5$-3MPA was 2.30 nm. This verifies the earlier claim that the size of $Zn_2Ga_2Se_5$-3MPA particles is smaller than that of ZnSe-3MPA.

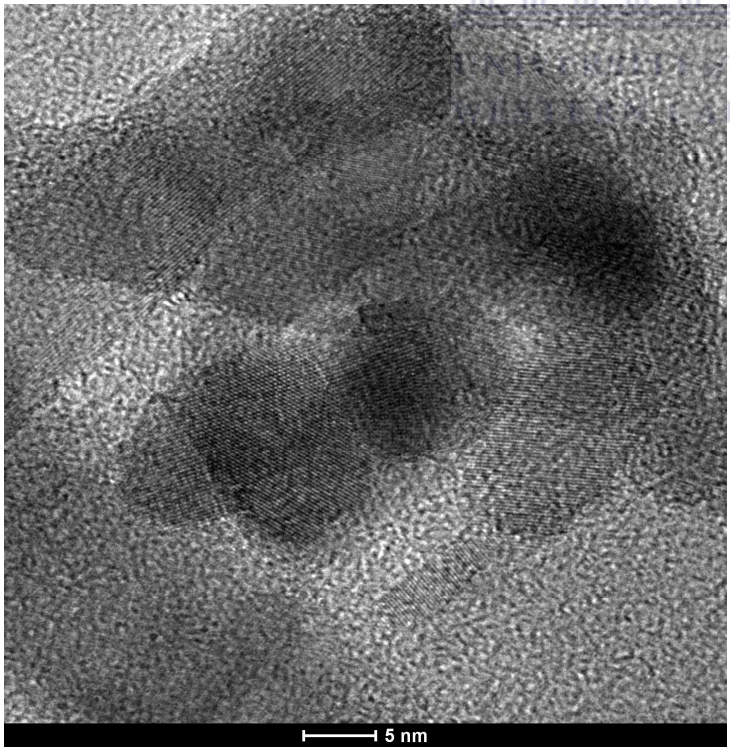

Figure 36: HRTEM micrograph of ZnSe-3MPA quantum dots.

The size of ZnSe-3MPA quantum dots estimated from the HRTEM is in good agreement with the calculated particle sizes using the experimental data derived from UV-vis absorption spectroscopy and equation (37). Both $Zn_2Ga_2Se_5$-3MPA and ZnSe-3MPA quantum dots show lattice fringes on their surface, indicating that the particles were crystalline [268].

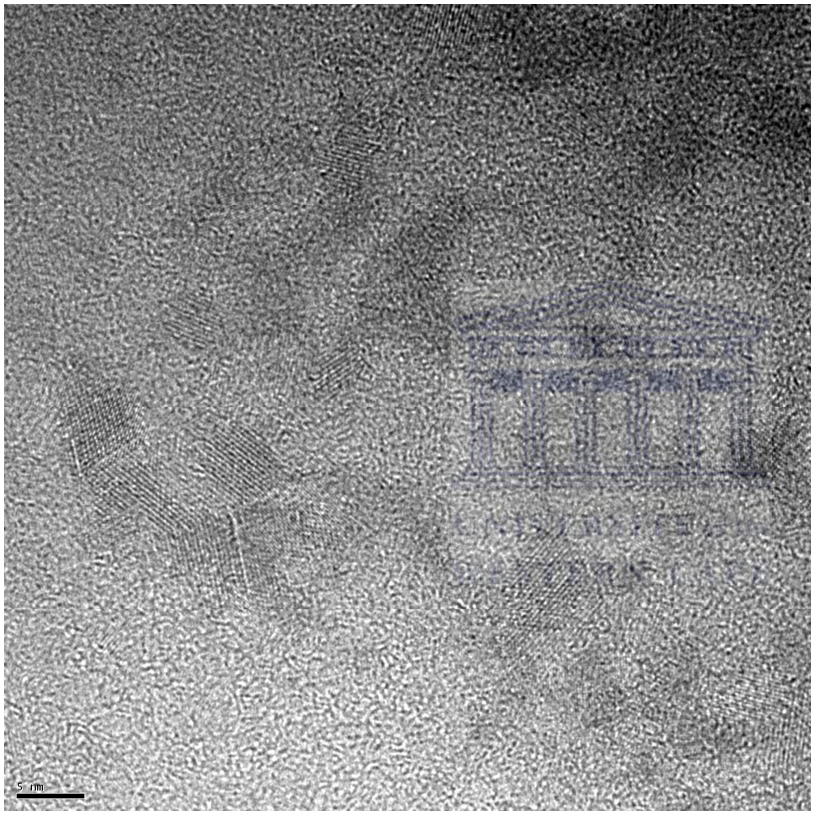

Figure 37: HRTEM micrograph of $Zn_2Ga_2Se_5$-3MPA quantum dots.

From the micrograph of the Ga_2Se_3-3MPA nanoparticles, non-aggregated particles with an average diameter of 65 nm were obtained.

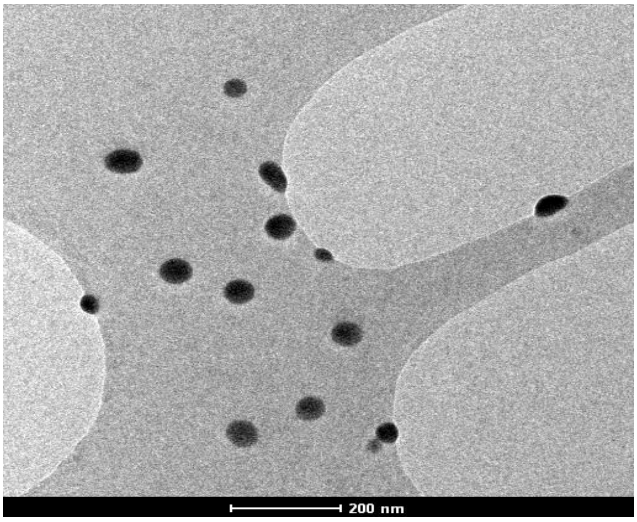

Figure 38: HRTEM micrograph of Ga_2Se_3-3MPA nanoparticles.

It follows that the Ga_2Se_3-3MPA with an average grain size around 65 nm seems too "large" to show a quantum confinement effect, and should be considered as Ga_2Se_3-3MPA nanoparticles.

4.8 Sub conclusions

The electrochemical studies of the binary ZnSe-3MPA quantum dots, Ga_2Se_3-3MPA nanocrystals and the ternary $Zn_2Ga_2Se_5$-3MPA quantum dots reveal that gallium-induced vacancies cause a significant enhancement in the conductivity of the $Zn_2Ga_2Se_5$-3MPA solution compared to that of ZnSe-3MPA and Ga_2Se_3-3MPA. The electrochemistry of adsorbed selenide quantum dots and nanocrystals studied here is largely influenced by their respective surface concentration and not their respective chemical composition. The fluorescence and UV-vis spectra show bands of $Zn_2Ga_2Se_5$-3MPA occurring midway between those of the corresponding binary systems, indicating that a new compound was successfully synthesized as opposed to a

matrix mixture of ZnSe-3MPA and Ga_2Se_3-3MPA. The optically determined band gaps are not in agreement with the electrochemically determined band gaps, due to the interference barrier between the quantum dot or nanocrystal film and the electrode.

CHAPTER 5

Results and Discussion 2: Characterization of binary and ternary telluride quantum dots.

5.1 Introduction

The understanding of the underlying physics and chemistry of telluride quantum dots in their strong confined regime and especially their band structure has imense importance in view of their applications. Haram et al [269] in their recent report used voltammetric techniques to elucidate the electronic band structure of CdSe quantum dots. Other studies [241, 270-274] established that anodic and cathodic peaks obtained from cyclic voltammograms are directly correlated with electron transfers mediated through HOMO (the valence band) and LUMO (the conduction band). The reports further observed that such mediated electronic transitions are not drastically affected by the nature of the capping ligands, agents or the solvent used. Under cyclic voltammetry, the charge transfer in the quantum dots can be viewed as formation of non-reacting electron-hole pairs and the potential difference between the cathodic and anodic peaks and has previously been found to correlate with single particle or quasi band gap estimated by scanning tunneling spectroscopy [222, 241, 270-271, 275].

5.1.1 Electrochemical interrogation of telluride quantum dot solution

Cyclic voltammetry of the $Zn_2Ga_2Te_5$-3MPA ternary quantum dots and its corresponding binary quantum dots (ZnTe-3MPA and Ga_2Te_3-3MPA), each self assembled on gold electrode

were studied within the potential range of -500 mV to 800 mV. Figure 39 below shows the cyclic voltammograms of ZnTe-3MPA self assembled on a gold electrode. On sweeping the potential from -500 mV to 800 mV and back to -500 mV, an anodic peak is observed at 300 mV (peak A_1) which results from oxidation of ZnTe-3MPA. At higher anodic potentials (500 mV) a less prominent peak (peak A_2) is observed and this may be attributed to passivation of ZnTe-3MPA quantum dots. At 650 mV, another anodic peak (peak A_3) appears and this is attributable to anodic stripping of the adsorbed ZnTe-3MPA quantum dots. However, this peak is evidently supressed, indicating that the 3MPA significantly promotes surface passivation of the quantum dots. The peaks in the region 500 mV to 650 mV do not show corresponding cathodic peaks on the reverse scan even with scan rates as low as 20 mV/s. Rather, a broad hump (A_4) in the potential region 200 mV to 400 mV is observed. This is indicative is a well known electron transfer followed by a chemical reaction (E-C), probably due to oxidation of telluride to tellurium [238]. Another peak (peak A_5) which is prominent is observed on the cathodic scan at -280 mV. This peak is found to be complementary to the anodic peak at 300 mV (peak A_1) and gives a peak separation of 580 mV, which is much higher than the Nernstian type of a quasi reversible system. This indicates that reduction of the ZnTe-3MPA is accompanied by formation of an anionic radical of the form $ZnTe^{-}\bullet$. Similar observations were made by Haram et al [269] for capped CdSe quantum dots.

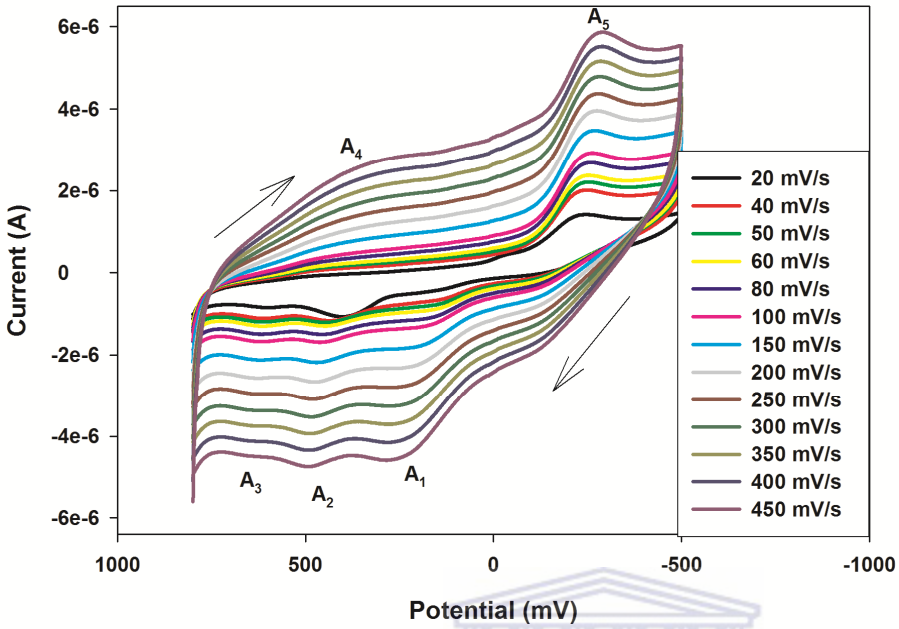

Figure 39: Cyclic voltammograms of Au|ZnTe-3MPA in phosphate buffer solution of pH 7.40.

The anodic peak positions are shifted to positive potentials while the cathodic peak positions are shifted to negative potentials with increasing scan rate. This indicates that the cathodic and anodic processes are governed by slow electron transfer processes. The anodic peak and cathodic currents exhibited a poor linear dependence on the root of scan rate (R^2 = 0.8525) but were highly linear with respect to the scan rate (R^2 = 0.9969), which is indicative of surface confined kinetic effects.

The cyclic voltammograms of pre-adsorbed Ga_2Te_3-3MPA quantum dots (Fig. 40 below) show a prominent peak at 430 mV (peak B_1) when the potential is scanned in the positive direction from -500 mV. At scan rates of 40 mV/s and below, only one peak is observed at this potential. As the scan rates increase beyond 50 mV/s, the peak exhibits a split, giving rise to a

weak peak at around 300 mV (peak B_2) and a strong peak at 490 mV (peak B_3). This peak represents the oxidation of the Ga_2Te_3-3MPA quantum dots and indicates that the oxidation of the quantum dots is a multi-electron transfer process in which the first electron transfer process is slower than the second. Compared with the ZnTe-3MPA, it is observed that whereas the oxidation of the Ga_2Te_3-3MPA quantum dots occur at 430 mV, that of ZnTe-3MPA occurs at 300mV. Moreover, the quantum dots' oxidative peak is more prominent in Ga_2Te_3-3MPA than in ZnTe-3MPA. Specifically, the anodic current generated during the oxidation of Ga_2Te_3-3MPA is twice that obtained with ZnTe-3MPA oxidation. Since tellurium is the common element in both quantum dots, it is reasonable to suggest that the anodic peak observed is actually related to oxidation of tellurium. To understand the differences in the current generated, it is important to consider the structural differences between Ga_2Te_3-3MPA and ZnTe-3MPA.

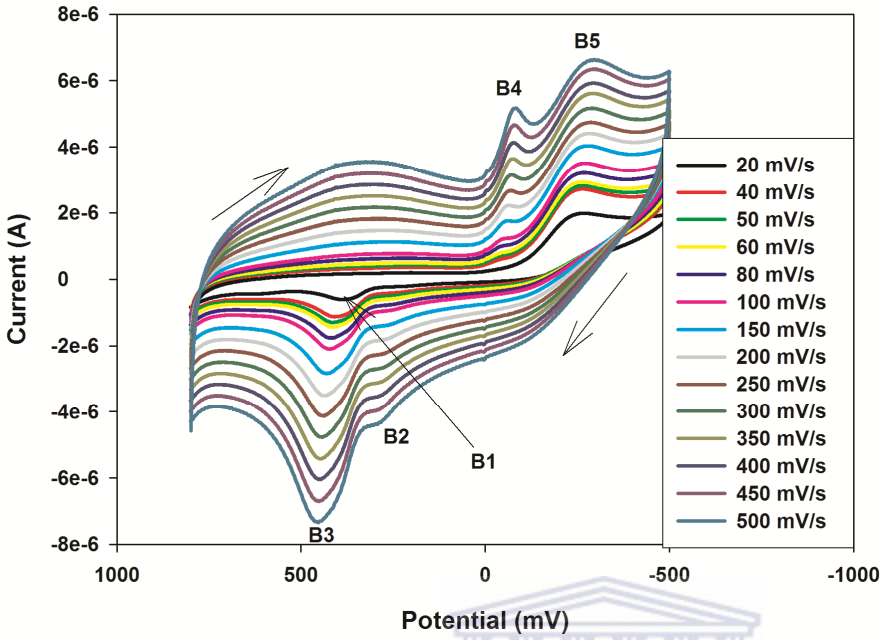

Figure 40: Cyclic voltammograms of Au|Ga_2Te_3-3MPA in phosphate buffer solution of pH 7.40.

Ga_2Te_3-3MPA contains a defected zinc blend type structure with one third of the gallium exhibiting vacancies as explained for Ga_2Se_3-3MPA. Similarly, the ZnTe-3MPA assumes a zinc blend type structure due to Zn-Te valence match. Tellurium surface state defects are therefore more prominent in Ga_2Te_3-3MPA than in ZnTe-3MPA, which means that Ga_2Te_3-3MPA contains a high number of oxidizable tellurium defects compared to ZnTe-3MPA. Since the amount of current generated during an electrochemical reaction is directly proportional to the amount of electro active species undergoing reaction, the high currents observed for the tellurium defect rich Ga_2Te_3-3MPA are envisaged. To further confirm this, the number of electrons transferred in the anodic processes of both quantum dots was evaluated from the linear relationship between the peak potentials and the natural logarithm of scan rate in accordance

with equations 32a and 32b described previously in this thesis (see section **4.1.1.2)**. For ZnTe-3MPA, the linear relationship was $E_{p,a}$=0.0335lnν + 0.5301 (R^2=0.9832) and $E_{p,a}$=0.0230lnν + 0.4780 (R^2=0.9878) for Ga_2Te_3-3MPA. The number of electrons transferred calculated from the slopes of these lines, assuming an electron transfer coefficient (α) as 0.5 were 2.23 for Ga_2Te_3-3MPA and 1.53 for ZnTe-3MPA. These values basically indicate that the tellurium oxidation was a two electron transfer process in each case. The standard rate constants related to the electronic transfer processes were also evaluated from intercepts of the linear plots. ZnTe-3MPA was found to exhibit a faster electron transfer rate at 2.6588 s^{-1} compared to Ga_2Te_3-3MPA at 3.8210 x 10^{-1} s^{-1}. The slow electron transfer observed in Ga_2Te_3-3MPA is due to presence of structural vacancies which hindered smooth transfer of electrons. With a one order of magnitude difference in the electron transfer rate between Ga_2Te_3-3MPA and ZnTe-3MPA, one would expect the anodic peak of Ga_2Te_3-3MPA to occur at more positive potentials than that of ZnTe-3MPA. This explains the shift in the tellurium oxidative peak from 300 mV in ZnTe-3MPA to 430 mV in Ga_2Te_3-3MPA. Another factor that influences the rate of electron transfer and thus oxidation potentials in surface confined electro active molecules is the surface concentration. This prompted an investigation of the surface concentration of the adsorbed quantum dots on the electrode surface. The surface concentration was evaluated from linear relationship between the anodic peak currents and scan rates for both quantum dots in accordance with Brown Anson's equation (equation 31a), also described previously (section **4.1.1.2)**. The plots (not shown) had linear regressions of $i_{p,a}$ = -6.6817 x 10^{-6}ν – 5.0666 x 10^{-7} (R^2= 0.9865) for Ga_2Te_3-3MPA and $i_{p,a}$ = -2.0387 x 10^{-6}ν – 1.7520 x 10^{-7} (R^2=0.9969) for ZnTe-3MPA. The corresponding surface concentrations were 8.8470 x 10^{-11} mol cm^{-2} and 2.6994 x 10^{-11} mol cm^{-2} for Ga_2Te_3-3MPA and

ZnTe-MPA respectively. Being with the same order of magnitude, it is unlikely that the surface concentration influenced the anodic peak potential for the two quantum dot systems.

The reverse scan shows reduction of the oxidized products at -250 mV (peak B_4), which like the anodic peak splits to give another peak at around 0 mV (peak B_5). The peak maxima are similar to that of ZnTe-3MPA and again indicate formation of a radical anion during the Ga_2Te_3-3MPA reduction. The electrochemical band gap determined from the onset anodic and cathodic waves using equations described previously (equations 25, 26 and 27) gave 0.578 ± 0.030 eV, which will later be compared with the optical band gap determined from the UV-vis absorption maxima.

Figure 41 below shows the cyclic voltammograms of $Zn_2Ga_2Te_5$-3MPA pre-adsorbed on a gold electrode. It was observed that the oxidation waves are similar to those of Ga_2Te_3-3MPA while the reduction waves resemble those of ZnTe-3MPA. A further investigation of the anodic was done using the relationship between the peak potentials and the natural logarithm of scan rate described above, as it was for the binary quantum dots. A linear regression of the form $E_{p,a}=0.0176\ln\nu + 0.4564$ ($R^2=0.9421$) was obtained. The number of electrons evaluated form the slope of the plot was 2.92, suggesting a three electron transfer process. Although this peak is observed at the same potential as that observed for oxidation of tellurium in ZnTe-3MPA, the number of electrons transferred points more towards gallium oxidation reactions than tellurium. To understand why gallium undergoes oxidation and not tellurium, it is important to note that the presence of zinc in the ternary $Zn_2Ga_2Te_5$-3MPA quantum dots creates a perfect valence match with respect to tellurium. The ternary $Zn_2Ga_2Te_5$-3MPA therefore experiences more surface state vacancies related to gallium than tellurium. In other words, the gallium is more available for

oxidation than tellurium, owing to the gallium related structural defects in the lattice. The occurrence of the oxidation peak at the same potential as that of tellurium potential maybe explained in terms of quantum confinement effects, the electron transfer rate as well as adsorbed nature of the quantum dots. Since electrons are confined in a very small three dimensional space, the electronic transitions for all species take place from a localized donor within the lattice to a localized acceptor. For a surface adsorbed species, the short proximity between the electro active molecule and the electrode ensures electron transfer within a very short time frame. The other factor (rate of electron transfer within the lattice and from the lattice to the electrode) was evaluated from the intercept of the linear dependence of the peak potentials on the natural log of scan rate. The evaluated value was found to be 19.5231 s^{-1}, which is the highest of the three quantum dot materials. It is also important to mention that the species available for oxidation in the $Zn_2Ga_2Te_5$-3MPA lattice (gallium) contains a high charge density compared to either tellurium or zinc. It is common knowledge that a molecule with a high charge density would be characterized by a high rate of charge transfer and vice versa. The high electron transfer rate and consequent oxidation of gallium at the same potential as that observed for tellurium is therefore not surprising. The surface concentration was also investigated to determine if it enhanced the electron transfer rate. From a plot of peak current versus scan rate with a regression equation of $i_{p,a}$ = -2.1181 x $10^{-7}\nu$ – 7.3358 x 10^{-7} (R^2= 0.9905), the surface concentration was found to be 1.4260 x 10^{-12} mol cm^{-2}. This is one order of magnitude less than the values obtained for the corresponding binary quantum dots and could not enhance the electron transfer process.

.

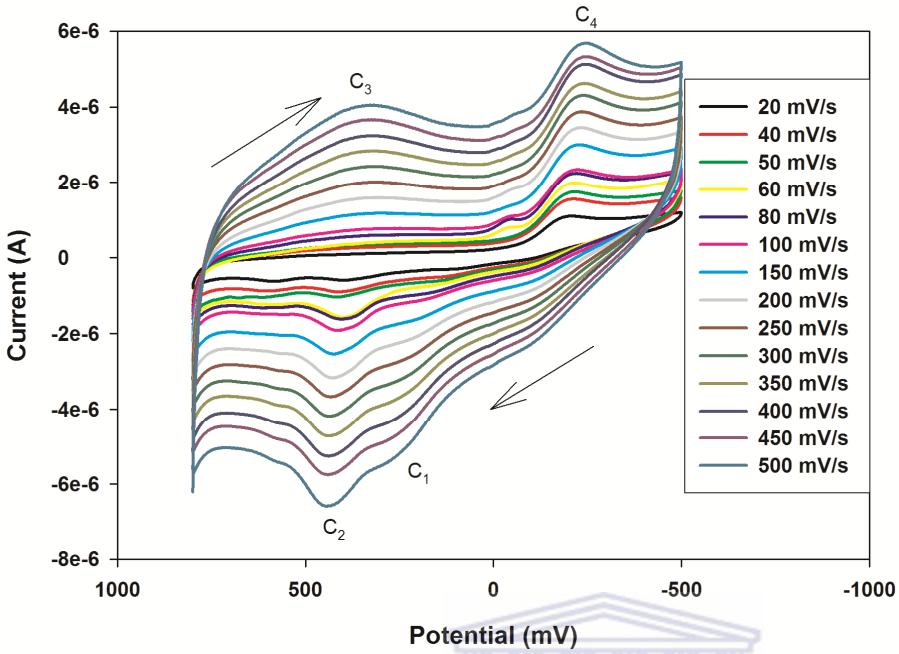

Figure 41: Cyclic voltammograms of Au|$Zn_2Ga_2Te_5$-3MPA in phosphate buffer solution of pH 7.40.

In the cathodic scan, two peaks are observed at scan rates below 100 mV/s. One peak which appears to be minor is observed around 100 mV while the other one (major) occurs at around 200 mV. As the scan rates increase beyond 100 mV/s, the minor peak merges with the major and the peak potential remains fairly constant. This behaviour was observed for ZnTe-3MPA quantum dots only at 20 mV/s after which the peaks merged at 40 mV/s. For the Ga_2Te_3-3MPA, the two reductive peaks remained prominent for all scan rates investigated. This indicates that the rate of electron transfer relative to the scan rate is high in $Zn_2Ga_2Te_5$-3MPA. At high scan rates however, the scan rate becomes sufficiently high to maintain the concentration of electroactive molecules at the electrode surface. This phenomenon is consistent with the highest

calculated electron transfer rate constant for $Zn_2Ga_2Te_5$-3MPA. The electrochemical band gap evaluated from the onset potentials of the main peaks was found to be 0.254 ± 0.071 eV.

For clarity of comparison of the cyclic voltammograms of the three types of quantum dots, cyclic voltammograms of each quantum dot system were extracted at 450 mV/s scan rate and plotted on the same axis as shown in the figure below.

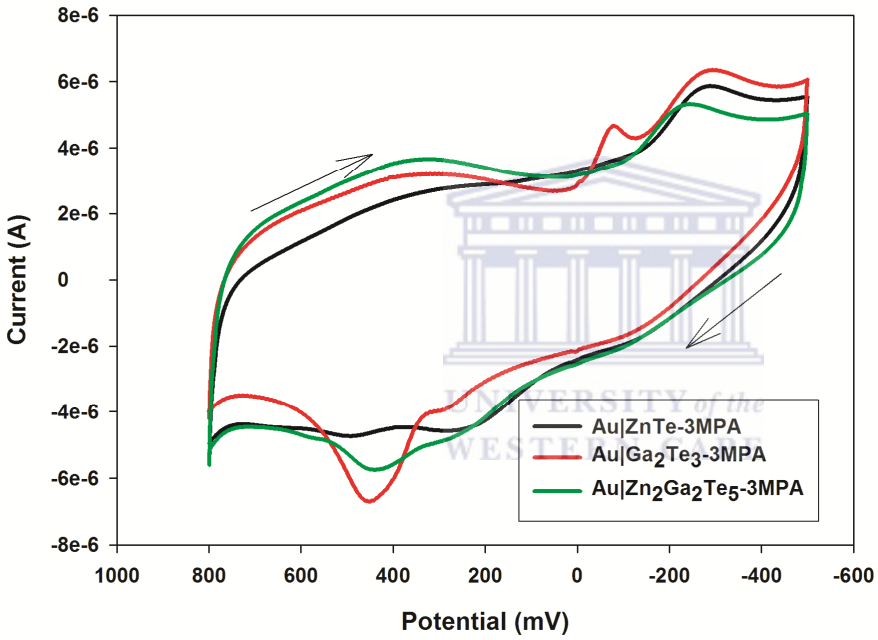

Figure 42: Cyclic voltammograms of Au|ZnTe-3MPA, Au|Ga_2Te_3-3MPA, and Au|$Zn_2Ga_2Te_5$-3MPA each in phosphate buffer solution of pH 7.40 at 450mV/s scan rate.

It is evident from the cyclic voltammograms that the anodic wave of $Zn_2Ga_2Te_5$-3MPA resembles that of Ga_2Te_3-3MPA while the anodic wave resembles that of ZnTe-3MPA. Notably the main cathodic peaks are observed to shift to more negative values in the order $Zn_2Ga_2Te_5$-3MPA, ZnTe-3MPA and Ga_2Te_3-3MPA. This sequence is consistent with the electron transfer

rate constants which decrease in the same order, i.e. 19.5231 s^{-1}, 2.6588 s^{-1} and 3.8210 x 10^{-1} s^{-1} for $Zn_2Ga_2Te_5$-3MPA, ZnTe-3MPA and Ga_2Te_3-3MPA respectively.

5.2 Spectroscopy of the telluride quantum dots

5.2. 1 Ultraviolet –visible spectroscopy (UV-vis).

The UV-vis spectra of the telluride quantum dots are shown in the figure below (Fig 43). ZnTe-MPA quantum dots show two absorption shoulders at 270 nm and 300 nm. These present a significant blue shift from the absorption edge of bulk ZnTe (531 -548 nm) [276-277]. Using the main absorption shoulder of the synthesized ZnTe-3MPA as (300 nm) and that of the bulk ZnTe as 532 nm, the size of the ZnTe-3MPA quantum dots was calculated from the effective mass model in accordance with the equation below [278].

$$E_{ZnTe-3MPA} - E_{ZnTebulk} = \frac{h^2\pi^2}{2\mu R^2} + \frac{1.8e^2}{\varepsilon R} \qquad (38)$$

Where $E_{ZnTe\text{-}3MPA}$ and E_{ZnTe} are the band gaps (eV) of the synthesized quantum dots and the bulk semiconductors respectively, h is the Planck's constant (6.62607 × 10^{-34} m^2 kg s^{-1}), μ is the electron–hole reduced effective mass (μ_{ZnTe} = $0.1m_0$ = 9.1095 x 10^{-32} Kg), R is the radius of the spherical confinement region while the last term is an estimate of electron–hole Coulomb interaction where e is the dielectric constant (ε_{ZnTe} = 8.7) and e is the elementary electric charge (1.6022 ×10^{-19} C). The estimated size (diameter, D where D=2R) of the ZnTe-3MPA was 5.56 nm. The shape of the absorption shoulder of Ga_2Te_3-3MPA at 240 nm is similar to that of Ga_2Se_3-3MPA. The two compounds are known to have a zinc –blend –type structure [254] and

this sharp absorption band of Ga_2Te_3-3MPA characterizes excitonic features of a homogeneous zinc blend-type defects in Ga_2Te_3-3MPA [263].

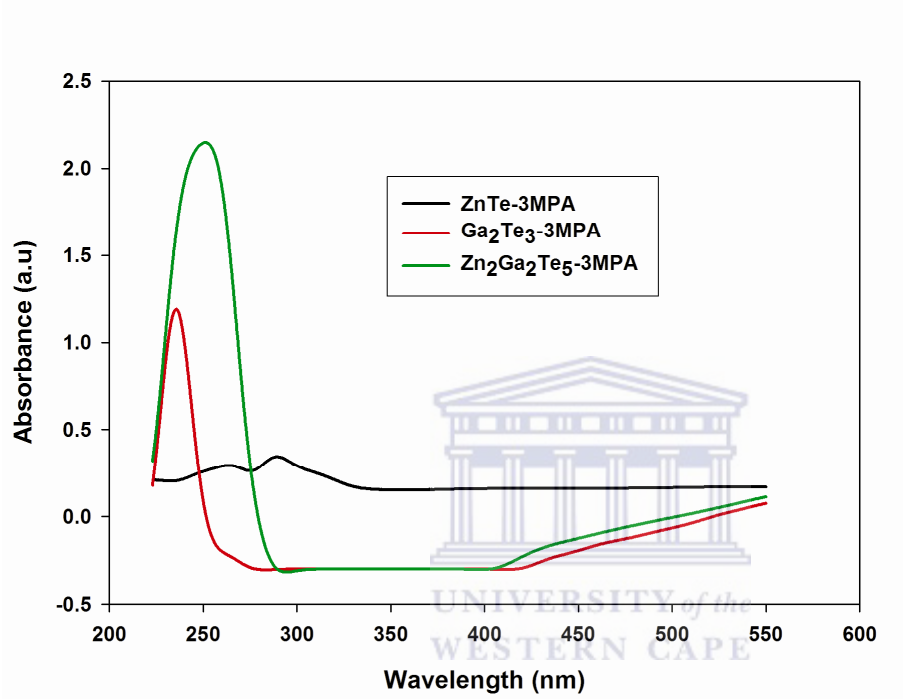

Figure 43: UV-vis spectra of ZnTe-3MPA, Ga_2Te_3-3MPA and $Zn_2Ga_2Te_5$-3MPA quantum dots.

The spectrum of $Zn_2Ga_2Te_5$-3MPA shows an absorption shoulder at 270 nm. Although its shape is similar to the spectra of Ga_2Te_3-3MPA and Ga_2Se_3-3MPA quantum dots discussed earlier, it is interesting to note that the absorption peak is at the same wavelength as that of the weak absorption of ZnTe-3MPA quantum dots. For similar reasons given for $Zn_2Ga_2Se_5$-3MPA earlier, this absorption is attributable to contributions of gallium doping of ZnTe-3MPA quantum dots.

5.2.2 Fluorescence spectroscopy

To study the photoluminescence properties of the ZnTe-3MPA quantum dot under 2D fluorescence spectroscopy, liquid samples were excited at 330 nm in and the emission monitored in the range 350 nm to 550 nm. The figure below depicts the results. The photoluminescence spectrum consists of a weak peak at around 370 which is attributable to self activated emissions of the ZnTe-3MPA quantum dots.

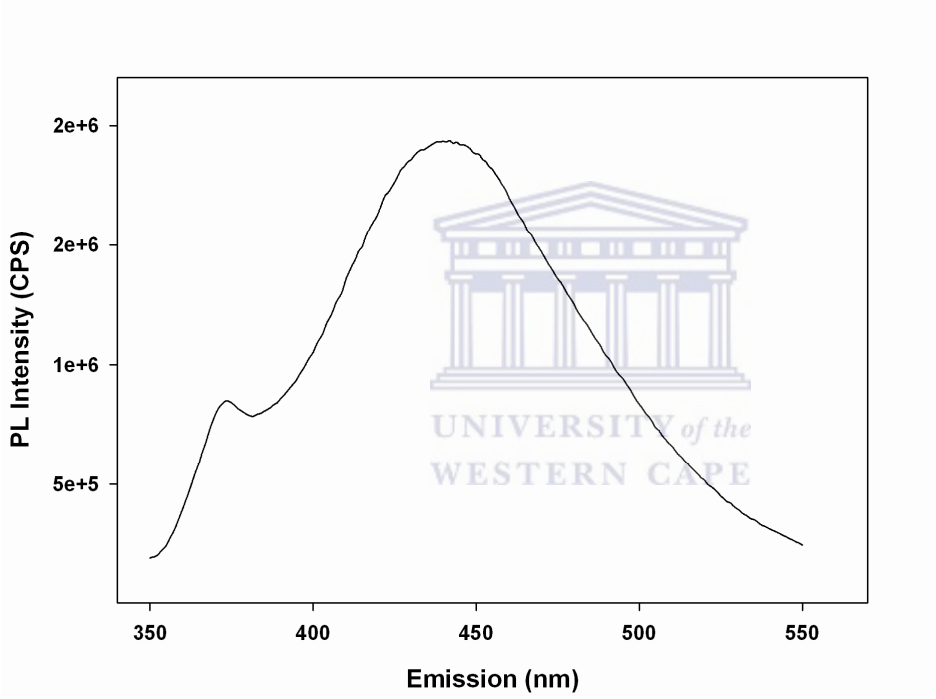

Figure 44: Fluorescence spectra of ZnTe-3MPA quantum dots.

At 450nm, the main photoluminescence appears and this is attributed to electron-hole recombination transitions (band edge emissions) of the ZnTe-3MPA. Beyond the band edge emissions, no observable electronic transitions took place as depicted by absence of peaks after 450 nm. It has been mentioned that photoluminescence peaks appearing after the band edge are characteristics of surface state emissions and defects. The absence of such peaks means lack of

surface defects in the ZnTe-3MPA quantum dots and this can be ascribed to perfect valence match between zinc and telluride ions.

To view all the photoluminescence features of ZnTe-3MPA within a wide spectral range, the liquid samples were exposed to three dimensional photoluminescence measurements, exciting within the range 300 nm to 350 nm and monitoring the emission spectra in the range of 320 nm to 550 nm. This gave rise to 3D EEM spectra whose topographic and contour plots are shown in figures 45 and 46 below.

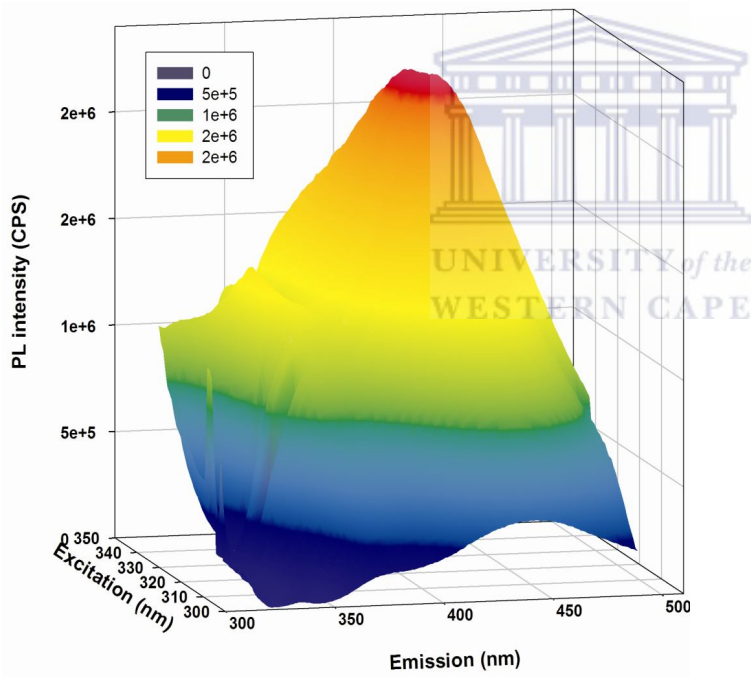

Figure 45: Topographic EEM plots of ZnTe-3MPA in aqueous solution.

The ZnTe-3MPA exhibit spectral features in two regions; a low intensity within the range $\lambda_{exc}/\lambda_{emi}$ = 332-339 nm/347-353 nm peaking at $\lambda_{exc}/\lambda_{emi}$ = 335 nm/370 nm. This is in agreement with the low intensity peak observed under 2D fluorescence and is attributable to self activated

emissions. In the second region within the range $\lambda_{exc}/\lambda_{emi}$ = 325-335 nm/405-435 nm is a high intensity peak reminiscence to that observed under 2D fluorescence and is associated with electron-hole transitions. The stokes shift obtained from this main spectral range was 80 nm to 100 nm which signifies narrow size distribution of the synthesized quantum dots.

A valuable property of quantum dots is their ability to exhibit a broad absorption window which increases towards the UV region [279]. This can allow for simultaneous excitation of different colour quantum dots at a single wavelength far from their respective emissions. This property can be studied by examining the contour EEM plots of 3D fluorescence spectra.

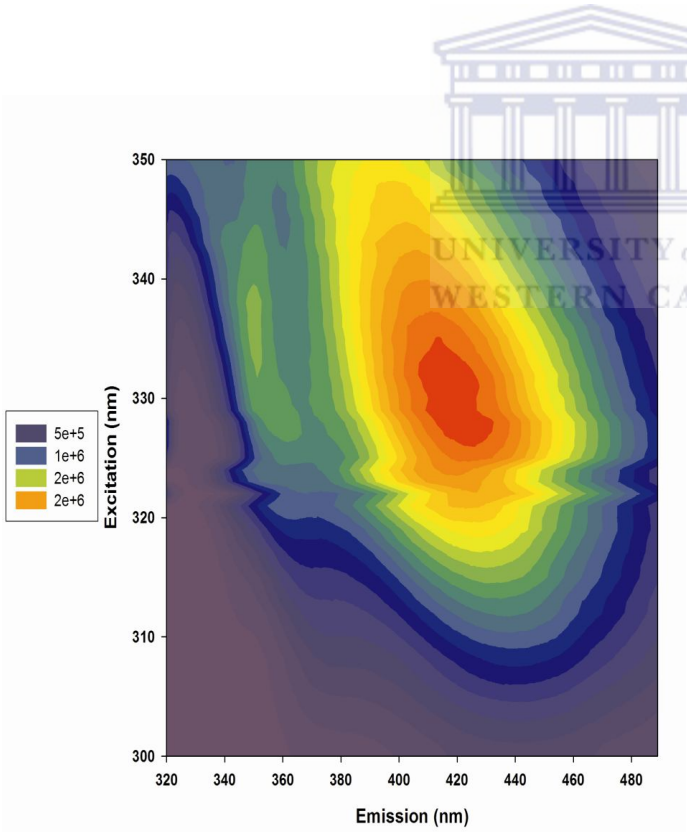

Figure 46: Contour EEM plots of ZnTe-3MPA in aqueous solution.

In the contour EEM plots shown above the emission characteristics of the ZnTe-3MPA are independent of the excitation wavelength. It is therefore possible to view the entire different emission colours of the ZnTe-3MPA quantum dots at the same time by only one laser excitation source. These quantum dots are thus suitable for multiplexing applications.

For Ga_2Te_3-3MPA, a 2D fluorescence spectrum was obtained by exciting liquid samples of the quantum dots at 320 nm and monitoring the emission in the range of 340 nm to 550 nm. The emission spectrum whose figure is shown below (Figure 47) depicts three peaks. The first two peaks; a low intensity peak at 370 nm and 450 nm are similar to those observed in the ZnTe-3MPA and are ascribed to self activated emissions (for the low intensity peak) and band edge emissions due to electron-hole recombination transitions (high intensity peak).

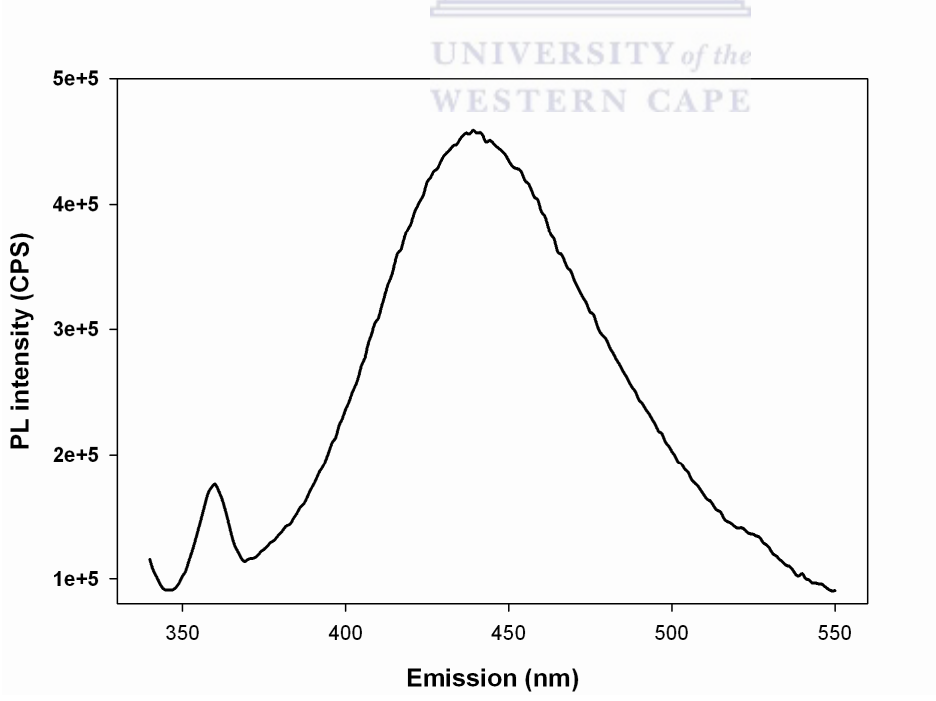

Figure 47: Fluorescence spectra of Ga_2Te_3-3MPA quantum dots.

The third peak, which is of very low intensity, occurs at approximately 530 nm. To understand the source of this emission, it is necessary to consider possible factors that cause distortions in fluorescence of semiconducting materials. Among the causes are distortions in the crystal structure, commonly known as point defects in the semiconducting materials. Point defects may result from orientation of the semiconductors' ions in abnormal locations of the crystal structure (Frenkel defects) or existence of vacancies in the lattice structure of the material due to missing ions (Schottky defects). Another possible cause of fluorescence distortions is the presence of impurity ions in the crystal lattice sites that are not normally occupied (interstitial defects). Such defects alter the normal absorption and dissipation of light energy within and near the structurally imperfect parts of the crystal. Considering the possible charged states of gallium in the Ga_2Te_3-3MPA, we realize that gallium contains three stable charge states, denoted as (+1/+2) and (+2/+3) for Ga^+, Ga^{2+} and Ga^{3+} [280]. The perturbation of the band edges by these charged impurities could give rise to interstitial defect interactions which delays electron-hole recombination. If this occurs, emissions resulting from trapped states are observed at wavelengths higher than the main band edge emission. Since this peak occurs after 450 nm (the main band edge emission), it may be attributed to surface state trap emissions.

The EEM measurements of the Ga_2Te_3-3MPA were done by exciting the samples in the range 300 to 340 nm and monitoring the emission in the range 320 to 550 nm, all at 1 nm increments. In the topographic and contour EEM diagrams shown below, a total intensity profile of the Ga_2Te_3-3MPA over the range of scanned excitation and emission wavelengths is observed, revealing new spectral features of the electronic transitions existing within the Ga_2Te_3-3MPA. For instance, whereas the electron-hole recombination peak was observed at 450 nm under 2D

fluorescence, the 3D EEM shows the same occurring in the range $\lambda_{exc}/\lambda_{emi}$ = 315-317 nm/405-420 nm.

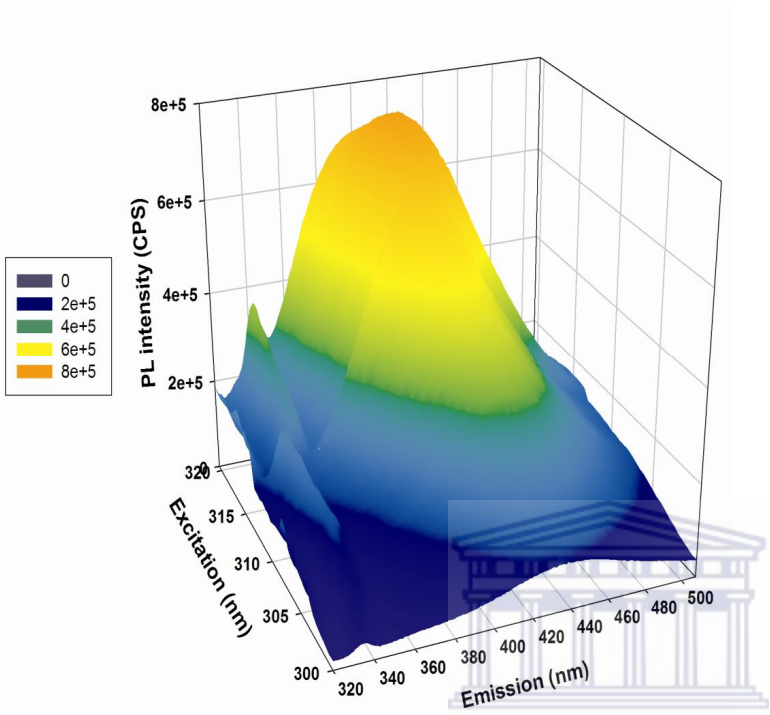

Figure 48: Topographic EEM plots of Ga_2Te_3-3MPA in aqueous solution.

Ga_2Te_3-3MPA exhibits relatively long stokes shift (90 to 103 nm), attributed to the extension of exciton wave-function to the outer 3-MPA. A notable difference between the fluorescence of ZnSe-3MPA and that of Ga_2Te_3-3MPA is that, Ga_2Te_3-3MPA records lower photoluminescence intensity profiles than ZnSe-3MPA in both 2D and 3D EEM matrices. Rather than manifesting themselves in form of surface state emissions, the contributions of the gallium related point defects in Ga_2Te_3-3MPA seemed to lower the photoluminescence intensity. Previous reports [281-282] observed that, unwanted defects such as vacancies cracks and stacking faults degrade the optical properties semiconducting materials.

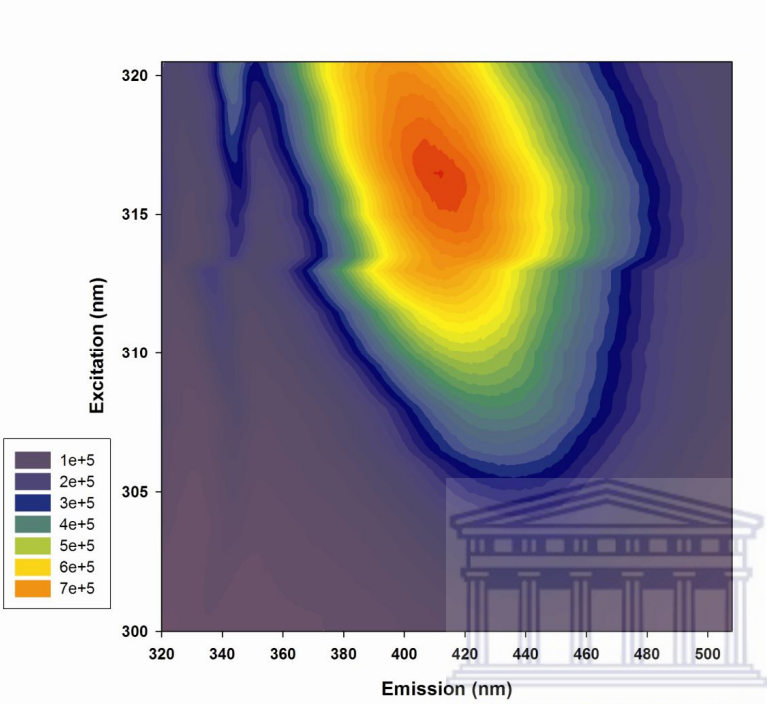

Figure 49: Contour EEM plots of Ga_2Te_3-3MPA in aqueous solution.

A close analysis of the contour plot reveals that variation of the excitation wavelength in the range of 315 nm to 317 nm does not affect the emission properties of Ga_2Te_3-3MPA. Comparing with the ZnTe-3MPA whose excitation range is 325-335 nm (for the band edge emission), we realize that the Ga_2Te_3-3MPA have a narrow excitation range. In fact, a narrow excitation range is a characteristic of fluorescent dyes [283-284], whose multiplexing applications are limited. Performing multiple simultaneous tests with Ga_2Te_3-3MPA would therefore be more difficult than if performed with ZnTe-3MPA.

The 2D fluorescence spectrum of $Zn_2Ga_2Te_5$-3MPA was obtained after exciting the sample at 300 and monitoring the emission within the range of 340 nm to 550 nm and the results are shown in the figure below. Within this range, the emission characteristics of $Zn_2Ga_2Te_5$-3MPA were similar to that of binary ZnTe-3MPA and Ga_2Te_3-3MPA quantum dots.

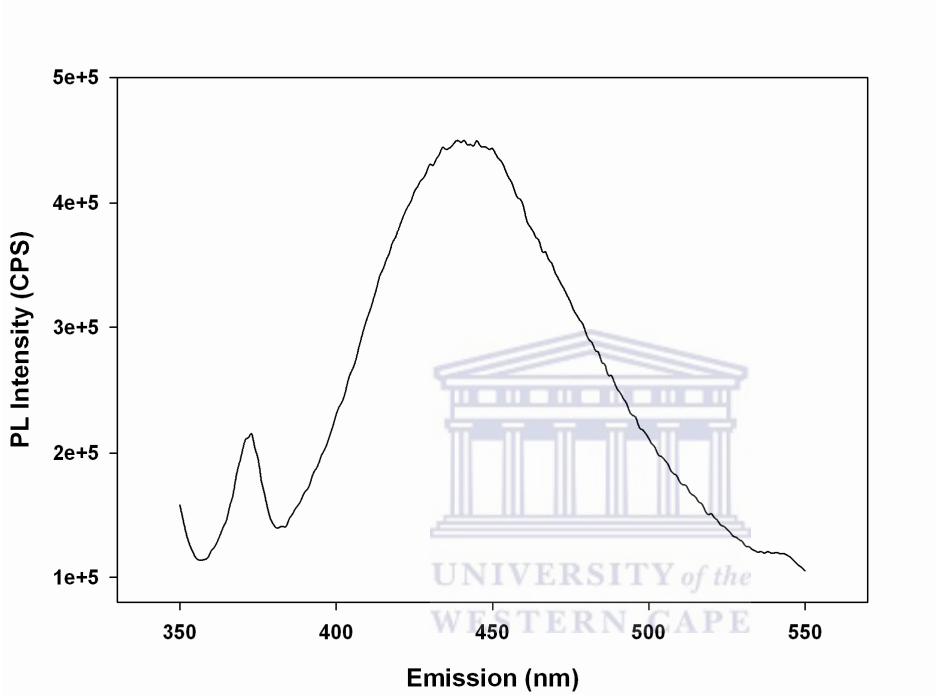

Figure 50: Fluorescence spectra of $Zn_2Ga_2Te_5$-3MPA quantum dots.

Specifically, self activated emissions were observed at 370 nm followed by electron-hole recombination transition at 450 nm. A notable difference of this spectra from the others is that the emission resulting from surface defects slightly red-shifted (from 530 nm for Ga_2Te_3-3MPA) to 455 nm for $Zn_2Ga_2Te_5$-3MPA). ZnTe-3MPA does not show this emission. The wavelength at which this emission occurs is therefore outside the range of transitional energies of possibly contributing binary quantum dots, which are ZnTe-3MPA and Ga_2Te_3-3MPA. It has already been established that ternary quantum dots containing two chalcogen atoms and one transitional

element exhibit linear dependence on the relative rations of the chalcogens [237], while ternary quantum dots containing two transitional elements and one chalcogen exhibit quasi linear dependence on the composition of the transitional metals [285-286]. Being a ternary quantum dot with two transitional metals and one chalcogen atom, the occurrence of red shifted transitional energies in $Zn_2Ga_2Te_5$-3MPA is known as optical bowing [287] and may be attributed to structural and electronic factors of the atoms in the ternary quantum dot. These factors include differences in their atomic sizes and electro negativity values [237] of in this case gallium, tellurium and zinc.

For EEM fluorescence measurements of $Zn_2Ga_2Te_5$-3MPA quantum dots, excitation from 300 to 380 nm with Emission monitored in the range 320 to 550 nm, all at 1 nm increments resulted to topographic and contour plots given in figures 51 and 52 below. The figures depict that high intensity spectral features of $Zn_2Ga_2Te_5$-3MPA emerged at wavelengths lower than that observed funder 2D fluorescence. Three fluorescence regions were observed with varying photoluminescence intensities. One region, which exhibited the highest intensity was observed in the range $\lambda_{exc}/\lambda_{emi}$ = 327-337 nm/398-425 nm, giving a stokes shift of 71 nm to 88 nm. This emission represents $Zn_2Ga_2Te_5$-3MPA electron-hole recombination transitions and the narrow stokes shift is an indication of narrow size distribution of the quantum dots. It also emerged that the band edge emissions of ternary $Zn_2Ga_2Te_5$-3MPA quantum dots occur within the same range of the corresponding binary quantum dots; λemi = 405-435 nm (for ZnTe-3MPA) and λemi 405-420 nm (for Ga_2Te_3-3MPA).

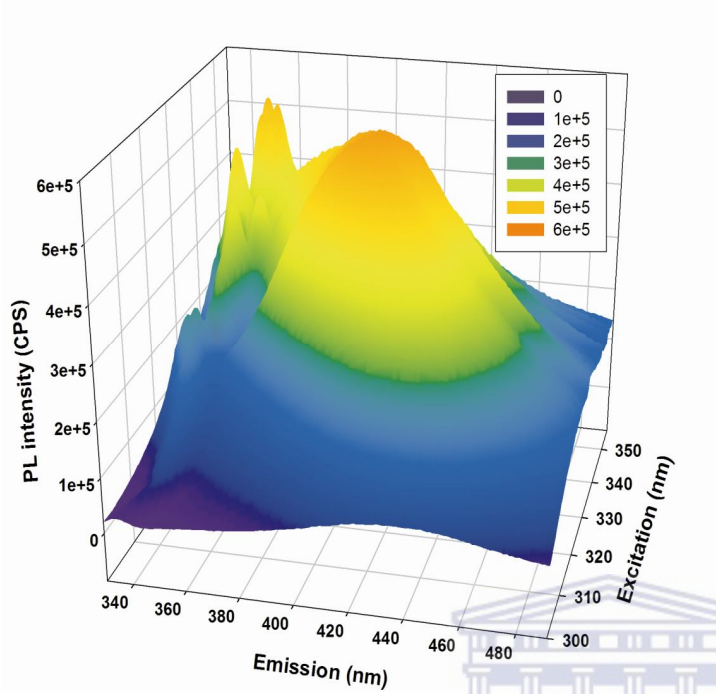

Figure 51: Topographic EEM plots of $Zn_2Ga_2Te_5$-3MPA in aqueous solution.

This may depict contributions of the transition energies of the ZnTe-3MPA and Ga_2Te_3-3MPA to the band edge emissions of the $Zn_2Ga_2Te_5$-3MPA. Comparatively, the photoluminescence intensity resulting from band edge emissions is observed to decrease in the order $Zn_2Ga_2Te_5$-3MPA <Ga_2Te_3-3MPA< ZnTe-3MPA. This is attributed to increasing number of dangling bonds [288-290] resulting from interstitial gallium valences.

The other two fluorescence regions, which are clearly observed in the contour plot below, are characterized by low intensity and occur within the range $\lambda_{exc}/\lambda_{emi}$ 346-348 nm/338-342 nm and 345- 347 nm/385-395 nm. The uniqueness of these emissions is that they occur at wavelengths lower than their respective excitation wavelengths.

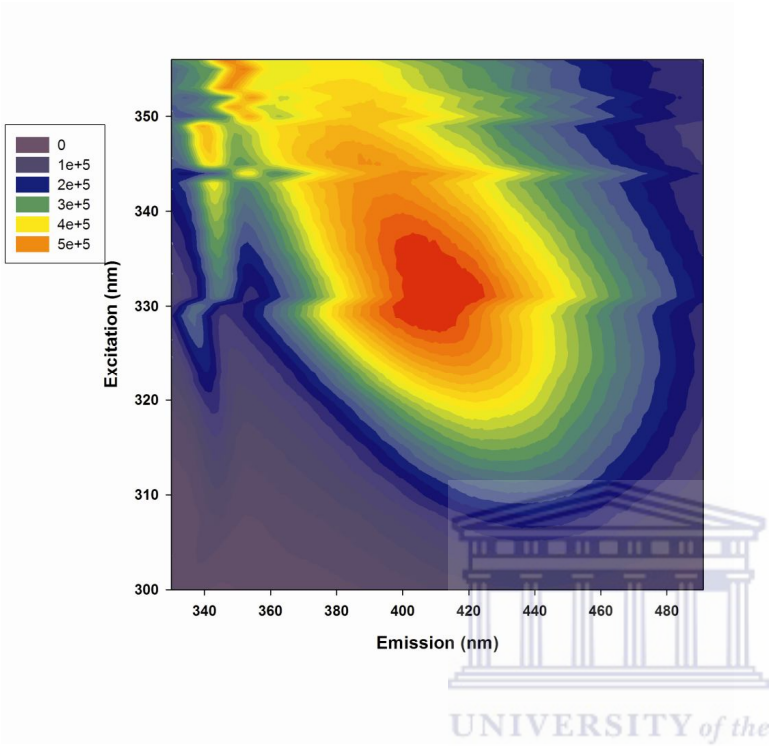

Figure 52: Contour EEM plots of $Zn_2Ga_2Te_5$-3MPA in aqueous solution.

It is expected that the emission of photons by $Zn_2Ga_2Te_5$-3MPA (fluorescence) is accompanied by loss of the absorbed energy through other non radiative transitions such as vibrations. One would thus expect emission to occur at lower wavelengths (since less energy is emitted) than the excitation wavelength. The abnormal $\lambda_{exc}/\lambda_{emi}$ combination observed in this case may be attributed to first order Raleigh scattering.

5.2.3 Fourier transforms infrared spectroscopy (FTIR)

The figure below shows the FTIR spectra of ZnTe-3MPA, Ga_2Te_3-3MPA and $Zn_2Ga_2Te_5$-3MPA quantum dots taken in the region 400 cm^{-1} to 4000 cm^{-1}. The bands observed in all quantum dots at A (1165 cm^{-1}), B (1250 cm^{-1}) and C (1485 cm^{-1}) are respectively associated with wagging, rocking and scissoring vibrations of $–CH_2$ groups of the 3MPA.

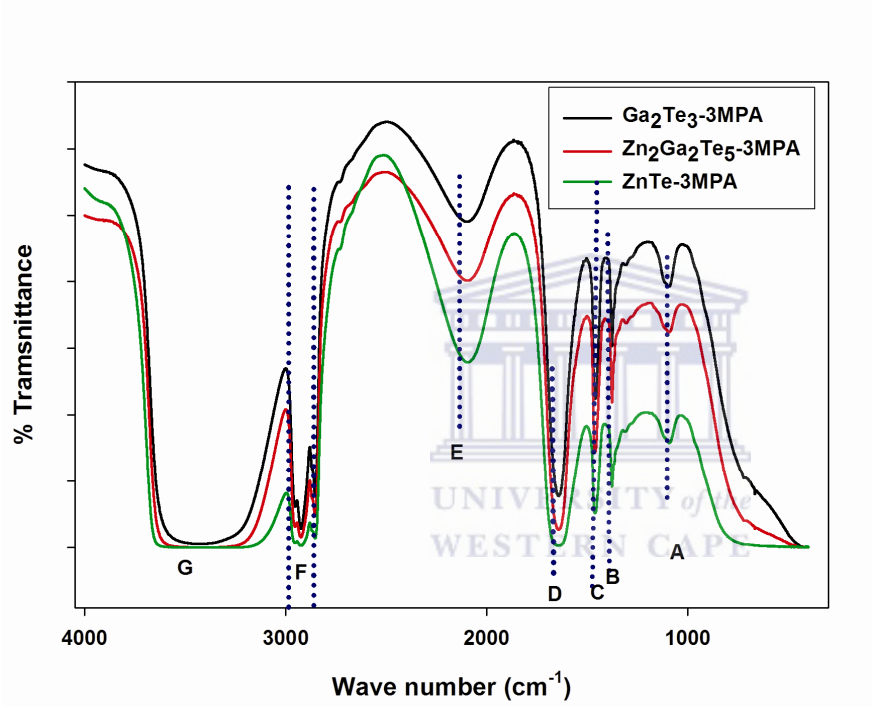

Figure 53: FTIR spectra of ZnTe-3MPA, Ga_2Te_3-3MPA and $Zn_2Ga_2Te_5$-3MPA quantum dots.

The bands associated with symmetric and asymmetric stretching vibrations of $–CH_2$ are also observed in all quantum dots in region F (2785 cm^{-1} to 2850 cm^{-1}). The stretching vibrations of –C=O are observed in D (1750 cm^{-1}) whereas the broad band in region G (around 3400 cm^{-1}) represents the stretching vibrations of the hydroxyl groups (-O-H) of the carboxylic acid part of

the 3MPA. The predominant vibration band of $-CH_2$ suggest clearly that 3MPA was successfully incorporated into the quantum dots as a capping agent.

5.2.4 X-ray diffraction spectroscopy (XRD)

XRD is a versatile, non-destructive technique that reveals detailed information about the chemical composition and crystallographic structure of natural and manufactured materials. The XRD patterns of ZnTe-3MPA quantum dots are shown in the figure below. The results indicate formation of a single phase ZnTe-3MPA quantum dot product.

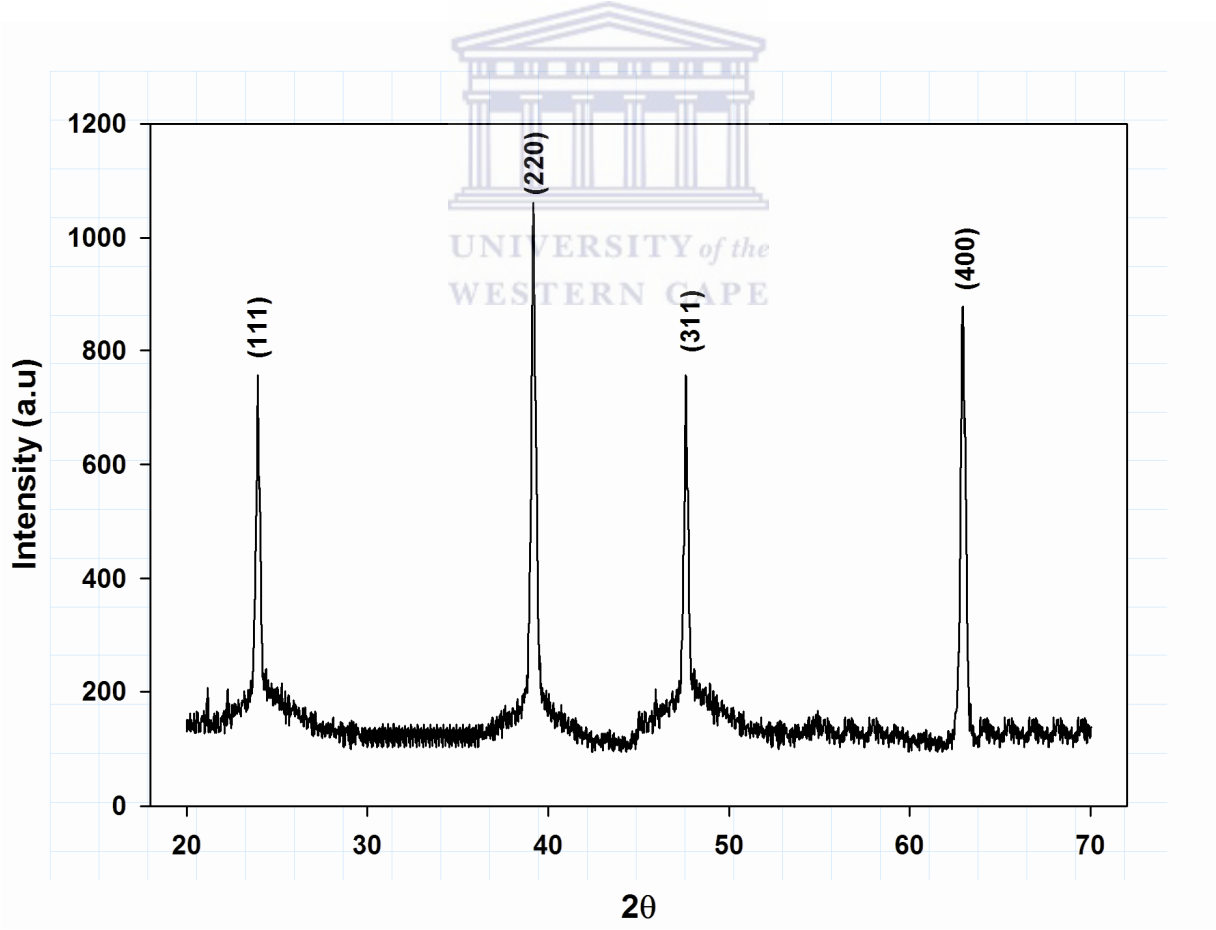

Figure 54: XRD patterns of ZnTe-3MPA quantum dots.

The XRD pattern of the ZnTe-3MPA showed the characteristic peaks of cubic system structure. The patterns display four characteristic diffraction peaks at 2θ values of approximately 25.5, 40 , 49 and 63 which were corresponded to the diffraction line produced by the (1 1 1), (2 2 0), (3 1 1) and (400) crystalline planes of ZnTe-3MPA

5.3 Microscopy telluride quantum dots

5.3.1 High resolution transmission electron microscopy

The transmission micrographs of $Zn_2Ga_2Te_5$-3MPA, Ga_2Te_3-3MPA and ZnTe-3MPA are shown in the figure below. Non- aggregated quantum dots with average diameters of 9.30 nm 6.80 nm and 5.30 for $Zn_2Ga_2Te_5$-3MPA, Ga_2Te_3-3MPA and ZnTe-3MPA respectively were observed. The HRTEM-estimated diameter of ZnTe-3MPA is in agreement with that calculated from its band edge absorption under UV-vis. The non-agglomeration of the quantum dots is a clear indication of successful capping by 3-MPA whereby electrostatic repulsion between the negatively dehydrogenated carboxylic acid groups keeps the quantum dots apart.

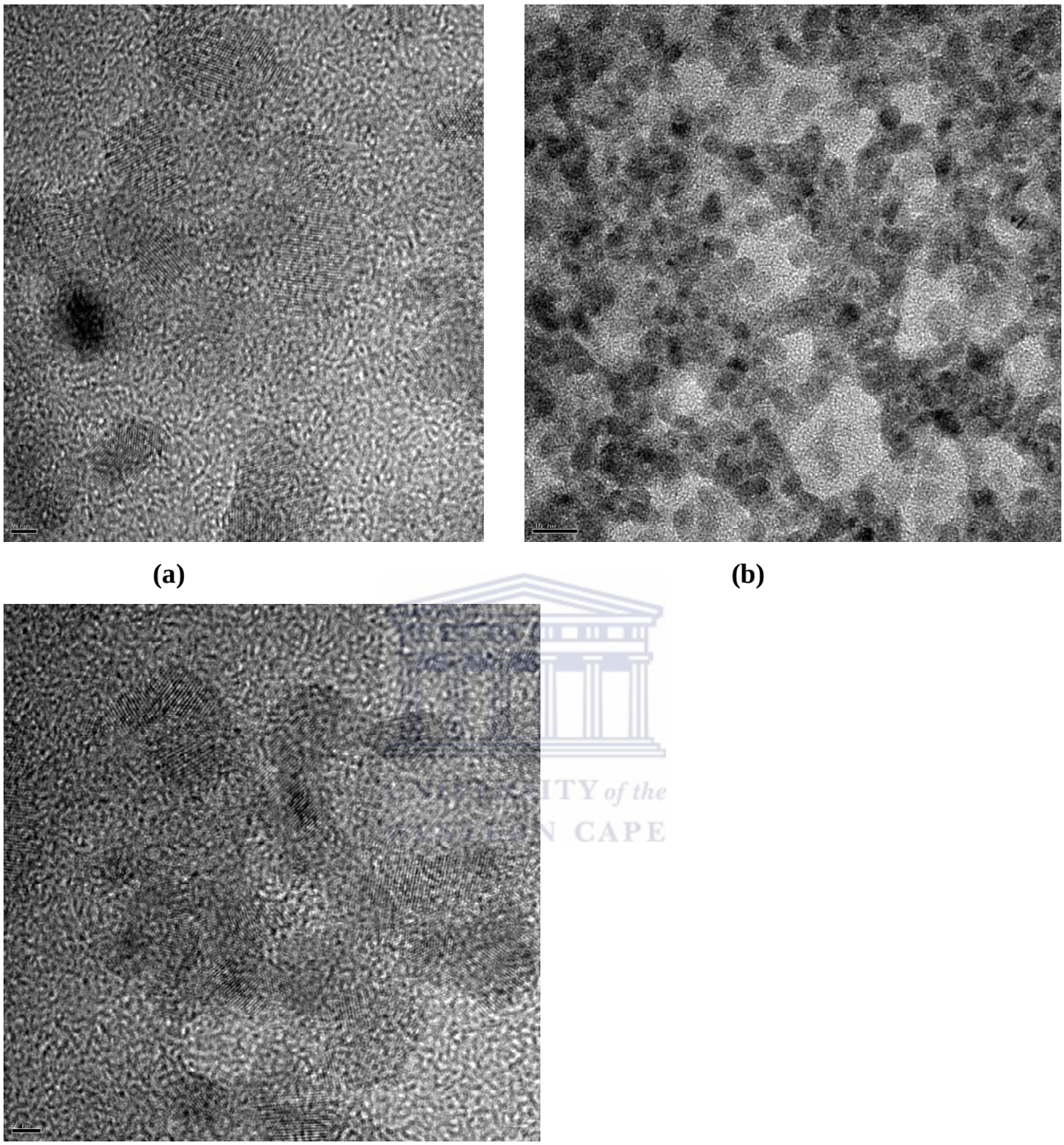

(a) **(b)**

(c)

Figure 55: HRTEM micrographs of (a) $Zn_2Ga_2Te_5$-3MPA, (b) Ga_2Te_3-3MPA and (c) ZnTe-3MPA.

This retention of the capping agent is in agreement with the FTIR results which showed vibrations characteristic to functional groups in the 3MPA. Lattice fridges depicting high crystalline of the materials are also evident in each micrograph.

5.3.2 Atomic force microscopy

The AFM images of the ZnTe-3MPA, $Zn_2Ga_2Te_5$-3MPA and Ga_2Te_3-3MPA quantum dots are shown in figures 56 (a), (b) and (c) below. While it is not easy to determine the exact size of the quantum dots based on AFM, the average size of the quantum dots appear to be on the order of a few nanometers.

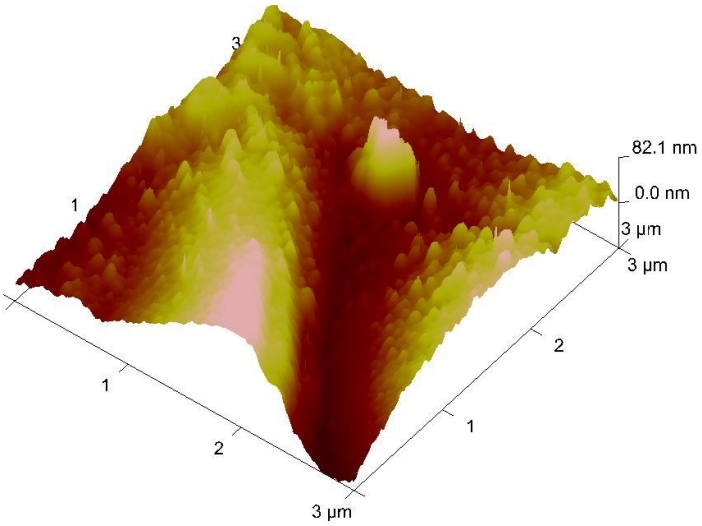

(a)

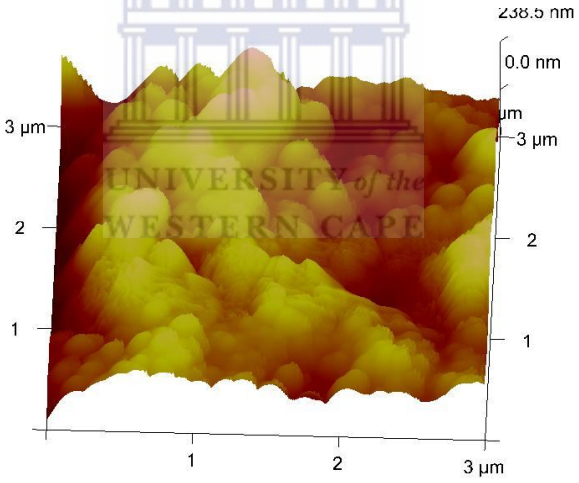

(b)

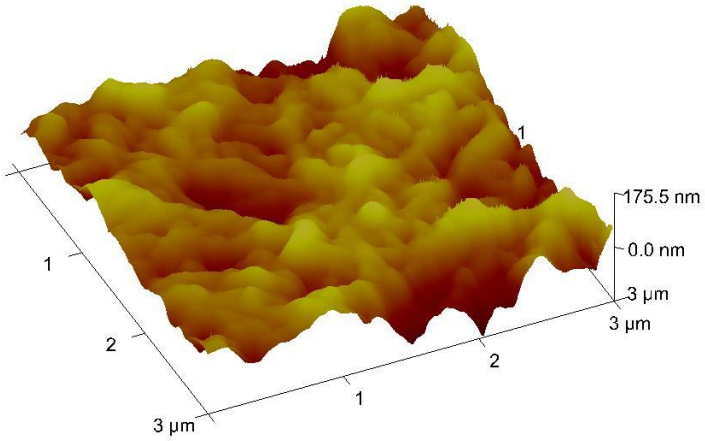

(c)

Figure 56: AFM images of (a) ZnTe-3MPA, (b) $Zn_2Ga_2Te_5$-3MPA and (C) Ga_2Te_3-3MPA.

It is however observable that significant size differences occur in the three types of quantum dots in the order ZnTe-3MPA, Ga_2Te_3-3MPA and $Zn_2Ga_2Te_5$-3MPA (from the smallest to the largest). This is consistent with the observations made using HRTEM.

5.4. Sub conclusions

The electron transfer rate constants for $Zn_2Ga_2Te_5$-3MPA, ZnTe-3MPA and Ga_2Te_3-3MPA are 19.5231 s^{-1}, 2.6588 s^{-1} and 3.8210 x 10^{-1} s^{-1} respectively. Thus, gallium-induced electrochemical enhancement in a ternary quantum dot system is evident. The electrochemistry of adsorbed telluride-ternary and binary quantum dots studied is largely influenced by their chemical composition. For the same reason given for the selenide-binary and ternary quantum dot/nanocrystals, the optically evaluated telluride band gaps are not in agreement with the

electrochemically evaluated telluride band gaps. Dangling bonds resulting from interstitial gallium valencies are found to lower the photoluminescence intensity in $Zn_2Ga_2Te_5$-3MPA. HRTEM and AFM also shows that the size of telluride quantum dots increases in the order ZnTe-3MPA (5.30 nm), Ga_2Te_3-3MPA (6.80nm) and $Zn_2Ga_2Te_5$-3MPA (9.30 nm). Gallium does not therefore seem to enhance the optical properties or decrease the size of the telluride quantum dots. FTIR confirms retention of the capping agent on the quantum dot surface.

CHAPTER 6

Results and Discussion 3: A potential masking approach in the detection of dopamine on 3-mercaptopropionic acid capped ZnSe quantum dots modified gold electrode in the presence of interferences.

6.1 Introduction

Dopamine (DA) is one of the most important catecholamine neurotransmitters in mammals that play crucial roles in the functioning of cardiovascular, renal, hormonal and central nervous system [291]. Loss of DA is associated with neurological disorders such as Parkinson's disease [292]. DA acts like a brain chemical to transmit messages to parts of the brain for coordination of body movement. Thus monitoring the DA levels can be an important marker for biomedical diagnosis. Among other methods which are based on spectroscopy and chromatography [293] for DA detection, electrochemical determination has an advantage owing due to the easy oxidizable nature of DA and cost. However, electrochemical detection has the challenge of eliminating interfering ascorbic acid and uric acid (also present in physiological fluid) because of the proximity in oxidation potential with DA [294]. At unmodified electrodes, dopamine, ascorbic acid (AA) and uric acid (UA) exhibit overlapping oxidation potentials while adsorption of oxidized products causes fouling [295]. Electrodes are modified to enhance response or selectivity towards a particular substrate. Materials such as redox polymers [296-297], dendrimers [138], nanoparticles [139, 298] are commonly used to prepare modified electrodes. In the analysis of dopamine in particular, gold nano film [299] carbon electrode modified with polyglycine [300], poly(acid chrome blue K) [292] and others [291, 301-302]

have recently been reported. In the preparation of modified electrodes, a unique class of nanoparticles called quantum dots are now emerging.

Quantum dots are semiconductor nanocrystals that range from 2 to 10 nm in size. They possess size-tunable optical and electronic properties. Their quantum size effects give rise to excellent electrical, optical and electrochemical properties, such as change of electrochemical potential of band edge [11]. Quantum dots have found potential applications in several areas, including catalysis, coatings, textiles, data storage, biotechnology, health care, biomedical, pharmaceutical industries and most recently, in bioanalytical chemistry [303]. When suitably functionalized with amphiphilic bifunctional molecules such as marcapto carboxylic acids [HS-$(CH_2)n$-COOH, n=1-15] [10], the small sizes of quantum dots can allow for rapid transfer of electrons to the surface of the target particles, resulting to a higher charge detaching efficiency [11]. Short chained capping agents such as mercaptopropionoc acid (MPA) have been used for self assembly on gold electrode [12] and are associated with enhanced electrochemical signals of the quantum dots towards target analytes [13]. Most applications of quantum dots in analytical purposes make use of their fluorescent properties [304-305]. Although quantum dots show excellent electrochemical properties when properly functionalized, their use in electrochemical systems for analytic purposes are at the onset [11, 88, 128]. ZnO semiconductors electrodeposited on the surface of a glassy carbon electrode for determination of DA in presence of AA and UA with a detection limit of 0.50 μM have been reported [306]. A gold electrode modified with 3-mercaptopropionic acid capped zinc selenide quantum dots for determination of DA in presence of excess interferences is presented.

Figure 57 depicts the enhancing effect of the Au/ZnSe-3MPA on the oxidation of DA. A well pronounced redox couple (**a/a′**) with peak separation of 61 mV is observed on the quantum dot modified electrode as compared to the weak redox pair of over 300 mV peak separation on the bare gold electrode. This peak enhancement is attributed to the following: i) electrostatic attraction between cationic dopamine and anionic quantum dot, (ii) high surface area and (iii) high conductivity of quantum dots. Modifying Au electrode with ZnSe-3MPA quantum dots therefore induced improved reversibility of electron transfer process, and consequently an efficient redox reaction towards dopamine at the Au/ZnSe-3MPA electrode.

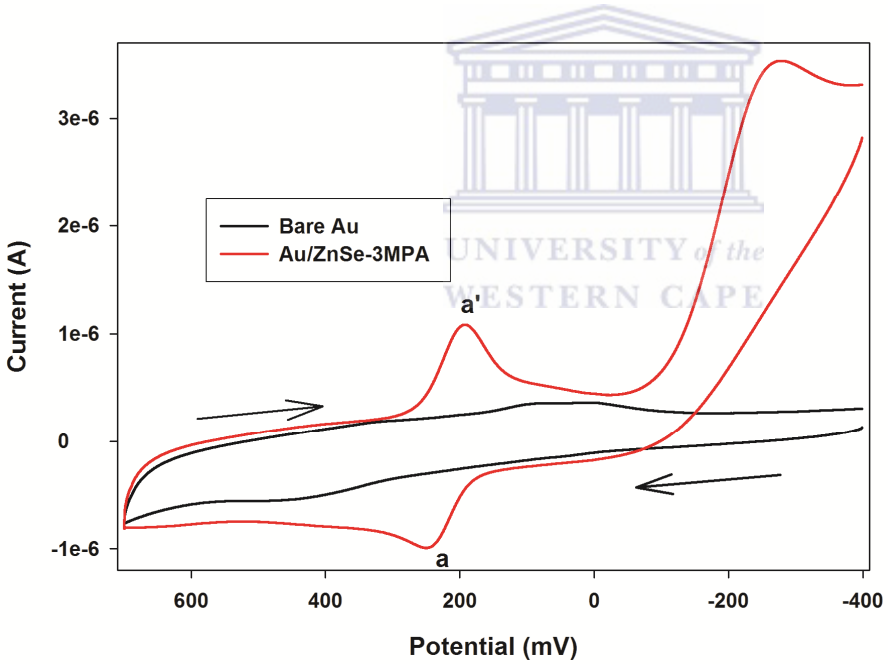

Figure 57: Cyclic voltammograms of 50 µM of dopamine on bare Au and Au/ZnSe-3MPA electrodes in phosphate buffer, 40 mV/s scan rate.

Quantitative evaluation of the observed potential shift (Fig. 57) using partition coefficient (K_{bare} and $K_{ZnSe\text{-}3MPA}$), to describe the interaction of DA with a bare gold and Au/ZnSe-3MPA electrodes, according to equation 39 [307] gave 1.15×10^{-7}.

$$E_{p,ZnSe-3MPA} - E_{p,bare} = \frac{RT}{nF} \ln \frac{K_{ZnSe-3MPA}}{K_{bare}} \qquad (39)$$

(where n =2, is the number of electrons transferred during oxidation of dopamine. F is the Faraday constant (96,584 C mol^{-1}), R is the gas constant (8.314 J $mol^{-1}K^{-1}$) and T is Kelvin temperature (298 K). This high ratio implies increased accumulative ability of the ZnSe-3MPA towards DA which further supports the reason for the higher peak current observed in figure 57.

The Au/ZnSe-3MPA electrode was also used in the oxidation of AU and AA separately. It can be seen from figure 58 that oxidation peaks of UA (430 mV, peak **b**), AA (593 mV, peak **c**) and DA (252 mV, peak **a**) are well defined. However, UA, and AA are irreversible as denoted by the absence of a corresponding cathodic peak. Thus the electro-oxidation of these three substrates occurs on the Au/ZnSe-3MPA electrode. Of interest is the oxidation potential of AA which occurred at 593 mV, contrary to ca 100 mV reported by previous studies [161, 292, 295, 308-310]. This anodic shift can be attributed to electrostatic repulsion between ascorbate anions [311] and negatively charged surface of the modified Au electrode which reduced the accumulative ability of the ZnSe-3MPA modifier towards ascorbic acid.

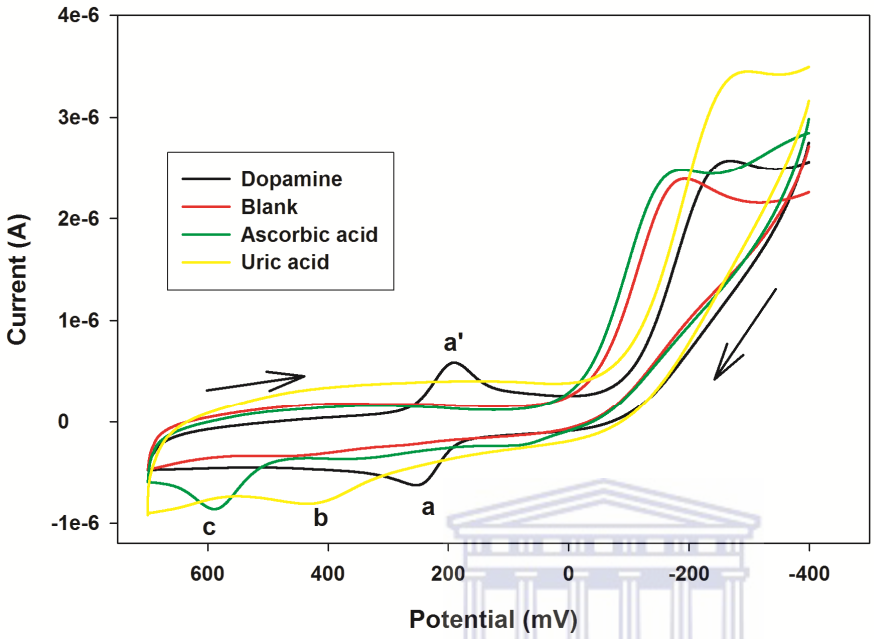

Figure 58: Cyclic voltammograms of overlay of 50 µM of DA, 50 µM UA and 50 µM AA, and blank on Au/ZnZe-3MPA electrodes in phosphate buffer, 40 mV/s scan rate: Peaks a, b and c are the oxidation peaks of DA, UA and AA respectively while peak a′ is the reduction peak of DA.

The interfacial kinetics of these substrates at the Au/ZnSe-3MPA electrode resulted into large oxidation peak potential differences between AA and DA (178 mV), and between UA and AA (163 mV), which set a premise for simultaneous detection of DA, AA and UA in a mixture of the three.

6.2 Electrochemical determination of dopamine in uric acid and ascorbic acid mixture on ZnSe-3MPA modified gold electrode

Using a narrower potential window of 0 to 700 mV (so as to exclude to the -267 mV quantum dot characteristic peak (Fig. 57)) voltammetric responses of a mixture of DA, UA and AA on the Au/ZnSe-3MPA electrode were measured (Fig. 59). Well resolved electrochemical responses attributed to 20 µM DA, 200 µM UA and 500 µM components similar to that recorded individually (Fig. 58) are shown in figure 59 (cyclic voltammetry) and figure 60 (Square wave voltammetry).

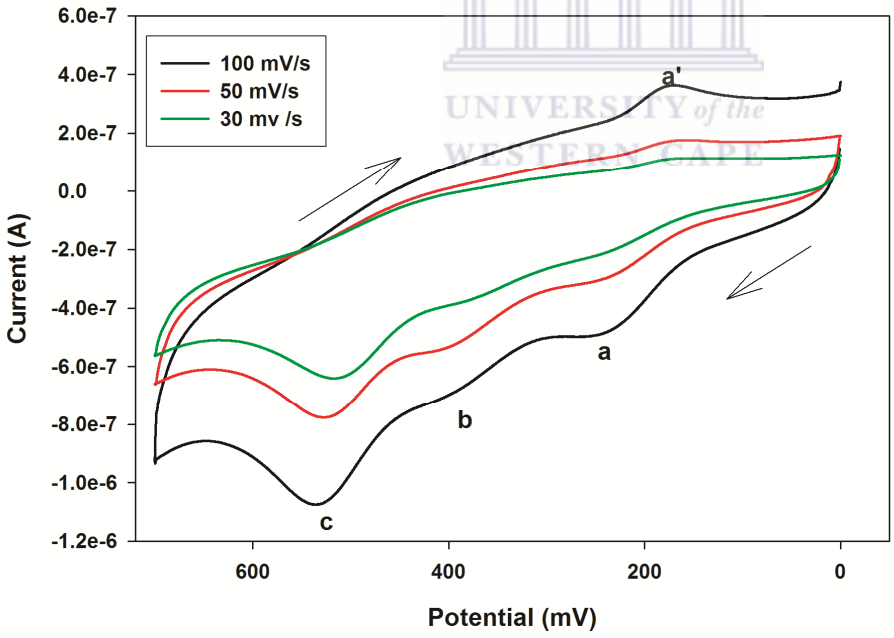

Figure 59: Cyclic voltammograms of a mixture of 20 µM DA, 200 µM UA and 500 µM AA on Au/ZnSe-3MPA electrode in a phosphate buffer, scan rates 30, 50 and 100 mV/s: Peaks a, b and c are the oxidation peaks of DA, UA and AA respectively while peak a′ is the reduction peak of DA.

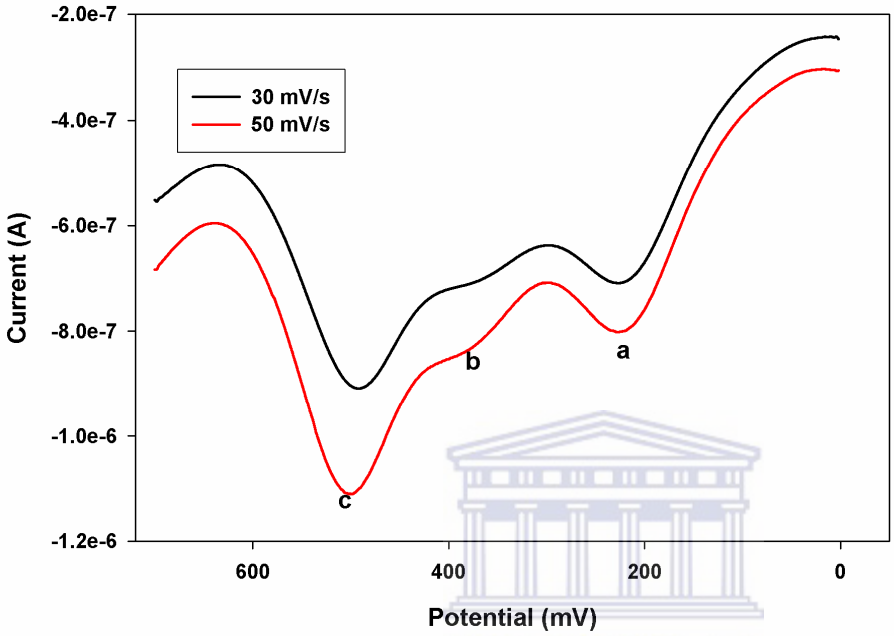

Figure 60: Anodic Square wave voltammograms of a mixture of 20 µM DA, 200 µM UA and 500 µM AA on Au/ZnSe-3MPA electrode in a phosphate buffer, scan rates 30 and 50 mV/s: Peaks a, b and c are the oxidation peaks of DA, UA and AA respectively.

Thus simultaneous determination of DA, UA and AA is feasible on the Au/ZnSe-3MPA electrode. Since the peak separation between DA and its closest electro-oxidizable compound (UA) is large enough for complete oxidation of DA to take place, the potential window was further narrowed to 0 - 400 mV. At this potential range, the electrochemistry of UA and AA is completely masked. It was observed that, only the DA peaks, which increased proportionately with increasing concentration, were observed for both square wave and cyclic voltammetry (Figs 61 and 62). From the SWV data, a linear DA concentration range of 3.00 x 10^{-8} M to 1.70 x10^{-7}

M (R^2=0.98) with sensitivity of 2.14 x 10^{-5} A/µM and a detection limit of 2.43 x 10^{-10} M (3SD, n=8) was calculated.

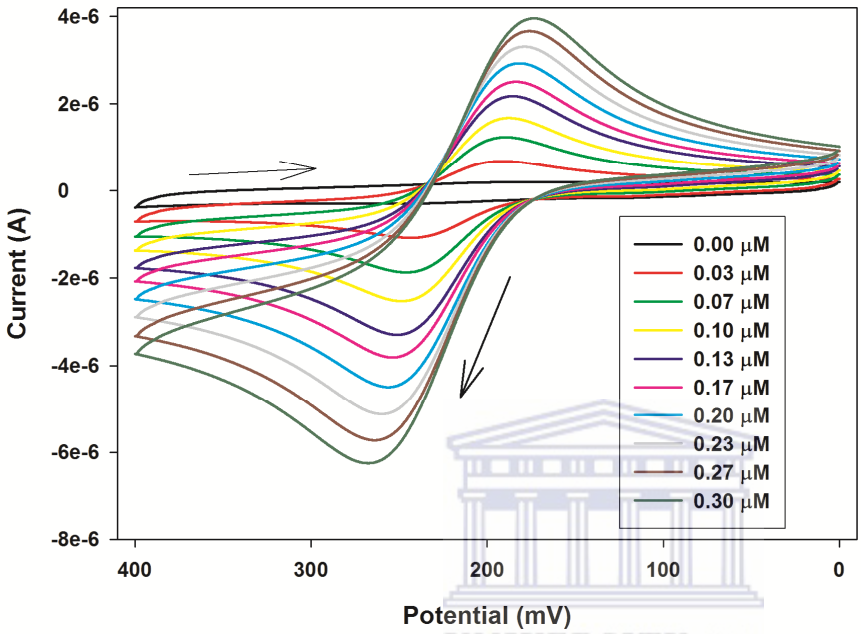

Figure 61: Cyclic voltammetric response of different DA concentrations in the presence of 200 µM UA and 500 µM AA, on a Au/ZnSe-3MPA electrode in phosphate buffer, 40 mV/s scan rate.

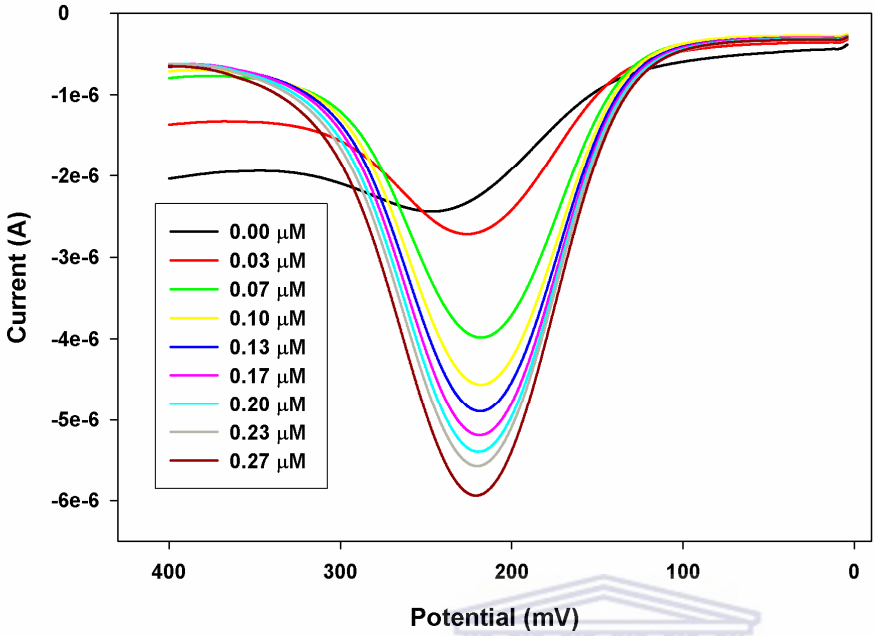

Figure 62: Anodic square wave voltammetric response of different DA concentrations in the presence of 200 µM UA and 500 µM AA, on a Au/ZnSe-3MPA electrode in phosphate buffer, 40 mV/s scan rate.

The occurrence of only DA peaks clearly indicated that the electroactivity of both AA and UA was successfully eliminated. These results show that, by narrowing the potential window, a Au/ZnSe-3MPA electrode can allow electrochemical "masking" of UA and AA, and afford significant detection of DA in presence of excess UA (> 6,500 times higher) and AA (>16,000 times higher). As control experiments, in the presence of a mixture of 0.1 µM DA + 500 µM AA + 200 µM, further additions of different volumes of 1 mM AA (Fig. 63) and UA (Fig. 64) did not alter or interfere with the electrochemical signal observed for dopamine. These further demonstrate the suitability of the potential masking approach.

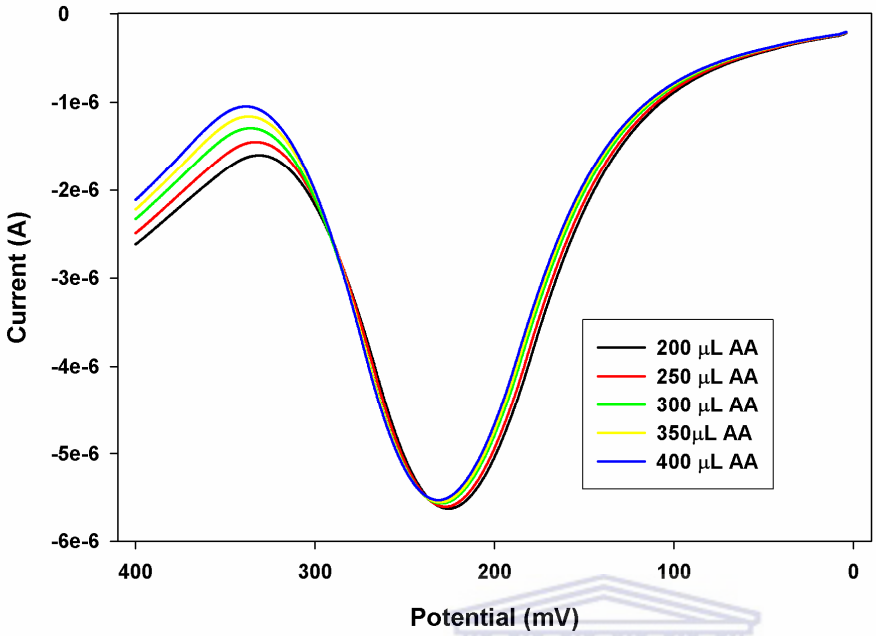

Figure 63: Anodic Square wave voltammetric response of DA in mixture of 0.1 µM DA + 500 µM AA + 200 µM UA, with further additions of increasing volumes from 1 mM AA stock solution in phosphate buffer, 40 mV/s scan rate.

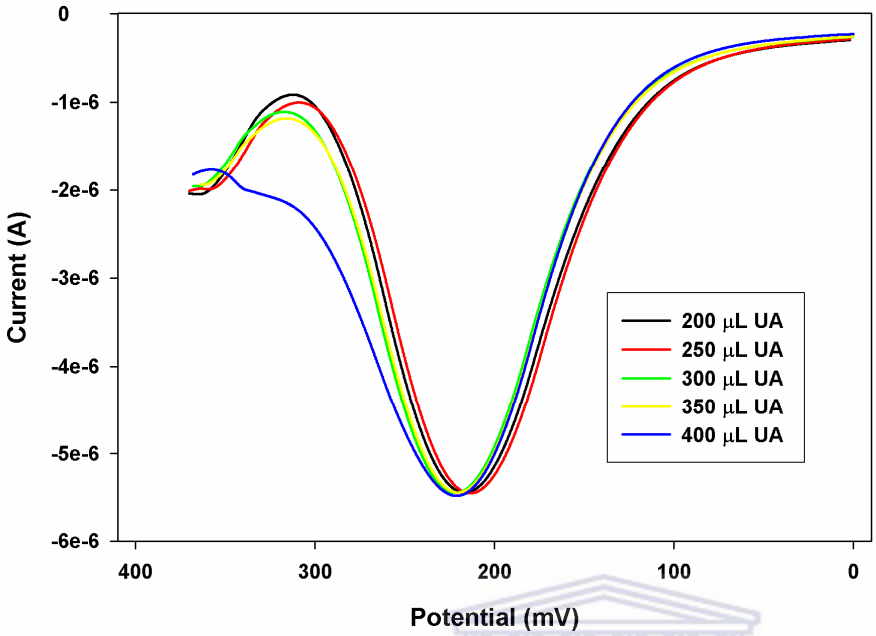

Figure 64: Anodic Square wave voltammetric response of DA in mixture of 0.1 µM DA + 500 µM AA + 200 µM UA, with further additions of increasing volumes from 1 mM UA stock solution in phosphate buffer, 40 mV/s scan rate.

The amperometric response of DA (in the mixture) at a fixed potential of 252 mV on the Au/ZnSe-3MPA electrode was also examined in order to determine the response time of the sensor as well as to compare its detection limit with that obtained from square wave voltammetry. From the steady state amperogram (Fig. 65), successive additions of DA resulted in favourable responses on the Au/ZnSe-3MPA electrode, achieving steady state within 8 seconds. The dependence of current response on DA concentration as shown in the calibration curve (Fig. 65 inset) was linear in range 3.30 x 10^{-8} M to 3.30 x10^{-7} M (R^2=0.99), with a sensitivity of 9.18 x10^{-6} A/µM and a detection limit of 5.65 x 10^{-10} M (3SD, n=8). Steady state amperometry shows a shorter response time and wider linear ranger but a lower detection limit

when compared to the square wave. However the detection limits obtained for both techniques are far much lower than the concentration of DA in human blood, 1.31 x 10^{-9} M [312].

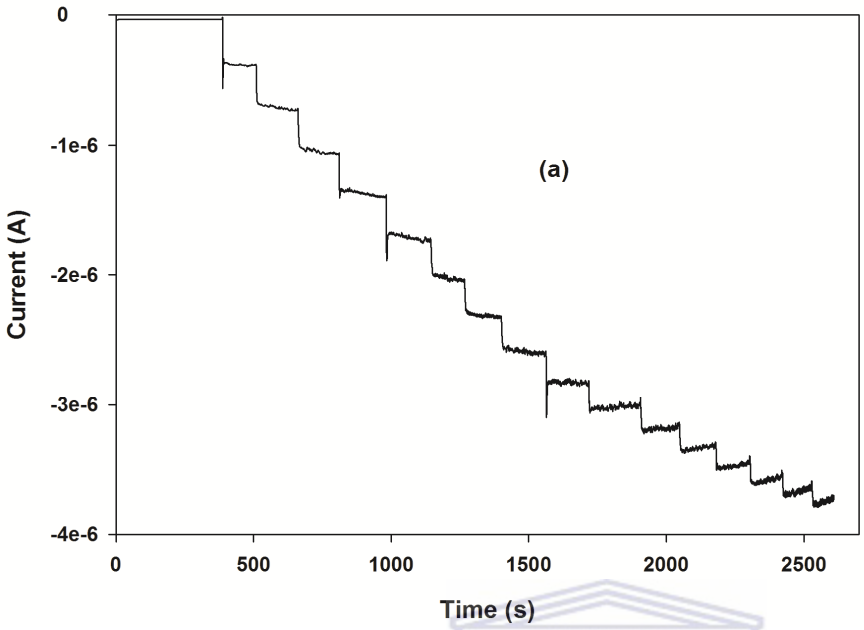

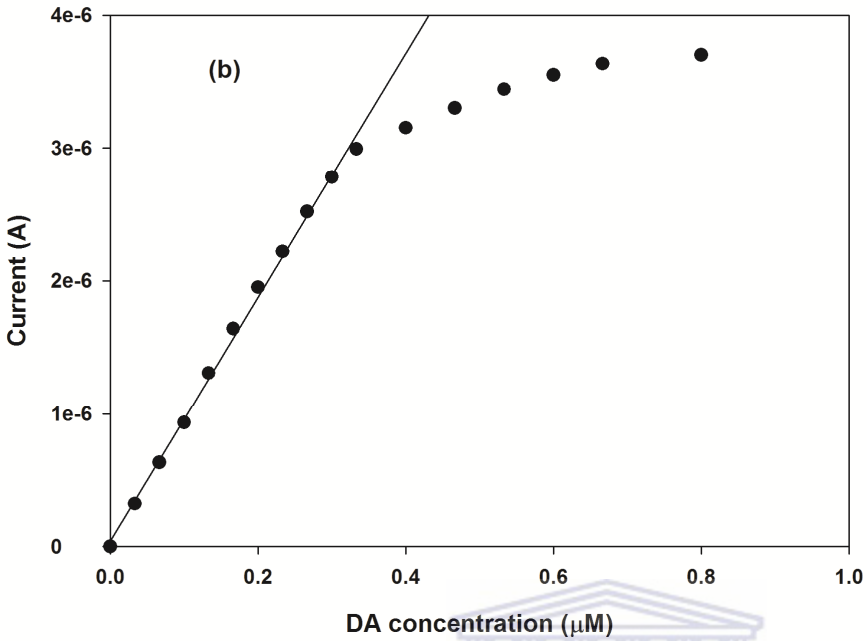

Figure 65: Amperometric response (a) and calibration curve (b) of DA (concentration range of 0.00 to 0.80 µM) on a Au/ZnSe-3MPA electrode in phosphate buffer.

6.3 Sub conclusion

In this chapter, the preparation of ZnSe-3MPA quantum dot modified gold electrode for analytical application is demonstrated. The nanoelectrode was used to detect dopamine in presence of excess ascorbic and uric acids interferences. The interfacial kinetics of these substances on quantum dots afforded the use of a novel potential masking approach where only dopamine was electroactive. With this approach a dopamine detection limit of 2.43 x 10^{-10} M (SWV) and 5.65 x 10^{-10} M (steady state amperometry) with fast response time was achieved.

CHAPTER 7

Results and Discussion 4: Impedimetric response of a label-free genosensor prepared on a 3-mercaptopropionic acid capped gallium selenide nanocrystal modified gold electrode.

7.1 Introduction

Metal selenide semiconducting nanoparticles produced from groups III and VI elements have attracted a lot of research attention due to their potential use as alternatives to nanomaterials from groups II and VI used in electrical, nonlinear optical, optoelectronic and photovoltaic devices [263]. Synthesis of gallium selenide has been achieved through molecular beam epitaxy [313], vapour phase epitaxy [314], chemical vapour deposition (CVD) [315], heterovalent exchange reaction involving groups V and V elements [316], thermal evaporation [317] and chemical close-spaced vapour transport [318], among others. These methods give rise to water insoluble and bio-incompatible materials that cannot find applications in bioanalytical chemistry. Synthesis of water soluble and bio-compatible gallium selenide nanocrystals would therefore open the applications of these materials in several areas including biotechnology, health care, biomedical and pharmaceutical industries as well as in bioanalytical chemistry. Water soluble gallium selenide nanocrystals have not been explored due to the rare cationic chemistry of aqueous Ga^{3+}. Whereas compounds of gallium in its univalent oxidation state have been reported [235], details of cationic existence of Ga^{3+} are scanty. In this work, the reaction between hot perchloric acid and gallium, according to equation 24 (refer to section 3.3.1.2), is presented as a source of Ga^{3+} for synthesis of gallium selenide nanocrystals (NCS).

Short amphiphilic bifunctional molecules such as mercaptopropionoc acid (MPA) are suitable capping materials for nanocrystals since they allow bioconjugation, solubilization, rapid transfer of electrons and enhanced electrochemical responses of the nanocrystals to target analytes [13]. Although nanocrystals show excellent electrochemical properties when functionalized, their use in electrochemical systems for analytic purposes has been very limited [11, 88, 128].

The detection of transgenic DNA in food products made from genetically modified organisms (GMOs) has recently become one of the mostly requested DNA-sensor applications. [208, 319]. This is due to: (i) the potential alterations in nutritional composition of GMO food and the functions of non-targeted genes; (ii) allergenicity or toxicity of the genetically modified product; and (iii) the possibility of horizontal gene transfer to non-targeted species and to the environment [19]. Recombinant DNA from GMOs has been found in air [22, 24], soil [25, 320-321] as well as in the food chain [26-27, 322-325]. The gene 5-enolpyruvylshikimate-3-phosphate synthase (CP4 epsps) is commonly used in genetic engineering of crops as a vector gene to confer glyphosate resistance in transgenic plants. In many parts of the world, legislations have been put in place to regulate the presence of genetically modified organisms in crops, foods and ingredients [16]. This has necessitated development of sensitive and reliable methods for detection, identification and quantification of genetically modified organisms (GMOs) in processed food. Various methods including quartz crystal microbalance [326-327], surface plasmon resonance [328-329], fluorescence [330] and electrochemistry [331] have been reported for DNA detection. Among these methods, electrochemical detection of DNA has received extensive attention due to its high sensitivity, excellent selectivity, simple instrumentation, rapidity and low production cost [32, 133, 174, 332]. Most electrochemical DNA biosensors are based on electrical transduction of DNA hybridization by an accompanied accumulation of redox

compounds such as dyes (methylene blue [44-45]) or metal complexes (ruthenium and osmium complexes [46]) at the DNA-modified electrode surface [43]. The hybridization reaction can be monitored by intrinsic signals of nucleic acids or electroactive labels such as enzymes and metal nanoparticles covalently bound to the target DNA [47-48] or by changes in interfacial properties [32, 333] such as conductance, resistance [334-336] and capacitance [335]. Electrical resistance and capacitance are sensitive indicators of surface properties and are suitable for the interrogation of DNA hybridization by electrochemical impedance spectroscopy (EIS) technique. This work reports a label-free impedimetric genosensor prepared on gold electrode that is modified with 3-mercaptopropionic acid-capped gallium selenide nanocrystals. The gallium selenide nanocrystals were used to create a large surface area on the electrode surface which ensured high loading of the probe DNA and improved rate of DNA hybridization on the electrode.

7.2 Impedimetric characteristics of the DNA modified electrode

Figure 66 below depicts the Bode (a) and Nyquist (b) plots for bare Au, Au|Ga_2Se_3-3MPA, Au|Ga_2Se_3-3MPA |ssDNA and Au|Ga_2Se_3-3MPA|dsDNA, all in 5 mM $Fe(CN)_6^{3-/4-}$. The Bode plots show remarkable differences in the electrochemistry of the Au|Ga_2Se_3-3MPA|ssDNA-$Fe(CN)_6^{3-/4-}$ and Au|Ga_2Se_3-3MPA|dsDNA-$Fe(CN)_6^{3-/4-}$ interfaces. The absolute phase angle increases from 49° (Au|Ga_2Se_3-3MPA|ssDNA) to 60° (Au|Ga_2Se_3-3MPA|dsDNA), accompanied by respective shift in the frequency at maximum phase (ω_{max}) from 316 Hz to 200 Hz. This indicates decrease in conductivity at the Au|Ga_2Se_3-3MPA|dsDNA-$Fe(CN)_6^{3-/4-}$ interface. It can be explained by the accumulation of negative charge from the DNA backbone

after hybridization which caused a higher barrier for the negatively charged $Fe(CN)_6^{3-/4-}$ anions and impeded the redox conversion at the electrode.

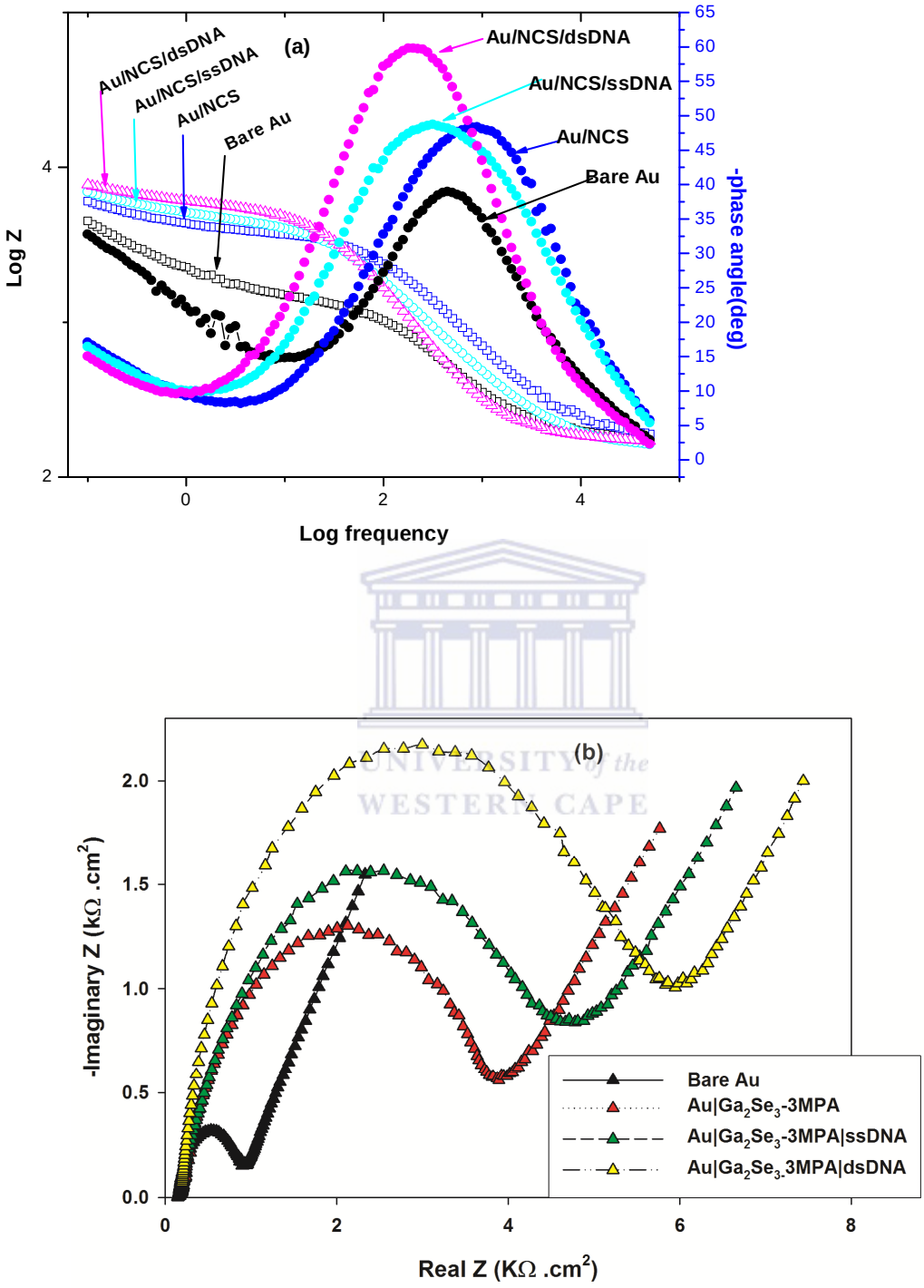

Figure 66: Bode (a) and Nyquist (b) plots of bare Au, Au|Ga_2Se_3-3MPA, Au|Ga_2Se_3-3MPA|ssDNA and Au|Ga_2Se_3-3MPA|dsDNA, all in 5 mM $Fe(CN)_6^{3-/4-}$.

From the Nyquist diagram, the diameters of the observed semicircles gave a first estimate of the charge transfer resistances, R_{ct}, at the two interfaces. The R_{ct} values were obtained by fitting EIS using a simple Randle's equivalent circuit (Refer to Fig 16). Compared with the Au|Ga_2Se_3-3MPA electrode, the Au|Ga_2Se_3-3MPA|ssDNA shows larger R_{ct} (3548 Ω, % error = 2.091), an indicative of electrostatic repulsion between the polyanionic backbone of ssDNA and the anionic $Fe(CN)_6^{3-/4-}$. Hybridization with 20 nM complementary DNA induced a further increase in R_{ct} to 4436 Ω (% error = 2.742), implying increase in negative charge at the surface of the electrode. All the impedimetric spectra in this figure 66 (b) above are characterized by one semicircle, an indication of one redox reaction taking place. For the Au|Ga_2Se_3-3MPA|dsDNA, the R_{ct} of the $Fe(CN)_6^{3-/4-}$ reports the dsDNA|$Fe(CN)_6^{3-/4-}$ interfacial kinetics. R_{ct} was therefore taken as the analytical parameter for the impedimetric detection of the target DNA.

7.3 Analytical performance of the impedimetric genosensor

Figure 67 shows the Nyquist plots obtained with the Au|Ga_2Se_3-3MPA|ssDNA electrode after dipping it into a stirred solution (0.100 M PBS, pH 7.40) containing different concentrations of the target DNA while holding the potential at 500 mV for 6 min.

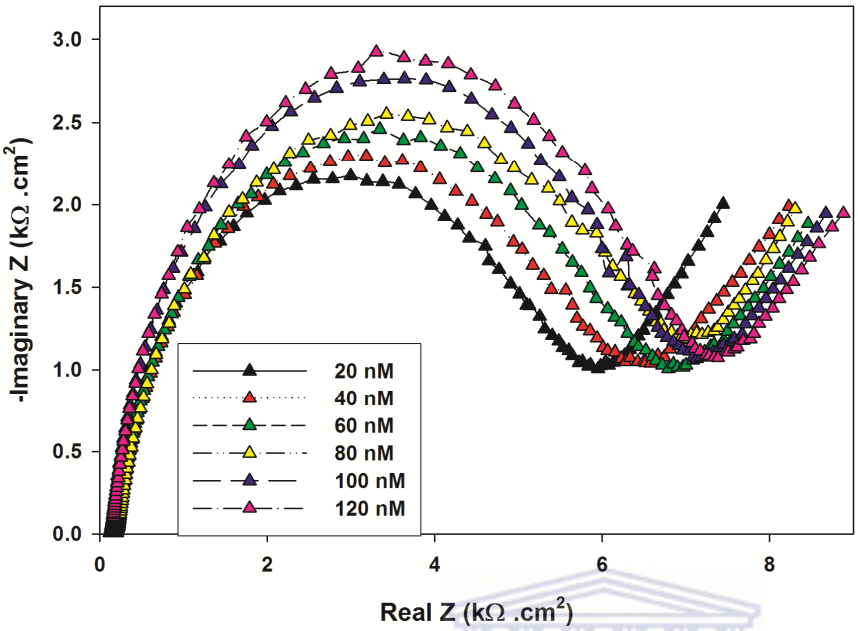

Figure 67: Nyquist plots of Au|Ga_2Se_3-3MPA|ssDNA electrode at different concentrations of the target DNA in 5 mM $Fe(CN)_6^{3-/4-}$.

The R_{ct} values increased with increasing concentration of the target DNA in the hybridization reaction. The change in the R_{ct} (ΔR_{ct}) defined as ΔR_{ct}= R_{ct}(dsDNA) - R_{ct}(ssDNA) was linear with the logarithm of the concentration of the target DNA within a concentration range from 20 to 140 nM (Fig. 68). The sensitivity of the genosensor was found to be 11.610 Ω/nM (r^2 = 0.999) and a

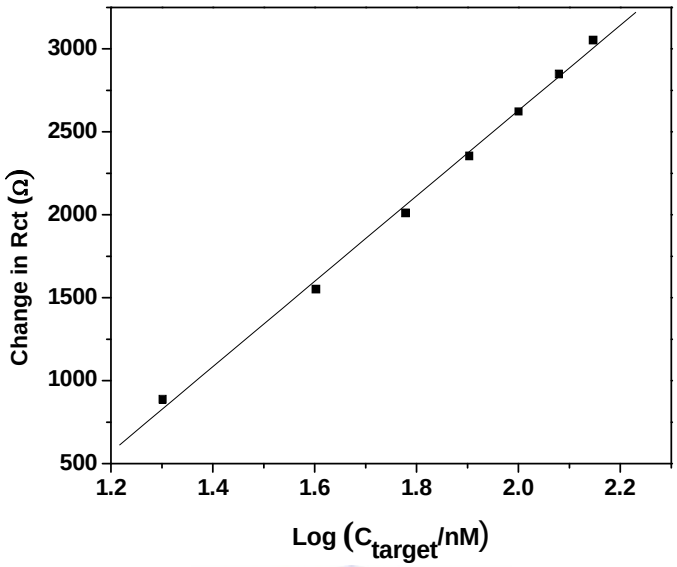

Figure 68: Calibration plot for the genosensor

detection limit of 0.660 nM (3SD, n = 8). The stability of the Au|Ga_2Se_3-3MPA|ssDNA genosensor was studied by measuring its impedimetric response to 100 nM target DNA concentration at different storage intervals for one month, storing it in PBS, pH 7.40 at 4 °C between the measurements. It was found to lose 28 % of its response within this time. We also prepared different Au|Ga_2Se_3-3MPA|ssDNA genosensors and measured individual impedimetric responses to a constant concentration of 100 nM target DNA after different storage times up to one month (1, 5,10, 15, 20, 25 and 30 days) and recorded a 17% loss in its response. Reproducibility studies were done by measuring the impedimetric responses of ten freshly prepared genosensors to 100 nM target DNA. An average change in R_{ct} of 2620 Ω was observed with a standard deviation of 2.36 Ω.

7.4 Discrimination among complementary, non-complementary and 3-base mismatched target sequences.

Figure 69 shows results obtained in the hybridization experiments performed to discriminate impedimetric signals among complementary, non-complementary and 3-base mismatched target sequences. The results are presented as the relative R_{ct} variation between the values obtained due to DNA hybridization or adsorption, and the values obtained due to the bare electrode are shown. The relative variation is represented as a ratio of delta increments according to the following equations 40a, 40b and 40c

$$\Delta_{Ratio} = \frac{\Delta R_{ct}(Sample)}{\Delta R_{ct}(Probe)} \quad (40a)$$

$$\Delta R_{ct}(Sample) = R_{ct}(Sample) - R_{ct}(Bare\ electrode) \quad (40b)$$

$$\Delta R_{ct}(Probe) = R_{ct}(Probe) - R_{ct}(Bare\ electrode) \quad (40c)$$

A Δ_{Ratio} value greater than 1 implies that ΔR_{ct} (Sample) > ΔR_{ct} (Product) and is an indicator of hybridization reactions. A Δ_{Ratio} value close to 1 implies that ΔR_{ct} (Sample) $\approx$ ΔR_{ct} (Product) and is an indicator of nonhybridization reactions or nonspecific adsorption [208].

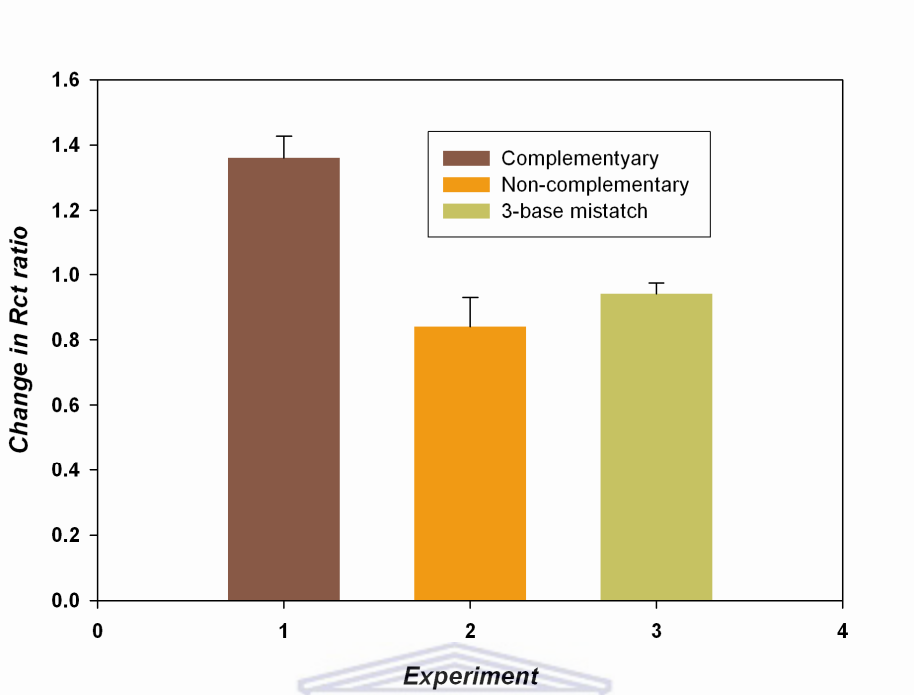

Figure 69: Ratio of the charge transfer after hybridization with complementary, non complementary and 3-base mismatch sequences, each at 100 nM concentration. Error bars correspond to triplicate experiments.

Hybridization with the complementary DNA gave a Δ_{Ratio} value greater than 1, an indication of a large ΔR_{ct}, induced by specific hybridization reaction between the probe DNA and the complementary DNA. The 3-base mismatch experiment gave a much lower value than the complementary. This is attributed to significantly low hybridization efficiency due to presence of 3 mismatches in the sequence. The value was also slightly higher than the non complementary, indicating that a certain degree of affinity interaction took place in spite of the three mismatches.

7.5 Sub conclusion

In this chapter, the application of genosensor based on novel water soluble and biocompatible Ga_2Se_3-3MPA nanocrystals is demonstrated. A label free impedimetric genosensor fabricated on the nanocrystal modified gold electrode exhibited high sensitivity towards the target DNA (sensitivity = 11.61 Ω/nM) with a detection limit of 0.66 nM (3SD, n = 8). It was able to discriminate between complementary, non-complementary and 3-base mismatched target sequences and maintained 87 % of its response towards the target DNA after one month.

CHAPTER 8

Results and Discussion 5: Voltammetric response of a label-free genosensor prepared on a 3-mercaptopropionic acid capped zinc selenide quantum dot modified gold electrode.

8.1 Introduction

DNA biosensors are essential devices for the determination of nucleic acid fragments from humans, animals, plants, bacteria and viruses; permeating monitoring of food and water contamination caused by micro organisms, detection of genetic disorders, identification of species, tissue matching, forensic applications [32, 162]. Detection of specific sequence of transgenic DNA is one of the most recent and requested DNA-sensor applications in the detection of genetically modified organisms (GMOs) in foods [208]. At present, various methods including quartz crystal microbalance [326-327], surface Plasmon resonance [328-329] fluorescence [330], western blots [30], mass spectroscopy, near infrared spectroscopy, southern blots, lateral flow strips, polymerase chain reactions (PCR), enzyme linked immunosorbent essay (ELISA) or PCR-ELISA and electrochemistry [331] have been reported for DNA detection [31]. However, these methods vary in the degree of reliability, reproducibility, robustness, cost, complexity and speed among other key performance aspects. Furthermore, most of these methods may not be effective in all analytical circumstances. For example, ELISA methods rely on specific binding between an antibody and a protein and any conformational changes in the tertiary structure of the protein may render the method ineffective. Such conformational changes are likely to occur during food processing. On the other hand, electrochemical DNA biosensors

offer high sensitivity, small dimensions, high selectivity, and compatibility with micro fabrication technology and miniaturization of instruments [49]. Electrochemical detection of DNA is also associated with simple instrumentation, rapidity and low production cost [32, 133, 174, 332]. The detection methods for electrochemical DNA hybridization are classified into two major protocols; direct and indirect detections [37].

In direct electrochemical detection of DNA hybridization, the signal monitored arises from oxidation of guanine [38]. Up on hybridization of single strand probe DNA with its complementary single strand target DNA, two major events, which affect the extent of oxidation of guanine base, take place. First, the electrochemical signal emanating from oxidation of the probe's free guanine bases decrease upon hybridization with cytosine bases on the target DNA. This is because; guanine becomes less accessible for oxidation after formation of the duplex hybrid chain. The other possibility is that, the guanine oxidation signal may increase due to increase in the total number of guanine bases in the double strand DNA compared to the single strand DNA. Measuring the decreased guanine oxidation signal in the immobilized probe is very limited as it cannot be used to quantify target DNA containing guanine bases [40]. To overcome this, inosine modified probe DNA (free from guanine base) can be used. The inosine moiety is capable of forming a base pair with the cytosine residue of the target [41] and its oxidation signal is well separated from the guanine signal. Following hybridization, the duplex formation is detected by monitoring the appearance of the targets guanine signal. The guanine oxidation signal in this case increases upon hybridization. However, due to lack of probe's oxidation signal, it is difficult to follow up its signal as well as optimizing its immobilization conditions. Moreover, the introduction of an extra nucleotide (inosine) increases the biosensor preparation protocols and hence its cost. This can be improved by use of a probe which contains preferably

only one or few guanine bases with several cytosines. The presence of guanine base in the probe DNA provides weak guanine oxidation signal, which allows one to monitor probe immobilization and consequently optimize its immobilization on the electrode [37, 42]. The cytosine bases in the probe are available for hybridization with target DNA that contains several guanine bases, hence enhancing the electrochemical signal. On the basis of this approach guanine oxidation signal remarkably increases after hybridization of probe with DNA target and therefore, can be easily recorded.

Indirect electrochemical DNA biosensors are based on electrical transduction of DNA hybridization by an accompanied accumulation of redox compounds at the DNA-modified electrode surface [43]. These redox compounds include organic dyes such as methylene blue [44-45] and metal complexes involving cobalt, ruthenium and osmium [46]. The hybridization reaction can as well be monitored by intrinsic signals of nucleic acids, electroactive labels such as enzymes and metal nanoparticles covalently bound to the target DNA [47-48] or changes in interfacial properties [32]. A new class of surface functionalized semiconducting nanocrystals (quantum dots) for covalent coupling of biomolecules is at the onset. Quantum dots possess size-tuneable optical and electronic properties and have been one of the fastest moving and exciting interfaces of nanotechnology in the past decades. This is due to their potential applications in several areas, including catalysis, coatings, textiles, data storage, biotechnology, health care, biomedical, pharmaceutical industries and most recently, in bioanalytical chemistry [5]. The power and scope of electrochemically and optically modulated quantum dots can be greatly enhanced by coupling them with biological recognition reactions and electrical processes, to form nanobioelectronics. This coupling also requires proper surface tailoring and functionalization of the quantum dots, to make them biocompatible [15]. Surface tailoring of

quantum dots involve suitable functionalization with amphiphilic bifunctional molecules such as marcapto carboxylic acids [HS-(CH_2)*n*-COOH, *n*=1-15] [10]. These molecules permeate rapid transfer of electrons between the small sizes of quantum dots and the surface of the target particles, resulting to a higher charge detaching efficiency [11]. For instance, a 3-mercaptopropionic acid capped zinc selenide quantum dot modified gold electrode showed excellent electrocatalytic oxidation of dopamine as described in our previous work [250]. Besides improving the nanocrystal electrochemistry, the marcapto carboxylic acids leave free carboxylic acid groups on the surface of the quantum dots, which can covalently link favourably with amine groups of biomolecules, thus conferring biocompatibility properties on the quantum dots. Our previous report on enzyme-quantum dot bioconjugation showed that ZnSe-3MPA quantum dots were not only biocompatible but also provided a stable microenvironment for immobilization of CYP3A4 with high retention of its catalytic properties [249]. In view of their excellent electrochemical and bioconjugation properties, quantum dot-biopolymer conjugates have a great potential for DNA diagnostics and can have profound impact in analysis of DNA in genetically modified foods. In this work, we report voltammetric detection of 5-enolpyruvylshikimate-3-phosphate synthase (CP4 epsps) sequence specific DNA. CP4 epsps is a common vector gene in glyphosate resistant transgenic plants. The probe DNA was covalently coupled on surface functionalized ZnSe quantum dots, previously self assembled on a gold electrode. After hybridization with the target DNA, the electrochemical signal resulting from oxidation of quinine is taken as the analytical signal.

8.2 Electrochemical characteristics of the DNA modified electrode

A properly designed probe layer using a well defined surface chemistry is essential for DNA sensors for prevention non-specific binding or other side reactions so that a high selectivity for a specific target can be achieved. For a DNA sensor of faradaic nature, increased amount of the electroactive molecules on the sensing surface enhances the electrochemical transduction signal. The quantum dot modifier was used to create a nanostructured/nanoscaled platform whose large surface area increased the ssDNA binding sites and consequently high DNA loading. A high amount of DNA on the electrode surface would increase the rate of hybridization on the electrode. To optimize the amount of DNA immobilized on the Au|ZnSe-3MPA electrode, a series of SWV experiments were performed using different amounts (4, 6, 8, 10 and 12 µL) of 20 µM amine terminated probe DNA containing three guanine bases. The representative square wave voltammograms are shown in figure 70 below. An increase in guanine oxidation signal was observed to increase with increasing amount of 20 µM immobilized probe DNA from 4 µL to 10 µL. This was attributed to an increase in the number of guanine bases resulting from high surface

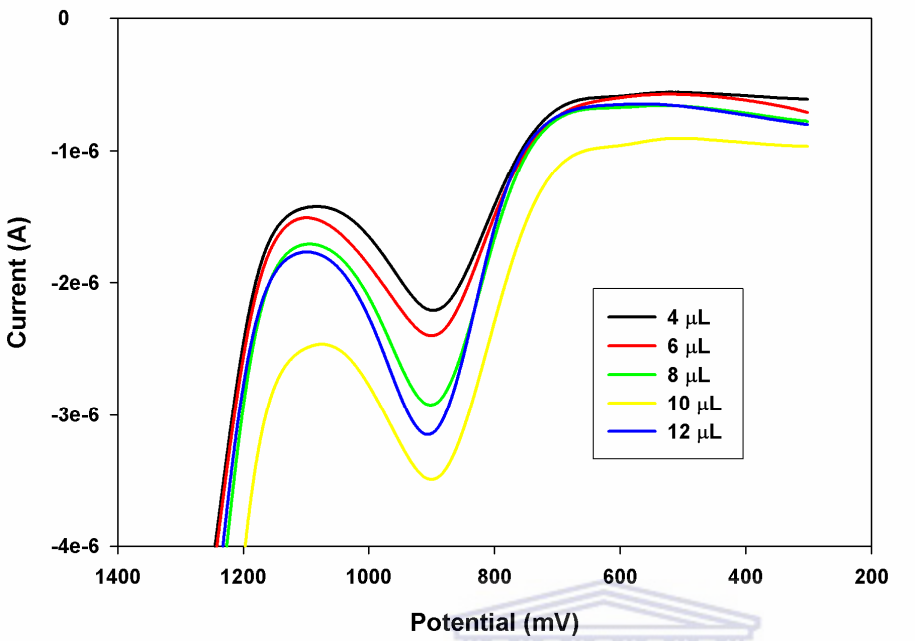

Figure 70: Anodic SWV response to different volumes of 20 µM amine terminated probe DNA immobilized on a Au|ZnSe-3MPA, in PBS, pH 7.40.

coverage/ enhanced adsorption of oligonucleotide sequences on the Au|ZnSe-3MPA surface. As the amount of immobilized probe DNA increased from 12 µL to 16 µL, the guanine signal was observed to decrease gradually levelled off beyond 16 µL (not shown). This may be attributed to excess adsorption of the oligonucleotide sequences on the Au|ZnSe-3MPA surface, making the guanine based in accessible for oxidation. It is therefore reasonable to suggest that the guanine signal can be affected by surface coverage of the Au|ZnSe-3MPA in excess of nucleic acids. A 10 µL of 20 µM amine terminated probe DNA was thus chosen as the optimum amount of probe DNA and was used in the subsequent experiments.

The effect of the ZnSe-3MPA quantum dots on the detection of the target DNA was investigated. Figures 71 and 72 show the SWV and DPV results for the progressive electrode modification. A square wave voltammogram of bare Au electrode in PBS, pH 7.40 showed a peak at around 950 mV while that of Au|ZnSe-3MPA electrode was broad and its current was lower than that of the bare. However, upon immobilization of the single strand probe DNA on the surface of the

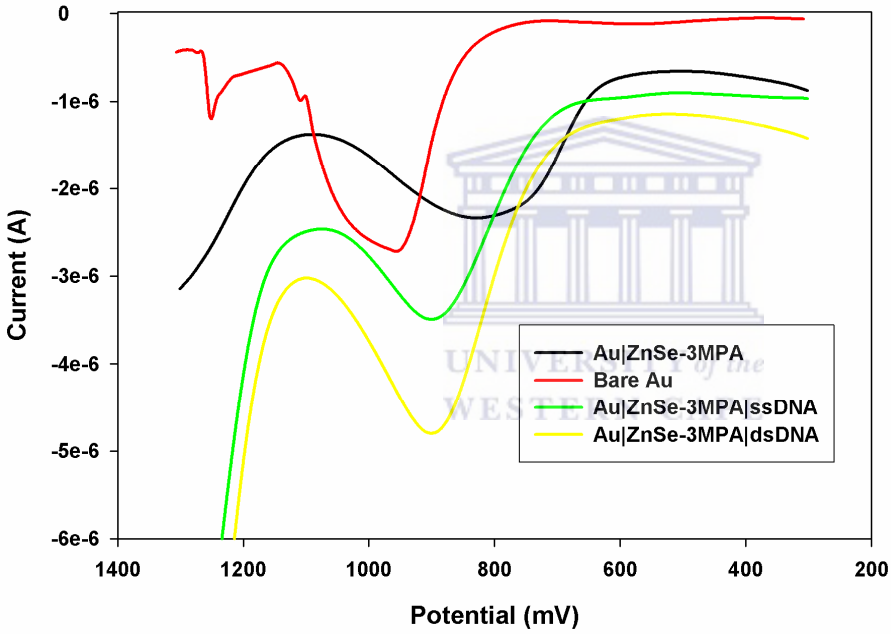

Figure 71: Anodic SWV of the bare Au, Au|ZnSe-3MPA, Au|ZnSe-3MPA|ssDNA and Au|ZnSe-3MPA|dsDNA, all in PBS, pH 7.40.

Au|ZnSe-3MPA, a well resolved peak with higher current was observed at around 900 mV which further increased upon hybridization. It is important to note that the electrochemical oxidation of bare gold electrode starts from 800 mV, with an anodic current peak at peak 910 mV, while the

cathodic current peak appears in the reverse scan at 570 mV. The peak observed for the bare electrode at 950 mV was therefore attributed to gold electrode oxidation reaction.

Natural nucleic acids are known to exhibit irreversible electrochemical reduction and oxidation at highly negative and positive potentials, respectively [337]. An oxidation peak attributed to guanine oxidation has been reported on gold electrodes between 700 mV and 800 mV (vs. Ag/AgCl) at pH 7.4 [338]. In this work, both DPV and SWV showed oxidation signals

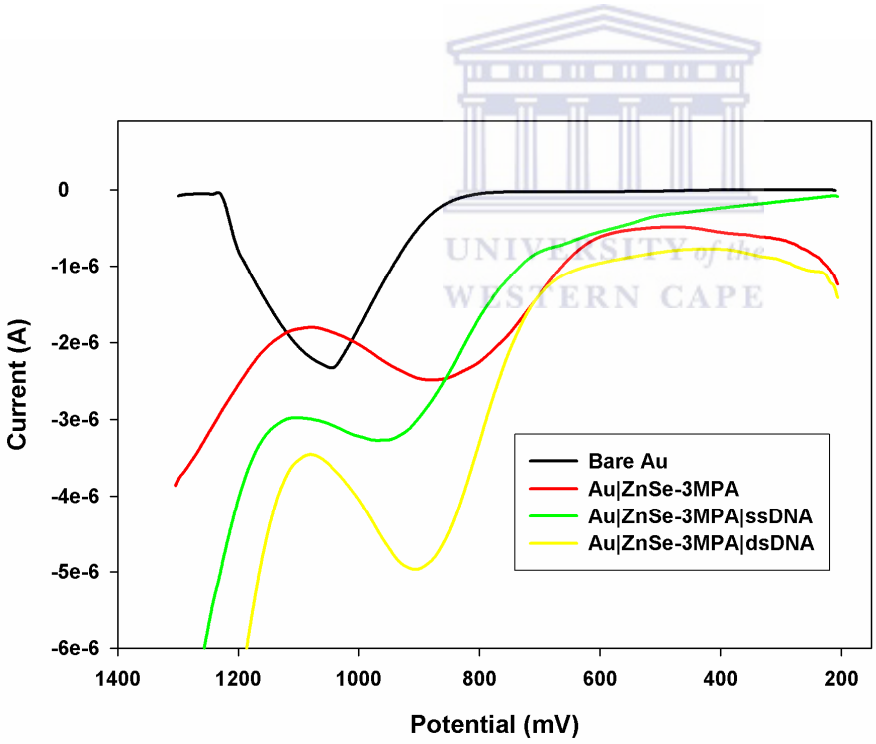

Figure 72: Anodic DPV of the bare Au, Au|ZnSe-3MPA, Au|ZnSe-3MPA|ssDNA and Au|ZnSe-3MPA|dsDNA, all in PBS, pH 7.40.

at 900 mV, which is within in the potential window of gold oxidation. The signal observed here is interpreted to result from catalytic oxidation of natural nucleic acids by gold. The ZnSe-3MPA modifier therefore does not shift the oxidation potential of guanine. Rather, the quantum dots offer increased surface area and binding sites for specific orientation of the probe DNA. This increased amount of immobilized probe DNA and hence high rate of hybridization, which in turn translated to changes in the rate of electron transfer reactions signified by increased catalytic current.

8.3 Voltammetric responses of the Au|ZnSe-3MPA|ssDNA genosensor to complementary DNA

Figures 73 and 74 below show the voltammetric responses (both SWV and DPV) and the corresponding calibration curves of the Au|ZnSe-3MPA|ssDNA genosensor to different concentrations of the complementary target oligonucleotide. After hybridization with the target DNA, electrochemical changes resulting from the oxidation of guanine were recorded as the analytical signals. In both SWV and DPV measurements, the peak currents were recorded with each measurement repeated four times.

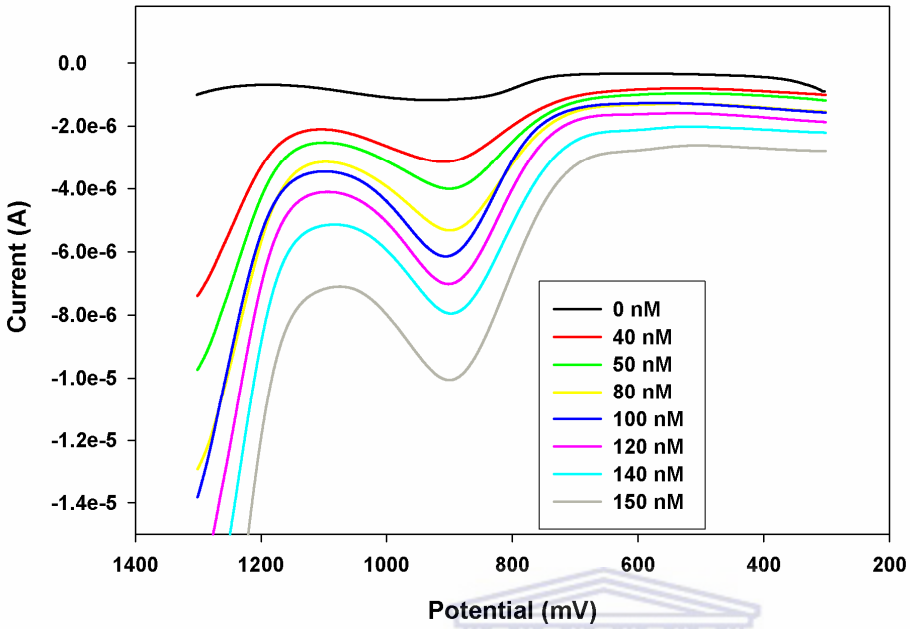

Figure 73: Anodic SWV response of the Au|ZnSe-3MPA|ssDNA genosensor to different concentrations of hybridized complementary target sequence in PBS, pH 7.40

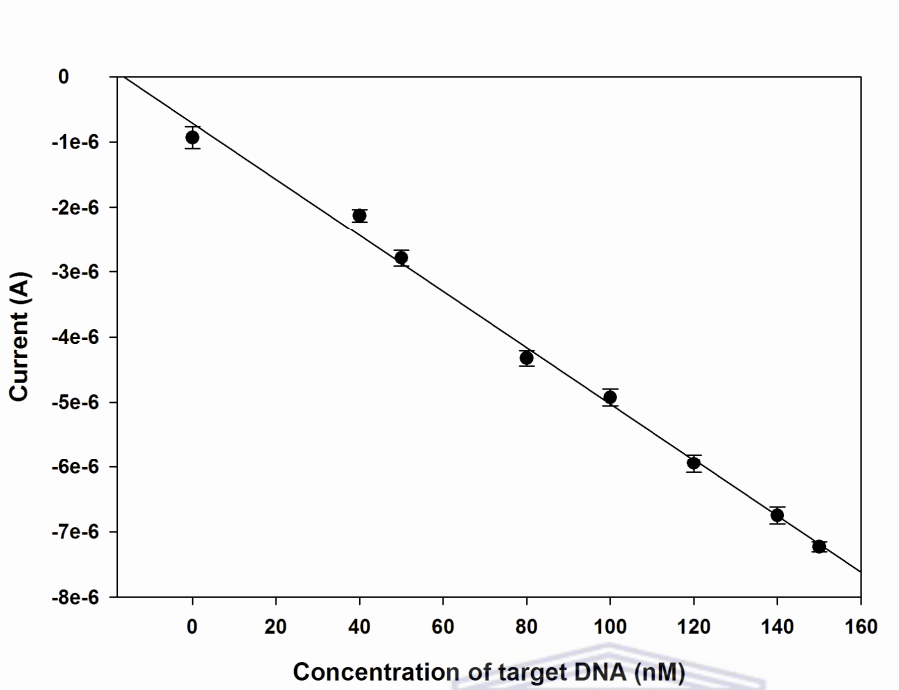

Figure 74: A plot of guanine oxidation current versus the concentration of hybridized complementary target sequence in PBS, pH 7.40 using SWV. The error bars correspond to replicate experiments.

Well defined guanine oxidation signals were observed in the range of target concentration between 40 nM and 150 nM. Up on further increase of the target concentration from 160 nM to 220 nM at intervals of 20 nM (not shown), negligible guanine oxidation signals were obtained and remained almost constant or decreased at 250 nM and beyond. This is an indication of surface saturation at the hybridization sites. The SWV current was linearly dependent on the concentration of the complementary target sequence in the range 40 nM to 150 nM (R^2 = 0.9947). A similar linear range was obtained with the DPV experiments with R^2 = 0.9933. The limit of detection (LOD) was evaluated by the equation: DL = 3SD/S, where SD is equivalent to the standard deviation of the average of the signal of eight measurements of the blank in the peak

potential of the catalytic oxidation of guanine [172] and S is the slope. The limit of detection was calculated as 4.36 nM for DPV and 1.17 nM for SWV.

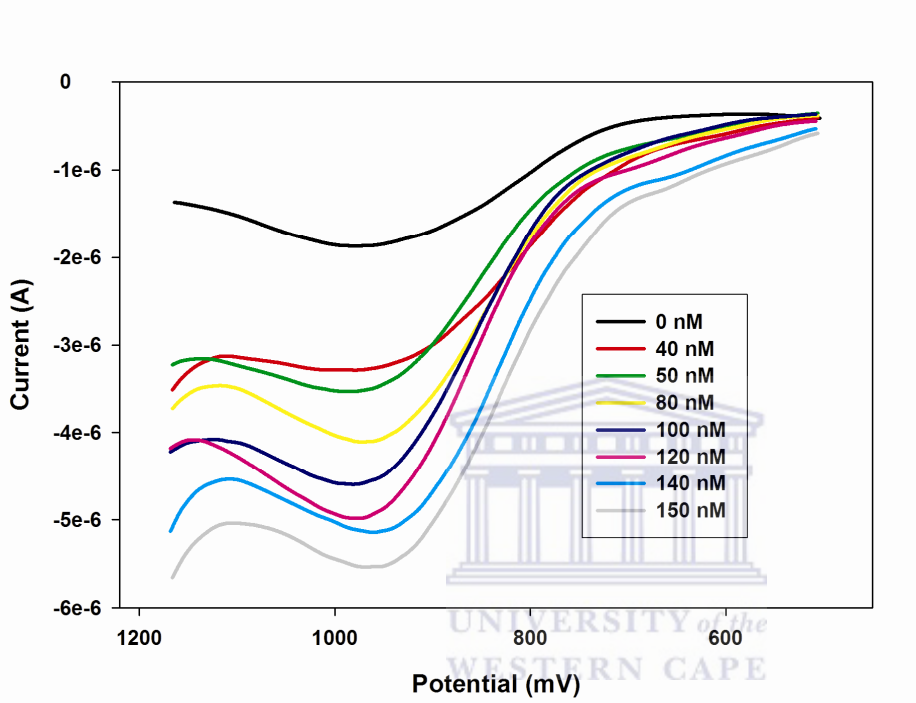

Figure 75: Anodic DPV response of the Au|ZnSe-3MPA|ssDNA genosensor to different concentrations of hybridized complementary target sequence in PBS, pH 7.40.

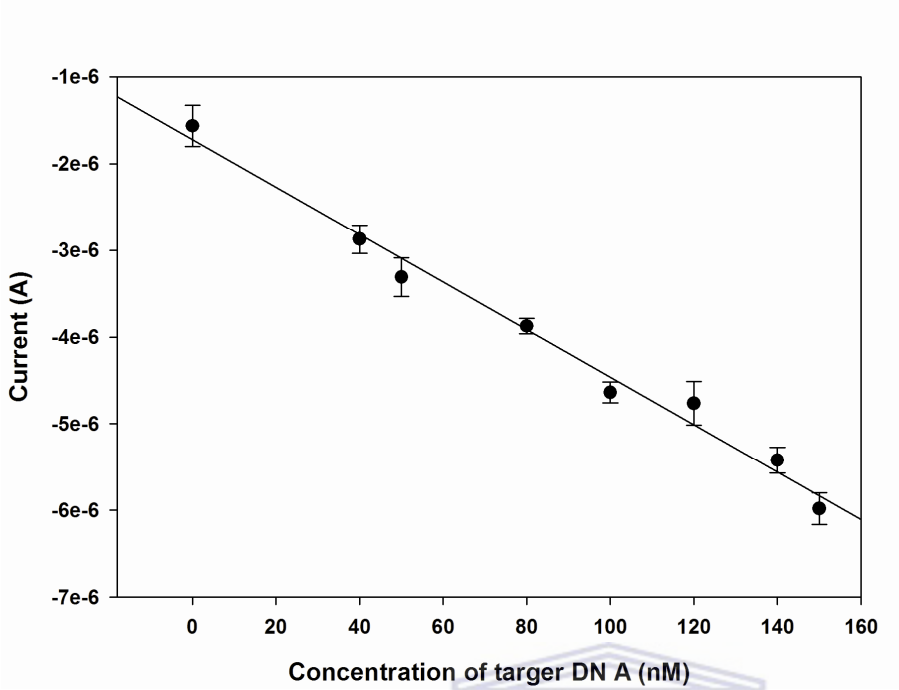

Figure 76: A plot of guanine oxidation current versus the concentration of hybridized complementary target sequence in PBS, pH 7.40 using DPV. The error bars correspond to four repeated experiments.

8.4 Discrimination among complementary, non-complementary and 3-base mismatched target sequences.

The ability of the Au|ZnSe-3MPA|ssDNA genosensor to discriminate among complementary, non-complementary and 3-base mismatched target sequences was investigated using 100 nM each of 3-base mismatch and non complementary target sequences instead of the complementary target sequence, and comparing the comparing the guanine oxidation signal of each with that of the complementary. After hybridization with the non complementary and 3 base mismatch sequences, the current signals obtained were 1.7426×10^{-6} A and 2.6724×10^{-6} A respectively.

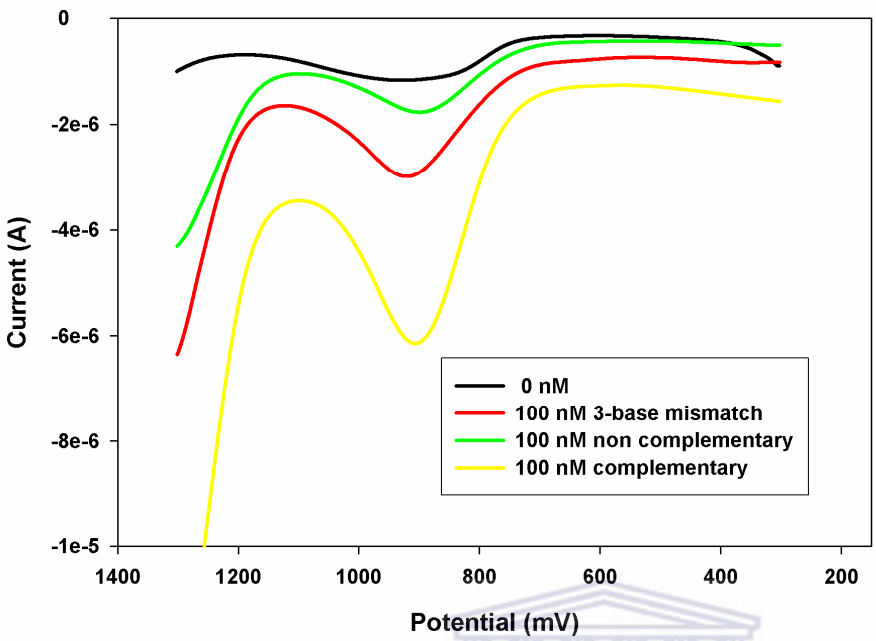

Figure 77: Anodic SWV response of the Au|ZnSe-3MPA|ssDNA genosensor to the working buffer (0 nM), 100 nM 3-base mismatch target, 100 nM non-complementary target and 100 nM complementary target.

Compared with the current signal (6.5724 x 10^{-6} A) obtain with the complementary sequence signal at the same concentration (100 nM), the responses of the non complementary and the 3 base mismatch correspond to 26.5139 % and 40.6609 % respectively. The higher response of the 3-base mismatch compared to that of the non complementary is an indication that some degree of hybridization occurred with the 3 base mismatch while the non complementary exhibited non specific adsorption. Similar degree of hybridization was also observed in the impedimetric detection of the same sequences on a gallium selenide modified electrode [339], also described previously in this thesis. When the same experiments were repeated with DPV

(Fig. 78 below), the current signals obtained with non complementary and the 3 base mismatch target sequences were 1.8475 x 10^{-6} A and 2.5483 x 10^{-6} A respectively.

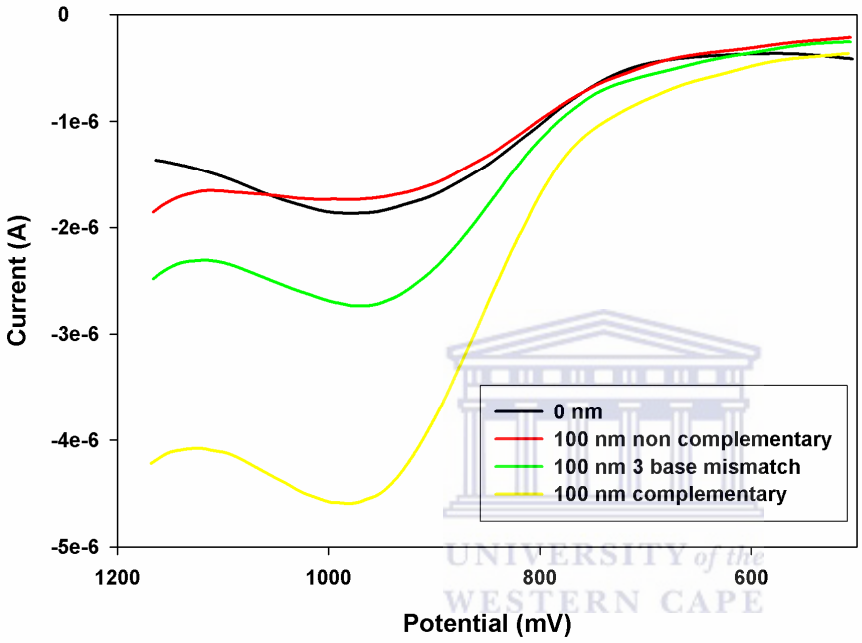

Figure 78: Anodic DPV response of the Au|ZnSe-3MPA|ssDNA genosensor to the working buffer (0 nM), 100 nM 3-base mismatch target, 100 nM non-complementary target and 100 nM complementary target.

When compared with the current signal obtained with the complementary target sequence (4.8796 x 10^{-6} A), the non complementary and the 3 base mismatch analytical responses corresponded with 37.8617 % and 52.2224 %. The non specific adsorption behaviour of the non complementary sequence on the surface of the Au|ZnSe-3MPA|ssDNA electrode is evident in this experiment since its response was more or less the same as that of the electrode in buffer

solution. These experiments show that the two genosensors are selective to the complementary target sequence.

The voltammetric results obtained by monitoring the guanine oxidation signals were matched with those obtained electrochemical impedance spectroscopy. Changes in the charge transfer resistance were taken as the analytical signal in electrochemical impedance spectroscopy as explained earlier. Up on formation of the polyanionic double strand DNA after hybridization, the transfer of electrons from the $Fe(CN)_6^{3-/4-}$ redox probe to the electrode surface was impeded and this was detected as increase in the charge transfer resistance. As shown in figure 79 below, the change in charge transfer resistance linearly increased with increase in the concentration of hybridized complementary target from 100 nM to 150 nM (R^2 = 0.9975). A detection limit of 1.32 nM and a sensitivity of 694.33 Ω/nM were evaluated from the calibration plot in Figure 80.

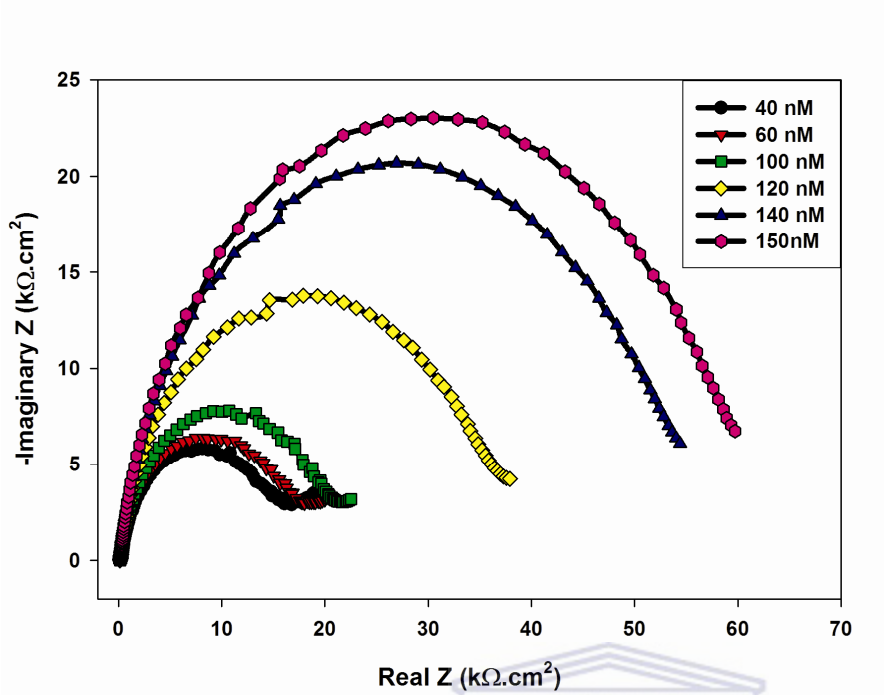

Figure 79: Impedimetric response of Au|ZnSe-3MPA|ssDNA to different concentrations of the complementary target sequence in 5.00 mM $Fe(CN)_6^{3-/4-}$.

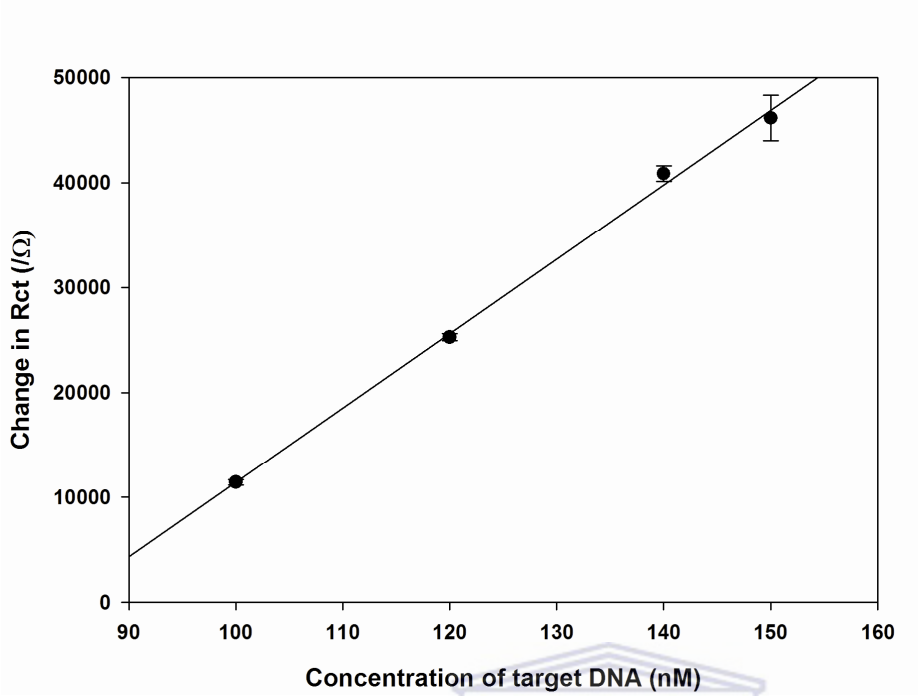

Figure 80: A plot of change in R_{ct} versus the logarithm of concentration of hybridized complementary target sequence in 5.00 mM $Fe(CN)_6^{3-/4-}$ using EIS. The error bars correspond to four repeated experiments.

At lower concentrations (between 20 nM and 100 nM), the change in charge transfer resistance was linearly depended on the logarithm of the concentration of the complementary target sequence.

It was generally observed that all analytical techniques exhibited good linearity, presenting linear correlation coefficients superior to 0.99, indicating that the complementary target can be determined by EIS, DPV or SWV. All analytical curves were carried out four times and a good repeatability of the experimental measurements was observed. These results suggest that the two voltammetric techniques as well as EIS are potentially applicable for the determination of transgenic CP4 epsps. In order to compare the analytical performance of the

genosensor using the three techniques, the key analytical parameters (sensitivity, linear range and detection limit) decribed above for each technique were isolated and tabulated as shown below.

Table 3: Tabulated analytical performance of the genosensor for the various techniques used.

	Linear range	**Sensitivity**	**Limit of detection**
DPV	40 – 150 nM	25.88 nA/nM	4.36 nM
SWV	40 – 150 nM	43.15 nA/nM	1.17 nM
EIS	100 – 150 nM	694.33 Ω/nM	1.32 nM

It is evident from the table that that all voltammetric techniques utilized presented a large linear range, high sensitivity and low detection limit. Although the sensitivity and detection limit of EIS was high, its linear range was found to be narrow and occurring at high concentrations of the target analyte. Of the two voltammetric techniques used however, SWV presented lower detection limit and higher sensitivity in relation to DPV, and could be chosen for CP4 epsps determination at low concentration level. The best analytical performance was obtained using SWV, due to considerable contribution of the anodic component in the resultant current as shown in figure 73.

8.5 Sub conclusions

In this chapter, square wave voltammetric and differential pulse voltammetric response of Au|ZnSe-3MPA|ssDNA genosensor to a CP4 epsps related target sequence is demonstrated, and compared with EIS response. By following the guanine oxidation signal, SWV and DPV presented an easy method to follow and optimize the probe DNA immobilization. Although DPV, SWV and EIS exhibited good analytical properties (repeatability and linearity sensitivity), SWV recorded the lowest detection limit of the three, posing an advantage in determination of CP4 epsps at low concentration level.

CHAPTER 9

Results and Discussion 6: Telluride quantum dot-impedimetric genosensors

9.1 Introduction

The large demand for DNA analysis calls for an extensive search for platforms upon which low-cost, easy-to-perform hybridization reactions, amplified analytical signals as well as high sensitivity and low detection limits can be achieved. In this chapter, three different platforms, namely Au|Ga_2Te_3-3MPA, Au|ZnTe-3MPA and Au|$Zn_2Ga_2Te_5$-3MPA are used as platforms for immobilization of the probe DNA and subsequent hybridization. A comparative discussion of the genosensor assembly for each platform is given. The hybridization reactions are monitored by following the changes in charge transfer resistance with increasing concentration in the target sequence.

9.2 Comparative electrochemical characteristics of the genosensor electrodes

The electrochemical impedance measurements were carried out in a background solution of 5.00 mM of $Fe(CN6)^{4-/3-}$ (0.10 M PBS of pH 7.40) at a bias potential of 200 mV. The frequency range was 50 kHz to 100 mHz at an amplitude of 10 mV. To view the progress of electrode preparation clearly, we considered changes in the charge transfer resistance at each step. Figure 81 below shows the results of Faradic impedance spectroscopy on bare gold electrode, Au|Ga_2Te_3-3MPA, Au|Ga_2Te_3-3MPA|ssDNA and Au|Ga_2Te_3-3MPA|dsDNA. Significance differences in the charge transfer resistance were observed upon progressive

electrode modification. At the bare gold electrode, a charge transfer resistance of 718 Ω was observed followed by a straight line which characterizes a diffusion limiting step of the electrochemical process [199]. The charge transfer resistance increased to 1275 Ω upon introduction of the Ga_2Te_3-3MPA quantum dots on the electrode surface due to electrostatic repulsion between the negatively charged quantum dots and the ferricyanide solution as explained earlier. The R_{ct} increases four times (to 5094 Ω) after immobilization of the single strand probe DNA as a result of repellence of redox probe from approaching electrode surface by negative charged polyanionic phosphate backbone of the ssDNA. After hybridization of the ssDNA probe with 20 nM of the complementary ssDNA, the R_{ct} increased six times (to 7678 Ω).

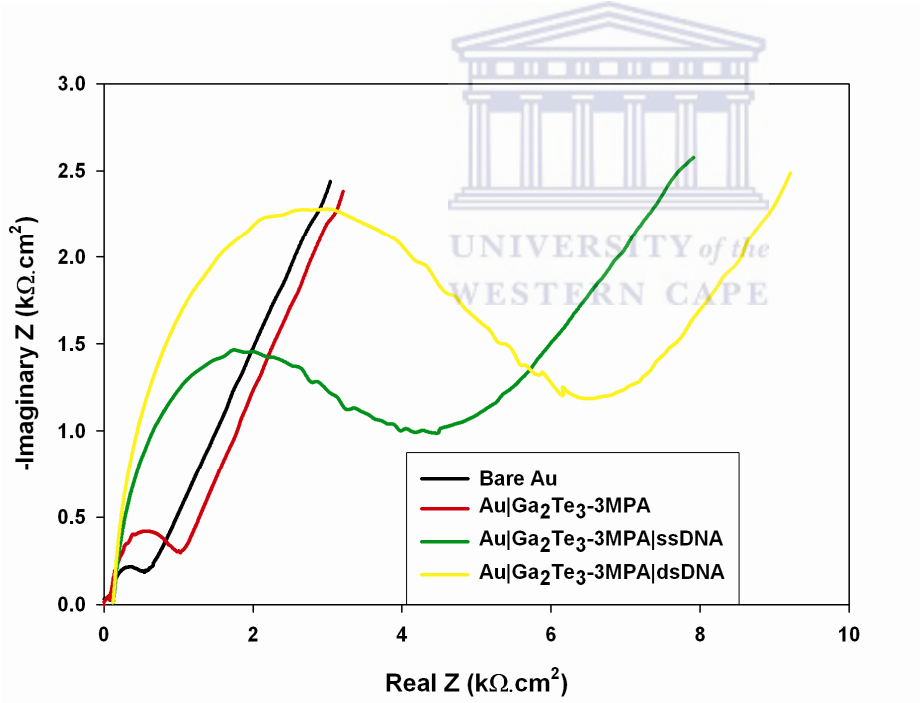

Figure 81: Nyquist plots of bare Au, Au|Ga_2Te_3-3MPA, Au|Ga_2Te_3-3MPA|ssDNA and Au|Ga_2Te_3-3MPA|dsDNA, all in 5.00 mM $Fe(CN)_6^{4-/3-}$.

It has already been mentioned that the DNA backbone contains negatively charged phosphate groups. The negatively charged back bone of the oligonucleotide probe DNA and the redox couple $Fe(CN)_6^{4-/3-}$ causes an electrostatic repulsion on the electrode-solution interface, impeding electron transfer process. Up on hybridization, the double stranded DNA increases the negative charge density even further and the R_{ct} increases. The electron transfer resistance at the different stages of electrode modification can be translated into important kinetic parameters such as heterogeneous rate transfer constant, standard exchange current and time constant. These parameters were calculated from the equations that follow:-

$$R_{ct} = \frac{RT}{nFi_o} \quad (8)$$

$$i_o = nFAk^0C^* \quad (9)$$

$$\varpi_{max} = \frac{1}{R_{ct} \times C_{dl}} \quad (2)$$

$$\tau = R_{ct} \times C_{dl} \quad (3)$$

The values obtained from these equations are tabulated as shown below.

Table 4: Kinetic parameters of $Fe(CN)_6^{4-/3-}$ on bare Au, Au|Ga_2Te_3-3MPA, Au|Ga_2Te_3-3MPA|ssDNA and Au|Ga_2Te_3-3MPA|dsDNA.

Kinetic parameters	Bare Au	Au|Ga_2Te_3-3MPA	Au|Ga_2Te_3-3MPA|ssDNA	Au|Ga_2Te_3-3MPA|dsDNA
i_0 (x 10^{-6} A)	35.724	27.70	5.0826	3.3890
k^0 (x 10^{-4} cm s^{-1})	36.841	28.5660	5.2418	3.4950
Ω_{max} (rad s^{-1})	4589	1256	628.3	44.88
τ (x 10^{-4} s rad^{-1})	2.1791	7.9577	15.9150	222.82

The standard exchange current is fundamental characteristic of electrode behaviour and offers information about the rate of oxidation or reduction at an electrode. From the table above, the exchange current is observed to decrease at each stage of electrode modification. It is important to mention that exchange current is a complex function of the concentration of both the reactants and products involved in the specific reaction described by the exchange current. This function is particularly dependent on the shape of the charge transfer barrier across the electrochemical interface. At each stage of electrode modification, a barrier in created in form of either Ga_2Te_3-3MPA, Ga_2Te_3-3MPA|ssDNA or Ga_2Te_3-3MPA|dsDNA, all of which increase the impedance of the redox probe to the electrode surface, hence progressive reduction in the exchange current. Surface impurities adsorbed on the electrode surface also affect its exchange current. For instance, presence of trace impurities markedly reduces the exchange current for the system. If we consider Ga_2Te_3-3MPA, Ga_2Te_3-3MPA|ssDNA or Ga_2Te_3-3MPA|dsDNA as impurities on the surface of the gold electrode, then the progressive decrease in the exchange current would be expected. A similar trend was observed for the heterogeneous rate transfer

constants. The bare electrode showed the highest heterogeneous rate transfer constant while the Ga_2Te_3-3MPA|dsDNA showed the lowest, an indication of increased charge transfer resistance at each step of electrode modification. There is also a progressive increase in time constant at each step of electrode modification, an observation which is in agreement with increase in charge transfer resistance described above.

The Bode plots (Fig. 82) below depict the changes in the phase angles and frequencies at the different stages of electrode modification. It is evident from the figure the absolute phase angle changes from 42 ° for bare Au to 54° for Ga_2Te_3-3MPA. When the ssDNA is immobilized on the surface of the Ga_2Te_3-3MPA, the absolute phase angle increases further to 65° and reaches 70 ° up on hybridization with 20 nM of the complementary target DNA.

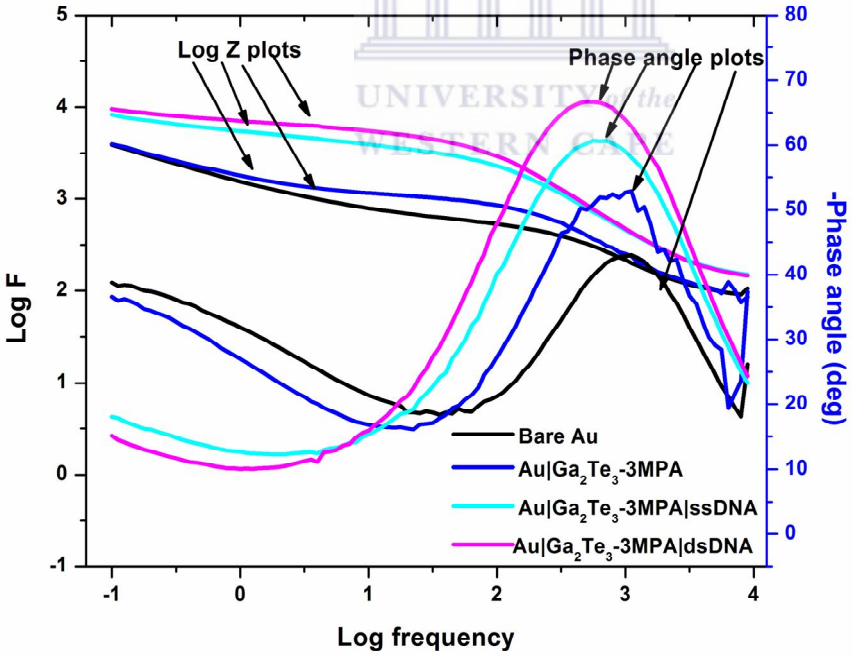

Figure 82: Bode plots of bare Au, Au|Ga_2Te_3-3MPA, Au| Ga_2Te_3-3MPA|ssDNA and Au|Ga_2Te_3-3MPA|dsDNA, all in 5.00 mM $Fe(CN)_6^{4-/3-}$.

The changes in the absolute phase angle are also accompanied by shifts in frequency in the order 730 Hz, 200 Hz, 100Hz and 71.43 Hz for the bare Au, Ga_2Te_3-3MPA, Ga_2Te_3-3MPA|ssDNA and Ga_2Te_3-3MPA|dsDNA respectively. Since the phase angles are very sensitive to the impedance data [340], it is reasonable to relate the phase angle values to the charge transfer resistance. The phase angle in the Bode plots and its corresponding frequency (frequency at the maximum phase angle, f_ϕ) are related to the charge transfer resistance according to equations below

$$f_\varphi = \frac{1}{4\pi \times R_{ct} C_{dl}} \sqrt{1 + \frac{R_{ct}}{Rs}} \qquad (41)$$

$$\varphi = \tan^{-1}\left(\frac{1}{1 + 2Rs/R_{ct}}\right) \qquad (42)$$

Equation 41 depicts an inverse relationship between the charge transfer resistance and the frequencies. The progressive decrease in frequencies at the various stages of electrode modification thus implies increasing charge transfer resistance and consequently increasing impedance. Equation 42 shows that the phase angle is directly proportional to the charge transfer resistance and the increase in phase angles at the various stages of electrode modification indicate increasing impedance of the redox probe to the surface of the electrode. Since time constant, $\tau = Rct \times Cdl$, equation 41 above can be written as

$$f_\varphi = \frac{1}{4\pi \times \tau} \sqrt{1 + \frac{Rct}{Rs}} \qquad (43)$$

Or

$$\tau = \frac{1}{4\pi \times f_{\varphi}} \sqrt{1 + \frac{Rct}{Rs}} \qquad (44)$$

This equation relates the time constant to the frequencies and shows that the time constant is inversely proportional to frequencies. This is in agreement with the results shown on the table (increasing time constants) and the frequencies calculated (decreasing frequencies) at each step of electrode modification. These results suggest that the Ga_2Te_3-3MPA quantum dots were successfully immobilized on the surface of the gold electrode and that the bio conjugation reactions with the probe ssDNA were achieved. Further increase in impedance beyond that of the Ga_2Te_3-3MPA|ssDNA also confirms that hybridization reactions took place.

Since a similar protocol was used for fabrication of Au|ZnTe-3MPA|ssDNA and Au|$Zn_2Ga_2Te_5$-3MPA|ssDNA genosensors, characterization of the electrodes at each modification stage followed a similar trend. The kinetic parameters that give information about the changes in impedance are tabulated after each platform.Figures 83 and 84 show the Nyquist plots and the Bode plots, respectively, for the fabrication of the Au|ZnTe-3MPA|ssDNA genosensor. The change in the kinetic parameters follows the same trend as in Ga_2Te_3-3MPA genosensor fabrication.

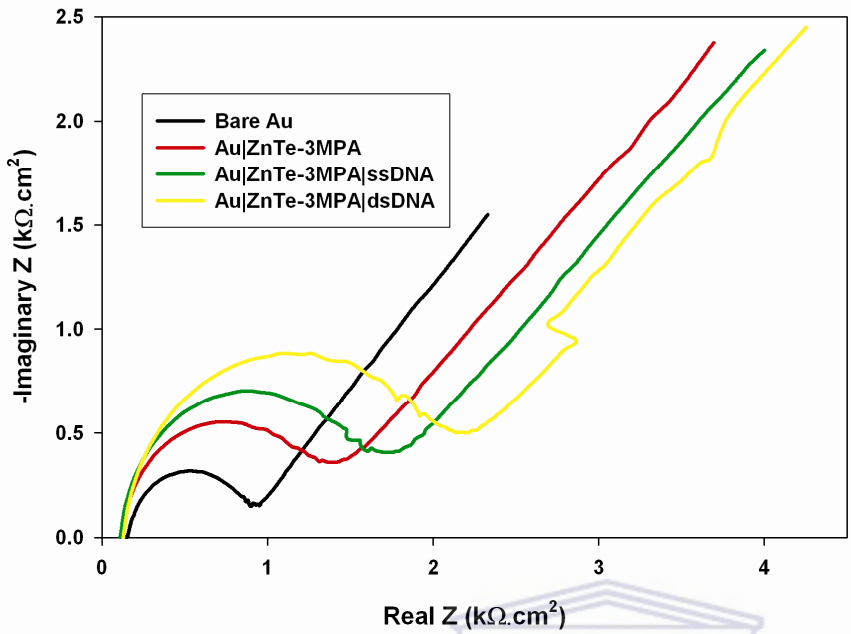

Figure 83: Nyquist plots of bare Au, Au|ZnTe-3MPA, Au|ZnTe-3MPA|ssDNA and Au|ZnTe-3MPA|dsDNA, all in 5.00 mM $Fe(CN)_6^{4-/3-}$.

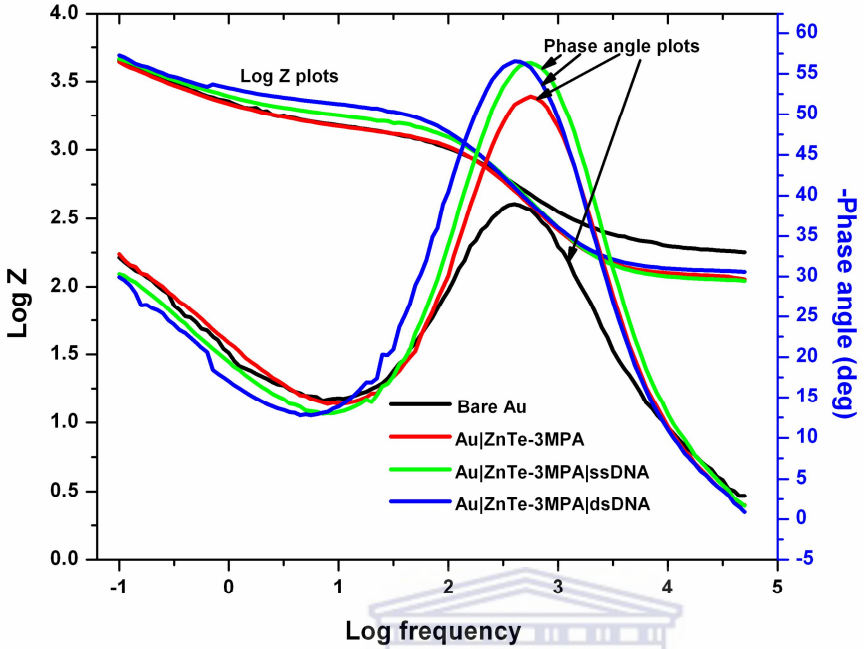

Figure 84: Bode plots of bare Au, Au|ZnTe-3MPA, Au|ZnTe-3MPA|ssDNA and Au|ZnTe-3MPA|dsDNA, all in 5.00 mM $Fe(CN)_6^{4-/3-}$

Table 5: Kinetic parameters of $Fe(CN)_6^{4-/3-}$ on bare Au, Au|ZnTe-3MPA, Au|ZnTe-MPA|ssDNA and Au|ZnTe-3MPA|dsDNA

Kinetic parameters	Bare Au	Au|ZnTe-3MPA	Au|ZnTe-MPA|ssDNA	Au|ZnTe-3MPA|dsDNA
i_0 (x 10^{-6} A)	35.724	22.8860	17.9950	13.9250
k^0 (x 10^{-4} cm s^{-1})	36.841	23. 6020	18.5580	14.3610
Ω_{max} (rad s^{-1})	4589	785	628	661
τ (x 10^{-4} s rad^{-1})	2.1791	12.7320	15.9150	17.8250

The standard exchange current and the heterogeneous rate constants decreased while the time constants increased at each step of genosensor fabrication. The absolute phase angle is also observed to increase, accompanied by respective shift in frequencies towards low values. These observations indicate decrease in conductivity of electrons at the redox probe-electrode interface and are indicators of successful fabrication of the genosensor. Further impedance increase on the Au|ZnTe-3MPA|dsDNA is a clear indication that hybridization can take place on the fabricated genosensor.

Figures 85 and 86 depict the Nyquist and Bode plots, respectively of the Au|$Zn_2Ga_2Te_5$-3MPA|ssDNA genosensor fabrication and its subsequent hybridization with the complementary target DNA. Again, changes in the standard exchange current, heterogeneous rate constants, frequencies and time constants at each step of electrode modification follow the same trend as observed for Au|ZnTe-3MPA|ssDNA and Ga_2Te_3-3MPA|ssDNA electrode assembly processes.

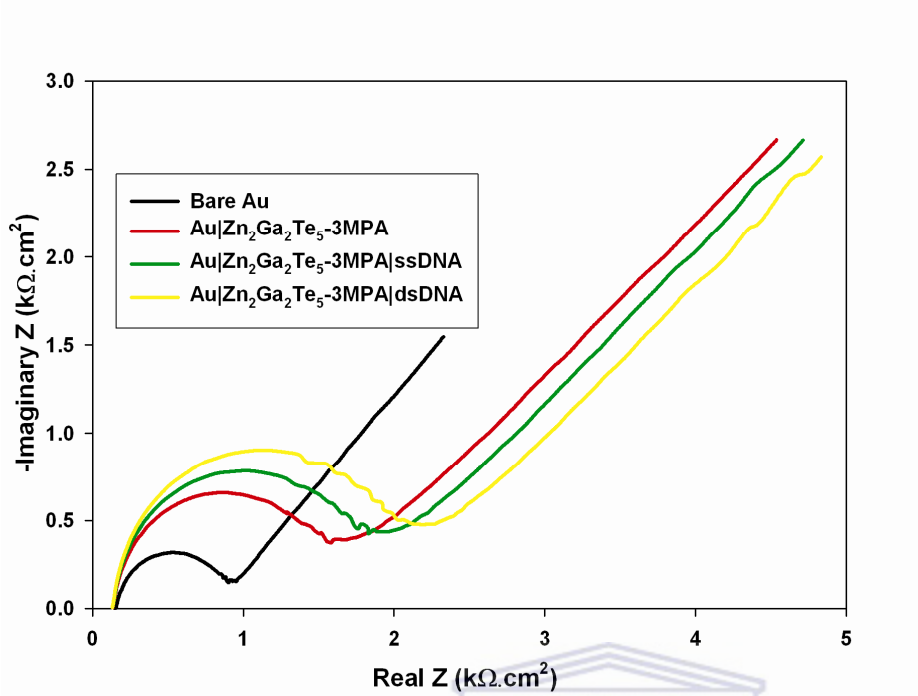

Figure 85: Nyquist plots of bare Au, Au|$Zn_2Ga_2Te_5$-3MPA, Au|$Zn_2Ga_2Te_5$-3MPA|ssDNA and Au|$Zn_2Ga_2Te_5$-3MPA|dsDNA, all in 5.00 mM $Fe(CN)_6^{4-/3-}$.

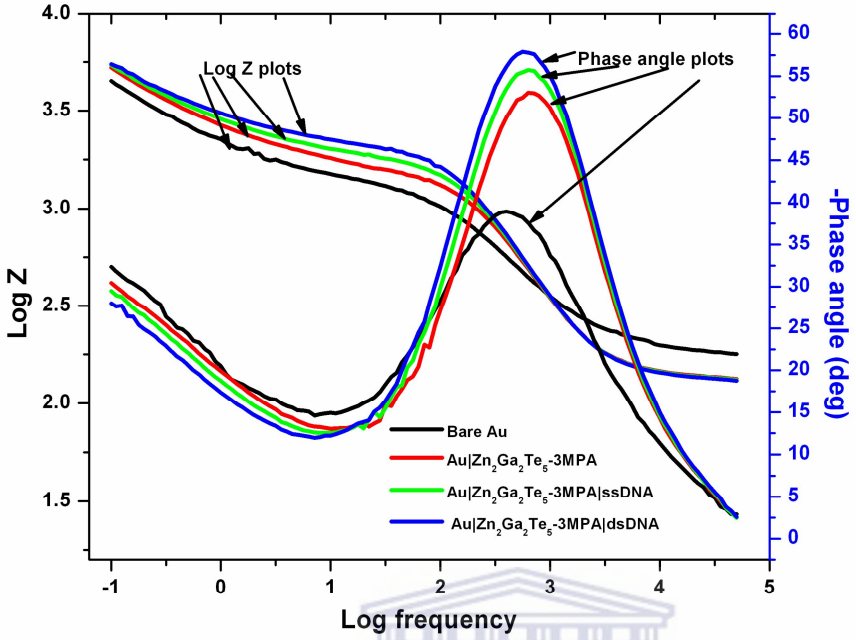

Figure 86: Bode plots of bare Au, Au|$Zn_2Ga_2Te_5$-3MPA, Au|$Zn_2Ga_2Te_5$-3MPA|ssDNA and Au|$Zn_2Ga_2Te_5$-3MPA|dsDNA, all in 5.00 mM $Fe(CN)_6^{4-/3-}$.

Table 6: Kinetic parameters of $Fe(CN)_6^{4-/3-}$ on bare Au, Au|$Zn_2Ga_2Te_5$-3MPA, Au|$Zn_2Ga_2Te_5$-3MPA|ssDNA and Au|$Zn_2Ga_2Te_5$-3MPA|dsDNA.

Kinetic parameters	Bare Au	Au|$Zn_2Ga_2Te_5$-3MPA	Au|$Zn_2Ga_2Te_5$-3MPA|ssDNA	Au|$Zn_2Ga_2Te_5$-3MPA|dsDNA
i_0 (x 10^{-6} A)	35.724	18.6480	16.2930	14.1010
k^0 (x 10^{-4} cm s^{-1})	36.841	19.2310	16.8030	14.5420
Ω_{max} (rad s^{-1})	4589	1256	1121	882
τ (x 10^{-4} s rad^{-1})	2.1791	7.9577	8.9127	11.3320

9.3 Analytical performance of the impedimetric telluride genosensors

The DNA hybridization was monitored by EIS, before and after the probe electrode was dipped into a stirred solution (0.1 M PBS, pH 7.40) containing different target DNA for 5 min, while holding the potential at + 500 mV. Like in the electrode preparation, the impedance spectra of the electrodes were measured in 5.00 mM $[Fe(CN)_6]^{4-/3-}$ solution and the results are shown in the figure below. The hybridization with the complementary target ssDNA caused an increase in the charge transfer resistance.

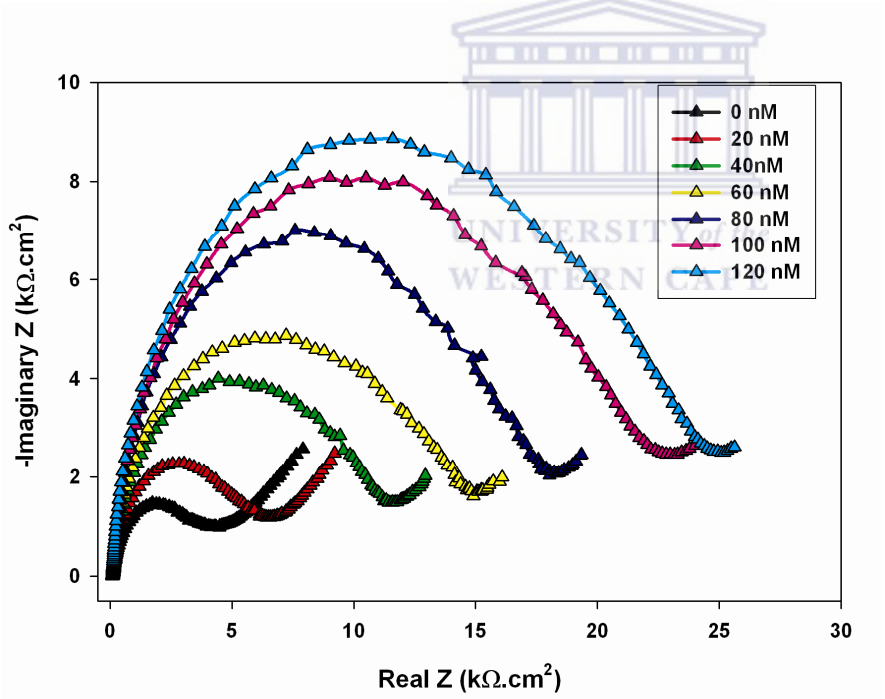

Figure 87: Hybridization response of the Au|Ga_2Te_3-3MPA|ssDNA genosensor to different concentrations of the complementary target.

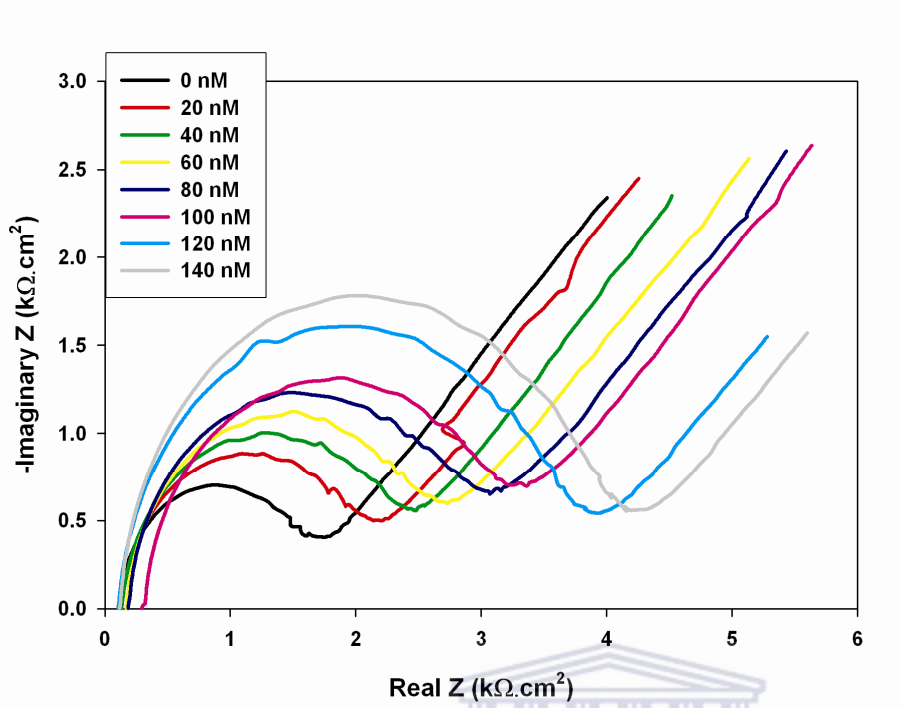

Figure 88: Hybridization response of the Au|ZnTe-3MPA|ssDNA genosensor to different concentrations of the complementary target.

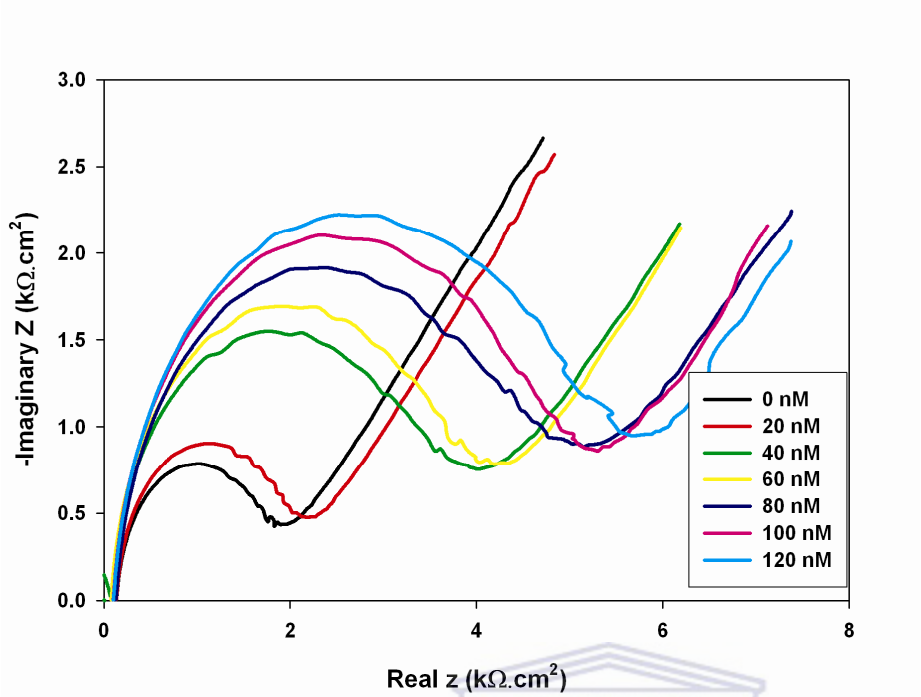

Figure 89: Hybridization response of the Au| $Zn_2Ga_2Te_5$-3MPA |ssDNA genosensor to different concentrations of the complementary target.

A comparative analysis of the sensitivity and the detection limit for each of the fabricated genosensors of shown in the table below.

Table 7: A comparative analysis of the sensitivity and the detection limit for Au|ZnTe-3MPA|ssDNA, Au|Ga_2Te_3-3MPA|ssDNA and Au|$Zn_2Ga_2Te_5$-3MPA|ssDNA genosensors

Genosensor	Sensitivity (Ω/nm)	LOD (nm)
Au|ZnTe-3MPA|ssDNA	173.03	1.4379
Au|Ga_2Te_3-3MPA|ssDNA	42.99	1.8279
Au|$Zn_2Ga_2Te_5$-3MPA|ssDNA	11.78	3.4148

From the table above, Au|ZnTe-3MPA|ssDNA shows the highest sensitivity and the lowest detection limit while the lowest sensitivity and highest detection limit are obtained for Au|$Zn_2Ga_2Te_5$-3MPA|ssDNA genosensor. It should be remembered that the ZnTe-3MPA had a particle size of 5.30 nm, Ga_2Te_3-3MPA 6.80 nm while $Zn_2Ga_2Te_5$-3MPA had 9.30 nm particle sizes. These results show a very high correlation between the particle size and the analytical performance. The high analytical performance of ZnTe-3MPA is therefore attributed to its increased surface area (due to smaller particle size) allowing for more binding sites (high probe DBA loading), high hybridization efficiency and consequently high impedance.

9.4 Reproducibility and stability of the genosensors.

The stability of the genosensors was studied using two approaches. In the first approach (recorded as Approach 1 in the table) impedimetric responses of independent Au|Ga_2Te_3-3MPA|ssDNA, Au|ZnTe-3MPA|ssDNA and Au|$Zn_2Ga_2Te_5$-3MPA|ssDNA genosensors to 100 nM target DNA concentration were measured at different storage intervals for one month,

storing them in PBS, pH 7.40 at 4 °C in between the measurements. In the second approach (recorded as approach 1 in the table), different Au|Ga_2Te_3-3MPA|ssDNA, Au|ZnTe-3MPA|ssDNA and Au|$Zn_2Ga_2Te_5$-3MPA|ssDNA genosensors were prepared and measured individual impedimetric responses to a constant concentration of 100 nM complementary target DNA after different storage times up to one month. Reproducibility studies were done by measuring the impedimetric responses of ten freshly prepared genosensors to 100 nM complementary target DNA. The stability is in each case recorded as the percentage loss in the genosensor's response to 100 nM complementary target sequence within the one month. The reproducibility was recorded as the average change in R_{ct} as a result of genosenor's response to 100 nM of the complementary target DNA. The standard deviations are stated with respect to 8 measurements.

The results are given in table 8 below.

Table 8: Stability and reprducibility characteristics of Au|Ga_2Te_3-3MPA|ssDNA, Au|ZnTe-3MPA|ssDNA and Au|$Zn_2Ga_2Te_5$-3MPA|ssDNA genosensors.

		Au|Ga_2Te_3-3MPA|ssDNA	Au|ZnTe-3MPA|ssDNA	Au|$Zn_2Ga_2Te_5$-3MPA|ssDNA
Stability	**Approach 1**	23 %	30 %	35 %
	Approach 2	12 %	19 %	22 %
Reproducibility		12704 ± 230 Ω	2166 ± 48 Ω	3728 ± 75 Ω

It is evident from these results that if a single probe electrode is used for measurements at different storage intervals, it loses more response that if the same was freshly prepared and used at different time intervals. Since approach 1 was used without regeneration of the sensor, the high loss of sensitivity could be attributed to accumulation of double stranded DNA formed during successive measurements, which reduced the number of targets binding sites.

9.5 Discrimination among complementary, not complementary and 3-base mismatch target sequences.

In order to evaluate discrimination characteristics of the genosensors, independent impedimetric measurements were done using 100 nM of the complementary, non complementary and a randomly placed three base mismatched target sequences. In each case, four measurements

were done. The results were expressed as relative variation of the charge transfer resistance values obtained due to either hybridization or non-specific adsorption and the value due to the bare electrode. For mathematical comparison, the relative variation was represented using equations 40a, 40b and 40c. This mathematical evaluation of discrimination aspects of impedimetric genosensors has been previously described [208, 341]. It is expected that if the probe electrode is dipped in a stirred PBS solution (pH 7.40) containing the complementary target sequence for 5 min while holding the potential constant at 500 mV, hybridization reactions will occur. The double strand DNA would then increase the negative charge density at the electrode surface and further impede electron transfer from the redox probe to the electrode. The charge transfer resistance in this case is expected to be higher than that of the probe electrode and the Δ_{Ratio} value should be greater than 1. If however a non-complementary target sequence is used instead of the complementary, non-specific adsorption would occur on the surface of the electrode. A negligible change in charge transfer resistance would in this be recorded and this would result from introduction of an additional layer on the electrode surface rather than from increase in charge density. In other words, the spectra will resemble that of the probe electrode and the Δ_{Ratio} value should be close to 1, i.e ΔR_{ct} (Sample) $\approx$ ΔR_{ct} (Product). In the third case where a three base mismatched target sequence is used instead of the complementary sequence, some degree of hybridization would be expected due to presence of some probe-target base paring. The impedance spectra in this case will have a larger semicircle than that of the probe electrode, but smaller than that of the complementary target sequence. The delta ratio values for each impedimetric genosensor were presented in form of histograms as shown below. The black bar in each histogram corresponds to R_{ct} variation of a hybridization reaction with the complementary target sequence. It is evident from the histograms that all hybridization reactions

had delta ratio values greater than 1. This is a confirmation that a double strand DNA was formed in each probe-complementary hybridization reactions.

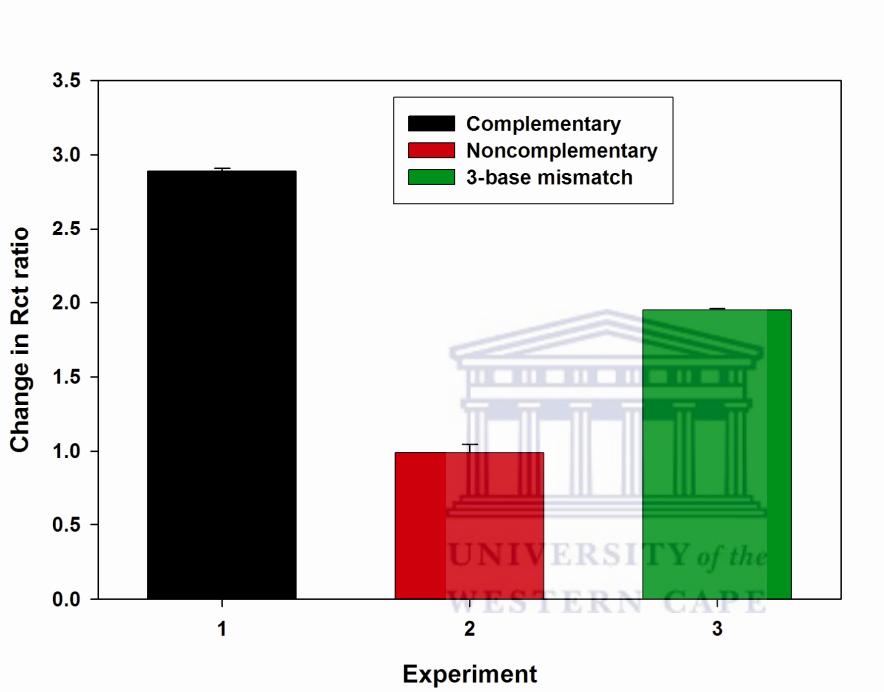

Figure 90: Discrimination among complementary, non complementary and three base mismatched target sequences in Au|Ga_2Te_3-3MPA|ssDNA.

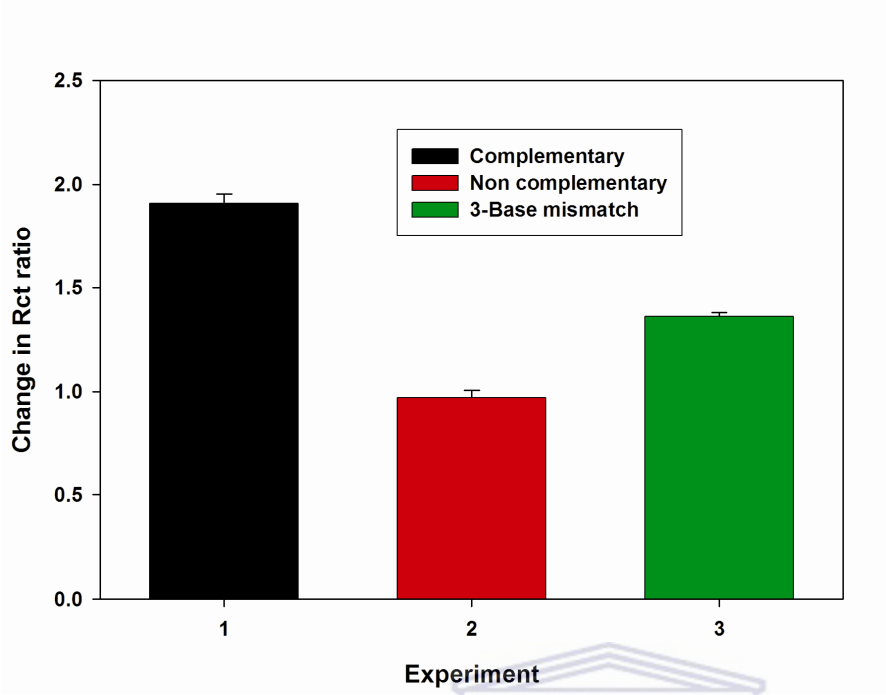

Figure 91: Discrimination among complementary, non complementary and three base mismatched target sequences in Au|ZnTe-3MPA|ssDNA.

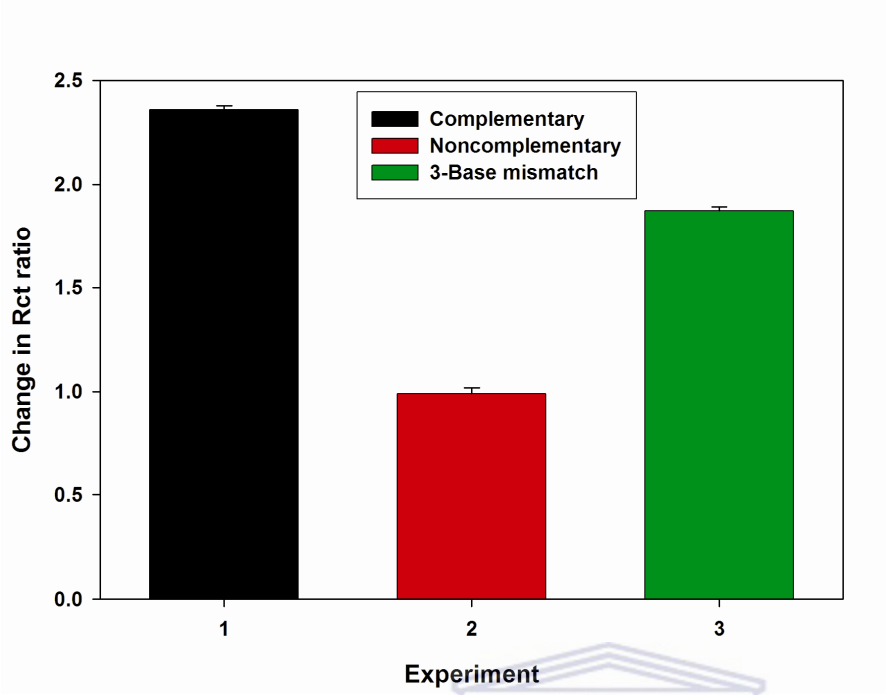

Figure 92: Discrimination among complementary, non complementary and three base mismatched target sequences in Au|$Zn_2Ga_2Te_5$-3MPA|ssDNA.

The red bar in each histogram corresponds to R_{ct} variation of a hybridization reaction with the non complementary target sequence. It is important to mention that the R_{ct} values obtained with the non-complementary target sequence for the four experiments in each genosensor were highly inconsistent. On average, ΔR_{ct}(Sample)/ΔR_{ct}(Product) values were less than 1 as depicted in the respective histograms. This is an indication that the non complementary sequence irregularly adsorbed on the surface of the probe electrode and that no double stranded DNA was formed. The green bar is significantly different in each case from the red bar. More consistent R_{ct} values than for the non complementary were obtained with the average ΔR_{ct}(Sample)/ΔR_{ct}(Product) being very greater. This is an indication of some degree of hybridization. The degree of hybridization is however significantly less from that of the

complementary target in each case. The three impedimetric genosensors therefore exhibited high discrimination among the complementary, non-complementary and 3 base mismatched target sequences.

9.6 Sub conclusions

In this chapter, a comparative analysis of impedimetric performance of three different telluride genosensors has been presented. The three genosensors demonstrated high specificity for the target complementary sequence. Owing to small size of the ZnTe-3MPA, the Au|ZnTe-3MPA|ssDNA exhibited high sensitivity and low detection limit. Fabricated genosensors even when used once after specific storage times were found to be more sensitive than single genosensors used several times, with regeneration procedures in between each measurement.

CHAPTER 10

Conclusions and recommendations

10.1 Conclusions

In this study, a rare cationic chemistry of gallium (III) has been explored as a source of cationic precursor for synthesis of novel biocompatible and water soluble-gallium based quantum dots. The trivalent gallium has also been used to tailor the optical and electrochemical properties of selenide and telluride quantum dots. In the process, this study has introduced novel biocompatible and water soluble binary-capped nanocrystals (Ga_2Se_3-3MPA) and quantum dots (Ga_2Te_3-3MPA). By use of Ga^{3+} to introduce structural vacancies in ZnSe-3MPA and ZnTe-3MPA quantum dots, novel water soluble and biocompatible ternary quantum dot systems in the form $Zn_2Ga_2Se_5$-3MPA and $Zn_2Ga_2Te_5$-3MPA were obtained. A bifunctional amphiphilic molecule (3-mercaptopropionic acid) used a capping agent rendered the quantum dots and nanocrystals biocompatible, soluble and stable. Electrostatic repulsion arising from dehydrogenated carboxyl groups on the surface of the quantum dot particles kept them non-agglomerated. Retention of the capping agent on the quantum dot surface was confirmed by FTIR studies, which showed characteristic bands related to C-H, C=O as well as –O-H groups.

The electrochemical studies of the binary ZnSe-3MPA quantum dots, Ga_2Se_3-3MPA nanocrystals and the ternary $Zn_2Ga_2Se_5$-3MPA quantum dots reveal that gallium-induced vacancies caused a significant enhancement in the conductivity of the $Zn_2Ga_2Se_5$-3MPA solution compared to that of ZnSe-3MPA and Ga_2Se_3-3MPA, all studied in solution. In the telluride-

binary and ternary quantum dot systems, gallium-induced electrochemical enhancement was evidence by significant increase in the electron transfer rate constants from 3.8210 x 10^{-1} s^{-1} (for Ga_2Te_3-3MPA) and 2.6588 s^{-1} (for ZnTe-3MPA) to 19.5231 s^{-1} ($Zn_2Ga_2Te_5$-3MPA). Whereas surface concentration largely influenced the electrochemistry of adsorbed selenide quantum dots and nanocrystals, chemical composition was found to influence the electrochemistry of adsorbed telluride quantum dots.

The fluorescence and UV-vis studies of the selenide quantum dots and nanocrystals showed bands of $Zn_2Ga_2Se_5$-3MPA occurring midway between those of the corresponding binary systems, indicating that an entirely new compound was formed. In fact, the bands of the $Zn_2Ga_2Se_5$-3MPA appeared to be an average of its constituent ZnSe-3MPA and Ga_2Se_3-3MPA binary systems, indicating the formation of a hybrid material. The optically determined band gaps were not in agreement with the electrochemically determined band gaps, due to the interference barrier between the quantum dot or nanocrystal film and the electrode. Gallium was found to significantly influence the particle size in the selenide ternary quantum dot system as evidenced by decrease of the particle size from 3.60 nm (for ZnSe-3MPA) and 65 nm (for Ga_2Se_3-3MPA) to 2.30 nm (for $Zn_2Ga_2Se_5$-3MPA). The trend was however reverse for the telluride quantum dots since the quantum dot increased in the order ZnTe-3MPA (5.30 nm), Ga_2Te_3-3MPA (6.80nm) and $Zn_2Ga_2Te_5$-3MPA (9.30 nm). Presence of gallium in the telluride quantum dot crystal structure was found to decrease the photoluminescence intensity due to presence of dangling bonds related to interstitial gallium vacancies. Gallium did not therefore seem to enhance the optical properties or decrease the size of the telluride quantum dots.

The other part of this study involved application of the synthesized quantum dots and nanocrystals in fabrication of sensing platforms for selected analytes. In the first part of the application, a ZnSe-3MPA quantum dot modified gold electrode was used for simultaneous detection of dopamine, uric acid and ascorbic acid, and consequently to mask the electrochemical oxidation of both uric acid and ascorbic acid, allowing detection of dopamine in their presence. The interfacial kinetics of these substances on quantum dots afforded the use of a novel potential masking approach where only dopamine was electroactive. With this approach a dopamine detection limit of 2.43 x 10^{-10} M (SWV) and 5.65 x 10^{-10} M (steady state amperometry) with fast response time was achieved.

The other target analyte detected in this study was a DNA sequence found in CP4 epsps, a common vector gene in glyphosate resistant transgenic crops. The quantum dots or nanocrystals were in each case used as a platform for immobilization of the probe DNA. Three techniques (EIS, DPV and SWV) were used to monitor hybridization events between the probe DNA and different targets (complementary-the CP4 epsps sequence section, non complementary and a three base mismatch). It was generally observed that all analytical techniques exhibited good linearity, presenting linear correlation coefficients superior to 0.99, indicating that the complementary target can be determined by EIS, DPV or SWV. Low limits of detection, ranging from 0.66 nM to 4.36 nM were obtained. These results indicate that the classical use of quantum dots as DNA tags or labels can be replaced with “use of quantum dots as platforms for probe DNA immobilization”, hence reducing the number of genosensor fabrication procedures, time of fabrication as well as the cost. Successful detection of the studied analytes on the binary and ternary quantum dot/nanocrystals platforms widens the scope of biocompatible nanostructured

platforms upon which other biomolecules of interest can be immobilized for a wide range of analytical purposes.

10.2 Recommendations

1. The modulation of optical and electrical properties of colloidal quantum dots by gallium has only been shown with ZnSe-3MPA and ZnTe-3MPA quantum dots, it would be interesting to investigate what effects gallium would have on other colloidal quantum dot systems.

2. X-ray photon electron spectroscopic (XPS) studies of the synthesized $Ga(ClO_4)_3.6H_2O$ precursor and all other synthesized quantum dots and nanocrystals is worthwhile, to probe the presence of respective atoms in each compound, elucidate their atomic transport and positions as well as incorporation of gallium in the ternary quantum dot systems.

3. A study on the mechanism resulting to different optical and size effects induced by gallium on tellurides and selenides would help understand why gallium had an effect of reduced particle size in selenides but an increased particle size in tellurides.

4. Since all syntheses were done at room temperature, a study on gallium induced-optical and electrical modulation as a function of temperature would be interesting.

5. Scanning electrochemical microscopic studies of all the materials used in this study would help probe their surface point reactivity, revealing all pathways and speed of such reactions.

6. The catalytic properties of the binary and ternary quantum dots were shown with dopamine, uric acid and ascorbic acid. An extension of the quantum dot modified electrodes (not only gold but also others) to detect other analytes of clinical and environmental interest would expand the scope of sensors. Likewise, the biocompatibility properties of the synthesized quantum dots and nanocrystals was demonstrated with DNA (for genosensors) and the enzyme cytochrome P450 3A4 (for detection of 17β estradiol [249], whose scope does not fall within this study), I would recommend the bioconjugation of the quantum dot electrodes with other enzymes and antibodies.

7. I would also highly recommend application of the genosensors for detection of CP4 epsps in transgenic glyphosate resistant soybean and corn.

References

1. Burda, C., X. Chen, R. Narayanan, and M.A. El-Sayed, *Chemistry and Properties of Nanocrystals of Different Shapes.* Chemical Reviews, 2005. **105**: p. 1025-1102.
2. Naik, R.R., S.J. Stringer, G. Agarwal, S.E. Jones, and M.O. Stone, *Biomimetic synthesis and patterning of silver nanoparticles*. Nat Mater, 2002. **1**(3): p. 169-172.
3. GHADIMI, Arya, CADEMARTIRI, Ludovico, KAMP, Ulrich, OZIN, and G. A., *Plasma within Templates : Molding Flexible Nanocrystal Solids into Multifunctional Architectures*. Vol. 7. 2007, Washington, DC, ETATS-UNIS: American Chemical Society. 5.
4. Medintz, L.I., H. Mattoussi, and . *Quantum dot-based resonance energy transfer and its growing application in biology*. Physical Chemistry Chemical Physics, 2009. **11**: p. 17-45.
5. Alivisatos, P., *The use of nanocrystals in biological detection*. Nat Biotech, 2004. **22**(1): p. 47-52.
6. Drbohlavova J, Adam V, Kizek R, and H. J., *Quantum dots - characterization, preparation and usage in biological systems.* International Journal of Molecular Sciences, 2009. **10**(2): p. 656-673.
7. Franzl, T., J. Müller, T.A. Klar, A.L. Rogach, J. Feldmann, D.V. Talapin, and H. Weller, *CdSe:Te Nanocrystals: Band-Edge versus Te-Related Emission*. The Journal of Physical Chemistry C, 2007. **111**(7): p. 2974-2979.

8. Bailey, R.E. and S. Nie, *Alloyed Semiconductor Quantum Dots: Tuning the Optical Properties without Changing the Particle Size*. Journal of American Chemical Society, 2003. **125**: p. 7100-7106.

9. Pradhan, N., D. Goorskey, J. Thessing, and X.G. Peng, *An alternative of CdSe nanocrystal emitters: Pure and tunable impurity emissions in ZnSe nanocrystals*. Journal of American Chemical Society, 2005. **127**: p. 17586-17587.

10. Aldana, J., Y.A. Wang, and X. Peng, *Photochemical Instability of CdSe Nanocrystals Coated by Hydrophilic Thiols*. Journal of American Chemical Society, 2001. **123** (36): p. 8844–8850.

11. Liu, M., G. Shi, L. Zhang, Y. Cheng, and L. Jin, *Quantum dots modified electrode and its application in electroanalysis of hemoglobin.* Electrochemistry Communications, 2006. **8**(2): p. 305-310.

12. Giz, M.J., B. Duong, and N.J. Tao, *In situ STM study of self-assembled mercaptopropionic acid monolayers for electrochemical detection of dopamine*. Journal of Electroanalytical Chemistry, 1999. **465**(1): p. 72-79.

13. Li, J., G. Zou, X. Hu, and X. Zhang, *Electrochemistry of thiol-capped CdTe quantum dots and its sensing application*. Journal of Electroanalytical Chemistry, 2009. **625**(1): p. 88-91.

14. Wang, J., *Nanoparticle-based electrochemical DNA detection.* Analytica Chimica Acta 2003. **500**: p. 247-257.

15. Willner, I. and B. Willner, *Functional nanoparticle architectures for sensoric, optoelectronic, and bioelectronic applications.* Pure and Applied Chemistry, 2002. **74**: p. 1773–1783.

16. Ahmed, F.E., *Detection of genetically modified organisms in foods.* Trends in Biotechnology, 2002. **20**(5): p. 215-223.

17. Saleh-Lakha, S. and B.R. Glick, *Is the battle over genetically modified foods finally over?* Biotechnology Advances, 2005. **23**(2): p. 93-96.

18. Panos, *Genetically Modified Crops. Greed or Need?* Trans IChemE 1999. **77**: p. 165-167.

19. Pelletier, D.L., *FDA's regulation of genetically engineered foods: Scientific, legal and political dimensions.* Food policy, 2006. **31**: p. 570-591.

20. Macek, T., P. Kotrba, A. Svatos, M. Novakova, K. Demnerova, and M. Mackova, *Novel roles for genetically modified plants in environmental protection.* Trends in Biotechnology, 2008. **26**(3): p. 146-152.

21. Taylor, S.L., *Food from genetically modified organisms and potential for food allergy.* Environmental toxicology and pharmacology 1997. **4**: p. 121-126.

22. Losey, J.E., L.S. Rayor, and M.E. Carter, *Transgenic pollen harms monarch larvae.* Nature, 1999. **399**: p. 214.

23. Goodman, R.E., S. Vieths, H.A. Sampson, D. Hill, M. Ebisawa, S.L. Taylor, and R. van Ree, *Allergenicity assessment of genetically modified crops[mdash]what makes sense?* Nat Biotech, 2008. **26**(1): p. 73-81.

24. Saxena, D., S. Flores, and G. Stotzky, *Insecticidal toxin in root exudates from Bt corn.* Nature 1999. **402**: p. 480.

25. Hay, I., M.-J. Morency, and A. Se´guin, *Assessing the persistence of DNA in decomposing leaves of genetically modified poplar trees.* Canadian Journal of Forest Research 2002. **32**: p. 977-982.

26. Chiueh, L.-C., Y.-L. Chen, and D.Y.-C. Shih, *Study on the detection method of six varieties of genetically modified maize on processed foods.* Journal of Food and Drug Analysis, 2002. **10**: p. 25-33.

27. Jennings, J.C., L.D. Albee, D.C. Kolwyck, J.B. Surber, M.L. Taylor, G.F. Hartnell, R.P. Lirette, and K.C. Glenn, *Attempts to detect transgenic and endogenous plant DNA and transgenic protein in muscle from broilers fed YieldGard corn borer corn.* . Poultry Science, 2003. **82**: p. 371-380.

28. REPUBLIC OF SOUTH AFRICA, D.O.A., *GENETICALLY MODIFIED ORGANISMS ACT, 1997 (ACT No. 15 OF 1997)*, in *Government Gazette*. 1997. p. 1-14.

29. Serageldin, I., *Biotechnology and Food Security in the 21st Century*. 1999. p. 387-389.

30. MacPhee, D.J., *Methodological considerations for improving Western blot analysis.* Journal of Pharmacological and Toxicological Methods. **In Press, Corrected Proof**.

31. Ding, C., Q. Zhang, J.-M. Lin, and S.-s. Zhang, *Electrochemical detection of DNA hybridization based on bio-bar code method.* Biosensors and Bioelectronics, 2009. **24**(10): p. 3140-3143.

32. Drummond, T.G., M.G. Hill, and J.K. Barton, *Electrochemical DNA sensors.* Nat Biotech, 2003. **21**(10): p. 1192-1199.

33. Cagnin, S., M. Caraballo, C. Guiducci, P. Martini, M. Ross, M. SantaAna, D. Danley, T. West, and G. Lanfranchi, *Overview of Electrochemical DNA Biosensors: New Approaches to Detect the Expression of Life.* Sensors, 2009. **9**(4): p. 3122-3148.

34. Yin, H., Y. Zhou, Q. Ma, S. Ai, P. Ju, L. Zhu, and L. Lu, *Electrochemical oxidation behavior of guanine and adenine on graphene-Nafion composite film modified glassy*

carbon electrode and the simultaneous determination. Process Biochemistry, 2010. **45**(10): p. 1707-1712.

35. Palecek, E., *Oscillographic Polarography of Highly Polymerized Deoxyribonucleic Acid.* Nature, 1960. **188**(4751): p. 656-657.

36. Li, Q., C. Batchelor-McAuley, and R.G. Compton, *Electrochemical Oxidation of Guanine: Electrode Reaction Mechanism and Tailoring Carbon Electrode Surfaces To Switch between Adsorptive and Diffusional Responses*. The Journal of Physical Chemistry B, 2010. **114**(21): p. 7423-7428.

37. Pournaghi-Azar, M.H., M.S. Hejazi, and E. Alipour, *Developing an electrochemical deoxyribonucleic acid (DNA) biosensor on the basis of human interleukine-2 gene using an electroactive label.* Analytica Chimica Acta, 2006. **570**(2): p. 144-150.

38. Komarova, E., M. Aldissi, and A. Bogomolova, *Direct electrochemical sensor for fast reagent-free DNA detection.* Biosensors and Bioelectronics, 2005. **21**(1): p. 182-189.

39. Wu, K., J. Fei, W. Bai, and S. Hu, *Direct electrochemistry of DNA, guanine and adenine at a nanostructured film-modified electrode.* Analytical and Bioanalytical Chemistry, 2003. **376**(2): p. 205-209.

40. Wang, J., G. Rivas, J.R. Fernandes, J.L. Lopez Paz, M. Jiang, and R. Waymire, *Indicator-free electrochemical DNA hybridization biosensor*. Analytica Chimica Acta, 1998. **375**(3): p. 197-203.

41. Case-Green, S.C. and E.M. Southern, *Studies on the base pairing properties of deoxyinosine by solid phase hybridisation to oligonucleotides.* Nucleic Acids Research, 1994. **22**(2): p. 131-136.

42. Pournaghi-Azar, M.H., M.S. Hejazi, and E. Alipour, *Detection of Human Interleukine-2 Gene Using a Label-Free Electrochemical DNA Hybridization Biosensor on the Basis of a Non-Inosine Substituted Probe*. Electroanalysis, 2007. **19**(4): p. 466-472.

43. Kafka, J., O. Pänke, B. Abendroth, and F. Lisdat, *A label-free DNA sensor based on impedance spectroscopy*. Electrochimica Acta, 2008. **53**(25): p. 7467-7474.

44. Ozkan, D., A. Erdem, P. Kara, K. Kerman, J. Justin Gooding, P.E. Nielsen, and M. Ozsoz, *Electrochemical detection of hybridization using peptide nucleic acids and methylene blue on self-assembled alkanethiol monolayer modified gold electrodes.* Electrochemistry Communications, 2002. **4**(10): p. 796-802.

45. Erdem, A., K. Kerman, B. Meric, U.S. Akarca, and M. Ozsoz, *Novel hybridization indicator methylene blue for the electrochemical detection of short DNA sequences related to the hepatitis B virus.* Analytica Chimica Acta, 2000. **422**(2): p. 139-149.

46. Maruyama, K., J. Motonaka, Y. Mishima, Y. Matsuzaki, I. Nakabayashi, and Y. Nakabayashi, *Detection of target DNA by electrochemical method*. Sensors and Actuators B: Chemical, 2001. **76**(1-3): p. 215-219.

47. Flechsig, G.-U. and T. Reske, *Electrochemical Detection of DNA Hybridization by Means of Osmium Tetroxide Complexes and Protective Oligonucleotides.* Analytical Chemistry, 2007. **79**(5): p. 2125-2130.

48. Pänke, O., A. Kirbs, and F. Lisdat, *Voltammetric detection of single base-pair mismatches and quantification of label-free target ssDNA using a competitive binding assay*. Biosensors and Bioelectronics, 2007. **22**(11): p. 2656-2662.

49. Gao, H., J. Zhong, P. Qin, C. Lin, and W. Sun, *Microplate electrochemical DNA detection for phosphinothricin acetyltransferase gene sequence with cadmium sulfide nanoparticles*. Microchemical Journal, 2009. **93**(1): p. 78-81.

50. Merkoci, A., M. Aldavert, S. Marin, and S. Alegret, *New materials for electrochemical sensing V: Nanoparticles for DNA labeling*. Trends in Analytical Chemistry 2005. **4**: p. 341-349.

51. Kawasaki, E.S. and A. Player, *Nanotechnology, nanomedicine, and the development of new, effective therapies for cancer*. Nanomedicine: Nanotechnology, Biology and Medicine, 2005. **1**(2): p. 101-109.

52. Kluson, P., H. Bartkova, and I. Budil, *Welcome in the nanoworld*. Chemicke Listy, 2007. **101**: p. 262-272.

53. Alivisatos, A.P., W. Gu, and C. Larabell, *Quantum dots as cellular probes*. Annual Review of Biomedical Engineering, 2005. **7**(1): p. 55-76.

54. Michalet, X., F.F. Pinaud, L.A. Bentolila, J.M. Tsay, S. Doose, J.J. Li, G. Sundaresan, A.M. Wu, S.S. Gambhir, and S. Weiss, *Quantum Dots for Live Cells, in Vivo Imaging, and Diagnostics*. Science, 2005. **307**(5709): p. 538-544.

55. Rogach, A.L., A. Eychmüller, S.G. Hickey, and S.V. Kershaw, *Infrared-Emitting Colloidal Nanocrystals: Synthesis, Assembly, Spectroscopy, and Applications*. Small, 2007. **3**(4): p. 536-557.

56. Alivisatos, A.P., *Semiconductor Clusters, Nanocrystals, and Quantum Dots*. Science, 1996. **271**(5251): p. 933-937.

57. Fujioka, K., M. Hiruoka, K. Sato, N. Manabe, R. Miyasaka, S. Hanada, A. Hoshino, R.D. Tilley, Y. Manome, K. Hirakuri, K. Yamamoto, and *Luminescent passive-oxidized silicon*

quantum dots as biological staining labels and their cytotoxicity effects at high concentration. Nanotechnology, 2008. **19**: p. 415102-415109.

58. Walling, M.A., J.A. Novak, J.R.E. Sheppard, and *Quantum Dots for Live Cell and In Vivo Imaging*. International Journal of Molecular Science, 2009. **10**: p. 441-491.

59. Hezinger, A.F.E., J. TeBmar, A. Gopferich, and . *Polymer coating of quantum dots-A powerful tool toward diagnostics and sensorics.* European Journal of Pharmaceutics and Biopharmaceutics, 2008. **68**: p. 138-152.

60. Jin, T., F. Fujii, Y. Komai, J. Seki, A. Seiyman, and Y. Yoshioka, *Preparation and Characterization of Highly Fluorescent, Glutathione-coated Near Infrared Quantum dots for in Vivo Fluorescent Imaging*. International Journal of Molecular Science, 2008. **9**: p. 2044-2061.

61. Chan, W.C.W., D.J. Maxwell, X. Gao, R.E. Bailey, M. Han, and S. Nie, *Luminescent quantum dots for multiplexed biological detection and imaging.* Current Opinion in Biotechnology, 2002. **13**(1): p. 40-46.

62. Benson, R.C. and H.A. Kues, *Fluorescence properties of indocyanine green as related to angiography*. Physics in Medicine and Biology, 1978. **23**: p. 159-163.

63. Gao, X., L. Yang, J.A. Petros, F.F. Marshall, J.W. Simons, and S. Nie, *In vivo molecular and cellular imaging with quantum dots.* Current Opinion in Biotechnology, 2005. **16**(1): p. 63-72.

64. Chan, W.C.W. and S. Nie, *Quantum Dot Bioconjugates for Ultrasensitive Nonisotopic Detection.* Science, 1998. **281**: p. 2016-2018.

65. Mattheakis, L.C., J.M. Dias, Y.-J. Choi, J. Gong, M.P. Bruchez, J. Liu, E. Wang, and . *Optical Coding of Mammalian Cells Using Semiconductor Quantum Dots.* Analytical Biochemistry, 2004. **327**: p. 200-208.

66. Galian, R.E. and M. Miguel de la Guardia, *The use of quantum dots in organic chemistry*. Trends in analytical chemistry, 2009. **28**: p. 279-291.

67. Li, H., W.Y. Shih, and W.-H. Shih, *Non-heavy-metal ZnS quantum dots with bright blue photoluminescence by a one-step aqueous synthesis.* Nanotechnology, 2007. **18** p. 205604-205609.

68. Derfus, A.M., W.C.W. Chan, and S.N. Bhatia, *Probing the Cytotoxicity of Semiconductor Quantum Dots.* Nanoletters, 2004. **4**(1): p. 11-18.

69. Lovrić, J., H.S. Bazzi, Y. Cuie, G.R.A. Fortin, F.M.W. ., and D. Maysinger, *Differences in subcellular distribution and toxicity of green and red emitting CdTe quantum dots.* Journal of Molecular Medicine, 2005. **83**: p. 377-385.

70. Hoshino, A., K. Fujioka, T. Oku, M. Suga, Y.F. Sasaki, T. Ohta, M. Yasuhara, K. Suzuki, and K. Yamamoto, *Physicochemical Properties and Cellular Toxicity of Nanocrystal Quantum Dots Depend on Their Surface Modification*. Nanoletters, 2004. **4**: p. 2163-2169.

71. Chang, E., N. Thekkek, W.W. Yu, V.L. Colvin, and R. Drezek, *Significance of evaluating quantum dot cytotoxicity based on intracellular uptake*. Small 2006. **12**: p. 1412-1417.

72. Zou, J., R.K. Baldwin, K.A. Pettigrew, S.M. Kauzlarich, and . *Solution Synthesis of Ultrastable Luminescent Siloxane-Coated Silicon Nanoparticles.* Nano Letters, 2004. **4**: p. 1181-1186.

73. Burch, R.E., H.K.J. Hahn, and J.F. Sullivan, *Newer aspects of the roles of zinc, manganese and copper in human nutrition.* Clinical Chemistry, 1975. **21**: p. 501-520.

74. Pradhan, N., D.M. Battaglia, Y.C. Liu, X.G. Peng, and . *Efficient, stable, small, and water-soluble doped ZnSe nanocrystal emitters as non-cadmium biomedical labels.* Nano Letters, 2007. **7**: p. 312-317.

75. Garon, E.B., L. Marcu, Q. Luong, O. Tchemiantchouk, G.M. Crooks, and H.P. Koeffler, *Quantum dot labeling and tracking of human leukemic, bone marrow and cord blood cells.* Leukemia Research, 2007. **31**(5): p. 643-651.

76. Narayanan, S.S. and S.K. Pal, *Aggregated CdS quantumdots: Host of biomolecular ligands.* Journal of physical Chemistry B, 2006. **110**: p. 24403-24409.

77. Dahan, M., T. Laurence, F. Pinaud, D.S. Chemla, A.P. Alivisatos, M. Sauer, and S. Weiss, *Time-gated biological imaging by use of colloidal quantum dots.* Opt. Lett., 2001. **26**(11): p. 825-827.

78. Pathak, S., S.-K. Choi, N. Arnheim, and M.E. Thompson, *Hydroxylated Quantum Dots as Luminescent Probes for in Situ Hybridization.* Journal of the American Chemical Society, 2001. **123**(17): p. 4103-4104.

79. Rosenthal, S.J., I. Tomlinson, E.M. Adkins, S. Schroeter, S. Adams, L. Swafford, J. McBride, Y. Wang, L.J. DeFelice, and R.D. Blakely, *Targeting Cell Surface Receptors with Ligand-Conjugated Nanocrystals.* Journal of the American Chemical Society, 2002. **124**(17): p. 4586-4594.

80. Penner, R.M., *Hybrid Electrochemical/Chemical Synthesis of quantum dots.* Accounts of chemical Research, 2000. **33,**: p. 78-86.

81. Murray, C.B., D.J. Norris, and M.G. Bawendi, *Synthesis and Characterization of Nearly Monodisperse CdE (E = sulfur, selenium, tellurium) Semiconductor Nanocrystallites.* Journal of American Chemical Society, 1993. **115**: p. 8706-8715.

82. Missous, M. and J. Ng, *Improvements of stacked self-assembled InAs/GaAs quantum dot structures for 1.3 mm applications.* Microelectronics Journal, 2006. **37**: p. 1446-1450.

83. Rinaldi, F., *Basics of Molecular Beam Epitaxy (MBE)*. 2002, Optoelectronics Department, University of Ulm.

84. Chen, K.S., I.K. Lin, and F.H. Ko, *Fabrication of 3D polymer mictrostructure using electron beam lithography and nanoimprinting technologies.* . Journal of Micromechanics and Micro Engineering 2005. **15**: p. 1894-1903.

85. Tomczak, N., D. Janczewski, M. Han, and G.J. Vancso, *Designer polymer-quantum dot architectures.* Progress in Polymer Science, 2009. **34**(5): p. 393-430.

86. Li, Y., Y. Ding, Y. Zhang, and Y. Qian, *Photophysical properties of ZnS quatum dots.* Journal of Physics and Chemistry of Solids, 1999. **60**: p. 13-15.

87. Zeng, H.Z., K.Q. Qiu, Y.Y. Du, and W.Z. Li, *A new way to synthesize ZnS nanopartices.* Chinese Chemical letters, 2007. **18**: p. 483-486.

88. Zhang, F., C. Li, X. Li, X. Wang, Q. Wan, Y. Xian, L. Jin, and K. Yamamoto, *ZnS quantum dots derived a reagentless uric acid biosensor.* Talanta, 2006. **68**(4): p. 1353-1358.

89. Bodas, D. and C.K. M., *Direct patterning of quantum dots on structured PDMS surface.* Sensors and Actuators B, 2007. **128**: p. 168-172.

90. Peng, Z.A. and P. X., *Mechanisms of the shape evolution of CdSe nanocrystals.* Journal of American Chemical Society 2001. **123**: p. 1389-1395.

91. Yu, W.W., Y.A. Wang, and X. Peng, *Formation and stability of size-, shape-, and structure-controlled CdTe nanocrystals: ligand effects on monomers and nanocrystals.* Chemistry of Materials, 2003. **15**: p. 4300-4308.

92. Aldana, J., Y.A. Wang, and X. Peng, *Photochemical instability of CdSe nanocrystals coated by hydrophilic thiols*. Journal of American Chemical Society, 2001. **123**: p. 8844-8850.

93. Wuister, S.F., I. Swart, F. van Driel, S.G. Hickey, and D.C. de Mello, *Highly luminescent water-soluble CdTe quantum dots.* Nano Letters, 2003. **3**: p. 503-507.

94. Pathak, S., S.K. Choi, N. Arnheim, and M.E. Thompson, *Hydroxylated quantum dots as luminescent probes for in situ hybridization*. Journal of American Chemical Society 2001. **123**: p. 4103-4104.

95. Kim, S. and M.G. Bawendi, *Oligomeric ligands for luminescent and stable nanocrystal quantum dots*. Journal of American Chemical Society, 2003. **125**: p. 14652-14653.

96. Pinaud, F., D. King, H.-P. Moore, and S. Weiss, *Bioactivation and cell targeting of semiconductor CdSe/ZnS nanocrystals with phytochelatin-related peptides.* Journal of American Chemical Society 2004. **126**: p. 6115-6123.

97. Guo, W., J.J. Li, Y.A. Wang, and X. Peng, *Conjugation chemistry and bioapplications of semiconductor box nanocrystals prepared via dendrimer bridging.* Chemistry Materials 2003. **15**: p. 3125-3133.

98. Gerion, D., F. Pinaud, S.C. Williams, W.J. Parak, D. Zanchet, S. Weiss, and A.P. Alivisatos, *Synthesis and Properties of Biocompatible Water-Soluble Silica-Coated CdSe/ZnS semiconductor Quantum dots*. Journal of Physical Chemistry 2001. **105**: p. 8861-8871.

99. Bailey, R.E., A.M. Smith, and S. Nie, *Quantum dots in biology and medicine*. Physica E 2004. **25**: p. 1-12.

100. Van Sark, W.G.J.H.M., P.L.T.M. Frederix, A.A. Bol, H.C. Gerritsen, and A. Meijerink, *Blueing, bleaching and blinking of single CdSe/ZnS quantum dots*. ChemPhysChem, 2002. **3**: p. 871-879.

101. Van Sark, W.G.J.H.M., P.L.T.M. Frederix, D.J. van de Heuvel, and H.C. Gerritsen, *Photo oxidation and photo bleaching of single CdSe/ZnS quantum dots probed by room temperature time resolved spectroscopy*. Journal of Physical Chemistry B, 2001. **105**: p. 8281-8284.

102. Uyenda, H.T., M. I.L., J.K. Jaiswal, S.M. Sanford, and H. Mattoussi, *Synthesis of Compact Multidentate Ligands to Prepare Stable Hydrophilic Quantum Dot Fluorophores*. Journal of American Chemical Society, 2005. **127**: p. 3870-3878.

103. Jin, T., F. Fujii, H. Sakata, M. Tamura, and M. Kinjo, *Amphiphilic p-sulfonatocalix[4]arene-coated CdSe/ZnS quantum dots for the optical detection of the neurotransmitter acetylcholine*. Chemistry Communications, 2005: p. 4300-4302.

104. Shang, B.Z., Y. Wang, and W.J. Jin, *Triethanolamine-capped CdSe quantum dots as fluorescent sensors for reciprocal recognition of mercury (II) and iodide in aqueous solution*. Talanta 2009. **78**: p. 364-369.

105. Liao, P., Z.Y. Yan, Z.J. Xu, and X. Sun, *A novel fluorescent assay for edaravone with aqueous functional CdSe quantum dots*. Spectrochimica Acta part A: Molecular and Biomolecular Spectroscopy, 2009. **72**: p. 1066-1070.

106. Oluwafemi, S.O., N. Revaprasadu, and A.J. Ramirez, *A novel one-spot route for the synthesis of water soluble cadmium selenide nanoparticles.* Journal of crystal growth, 2008. **310**: p. 3230-3234.

107. Crooks, R.M., M.Q. Zhao, L. Sun, V. Chechik, and L.K. Yeung, *Dendrimer-encapsulated metal nanoparticles: synthesis, characterization and applications to catalysis.* Accounts of Chemical Research, 2001. **34**: p. 181-190.

108. Wisher, A.C., V. Bronstein, and V. Chechik, *Thiolated PAMPAM dendrimer-coated CdSe/ZnSe nanoparticles as protein transfection agents*. . Chemical Communication, 2006: p. 1637-1639.

109. Lemon, B.I. and R.M. Crooks, *Preparation and Characterization of Dendrimer-Encapsulated CdS semiconductor quantum dots*. Journal of American Chemical Society 2000. **122**: p. 12886-12887.

110. Moore, D.E. and K. Patel, *Q-CdS Photoluminescence Activation on Zn2+ and Cd2+ Salt Introduction.* Langmuir 2001. **1**: p. 2541-2544.

111. Costa-Fernandez, J.M., R. Pereiro, and A.S. Medel, *The use of luminescence quantum dots for optical sensing*. Trends in Analytical Chemistry, 2006. **25**: p. 207-217.

112. Gattas-Asfura, K.M. and R.M. Leblanc, *Peptide coated quantum dots for the optical detection of copper(II) and silver(I).* Chemical Communications 2003. **7**: p. 2684-2685.

113. Fernandez, M.T., W.J. Jin, J.M. Costa-Fernandez, and S.-M. Pereiro, *Surface modified CdSe quantum dots for the sensitive and selective determination of Cu(II) in aqueous solutions by luminescence measurements.* Analytica Chimica Acta, 2005. **549**: p. 20-25.

114. Xie, H.Y., J.G. Liang, Z.L. Zhang, Y. Liu, Z.K. He, and D.W. Pang, *Luminescence CdSe-ZnS quantum dots as selective Cu2+ probe.* Spectrochimica Acta Part A: Molecular and Biomolecular Spectroscopy, 2004. **60**: p. 2527-2530.

115. Bo, C. and Z. Ping, *A new determining method of copper(II) ions at ng ml-1 levels based on quenching of the water soluble nanocrystals fluorescence.* Analytical and Bioanalytical Chemistry, 2005. **38**: p. 986-992.

116. Chen, Y. and Z. Rosenzweing, *Luminescence CdS quantum dots as selective ion probes.* Analytical Chemistry, 2002. **74**: p. 5132-5138.

117. Jin, W.J., J.M. Costa-Fernandez, and A.S. Medel, *Surface modified CdSe quantum dots as luminescence probes for cyanide determination.* Analytica Chimica Acta, 2004. **43**: p. 1-8.

118. Jin, W.J., M.T. Fernandez-Argulles, J.M. Costa-Fernandez, R. Pereiro, and A.S. Medel., *Photo activated luminescence CdSe quantum dots as sensitive cyanide probes in aqueous solutions.* Chemical Communications, 2005: p. 883-885.

119. Duong, H.D. and J. Rhee, *Use of CdSe/ZnS core-shell quantum dots as energy transfer donors in sensing glucose.* Talanta 2007. **73**: p. 899-905.

120. Yuan, J., W. Guo, and E. Wang, *Quantum dots-bienzymatic hybrid system for the sensitive determination of glucose.* Biosensors and Bioelectronics, 2008. **23**: p. 1567-1571.

121. Huang, C.P., S.W. Liu, T.M. Chen, and Y.K. Li, *A new approach for quantitative determination of glucose by using CdSe/ZnS quantum dots.* Sensors and Actuators B 2008. **130**: p. 338-342.

122. Yuan, J., W. Gui, J. Yin, and E. Wang, *Glutathione-capped CdTe quantum dots for the sensitive detection of glucose.* Talanta 2009. **77**: p. 1858-1863.

123. Suman, K., A., *Recent advances in DNA biosensor.* Sensors and Transducers Journal, 2008. **92**: p. 122-133.

124. Garon, B.E., L. Marcu, Q. Luong, O. Tcherniantchouk, G.M. Crooks, and H.P. Koeffler, *Quantum dots labeling and tracking of human leukemic, bone marrow and cord blood cells.* Leukemia Research, 2007. **31**: p. 643-651.

125. Sun, J.F., C.L. Ren, L.H. Liu, and X.G. Chen, *CdTe quantum dots as fluorescence sensor for the determination of vitamin B6 in aqueous solution.* Chinese Chemical Letters, 2008. **19**: p. 855-859.

126. Xu, C., B. Xing, and J. Rao, *A self-assembled quantum dot probe for detecting β-lactamase activity.* Biochemical and Biophysical Research Communications, 2006. **344**: p. 931-935.

127. Yen, H.C., Y.P. Ho, and T.H. Wang, *Quantum dot-mediated biosensing assays for specific nucleic acid detection.* Nanomedicine 2005. **1**: p. 115-121.

128. Wang, Z., Q. Xu, H.-Q. Wang, Q. Yang, J.-H. Yu, and Y.-D. Zhao, *Hydrogen peroxide biosensor based on direct electron transfer of horseradish peroxidase with vapor deposited quantum dots.* Sensors and Actuators B: Chemical, 2009. **138**(1): p. 278-282.

129. Xu, Y.X., J.G. Liang, C.G. Hu, F. Wang, S.S. Hu, and Z.K. He, *A hydrogen peroxide biosensor based on the direct electrochemistry of hemoglobin modified with quantum dots.* Journal of Biology and Inorganic Chemistry 2007. **12**: p. 421-427.

130. Xiao, Y., H.X. Ju, and H.Y. Chen, *Direct Electrochemistry of Horseradish peroxidase on a Colloid/Cysteamine-Modified Gold Electrode.* Analytical Biochemistry, 2000. **278**: p. 22-28.

131. Pividori, M.I., A. Merkoçi, and S. Alegret, *Electrochemical genosensor design: immobilisation of oligonucleotides onto transducer surfaces and detection methods.* Biosensors and Bioelectronics, 2000. **15**(5-6): p. 291-303.

132. Mannelli, I., M. Minunni, S. Tombelli, R. Wang, M. Michela Spiriti, and M. Mascini, *Direct immobilisation of DNA probes for the development of affinity biosensors.* Bioelectrochemistry, 2005. **66**(1-2): p. 129-138.

133. Wang, J., *Electrochemical nucleic acid biosensors*. Analytica Chimica Acta, 2002. **469**(1): p. 63-71.

134. Watterson, J.H., P.A.E. Piunno, C.C. Wust, and U.J. Krull, *Effects of Oligonucleotide Immobilization Density on Selectivity of Quantitative Transduction of Hybridization of Immobilized DNA.* Langmuir, 2000. **16**(11): p. 4984-4992.

135. Zhang, R.-Y., D.-W. Pang, Z.-L. Zhang, J.-W. Yan, J.-L. Yao, Z.-Q. Tian, B.-W. Mao, and S.-G. Sun, *Investigation of Ordered ds-DNA Monolayers on Gold Electrodes.* The Journal of Physical Chemistry B, 2002. **106**(43): p. 11233-11239.

136. Tully, E., S.P. Higson, and R. O'Kennedy, *The development of a [`]labeless' immunosensor for the detection of Listeria monocytogenes cell surface protein, Internalin B.* Biosensors and Bioelectronics, 2008. **23**(6): p. 906-912.

137. Zhu, N., Z. Chang, P. He, and Y. Fang, *Electrochemically fabricated polyaniline nanowire-modified electrode for voltammetric detection of DNA hybridization.* Electrochimica Acta, 2006. **51**(18): p. 3758-3762.

138. Arotiba, O.A., J.H. Owino, P.G. Baker, and E.I. Iwuoha, *Electrochemical impedimetry of electro-deposited poly(propylene imine) dendrimer monolayer*. Journal of Electroanalytical Chemistry, 2009.

139. Arotiba, O., J. Owino, E. Songa, N. Hendricks, T. Waryo, N. Jahed, P. Baker, and E. Iwuoha, *An Electrochemical DNA Biosensor Developed on a Nanocomposite Platform of Gold and Poly(propyleneimine) Dendrimer*. Sensors, 2008. **8**(11): p. 6791-6809.

140. Gore, M.R., V.A. Szalai, P.A. Ropp, I.V. Yang, J.S. Silverman, and H.H. Thorp, *Detection of Attomole Quantitites of DNA Targets on Gold Microelectrodes by Electrocatalytic Nucleobase Oxidation*. Analytical Chemistry, 2003. **75**(23): p. 6586-6592.

141. Zhang, S., G. Wright, and Y. Yang, *Materials and techniques for electrochemical biosensor design and construction*. Biosensors and Bioelectronics, 2000. **15**(5-6): p. 273-282.

142. Malhotra, B.D., A. Chaubey, and S.P. Singh, *Prospects of conducting polymers in biosensors.* Analytica Chimica Acta, 2006. **578**(1): p. 59-74.

143. Tam, P.D., T. Trung, M.A. Tuan, and N.D. Chien, *Electrochemical direct immobilization of DNA sequences for label-free herpes virus detection.* Journal of Physics: Conference series, 2009. **187**: p. 1-8.

144. Pack, S.P., N.K. Kamisetty, M. Nonogawa, Kamakshaiah, C. Devarayapalli, K. Ohtani, K. Yamada, Y. Yoshida, TsutomuKodaki, and K. Makino, *Direct immobilization of DNA oligomers onto the amine-functionalized glass surface for DNA microarray fabrication through the activation-free reaction of oxanine*. Nucleic Acids Research, 2007. **35**: p. 1-10.

145. Dufva, M., *Fabrication of high quality microarrays.* Biomolecular Engineering, 2005. **22**(5-6): p. 173-184.

146. Kamisetty, N., S. Pack, M. Nonogawa, K. Devarayapalli, T. Kodaki, and K. Makino, *Development of an efficient amine-functionalized glass platform by additional silanization treatment with alkylsilane*. Analytical and Bioanalytical Chemistry, 2006. **386**(6): p. 1649-1655.

147. Lai, R.Y., D.S. Seferos, A.J. Heeger, G.C. Bazan, and K.W. Plaxco, *Comparison of the Signaling and Stability of Electrochemical DNA Sensors Fabricated from 6- or 11-Carbon Self-Assembled Monolayers†*. Langmuir, 2006. **22**(25): p. 10796-10800.

148. Daniels, J.S. and N. Pourmand, *Label-Free Impedance Biosensors: Opportunities and Challenges.* Electroanalysis, 2007. **19**(12): p. 1239-1257.

149. Boubour, E. and R.B. Lennox, *Stability of ω-Functionalized Self-Assembled Monolayers as a Function of Applied Potential*. Langmuir, 2000. **16**(19): p. 7464-7470.

150. Boubour, E. and R.B. Lennox, *Potential-Induced Defects in n-Alkanethiol Self-Assembled Monolayers Monitored by Impedance Spectroscopy.* The Journal of Physical Chemistry B, 2000. **104**(38): p. 9004-9010.

151. Carraraa, S., F.K. Gürkaynak, C. Guiduccic, Claudio Stagnic, L. Beninic, Y. Leblebici, B. Samorìa, and G.D. Michelib, *Interface Layering Phenomena in Capacitance Detection of DNA with Biochips.* Sensors & Transducers Journal,, 2007. **76**: p. 969-977.

152. Lao, R., S. Song, H. Wu, L. Wang, Z. Zhang, L. He, and C. Fan, *Electrochemical Interrogation of DNA Monolayers on Gold Surfaces.* Analytical Chemistry, 2005. **77**(19): p. 6475-6480.

153. Benters, R., C.M. Niemeyer, and D. Wöhrle, *Dendrimer-Activated Solid Supports for Nucleic Acid and Protein Microarrays.* ChemBioChem, 2001. **2**(9): p. 686-694.

154. Zammatteo, N., L. Jeanmart, S. Hamels, S. Courtois, P. Louette, L. Hevesi, and J. Remacle, *Comparison between Different Strategies of Covalent Attachment of DNA to Glass Surfaces to Build DNA Microarrays.* Analytical Biochemistry, 2000. **280**(1): p. 143-150.

155. Livnah, O., E.A. Bayer, M. Wilchek, and J.L. Sussman, *Three-dimensional structures of avidin and the avidin-biotin complex.* Proceedings of the National Academy of Sciences of the United States of America, 1993. **90**(11): p. 5076-5080.

156. Asai, T., R. Trinh, P.P. Ng, M.L. Penichet, L.A. Wims, and S.L. Morrison, *A human biotin acceptor domain allows site-specific conjugation of an enzyme to an antibody-avidin fusion protein for targeted drug delivery.* Biomolecular Engineering, 2005. **21**(6): p. 145-155.

157. Wu, K.K., *Analysis of Protein-DNA Binding by Streptavidin-Agarose Pulldown*, in *Gene Mapping, Discovery, and Expression*, M. Bina, Editor. 2006, Humana Press. p. 281-290.

158. Gadgil, H., L.A. Jurado, and H.W. Jarrett, *DNA Affinity Chromatography of Transcription Factors.* Analytical Biochemistry, 2001. **290**(2): p. 147-178.

159. Wang, J., G. Liu, R.M. Jan, and Q. Zhu, *Electrochemical detection of DNA hybridization based on carbon -nanotubes loaded with CdS tags.* Electrochemistry Communications, 2003. **5**: p. 1000-1004.

160. Wang, J., G. Liu, R. Polsky, and A. Merkoci, *Electrochemical stripping detection of DNA hybridization based on cadmium sulfide nanoparticle tags.* Electrochemistry Communications, 2002. **4**: p. 722-726.

161. Zhu, S., H. Li, W. Niu, and G. Xu, *Simultaneous electrochemical determination of uric acid, dopamine, and ascorbic acid at single-walled carbon nanohorn modified glassy carbon electrode.* Biosensors and Bioelectronics, 2009. **25**(4): p. 940-943.

162. Sun, W., J. Zhong, P. Qin, and K. Jiao, *Electrochemical biosensor for the detection of cauliflower mosaic virus 35 S gene sequences using lead sulfide nanoparticles as oligonucleotide labels.* Analytical Biochemistry 2008. **377**: p. 115-119.

163. Du, P., H. Li, and W. Cao, *Construction of DNA sandwich electrochemical biosensor with nanoPbS nanoAu tags on magnetic microbeads.* Biosensors and Bioelectronics, 2009. **24**: p. 3223-3228.

164. Hu, K., P. Liu, S. Ye, and S. Zhang, *Ultrasensitive electrochemical detection of DNA based on PbS nanoparticle tags and nanoporous gold electrode*. Biosensors and Bioelectronics, 2009. **24**: p. 3113-3119.

165. Sun, W., J. Zhong, B. Zhang, and K. Jiao, *Application of cadmium sulfide nanoparticles as oligonucleotide labels for the electrochemical detection of NOS terminator gene sequence.* Analytical and Bioanalytical Chemistry 2007. **389**: p. 2179-2184.

166. Huang, D., H. Liu, B. Zhang, K. Jiao, X. Fu, and . *Highly sensitive electrochemical detection of sequence-specific DNA of 35S promoter of cauliflower mosaic virus gene using CdSe quantum dots and gold nanoparticles*. . Microchimica Acta, 2009. **165**: p. 243-248.

167. Bonanni, A. and M. del Valle, *Use of nanomaterials for impedimetric DNA sensors: A review.* Analytica Chimica Acta, 2010. **678**(1): p. 7-17.

168. Wang, J., *Nanomaterial-based electrochemical biosensors.* Analyst, 2005. **130**(4): p. 421-426.

169. Xu, Y., Y. Jiang, H. Cai, P.-G. He, and Y.-Z. Fang, *Electrochemical impedance detection of DNA hybridization based on the formation of M-DNA on polypyrrole/carbon nanotube modified electrode.* Analytica Chimica Acta, 2004. **516**(1-2): p. 19-27.

170. Xu, Y., X. Ye, L. Yang, P. He, and Y. Fang, *Impedance DNA Biosensor Using Electropolymerized Polypyrrole/Multiwalled Carbon Nanotubes Modified Electrode.* Electroanalysis, 2006. **18**(15): p. 1471-1478.

171. Bonanni, A., M.I. Pividori, and M. del Valle, *Impedimetric detection of influenza A (H1N1) DNA sequence using carbon nanotubes platform and gold nanoparticles amplification.* Analyst, 2010. **135**(7): p. 1765-1772.

172. Caliskan, A., A. Erdem, and H. Karadeniz, *Direct DNA Hybridization on the Single-Walled Carbon Nanotubes Modified Sensors Detected by Voltammetry and Electrochemical Impedance Spectroscopy*. Electroanalysis, 2009. **21**(19): p. 2116-2124.

173. Jiang, C., T. Yang, K. Jiao, and H. Gao, *A DNA electrochemical sensor with poly-l-lysine/single-walled carbon nanotubes films and its application for the highly sensitive EIS detection of PAT gene fragment and PCR amplification of NOS gene*. Electrochimica Acta, 2008. **53**(6): p. 2917-2924.

174. Palecek, E., *Past, present and future of nucleic acids electrochemistry*. Talanta, 2002. **56**(5): p. 809-819.

175. Peng, H., C. Soeller, M.B. Cannell, G.A. Bowmaker, R.P. Cooney, and J. Travas-Sejdic, *Electrochemical detection of DNA hybridization amplified by nanoparticles*. Biosensors and Bioelectronics, 2006. **21**(9): p. 1727-1736.

176. Travas-Sejdic, J., H. Peng, R.P. Cooney, G.A. Bowmaker, M.B. Cannell, and C. Soeller, *Amplification of a conducting polymer-based DNA sensor signal by CdS nanoparticles.* Current Applied Physics, 2006. **6**(3): p. 562-566.

177. Ghanbari, K., S.Z. Bathaie, and M.F. Mousavi, *Electrochemically fabricated polypyrrole nanofiber-modified electrode as a new electrochemical DNA biosensor.* Biosensors and Bioelectronics, 2008. **23**(12): p. 1825-1831.

178. Peng, H., C. Soeller, and J. Travas-Sejdic, *Novel Conducting Polymers for DNA Sensing.* Macromolecules, 2007. **40**(4): p. 909-914.

179. Peng, H., C. Soeller, N.A. Vigar, V. Caprio, and J. Travas-Sejdic, *Label-free detection of DNA hybridization based on a novel functionalized conducting polymer.* Biosensors and Bioelectronics, 2007. **22**(9-10): p. 1868-1873.

180. Feng, Y., T. Yang, W. Zhang, C. Jiang, and K. Jiao, *Enhanced sensitivity for deoxyribonucleic acid electrochemical impedance sensor: Gold nanoparticle/polyaniline nanotube membranes.* Analytica Chimica Acta, 2008. **616**(2): p. 144-151.

181. Zhou, N., T. Yang, C. Jiang, M. Du, and K. Jiao, *Highly sensitive electrochemical impedance spectroscopic detection of DNA hybridization based on Aunano-CNT/PANnano films.* Talanta, 2009. **77**(3): p. 1021-1026.

182. Yang, J., T. Yang, Y. Feng, and K. Jiao, *A DNA electrochemical sensor based on nanogold-modified poly-2,6-pyridinedicarboxylic acid film and detection of PAT gene fragment.* Analytical Biochemistry, 2007. **365**(1): p. 24-30.

183. Arotiba, O.A., A. Ignaszak, R. Malgas, A. Al-Ahmed, P.G.L. Baker, S.F. Mapolie, and E.I. Iwuoha, *An electrochemical DNA biosensor developed on novel multinuclear*

nickel(II) salicylaldimine metallodendrimer platform. Electrochimica Acta, 2007. **53**(4): p. 1689-1696.

184. Arotiba, O.A., P.G. Baker, B.B. Mamba, and E.I. Iwuoha, *The Application of Electrodeposited Poly(Propylene imine) Dendrimer as an Immobilisation Layer in a Simple Electrochemical DNA Biosensor*. International Journal of Electrochemical Science, 2011. **6**: p. 673 - 683.

185. Fu, Y., R. Yuan, L. Xu, Y. Chai, X. Zhong, and D. Tang, *Indicator free DNA hybridization detection via EIS based on self-assembled gold nanoparticles and bilayer two-dimensional 3-mercaptopropyltrimethoxysilane onto a gold substrate*. Biochemical Engineering Journal, 2005. **23**(1): p. 37-44.

186. Irina, K., M. Mihaela, S. Monica, I. Teodora, B. Adina, C. Florea, and D. Mihai, *Study of the Micro- and Nanostructured Silicon for Biosensing and Medical Applications*. Journal of Biomedical Nanotechnology, 2009. **5**: p. 300-309.

187. Vamvakaki, V. and N.A. Chaniotakis, *DNA Stabilization and Hybridization Detection on Porous Silicon Surface by EIS and Total Reflection FT-IR Spectroscopy*. Electroanalysis, 2008. **20**(17): p. 1845-1850.

188. Moreno-Hagelsieb, L., P.E. Lobert, R. Pampin, D. Bourgeois, J. Remacle, and D. Flandre, *Sensitive DNA electrical detection based on interdigitated Al/Al2O3 microelectrodes.* Sensors and Actuators B: Chemical, 2004. **98**(2-3): p. 269-274.

189. Bonanni, A., M.J. Esplandiu, and M. del Valle, *Signal amplification for impedimetric genosensing using gold-streptavidin nanoparticles.* Electrochimica Acta, 2008. **53**(11): p. 4022-4029.

190. Xu, Y., H. Cai, P.-G. He, and Y.-Z. Fang, *Probing DNA Hybridization by Impedance Measurement Based on CdS-Oligonucleotide Nanoconjugates.* Electroanalysis, 2004. **16**(1-2): p. 150-155.

191. Kjällman, T.H.M., H. Peng, C. Soeller, and J. Travas-Sejdic, *A CdTenanoparticle-modified hairpin probe for direct and sensitive electrochemical detection of DNA* Analyst, 2010. **135**: p. 488-494.

192. Mirceski, V., R. Gulaboski, B. Jordanoski, and S. Komorsky-Lovric, *Square-wave voltammetry of 5-fluorouracil.* Journal of Electroanalytical Chemistry, 2000. **490**(1-2): p. 37-47.

193. Mbindyo, J., L. Zhou, Z. Zhang, J.D. Stuart, and J.F. Rusling, *Detection of Chemically Induced DNA Damage by Derivative Square Wave Voltammetry*. Analytical Chemistry, 2000. **72**(9): p. 2059-2065.

194. Rusling, J.F., L. Zhou, B. Munge, J. Yang, C. Estavilloa, and J.B. Schenkmanb, *Applications of polyion Đlms containing biomolecules to sensing toxicity.* Faraday Discussions of the Chemical Society, 2000. **116**: p. 77-87.

195. Mugweru, A. and J.F. Rusling, *Catalytic square-wave voltammetric detection of DNA with reversible metallopolymer-coated electrodes.* Electrochemistry Communications, 2001. **3**(8): p. 406-409.

196. Masarik, M., R. Kizek, K. Kramer, S. Billova, M. Brazdova, J. Vacek, M. Bailey, F. Jelen, and J. Howard, *Application of avidin-biotin technology and adsorptive transfer stripping square-wave voltammetry for detection of DNA hybridization and avidin in transgenic avidin maize.* Analytical Chemistry, 2003. **75**: p. 2663-2669.

197. Sabzi, R.E., B. Sehatnia, M.H. Pournaghi-Azar, and M.S. Hejazi, *Electrochemical Detection of Human Papilloma Virus (HPV) Target DNA Using MB on Pencil Graphite Electrode*. Journal of Iranian Chemical Society, 2008. **5**: p. 476-483.

198. Zhang, K. and Y. Zhang, *Lable-Free Electrochemical DNA Sensor Based on Gold Nanoparticles/Poly(neutral red) Modified Electrode.* Electroanalysis, 2010. **22**(6): p. 673-679.

199. Du, P., H. Li, Z. Mei, and S. Liu, *Electrochemical DNA biosensor for the detection of DNA hybridization with the amplification of Au nanoparticles and CdS nanoparticles.* Bioelectrochemistry, 2009. **75**(1): p. 37-43.

200. Scholes, G.D., M. Jones, and S. Kumar, *Energetics of Photoinduced Electron-Transfer Reactions Decided by Quantum Confinement.* The Journal of Physical Chemistry C, 2007. **111**(37): p. 13777-13785.

201. Gavalasa, V.G., N.A. Chaniotakisa, and T.D. Gibsonb, *Improved operational stability of biosensors based on enzyme-polyelectrolyte complex adsorbed into a porous carbon electrode.* Biosensors and Bioelectronics, 1998. **13** p. 1205-1211.

202. BUCK, R.P. and E. LINDNERI, *RECOMENDATIONS FOR NOMENCLATURE OF ION-SELECTIVE ELECTRODES.* Pure and Applied Chemistry, 1994. **66**: p. 2527-2536.

203. Zhang, X., H. Ju, and J. Wang, *Electrochemical Sensors, Biosensors and their Biomedical applications*. 2008, San Diego: Academic press, Elsevier.

204. Park, J.-Y. and S.-M. Park, *DNA Hybridization Sensors Based on Electrochemical Impedance Spectroscopy as a Detection Tool.* Sensors, 2009. **9**(12): p. 9513-9532.

205. Bard, A.J. and L.R. Faulkner, *Electrochemical methods: Fundamentals and applications*. 2nd edition ed. 2000, New York: Wiley.

206. Akagi, Y., M. Makimura, Y. Yokoyama, M. Fukazawa, S. Fujiki, M. Kadosaki, and K. Tanino, *Development of a ligation-based impedimetric DNA sensor for single-nucleotide polymorphism associated with metabolic syndrome.* Electrochimica Acta, 2006. **51**(28): p. 6367-6372.

207. Katz, E. and I. Willner, *Probing Biomolecular Interactions at Conductive and Semiconductive Surfaces by Impedance Spectroscopy: Routes to Impedimetric Immunosensors, DNA-Sensors, and Enzyme Biosensors.* Electroanalysis, 2003. **15**: p. 913-947.

208. Bonanni, A., M.J. Esplandiu, and M. del Valle, *Impedimetric genosensors employing COOH-modified carbon nanotube screen-printed electrodes.* Biosensors and Bioelectronics, 2009. **24**(9): p. 2885-2891.

209. Macdonald, D.D., *Reflections on the history of electrochemical impedance spectroscopy.* Electrochimica Acta, 2006. **51**(8-9): p. 1376-1388.

210. Farace, G., G. Lillie, T. Hianik, P. Payne, and P. Vadgama, *Reagentless biosensing using electrochemical impedance spectroscopy*. Bioelectrochemistry, 2002. **55**(1-2): p. 1-3.

211. Huang, H., Z. Liu, and X. Yang, *Application of electrochemical impedance spectroscopy for monitoring allergen-antibody reactions using gold nanoparticle-based biomolecular immobilization method*. Analytical Biochemistry, 2006. **356**(2): p. 208-214.

212. Tlili, C., H. Korri-Youssoufi, L. Ponsonnet, C. Martelet, and N.J. Jaffrezic-Renault, *Electrochemical impedance probing of DNA hybridisation on oligonucleotide-functionalised polypyrrole*. Talanta, 2005. **68**(1): p. 131-137.

213. Kharitonov, A.B., L. Alfonta, E. Katz, and I. Willner, *Probing of bioaffinity interactions at interfaces using impedance spectroscopy and chronopotentiometry.* Journal of Electroanalytical Chemistry, 2000. **487**(2): p. 133-141.

214. Rout, T.K., *Electrochemical impedance spectroscopy study on multi-layered coated steel sheets.* Corrosion Science, 2007. **49**(2): p. 794-817.

215. Lisdat, F. and D. Schäfer, *The use of electrochemical impedance spectroscopy for biosensing.* Analytical and Bioanalytical Chemistry, 2008. **391**: p. 1555-1567.

216. Wang, Y., S.R. Belding, E.I. Rogers, and R.G. Compton, *A kinetic and mechanistic study of the electrochemical oxidation of hydroquinone in 1-ethyl-3-methylimidazolium bis(trifluoromethanesulfonyl)imide, [C2mim][NTf2].* Journal of Electroanalytical Chemistry, 2011. **650**(2): p. 196-204.

217. Nicholson, R.S., *Theory and Application of Cyclic Voltammetry for Measurement of Electrode Reaction Kinetics.* Analytical Chemistry, 1965. **37**(11): p. 1351-1355.

218. Nicholson, R.S., *Theory and Application of Cyclic Voltammetry for Measurement of Electrode Reaction Kinetics.* Analytical Chemistry, 1965. **37**: p. 1351–1355.

219. Lavagnini, I., R. Antiochia, and F. Magno, *An Extended Method for the Practical Evaluation of the Standard Rate Constant from Cyclic Voltammetric Data.* Electroanalysis, 2004. **16**(6): p. 505-506.

220. Haram, S.K., B.M. Quinn, and A.J. Bard, *Electrochemistry of CdS Nanoparticles: A Correlation between Optical and Electrochemical Band Gaps.* Journal of the American Chemical Society, 2001. **123**(36): p. 8860-8861.

221. Poznyak, S.K., N.P. Osipovich, A. Shavel, D.V. Talapin, M. Gao, A. Eychmüller, and N. Gaponik, *Size-Dependent Electrochemical Behavior of Thiol-Capped CdTe Nanocrystals in Aqueous Solution.* The Journal of Physical Chemistry B, 2005. **109**(3): p. 1094-1100.

222. Kuçur, E., W. Bücking, R. Giernoth, and T. Nann, *Determination of Defect States in Semiconductor Nanocrystals by Cyclic Voltammetry*. The Journal of Physical Chemistry B, 2005. **109**(43): p. 20355-20360.

223. Ullah, M.H., I. Kim, and C.-S. Ha, *pH selective synthesis of ZnS nanocrystals and their growth and photoluminescence.* Materials Letters, 2007. **61**(21): p. 4267-4271.

224. Nakaoka, Y. and Y. Nosaka, *Electron Spin Resonance Study of Radicals Produced by Photoirradiation on Quantized and Bulk ZnS Particles.* Langmuir, 1997. **13**(4): p. 708-713.

225. Lichtman, J.W. and J.-A. Conchello, *Fluorescence microscopy.* Nat Meth, 2005. **2**(12): p. 910-919.

226. Taylor, D.L. and E.D. Salmon, eds. *Basic fluorescence microscopy*. Methods in Cell Biology., ed. Y.-L. Wang and D.L. Taylor. Vol. 29. 1989, Academic Press, Inc.,: Boston. 207-237.

227. Birks, J.B., *The Photophysics of Aromatic Molecules*. 1970, London: Wiley.

228. Nakashima, K., K. Yuda, Y. Ozaki, and I. Noda, *Two-dimensional fluorescence correlation spectroscopy II: spectral analysis of derivatives of anthracene and pyrene in micellar solutions.* Spectrochimica Acta Part A: Molecular and Biomolecular Spectroscopy, 2004. **60**(8-9): p. 1783-1791.

229. Birch, D.J.S., *Multiphoton excited fluorescence spectroscopy of biomolecular systems.* Spectrochimica Acta Part A: Molecular and Biomolecular Spectroscopy, 2001. **57**(11): p. 2313-2336.

230. Baker, A., *Fluorescence Excitation−Emission Matrix Characterization of Some Sewage-Impacted Rivers.* Environmental Science & Technology, 2001. **35**(5): p. 948-953.

231. Lu, X. and R. Jaffe, *Interaction between Hg(II) and natural dissolved organic matter: a fluorescence spectroscopy based study.* Water Research, 2001. **35**(7): p. 1793-1803.

232. Peuravuori, J., R. Koivikko, and K. Pihlaja, *Characterization, differentiation and classification of aquatic humic matter separated with different sorbents: synchronous scanning fluorescence spectroscopy.* Water Research, 2002. **36**(18): p. 4552-4562.

233. Sharpless, C.M. and L.B. McGown, *Effects of Aluminum-Induced Aggregation on the Fluorescence of Humic Substances.* Environmental Science & Technology, 1999. **33**(18): p. 3264-3270.

234. Andrade, J.J., J. A. G. Brasil, P.M.A. Farias, A. Fontes, and B.S. Santos, *Synthesis and characterization of blue emitting ZnSe quantum dots.* Microelectron. J., 2009. **40**(3): p. 641-643.

235. Durrant, P.J. and B. Durrant, *Introduction to Advanced Inorganic Chemistry*. 1962, New York: Wiley.

236. Ohta, T., D.A. Schmidt, S. Meng, A. Klust, A. Bostwick, Q. Yu, M.A. Olmstead, and F.S. Ohuchi, *Intrinsic Vacancy-Induced Nanoscale Wire Structure in Heteroepitaxial Ga2Se3/Si(001).* Physical Review Letters, 2005. **94**(11): p. 116102.

237. Gurusinghe, N.P., N.N. Hewa-Kasakarage, and M. Zamkov, *Composition-Tunable Properties of CdSxTe1−x Alloy Nanocrystals.* The Journal of Physical Chemistry C, 2008. **112**(33): p. 12795-12800.

238. Bae, Y., N. Myung, and A.J. Bard, *Electrochemistry and Electrogenerated Chemiluminescence of CdTe Nanoparticles*. Nano Letters, 2004. **4**(6): p. 1153-1161.

239. Admassie, S., O. Inganäs, W. Mammo, E. Perzon, and M.R. Andersson, *Electrochemical and optical studies of the band gaps of alternating polyfluorene copolymers*. Synthetic Metals, 2006. **156**(7-8): p. 614-623.

240. Misra, A., P. Kumar, R. Srivastava, S.K. Dhawan, M.N. Kamalasanan, and S. Chandra, *Electrochemical and optical studies of conjugated polymers for three primary colours.* Indian Journal of pure and Applied Physics, 2005. **43**: p. 921-925.

241. Erol, K., R. Jürgen, U.G. A, and N. Thomas, *Determination of quantum confinement in CdSe nanocrystals by cyclic voltammetry*. journal of Chemical Physics, 2003. **19**: p. 2333-2337.

242. Bredas, J.L., R. Silbey, D.S. Boudreaux, and R.R. Chance, *Chain-length dependence of electronic and electrochemical properties of conjugated systems: polyacetylene, polyphenylene, polythiophene, and polypyrrole.* Journal of the American Chemical Society, 1983. **105**(22): p. 6555-6559.

243. Laviron, E., *The use of linear potential sweep voltammetry and of a.c. voltammetry for the study of the surface electrochemical reaction of strongly adsorbed systems and of redox modified electrodes*. Journal of Electroanalytical Chemistry, 1979. **100**(1-2): p. 263-270.

244. Greef, R., R. Peat, L.M. Peter, D. Pletcher, and J. Robinson, eds. *Instruental methods in electrochemistry*. Elis Horwood Series in Physical Chemistry, ed. T.J. Kemp. 1990, Elis Horwood: New York.

245. Dong, S. and J. Li, *Self-assembled monolayers of thiols on gold electrodes for bioelectrochemistry and biosensors*. Bioelectrochemistry and Bioenergetics, 1997. **42**(1): p. 7-13.

246. Laviron, E. and L. Roullier, *Electrochemical reactions with adsorption of the reactants and electrosorption. Simple analytical solutions for a Henry isotherm.* Journal of Electroanalytical Chemistry, 1998. **443**(2): p. 195-207.

247. Aoki, K., K. Tokuda, and H. Matsuda, *Theory of stationary current-potential curves at microdisk electrodes for quasi-reversible and totally irreversible electrode reactions.* Journal of Electroanalytical Chemistry and Interfacial Electrochemistry, 1987. **235**(1-2): p. 87-96.

248. Osipovich, N.P., A. Shavel, S.K. Poznyak, N. Gaponik, and A. Eychmüller, *Electrochemical Observation of the Photoinduced Formation of Alloyed ZnSe(S) Nanocrystals*. The Journal of Physical Chemistry B, 2006. **110**(39): p. 19233-19237.

249. Ndangili, P.M., A.M. Jijana, P.G.L. Baker, and E.I. Iwuoha, *3-Mercaptopropionic acid capped ZnSe quantum dot-cytochrome P450 3A4 enzyme biotransducer for 17[beta]-estradiol.* Journal of Electroanalytical Chemistry, 2011. **653**(1-2): p. 67-74.

250. Ndangili, P.M., O.A. Arotiba, P.G.L. Baker, and E.I. Iwuoha, *A potential masking approach in the detection of dopamine on 3-mercaptopropionic acid capped ZnSe quantum dots modified gold electrode in the presence of interferences.* Journal of Electroanalytical Chemistry, 2010. **643**(1-2): p. 77-81.

251. Lyons, M.E.G. and G.P. Keeley, *The Redox Behaviour of Randomly Dispersed Single Walled Carbon Nanotubes both in the Absence and in the Presence of Adsorbed Glucose Oxidase*. Sensors, 2006. **6**: p. 1791-1826.

252. Christian Henke, C.S., Andreas Janshoff, Gerhard Steffan, Heinrich Luftmann, Manfred Sieber, and Hans-Joachim Galla, *Self-Assembled Monolayers of Monofunctionalized Cyclodextrins onto Gold: A Mass Spectrometric Characterization and Impedance Analysis of Host−Guest Interaction.* Analytical Chemistry, 1996. **68** (18): p. 3158–3165.

253. Sabatani, E., J. Cohen-Boulakia, M. Bruening, and I. Rubinstein, *Thioaromatic monolayers on gold: a new family of self-assembling monolayers.* Langmuir, 2002. **9**(11): p. 2974-2981.

254. Kim, C.-e., K. Kurosaki, M. Ishimaru, H. Muta, and S. Yamanaka, *Effect of Vacancy Distribution on the Thermal Conductivity of Ga2Te3 and Ga2Se3.* Journal of Electronic Materials, 2011. **40**(5): p. 999-1004.

255. Gaponik, N., S.K. Poznyak, N.P. Osipovich, A. Shavel, and A. Eychmüller, *Electrochemical probing of thiol-capped nanocrystals.* Microchimica Acta, 2008. **160**(3): p. 327-334.

256. Wang, J., M. Musameh, and Y. Lin, *Solubilization of Carbon Nanotubes by Nafion toward the Preparation of Amperometric Biosensors.* Journal of the American Chemical Society, 2003. **125**(9): p. 2408-2409.

257. Gosser, J.D.K., *Cyclic Voltammetry :simulations and Analysis of Reaction Mechanisms*. 1993, Newyork: VCH Publishers Inc.

258. Ozoemena, K.I., *Recent advances in analytical electrochemistry*. 2007, Transworld Research Network: Kerala.

259. Sabatani, E., J. Cohen-Boulakia, M. Bruening, and I. Rubinstein, *Thioaromatic monolayers on gold: a new family of self-assembling monolayers.* Langmuir, 1993. **9**(11): p. 2974-2981.

260. Beri, R.K., P. More, B.G. Bharate, and P.K. Khanna, *Band-gap engineering of ZnSe quantum dots via a non-TOP green synthesis by use of organometallic selenium compound.* Current Applied Physics, 2010. **10**(2): p. 553-556.

261. Taheri, S.M. and M.H. Yousefi, *Tuning luminescence of 3d transition-metal doped quantum particles: Ni+2: CdS and Fe+3: CdS.* Brazilian Journal of Physics, 2010. **40**: p. 301-305.

262. Ghosh, S., D. Ghosh, P.K. Bag, S.C. Bhattacharya, and A. Saha, *Aqueous synthesis of ZnTe/dendrimer nanocomposites and their antimicrobial activity: implications in therapeutics.* Nanoscale, 2010. **3**: p. 1139-1148.

263. Gujar, T.P., V.R. Shinde, J.-W. Park, H.K. Lee, K.-D. Jung, and O.-S. Joo, *Electrodeposition of photoactive 1D gallium selenide quantum dots*. Electrochimica Acta, 2008. **54**(2): p. 829-834.

264. Jiang, Y., X.-M. Meng, W.-C. Yiu, J. Liu, J.-X. Ding, C.-S. Lee, and S.-T. Lee, *Zinc Selenide Nanoribbons and Nanowires*. The Journal of Physical Chemistry B, 2004. **108**(9): p. 2784-2787.

265. Wageh, S., L. Shu-Man, F.T. You, and X. Xu-Rong, *Optical properties of strongly luminescing mercaptoacetic-acid-capped ZnS nanoparticles.* Journal of Luminescence, 2003. **102-103**: p. 768-773.

266. Brito, R., R. Tremont, O. Feliciano, and C.R. Cabrera, *Chemical derivatization of self-assembled 3-mercaptopropionic and 16-mercaptohexadecanoic acids at platinum*

surfaces with 3-aminopropyltrimethoxysilane: a spectroscopic and electrochemical study. Journal of Electroanalytical Chemistry, 2003. **540**: p. 53-59.

267. Sainsbury, T., T. Ikuno, D. Okawa, D. Pacile´, J.M.J. Fre´chet, and A. Zettl, *Self-Assembly of Gold Nanoparticles at the Surface of Amine-and thiol-Functionalized Boron Nitride Nanotubes.* Journal of Physical Chemistry, 2007. **111**: p. 12992-12999.

268. Li, H., W.Y. Shih, and W.-H. Shih, *Stable aqueous ZnS quantum dots obtained using (3-mercaptopropyl)trimethoxysilane as a capping molecule*. Nanotechnology, 2007(49): p. 495605.

269. Haram, S.K., A. Kshirsagar, Y.D. Gujarathi, P.P. Ingole, O.A. Nene, G.B. Markad, and S.P. Nanavati, *Quantum Confinement in CdTe Quantum Dots: Investigation through Cyclic Voltammetry Supported by Density Functional Theory (DFT).* The Journal of Physical Chemistry C, 2011. **115**(14): p. 6243-6249.

270. Inamdar, S.N., P.P. Ingole, and S.K. Haram, *Determination of Band Structure Parameters and the Quasi-Particle Gap of CdSe Quantum Dots by Cyclic Voltammetry*. ChemPhysChem, 2008. **9**(17): p. 2574-2579.

271. Querner, C., P. Reiss, S. Sadki, M. Zagorska, and A. Pron, *Size and ligand effects on the electrochemical and spectroelectrochemical responses of CdSe nanocrystals.* Physical Chemistry Chemical Physics, 2005. **7**(17): p. 3204-3209.

272. Kuçur, E., W. Bücking, S. Arenz, R. Giernoth, and T. Nann, *Heterogeneous Charge Transfer of Colloidal Nanocrystals in Ionic Liquids.* ChemPhysChem, 2006. **7**(1): p. 77-81.

273. Shalom, M., S. Rühle, I. Hod, S. Yahav, and A. Zaban, *Energy Level Alignment in CdS Quantum Dot Sensitized Solar Cells Using Molecular Dipoles.* Journal of the American Chemical Society, 2009. **131**(29): p. 9876-9877.

274. Markus, T.Z., M. Wu, L. Wang, D.H. Waldeck, D. Oron, and R. Naaman, *Electronic Structure of CdSe Nanoparticles Adsorbed on Au Electrodes by an Organic Linker: Fermi Level Pinning of the HOMO.* The Journal of Physical Chemistry C, 2009. **113**(32): p. 14200-14206.

275. Franceschetti, A. and A. Zunger, *Pseudopotential calculations of electron and hole addition spectra of InAs, InP, and Si quantum dots.* Physical Review B, 2000. **62**(4): p. 2614.

276. Wan, B., C. Hu, B. Feng, J. Xu, Y. Zhang, and Y. Tian, *Optical properties of ZnTe nanorods synthesized via a facile low-temperature solvothermal route.* Materials Science and Engineering: B, 2010. **171**(1-3): p. 11-15.

277. Bang, J., J. Park, J.H. Lee, N. Won, J. Nam†, J. Lim, B.Y. Chang, H.J. Lee, Bonghwan Chon, J. Shin, J.B. Park, J.H. Choi, K. Cho, S.M. Park, T. Joo, and S. Kim, *ZnTe/ZnSe (Core/Shell) Type-II Quantum Dots: Their Optical and Photovoltaic Properties.* Chemistry of Materials, 2010. **22**: p. 233–240.

278. Dantas, N.O., A. dos Santos Silva, S.W. da Silva, P. César de Morais, M.A. Pereira-da-Silva, and G. Eugênio Marques, *ZnTe nanocrystal formation and growth control on UV-transparent substrate*. Chemical Physics Letters, 2010. **500**(1-3): p. 46-48.

279. Yu, W.W., E. Chang, R. Drezek, and V.L. Colvin, *Water-soluble quantum dots for biomedical applications.* Biochemical and Biophysical Research Communications, 2006. **348**(3): p. 781-786.

280. Yue, L.-y., Z.-c. Zhang, and X. Chen, *Absorption and fluorescence spectra of gallium phosphide(GaP) nanoparticles.* Transactions of Nonferrous Metals Society of China, 2006. **16**(4): p. 863-867.

281. Griesebock, B., M. Egen, and R. Zentel, *Large Photonic Films by Crystallization on Fluid Substrates.* Chemistry of Materials, 2002. **14**(10): p. 4023-4025.

282. Nelson, E.C., F. García-Santamaría, and P.V. Braun, *Lattice-Registered Two-Photon Polymerized Features within Colloidal Photonic Crystals and Their Optical Properties.* Advanced Functional Materials, 2008. **18**(13): p. 1983-1989.

283. Moeno, S. and T. Nyokong, *The photophysical studies of a mixture of CdTe quantum dots and negatively charged zinc phthalocyanides*. Polyhedron, 2008. **27**: p. 1953-1958.

284. Li, H., W.Y. Shih, and W.-H. Shih, *Synthesis and Characterization of Aqueous Carboxyl-Capped CdS Quantum Dots for Bioapplications.* Industrial & Engineering Chemistry Research, 2007. **46**(7): p. 2013-2019.

285. Swafford, L.A., L.A. Weigand, M.J. Bowers, J.R. McBride, J.L. Rapaport, T.L. Watt, S.K. Dixit, L.C. Feldman, and S.J. Rosenthal, *Homogeneously Alloyed CdSxSe1-x Nanocrystals: Synthesis, Characterization, and Composition/Size-Dependent Band Gap*. Journal of the American Chemical Society, 2006. **128**(37): p. 12299-12306.

286. Yang, C.C. and S. Li, *Size, Dimensionality, and Constituent Stoichiometry Dependence of Bandgap Energies in Semiconductor Quantum Dots and Wires*. The Journal of Physical Chemistry C, 2008. **112**(8): p. 2851-2856.

287. Bailey, R.E. and S. Nie, *Alloyed Semiconductor Quantum Dots: Tuning the Optical Properties without Changing the Particle Size*. Journal of the American Chemical Society, 2003. **125**(23): p. 7100-7106.

288. Byun, H.-J., W.-S. Song, and H. Yang, *Facile consecutive solvothermal growth of highly fluorescent InP/ZnS core/shell quantum dots using a safer phosphorus source.* Nanotechnology, 2011. **22**: p. 235605- 235610.

289. Adam, S., D.V. Talapin, H. Borchert, A. Lobo, C. McGinley, A.R.B. de Castro, M. Haase, H. Weller, and T. Moller, *The effect of nanocrystal surface structure on the luminescence properties: Photoemission study of HF-etched InP nanocrystals.* The Journal of Chemical Physics, 2005. **123**(8): p. 084706-10.

290. Talapin, D.V., N. Gaponik, H. Borchert, A.L. Rogach, M. Haase, and H. Weller, *Etching of Colloidal InP Nanocrystals with Fluorides: Photochemical Nature of the Process Resulting in High Photoluminescence Efficiency*. The Journal of Physical Chemistry B, 2002. **106**(49): p. 12659-12663.

291. Pandurangachar, M., B.E.K. Swamy, U. Chandra, O. Gilbert, and B.S.Sherigara, *Simultaneous Determination of Dopamine, Ascorbic Acid and Uric Acid at Poly(Patton and Reeder's) modified Carbon Paste Electrode.* International Journal of Electrochemical Society, 2009. **4**: p. 672 - 683.

292. Zhang, R., G.-D. Jin, D. Chen, and X.-Y. Hu, *Simultaneous electrochemical determination of dopamine, ascorbic acid and uric acid using poly(acid chrome blue K) modified glassy carbon electrode.* Sensors and Actuators B: Chemical, 2009. **138**(1): p. 174-181.

293. Guan, C.L., J. Ouyang, Q.L. Li, B.H. Liu, and W.R.G. Baeyens, *Simultaneous determination of catecholamines by ion chromatography with direct conductivity detection.* Talanta, 2000. **50**(6): p. 1197-1203.

294. Wu, K. and S. Hu, *Electrochemical Study and Selective Determination of Dopamine at a Multi-Wall Carbon Nanotube-Nafion Film Coated Glassy Carbon Electrode.* Journal of Microchimica Acta, 2004. **144**: p. 131–137.

295. Huang, J., Y. Liu, H. Hou, and T. You, *Simultaneous electrochemical determination of dopamine, uric acid and ascorbic acid using palladium nanoparticle-loaded carbon nanofibers modified electrode.* Biosensors and Bioelectronics, 2008. **24**(4): p. 632-637.

296. Songa, E.A., O.A. Arotiba, O.J.H. O, N. Jahed, P.G.L. Baker, and E.I. Iwuoha, *Electrochemical detection of glyphosate herbicide using horseradish peroxidase immobilized on sulfonated polymer matrix.* Bioelectrochemistry 2009. **75**: p. 117-123.

297. Owino, J.H.O., O.A. Arotiba, N. Hendricks, E.A. Songa, N. Jahed, T.T. Waryo, R.F. Ngece, P.G.L. Baker, and E.I. Iwuoha, *Electrochemical Immunosensor Based on Polythionine/Gold Nanoparticles for the Determination of Aflatoxin B1.* Sensors, 2008. **8**(12): p. 8262-8274.

298. Arotiba, O.A., E.A. Songa, P.G. Baker, and E.I. Iwuoha, *Dendrimeric gold-poly(propylene imine) electrochemical DNA nanobiosensor.* chimica oggi • Chemistry Today •, 2009. **27**: p. 55-58

299. Ge, P.-Y., Y. Du, J.-J. Xu, and H.-Y. Chen, *Selective detection of dopamine based on the unique property of gold nanofilm.* Journal of Electroanalytical Chemistry, 2009. **633**(1): p. 182-186.

300. Gilbert, O., B.E. Kumara Swamy, U. Chandra, and B.S. Sherigara, *Simultaneous detection of dopamine and ascorbic acid using polyglycine modified carbon paste electrode: A cyclic voltammetric study.* Journal of Electroanalytical Chemistry, 2009. **636**(1-2): p. 80-85.

301. Shankar, S., B.E. Kumara Swamy, U. Chandra, J.G.Manjunatha, and B.S. Sherigara, *Simultaneous Determination of Dopamine, Uric Acid and Ascorbic Acid with CTAB Modified Carbon Paste Electrode*. International Journal of Electrochemical Society, 2009. **4**: p. 592 - 601.

302. Zare, H.R., N. Nasirizadeh, and M. Mazloum Ardakani, *Electrochemical properties of a tetrabromo-p-benzoquinone modified carbon paste electrode. Application to the simultaneous determination of ascorbic acid, dopamine and uric acid.* Journal of Electroanalytical Chemistry, 2005. **577**(1): p. 25-33.

303. Drbohlavova, J., V. Adam, R. Kizek, and J. Hubalek, *Quantum dots - characterization, preparation and usage in biological systems.* International Journal of Molecular Sciences, 2009. **10**(2): p. 656-673.

304. Lai, Y., Y. Yu, P. Zhong, J. Wu, Z. Long, and C. Liang, *Development of Novel Quantum Dots as Fluorescent Sensors for Application in Highly Sensitive Spectrofluorimetric Determination of Cu²*. Analytical Letters, 2006. **39**(6): p. 1201 - 1209.

305. Huang, C., C. Wu, J. Lai, S. Li, J. Zhen, and Y. Zhao, *CdS Quantum Dots as Fluorescence Probes for the Detection of Selenite.* Analytical Letters, 2008. **41**(11): p. 2117 - 2132.

306. Tang, C.-F., S.A. Kumar, and S.-M. Chen, *Zinc oxide/redox mediator composite films-based sensor for electrochemical detection of important biomolecules.* Analytical Biochemistry, 2008. **380**(2): p. 174-183.

307. Tsou, Y.-M. and F.C. Anson, *Shifts in Redox Formal Potentials Accompanying the Incorporation of Cationic Complexes in Perfluoro Polycarboxylate and Polysulfonate*

Coatings on Graphite Electrodes. Journal of the Electrochemical Society, 1984. **131**(3): p. 595-601.

308. Cao, X., L. Luo, Y. Ding, X. Zou, and R. Bian, *Electrochemical methods for simultaneous determination of dopamine and ascorbic acid using cetylpyridine bromide/chitosan composite film-modified glassy carbon electrode*. Sensors and Actuators B: Chemical, 2008. **129**(2): p. 941-946.

309. Gopalan, A.I., K.-P. Lee, K.M. Manesh, P. Santhosh, J.H. Kim, and J.S. Kang, *Electrochemical determination of dopamine and ascorbic acid at a novel gold nanoparticles distributed poly(4-aminothiophenol) modified electrode.* Talanta, 2007. **71**(4): p. 1774-1781.

310. Wang, P., Y. Li, X. Huang, and L. Wang, *Fabrication of layer-by-layer modified multilayer films containing choline and gold nanoparticles and its sensing application for electrochemical determination of dopamine and uric acid*. Talanta, 2007. **73**(3): p. 431-437.

311. Shervedani, R.K., M. Bagherzadeh, and S.A. Mozaffari, *Determination of dopamine in the presence of high concentration of ascorbic acid by using gold cysteamine self-assembled monolayers as a nanosensor.* Sensors and Actuators B: Chemical, 2006. **115**(2): p. 614-621.

312. Planz, G. and R. Planz, *Dopamine-β-hydroxylase, adrenaline, noradrenaline and dopamine in the venous blood of adrenal gland of man: A comparison with levels in the periphery of the circulation* Journal of Cellular and Molecular Life Sciences, 1979. **35**: p. 207-208.

313. Ueno, K., S. Tokuchi, K. Saiki, and A. Koma, *Epitaxial growth of a vacancy-ordered Ga2Se3 thin film on a vicinal Si(0 0 1) substrate*. Journal of Crystal Growth, 2002. **237-239**(Part 2): p. 1610-1614.

314. Wright, A.C., J.O. Williams, A. Krost, W. Richter, and D.R.T. Zahn, *High resolution and conventional transmission electron microscopy of Ga2Se3 thin films grown by vapour phase epitaxy*. Journal of Crystal Growth, 1992. **121**(1-2): p. 111-120.

315. Park, J.-H., M. Afzaal, M. Helliwell, M.A. Malik, P. O'Brien, and J. Raftery, *Chemical Vapor Deposition of Indium Selenide and Gallium Selenide Thin Films from Mixed Alkyl/Dialkylselenophosphorylamides*. Chemistry of Materials, 2003. **15**(22): p. 4205-4210.

316. Märkl, A., M. von der Emde, C. Nowak, W. Richter, and D.R.T. Zahn, *Investigation of Se capping of epitaxial Ga2Se3 layers*. Surface Science, 1995. **331-333**(Part 1): p. 631-635.

317. Afifi, M.A., A.E. Bekheet, H.T. El-Shair, and I.T. Zedan, *Determination and analysis of optical constants for Ga2Se3 films near absorption edge*. Physica B: Condensed Matter, 2003. **325**: p. 308-318.

318. Rusu, M., S. Wiesner, S. Lindner, E. Strub, J. R¨ohrich, RW¨urz, WFritsch, W. Bohne, T. Schedel-Niedrig, M.C. Lux-Steiner, C. Giesen, and M. Heuken, *Deposition and characterization of Ga2Se3 thin films prepared by a novel chemical close-spaced vapour transport technique*. Journal of Physics: Condensed Matter, 2003 **15**: p. 8185-8193.

319. Raoof, J.-B., M.S. Hejazi, R. Ojani, and E.H. Asl, *A Comparative Study of Carbon Nanotube paste Electrode for Development of Indicator-free DNA Sensors Using DPV*

and EIS: Human Interleukin-2 Oligonucleotide as a Model. International Journal of Electrochemical Science, 2009. **4**: p. 1436-1451.

320. Widmer, F., R.J. Seidler, K.K. Donegan, and G.L. Reed, *Quantification of transgenic plant marker gene persistence in the field.* Molecular Ecology, 1997. **6**: p. 1-7.

321. Gebhard, F. and K. Smalla, *Monitoring field releases of genetically modified sugar beets for persistence of transgenic plant DNA and horizontal gene transfer.* FEMS Microbiol Ecology, 1999. **28**: p. 261-272.

322. Quist, D. and I.H. Chapela, *Transgenic DNA introgressed into traditional maize landraces in Oaxaca, Mexico.* Nature 2001. **414**: p. 541-543.

323. Vaı¨tilingom, M., H. Pijnenburg, F. Gendre, and P. Brignon, *Realtime quantitative PCR detection of genetically modified Maximizer maize and Roundup Ready soybean in some representative foods.* Journal of Agricultural and Food Chemistry, 1999. **47**: p. 5261-5266.

324. Permingeat, H.R., M.I. Reggiardo, and R.H. Vallejos, *Detection and quantification of transgenes in grains by multiplex and realtime PCR.* Journal of Agricultural and Food Chemistry 2002. **50**: p. 4431-4436.

325. Duggan, P.S., P.A. Chambers, J. Heritage, and J.M. Forbes, *Survival of free DNA encoding antibiotic resistance from transgenic maize and the transformation activity of DNA in ovine saliva, ovine rumen fluid and silage effluent.* FEMS Microbiology Letters, 2000. **191**: p. 71-77.

326. Minunni, M., S. Tombelli, E. Mariotti, and M. Mascini, *Biosensors as new analytical tool for detection of Genetically Modified Organisms (GMOs).* Fresenius' Journal of Analytical Chemistry, 2001. **369** p. 589-593.

327. Mannelli, I., M. Minunni, S. Tombelli, and M. Mascini, *Quartz crystal microbalance (QCM) affinity biosensor for genetically modified organisms (GMOs) detection.* Biosensors and Bioelectronics, 2003. **18**(2-3): p. 129-140.

328. Giakoumaki, E., M. Minunni, S. Tombelli, I.E. Tothill, M. Mascini, P. Bogani, and M. Buiatti, *Combination of amplification and post-amplification strategies to improve optical DNA sensing.* Biosensors and Bioelectronics, 2003. **19**(4): p. 337-344.

329. Feriotto, G., M. Borgatti, C. Mischiati, N. Bianchi, and R. Gambari, *Biosensor Technology and Surface Plasmon Resonance for Real-Time Detection of Genetically Modified Roundup Ready Soybean Gene Sequences.* Journal of Agricultural and Food Chemistry, 2002. **50**(5): p. 955-962.

330. Gerion, D., W.J. Parak, S.C. Williams, D. Zanchet, C.M. Micheel, and A.P. Alivisatos, *Sorting Fluorescent Nanocrystals with DNA.* Journal of the American Chemical Society, 2002. **124**(24): p. 7070-7074.

331. Sassolas, A., B.D. Leca-Bouvier, and L.J. Blum, *DNA Biosensors and Microarrays.* Chemical Reviews, 2007. **108**(1): p. 109-139.

332. Fan, C., K.W. Plaxco, and A.J. Heeger, *Biosensors based on binding-modulated donor-acceptor distances.* Trends in Biotechnology, 2005. **23**(4): p. 186-192.

333. Ziyatdinova, G., J. Galandova, and J. Labuda, *Impedimetric Nanostructured Disposable DNA-based Biosensors for the Detection of Deep DNA Damage and Effect of Antioxidants.* International Journal of Electrochemical Science, 2008. **3**: p. 223-235.

334. Vagin, M.Y., A.A. Karyakin, and T. Hianik, *Surfactant bilayers for the direct electrochemical detection of affinity interactions.* Bioelectrochemistry, 2002. **56**(1-2): p. 91-93.

335. Pan, S. and L. Rothberg, *Chemical Control of Electrode Functionalization for Detection of DNA Hybridization by Electrochemical Impedance Spectroscopy*. Langmuir, 2005. **21**(3): p. 1022-1027.

336. Lee, T.-Y. and Y.-B. Shim, *Direct DNA Hybridization Detection Based on the Oligonucleotide-Functionalized Conductive Polymer*. Analytical Chemistry, 2001. **73**(22): p. 5629-5632.

337. Abbaspour, A., M.A. Mehrgardi, and R. Kia, *Electrocatalytic oxidation of guanine and ss-DNA at a cobalt (II) phthalocyanine modified carbon paste electrode*. Journal of Electroanalytical Chemistry, 2004. **568**: p. 261-266.

338. Ferapontova, E.E. and E. Domínguez, *Direct Electrochemical Oxidation of DNA on Polycrystalline Gold Electrodes*. Electroanalysis, 2003. **15**(7): p. 629-634.

339. Ndangili, P.M., A.N. Jijana, R.A. Olowu, S.N. Mailu, F.R. Ngece, A. Williams, T.T. Waryo, P.G.L. Baker, and E.I. Iwuoha, *Impedimetric Response of a Label-Free Genosensor Prepared on a 3-Mercaptopropionic Acid Capped Gallium Selenide Nanocrystal Modified Gold Electrode*. International Journal of Electrochemical Science, 2011. **6**: p. 1438 - 1453.

340. Arotiba, O.A., P.G. Baker, B.B. Mamba, and E.I. Iwuoha, *The Application of Electrodeposited Poly(Propylene imine) Dendrimer as an Immobilisation Layer in a Simple Electrochemical DNA Biosensor*. International Journal of Electrochemical Science, 2011. **2011**: p. 673 - 683.

341. Bonanni, A., M. Esplandiu, M. Pividori, S. Alegret, and M. del Valle, *Impedimetric genosensors for the detection of DNA hybridization*. Analytical and Bioanalytical Chemistry, 2006. **385**(7): p. 1195-1201.

UNIVERSITY of the
WESTERN CAPE